博士論文

Doctorate Dissertation

地球史を通した上部マントルの組成変化と多様性：中央海嶺系・沈み込み帯初期由来マントルと太古代カンラン岩からの制約

Compositional change and heterogeneity of the upper mantle throughout Earth's history: Constraints from mantle peridotites from mid-ocean ridges and nascent subduction zones and the Archean ultramafic rocks

金沢大学大学院自然科学研究科

自然システム学専攻

Division of Natural System,

Graduate School of Natural Science and Technology,

Kanazawa University

学籍番号　2124062007

氏名　西尾　郁也　Ikuya Nishio

主任指導教員名　森下知晃　Tomoaki Morishita

提出年月　2024 年 1 月

Contents

List of Figures

List of Tables

Abstract

Thermal history of the Earth is the one of most important issues in geoscience. Assessing how hot the early Earth was compared to the present Earth and identifying the timing and mechanisms behind these temperature shifts are critical for understanding Earth's thermal history. The mantle transfers heat to the surface by convection, which affects to plate tectonics and in turn, plate tectonics affects the thermal state of the mantle. Plate tectonics is the unique feature of the Earth in the solar system. Nevertheless, understanding the geodynamics of the early Earth remains a central, unsolved problem (e.g., Korenaga, 2013; Palin et al., 2020). Understanding of the geological evolution of the lithosphere and the processes behind plate tectonics requires knowledge of the structure, composition, and secular evolution of the lithosphere (e.g., Walter, 2014).

This study delves into the heterogeneity and diversity of lithospheric mantle from different geological setting or ages, to understand the importance and difference of mantle processes such as partial melting, metasomatism, melt-rock reaction, fluids, and recycling. The investigation focuses on abyssal peridotites from mid-ocean ridges, ultra-depleted peridotites from supra-subduction zone ophiolites, and Archean ultramafic rocks from Greenland. Abyssal peridotites are best understood through the data accumulation of large numbers of scientific cruises, which facilitates statistical evaluation of the contributions of mantle processes (Warren, 2016). Ultra-depleted mantle peridotites from supra-subduction zone ophiolites represent endmembers of the oceanic lithosphere. Their formation processes are not well understood, but they are important for understanding the mantle conditions during the subduction initiation. The Archean ultramafic rocks in Greenland prompt an examination of their formation dynamics, yet the cumulative origin vs. residual origin remains unsolved. This research contributes to a nuanced understanding of mantle evolution by scrutinizing diverse rock samples and their geological contexts.

Chapter 2 studied abyssal peridotites that come from the Earth's mantle, beneath the oceanic crust. They are exposed on the seafloor near mid-ocean ridges, the sites at which new oceanic crust forms by melting the mantle below. A large database of chemical analyses of clinopyroxenes from these abyssal peridotites was analyzed using multivariate statistical methods to understand what controls their chemical composition. The results simplify the complex chemical variations in these clinopyroxenes to just two main variables. The first group (85% of the clinopyroxene database) can be explained by forming in mantle rocks that melted by varying degrees during the melting process that leads to the formation of oceanic crust. The second group (15% of the clinopyroxene database) cannot be explained by simple melting processes. Instead, these mantle rocks were first partially melted, and then reacted with melts that originated deeper in the mantle and passed through them. All clinopyroxene groups are present in most mid-ocean ridges, showing that the composition of abyssal peridotites is variable even on each ridge.

Chapter 3 studied mineral major and trace element compositions of ultra-depleted peridotites from the Kamuikotan zone, Japan to elucidate mantle process and the role of water in the mantle during subduction initiation. Geochemical models were then generated to constrain the melting conditions and their relation to boninitic melts. The peridotites are characterized by minerals with high Mg/Fe and Cr/Al ratios, and olivine and orthopyroxene with low Ti and Y contents. The mineral compositions suggest that these peridotites are among the most depleted peridotites on Earth. Orthopyroxene compositions characterized by Zr and Sr enrichments relative to Ti and Y depletion cannot be solely explained by melt extraction from typical mantle compositions. Modeling of influx melting reproduces orthopyroxene trace element compositions of ultra-depleted harzburgites formed after high degrees (>30%) of slab-fluid influx melting at a low influx rate and melt fraction. The instantaneous fractional melts equilibrated with residues produced by the melting model and the melts, which equilibrated with amphiboles have similar trace elements patterns as boninites. However, the instantaneous fractional melts have low trace element abundances indicating that ultra-depleted harzburgites are residues after extraction of refractory melts. Boninites are probably accumulated melts formed during the melting processes, or fractionated melt from the instantaneous fractional melts. High temperatures and continuous fluid supply are key to the formation of ultra-depleted peridotites and boninites during subduction initiation.

Chapter 4 and 5 studied numerous ultramafic rocks occurring as lens-shaped bodies in the Archean continental crust from southern West Greenland. As some of the oldest exposed ultramafic bodies, determining their origin, as mantle segments or magmatic cumulates, is an important yet controversial issue. The origin of these Archean ultramafic rocks remains unclear, in-part because these rocks have undergone metasomatic modification since their formation, yet the effects of this metasomatism have so far not been assessed in detail, despite being crucial for understanding their geochemical evolution. Petrology, mineral and whole-rock chemistry of the largest ultramafic body located within the Mesoarchean Akia terrane, known as the Ulamertoq and Ujaragssuit Nunât layered ultramafic body, were examined to elucidate the poly-metamorphic and metasomatic events that overprinted the protolith and origin of the rocks. Pronounced lithologic zoning from hydrous mineral-rich layers to orthopyroxene-rich ultramafic rocks at the boundaries between ultramafic rocks and the granitoid country rocks was formed locally by metasomatic reactions related to the granitoids. The main body of ultramafic rocks away from the contacts, the fine-grained orthopyroxene aggregates and large poikilitic orthopyroxenes have low Cr_2O_3 and CaO contents, suggesting a secondary origin. Lithological and compositional variations represent differences in the proportions of metasomatic orthopyroxene and/or amphibole and phlogopite added to a cumulative dunitic protolith. This petrological work demonstrates that it is important to consider the effects of multi-stage metasomatism and metamorphism in order to elucidate the origin of the Archean ultramafic rocks in Greenland and elsewhere. We then studied the Ujaragssuit Nunât layered ultramafic body from southern West Greenland, which contains some of Earth's oldest chromitites, and collated large chromitite dataset to investigate their parental magma compositions and tectonic settings. Spinel major and trace elements and whole-rock platinum

group element (PGE) compositions in the Ujaragssuit samples were altered by metamorphic and metasomatic events, overprinting the primary igneous compositions in most ultramafic rocks except for massive chromitites. Both Ujaragssuit massive chromitites and other Archean to Proterozoic layered intrusion chromitites show high Cr# and Ti/V ratio in spinel, and high whole-rock Ir contents. These features are consistent with komatiitic parental magmas and indicate their formation in plume settings. Geochemical links between layered intrusions, komatiites, TTG, and depleted cratonic mantle peridotites indicate that komatiitic magma played an important role in the formation of cratons and layered intrusions represent a missing complement to depleted cratonic mantle.

Acknowledgement

I would like to express my sincere gratitude to the many individuals who have contributed to the completion of this doctoral thesis.

First and foremost, I am deeply thankful to my two supervisors, Tomoaki Morishita and Kristoffer Szilas, whose guidance and unwavering support have been invaluable throughout my PhD. Thank you for offering many opportunities, that have not only shaped this thesis but has also had a profound impact on my growth as a researcher.

I extend my appreciation to Keita Itano, Pedro Waterton, and Akihiro Tamura, for their supervisions, encouragements, insightful feedback. Your expertise and commitment to excellence have enriched the quality of this research.

I would like to thank my colleagues in Kanazawa and Copenhagen for providing me with a stimulating, academic, and fun environment to work in: JM, Sampriti, Aliz, Natasha, Benjamin, Lingyu, Yuesheng, Maja, Smantha, Jesper, Toni, Henrique, and Marie. The exchange of ideas and the cultures made my journey invaluable.

Finally, to my family, friends, and my partner Isa for your incredible support throughout this process. I am truly fortunate to have had such a supportive network. Thank you all for being a part of this significant chapter in my academic and personal life.

Chapter 1

1 Background and motivation

1.1 Thermal state of the Earth's mantle

Thermal history of the Earth is the one of most important issues in geoscience (Cawood et al., 2022; Herzberg et al., 2010; Korenaga, 2013; Ozawa and Nagahara, 2013). Assessing how hot the early Earth was compared to the present Earth and identifying the timing and mechanisms behind these temperature shifts are critical for understanding the evolution of the Earth.

The Earth's mantle is the largest layer of the Earth and is 2900 km thick, accounting for about 82% of the volume and 65% of the mass. It constitutes most of the silicate part of the Earth from the base of the crust (0.6 % of the silicate mass) to the top of the metallic core (Helffrich and Wood, 2001). The mantle transfers heat to the surface by convection and plays an important role for the thermal history of the Earth (e.g., Korenaga, 2013). Thermal evolution models for the Earth's mantle depend on the balance between heat production by radiogenic elements in the mantle and surface heat loss by mantle convection. The thermal state can be estimated by combining petrological and geophysical approaches.

From a geophysical perspective, it is possible to estimate the thermal history of the Earth, encompassing factors such as temperature, pressure, and chemical composition (Korenaga, 2013). The amount of internal heating is often expressed in terms of its relative contribution to the mantle heat flux as $Ur(t) \equiv H(t)/Q(t)$, which is termed the convective Urey ratio. H is internal heating by radioactive elements, Q is surface heat loss by mantle convection, and t is the time of interest. Combining petrological and geophysical data, the present-day Urey ratio was estimated to be 0.23 to 0.38 and a thermal maximum at 2.5–3.0 Ga (Herzberg et al., 2010). The early Earth's mantle was hotter; therefore, the heat flux was greater than the present.

Petrological estimates of Earth's thermal history are based on information from rocks formed in Earth's crust and mantle, or from extraterrestrial materials that have become Earth's parent material. Magma compositions provide information on the mantle potential temperature and temperature-pressure information from metamorphic rocks, and mantle rocks provide geothermal gradients (Boyd, 1973; Brown and Johnson, 2018; Herzberg et al., 2010; Kimura et al., 2017; Mckenzie and Bickle, 1988; Palin et al., 2020).

Herzberg et al. (2010) estimated and compared mantle potential temperatures from non-arc basaltic magmas. They found mantle temperatures of 1500–1600 °C (mantle potential temperature) at 2.5–3 Ga. This suggests that the mantle potential temperature of the early Earth was higher than that of the modern mantle, which is 1350 ± 50 °C for mid-ocean ridges (Langmuir et al., 1992). Komatiites, which are formed by high degrees of partial melting, are rare but observed in the Precambrian geologic units. In contrast, there is only one record of komatiite occurrence in the Phanerozoic period. This temporal distribution provides evidence in support of the concept of a hotter early Earth (e.g., Waterton and Arndt, 2024). Komiya et al. (2004, 1999) also estimated the mantle potential temperature from the pillow basalts associated with the accretionary complex from the Archean geological belt. They proposed that plate tectonics was in operation in the Eoarchean and estimated the mantle potential temperature to be about 1480 °C. However, the onset of plate tectonics remains a subject of ongoing debate, and there is controversy surrounding the geological setting of the studied area (e.g., Webb et al., 2020).

Ophiolites are a suite of temporally and spatially associated ultramafic, mafic, and felsic rocks that represent a portion of the oceanic crust and lithosphere (e.g., Dilek and Furnes, 2014; Furnes et al., 2014). Their temporal distributions show several restricted periods with increased occurrence, referred to as “ophiolite pulses”. These pulses occur in the late Neoproterozoic, Cambrian-Ordovician, and Jurassic-Cretaceous times (e.g., Vaughan and Scarrow, 2003). Therefore, they can be an indication of the thermal state and its temporal change, Kimura et al. (2020) estimated the thermal state of the upper mantle to be about 1350 ± 40 °C from ultramafic dikes within the Cambrian-Ordovician ophiolite, which is similar to that of the present mid-ocean ridge mantle. However, it should be noted that the formation processes and compositions of ophiolites are diverse, as they are a reflection of the different formation environments (Dilek and Furnes, 2014; Pearce, 2014).

Craton is the oldest parts of the continents, which have been long-lived since their formation in the Archean (e.g., Pearson et al., 2021). The formation of cratons suggests the presence of a cooler early mantle lithosphere, despite the higher temperatures on early Earth. The geothermal gradient observed within Archean cratons appears to be comparable to present cratons. This observation is reinforced by pressure and temperature estimates derived from xenoliths and diamond inclusions, which align closely with the modern cratonic geotherms (e.g., Boyd et al., 1985). However, diamond stabilizes below ~1250 °C at a depth of 150 km, which is insufficient for the hotter Archean mantle condition (Ballard and Pollack, 1988; Hoare et al., 2022). The new geothermal gradient model of Hoare et al. (2022) considers such time-corrected heat production and suggests that the craton was thicker, and the lithosphere-asthenosphere boundary reached up to ~350 km if the mantle potential temperature was 1350 °C in the Archean and the lithosphere has been eroded since then.

The mantle transfers heat to the surface by convection, which affects to plate tectonics, in turn, plate tectonics affects the thermal state of the mantle, resulting in different conditions in each geological setting.

1.2 Composition of the lithospheric mantle

Plate tectonics is characterized by the subduction of oceanic lithosphere and the unique feature of the Earth in the present solar system (Korenaga, 2020). Nevertheless, understanding the geodynamics of the early Earth remains a central, unsolved issue (e.g., Korenaga, 2013; Palin et al., 2020). Understanding of the geological evolution of the lithosphere and the processes behind plate tectonics are therefore crucial. It requires knowledge of the structure, composition, and secular evolution of the lithosphere (e.g., Akizawa, 2023; Walter, 2014).

Mantle-derived rocks occur at the surface, either as tectonic fragments or as xenoliths transported upward by magmatic processes (Bodinier and Godard, 2014; Pearson et al., 2014; Pearson and Nowell, 2002). These rocks are predominantly peridotite and minor portion of eclogite and pyroxenite and variation in mineralogic and chemical composition provide an important constraint on the upper mantle process and condition. Mineralogical and major element variations in mantle peridotites provide strong evidence that melt extraction played a predominant role in the origin of mantle lithosphere of all ages and provenances (Walter, 2014). Modeled peridotite composition at upper most mantle conditions are lherzolite, which contain olivine (50–60 modal %), orthopyroxene and clinopyroxene (30–40 %) and pressure-dependent aluminous mineral (plagioclase, spinel, and garnet) constituting the reminder (e.g., Workman and Hart, 2005). The natural samples generally show compositional differences between samples of the Archean cratonic mantle, younger off-cratonic subcontinental mantle, and modern oceanic mantle. Despite the modeled homogeneous composition and a general trend of depletion with age, the mantle rocks exhibit diverse mineralogical and chemical compositions, demonstrating the heterogeneity of the Earth's mantle (Hofmann, 2014; Walter, 2014; Warren, 2016).

Oceanic mantle is one of the most well understood regions, oceanic mantle has diversity in terms of trace and isotopic compositions as well as major compositions and mineral assemblages (Hofmann, 2014). The study on volcanic rocks demonstrated that the isotopic and trace element chemistry of oceanic basalts indicates that the mantle contains several isotopically and chemically distinct components, reflecting its evolution. This evolution resulted from several factors, including depletion of trace elements during partial melting, possible replenishment from the deeper, less depleted regions, and recycling of oceanic crust and lithosphere. Therefore, understanding the compositional heterogeneity and diversity of peridotites is important direct information for understanding mantle processes and conditions in different geodynamic setting and for estimating the thermal state of the present to early Earth’s mantle.

1.3 Overview of this thesis

1.3.1 Motivation and objective

The mantle heterogeneity is the results of the complex mantle processes. Partial melting is the primary control of the depletion of mantle peridotites (Walter, 2014), but the differences in melting conditions such as pressure, temperature, and the presence or absence of volatiles changes chemical and physical properties of mantle rocks (e.g., Asimow et al., 2004). Other mantle processes such as metasomatism, refertilization, melt-rock reaction, and recycling of older crustal/lithospheric material contribute to the heterogeneity.

There is a general trend of depletion through ages that Archean cratonic mantle is more depleted than present oceanic lithospheric mantle. However, several ultra-depleted peridotites as modern mantle fragments and fertile Archean peridotites have been observed. Therefore, the contribution of mantle processes such as partial melting, metasomatism, melt-rock reaction, role of volatiles, and recycled material should be carefully investigated for a better understanding the evolution of the Earth's mantle. To investigate the to the compositional variations resulting from mantle processes in different settings and ages, I studied abyssal peridotites (Nishio et al., 2022a), ultra-depleted peridotites from supra-subduction zone ophiolites (Nishio et al., 2023), and the Archean ultramafic rocks from southern West (SW) Greenland (Nishio et al., 2022b).

Abyssal peridotites represent the oceanic mantle beneath the mid-ocean ridges, which is the best understood region, and the conditions and processes in the mid-ocean ridge mantle have been studied in detail (e.g., Niu, 2004; Warren, 2016). Therefore, the large database and knowledge of abyssal peridotites allow us to conduct statistical evaluations on the importance of the variable mantle processes, i.e. partial melting, melt-rock reaction, metasomatism and/or recycled materials, that are responsible for the diversity and heterogeneity.

Ultra-depleted mantle peridotites from supra-subduction zone ophiolites represent the endmember of the oceanic mantle (e.g., Barrett et al., 2022). These peridotites are thought to have formed under hydrous conditions during the early stages of oceanic plate subduction. However, their formation process and the generality of these rocks are not well constrained. Furthermore, since these peridotites are depleted to the same extent as cratonic mantle peridotites, it is an important indicator for evaluating the necessity of modern subduction in the formation of the cratonic mantle. I studied the formation process to understand the role of water and temperature-pressure conditions.

The Archean ultramafic rocks in SW Greenland are depleted, but some are fertile. There is ongoing debate as to whether they formed as cumulative peridotites or residual mantle peridotites, and about the geodynamics of the formation. My study is on the causes of the origin and the diversity of these Archean ultramafic rocks to understand the early Earth's geodynamics.

1.3.2 Thesis structure

The following body of this thesis is divided up into five chapters. Chapter 2, 3, 4, and 5 have been individually published or prepared for submission. Each chapter contains its own introduction, result, discussion, and conclusion. In chapter 6, I summarize these works and provide future perspectives.

Chapter 2 is a study of trace element variations in clinopyroxene from abyssal peridotites using the multivariate statistical analysis and geochemical modeling. This chapter has been published in Geochemistry, Geophysics, Geosystems as Ikuya Nishio, Keita Itano, Pedro Waterton, Akihiro Tamura, Kristoffer Szilas, and Tomoaki Morishita (2022) "Compositional Data Analysis (CoDA) of Clinopyroxene From Abyssal Peridotites".

Chapter 3 is a study of the formation process of ultra-depleted peridotite at subduction initiation. This chapter has been published in Journal of Geophysical Research: Solid Earth as Ikuya Nishio, Tomoaki Morishita, Akihiro Tamura, Keita Itano, Shun Takamizawa, Yuji Ichiyama, Shoji Arai, Natasha Barrett, and Kristoffer Szilas (2023) "Formation of Ultra-Depleted Mantle Peridotites and Their Relationship With Boninitic Melts: An Example From the Kamuikotan Unit, Hokkaido, Japan".

Chapter 4 is a study of the complex metasomatic modification of the Archean ultramafic cumulates focusing on silicate mineral chemistry. This chapter has been published in Journal of Petrology as Ikuya Nishio, Tomoaki Morishita, Keita Itano, Juan Miguel Guotana, Akihiro Tamura, Kristoffer Szilas, Yumiko Harigane, Kenichiro Tani, and D. Graham Pearson (2022) "Metasomatic Modification of the Mesoarchean Ulamertoq Ultramafic Body, Southern West Greenland".

Chapter 5 is a study of the Archean layered intrusion focusing on spinel chemistry. This chapter is intended for publication to international journals as Ikuya Nishio, Tomoaki Morishita, Pedro Waterton, Akihiro Tamura, Keita Itano, Simon Hansen Serre, Jane Lund Plesner, Kanta Takahashi, Ken Tani, Yumiko Harigane, Hikaru Sawada, and Kristoffer Szilas "Komatiitic layered intrusions as a missing complement to depleted cratonic mantle".

Chapter 2

2 Trace element variations in clinopyroxene from abyssal peridotites: Insights from multivariate statistical analyses

2.1 Introduction

Mid-ocean ridges are the largest mountain chain and the most active system of volcanoes in the solar system and are products of the separation and spreading of tectonic plates, playing a significant role in the Earth's system (Searle, 2013). The system wraps around the globe and spans about 65000 km length.

Mantle upwelling beneath ocean ridges results in adiabatic decompression melting, producing oceanic lithosphere. Mid-ocean ridges are a major source of crust-mantle differentiation on Earth, through the processes of partial melting, melt transport and reaction, and fractional crystallization in the crust and uppermost mantle (Kelemen et al., 1997). Abyssal peridotites provide direct samples of oceanic upper mantle and are important for understanding mantle chemistry and how oceanic lithosphere develops (Bonatti, 1968; Dick, 1989; Niu, 2004).

Partial melting of the upper mantle beneath mid-ocean ridges depends on the chemical composition of the mantle, including water content, and the potential temperature (Asimow et al., 2004). Partial melt forms at grain boundaries and begins to move when they are connected, resulting in the separation of melt and solid phases (Toramaru and Fujii, 1986). The degree of mantle depletion generally increases with decreasing depth due to greater decompression melting toward the top of the triangular melting region (Langmuir and Forsyth, 2007).

Residual peridotites formed by this decompression melting may react with upwelling melts, forming olivine at the expense of pyroxenes and producing dunite channels (Kelemen et al., 1995). Rare-Earth element (REE) abundances in clinopyroxenes have been used to estimate the degree and conditions of partial melting and reactions with melts (Johnson et al., 1990; le Roux et al., 2014). Despite these advances, and the existence of large databases of clinopyroxene chemistry (Warren, 2016),

systematic, statistically rigorous analyses of clinopyroxene compositional variation have not yet been attempted.

Data analysis using statistical and machine learning methods has recently been applied to the Earth sciences, showing great promise in classifications of geochemical data (Itano et al., 2020; Iwamori et al., 2017; Jorgenson et al., 2022; Lawley, 2016; Lawley et al., 2022; Stracke et al., 2022; Ueki et al., 2018; Yoshida et al., 2018). However, its application to ultramafic rocks is relatively rare (Lawley et al., 2020b, 2018; Qin et al., 2022). We present compositional data analysis (CoDA) including PCA and *k*-means clustering on a large database of abyssal peridotite clinopyroxene compositions and combine this with a series of melting models, to better understand clinopyroxene compositional systematics in abyssal peridotites.

2.2 Methods and data

2.2.1 Trace element compositions of clinopyroxene from residual abyssal peridotites

We collated mineral chemistry data (n = 1162; Supplementary Figure A1 and the database is available (https://doi.org/10.5281/zenodo.6791966) in additional supporting information) from abyssal peridotites, combining the data set of Warren (2016) with recent data (Birner et al., 2021, 2018; Frisby et al., 2016; Grambling et al., 2022; Harigane et al., 2022, 2016; Hesse et al., 2015; Li et al., 2017; Seyler and Brunelli, 2018; Silantyev et al., 2015, 2011; Urann et al., 2020; Wang et al., 2019). The database includes mineral chemistry from residual spinel-bearing harzburgite, lherzolite, and unclassified peridotite. Plagioclase-bearing peridotites and gabbro/pyroxenite/dunite vein-bearing peridotites were excluded on the basis that they likely underwent metasomatic modification due to melt infiltration (e.g., Akizawa et al., 2020; Morishita et al., 2007; Tamura et al., 2008). The database was screened to include only samples with clinopyroxene trace element data for the elements, Ce, Nd, Sm, Eu, Dy, Er, Yb, Ti, Sr, and Zr because CoDA cannot be performed on a data set with missing values. Where Ti (ppm) values were missing, TiO_2 (wt.%) was converted to Ti ppm and used in its place.

This screening results in a data set of 267 samples (Figure 1). Of these 100 clinopyroxenes are from lherzolites, 114 are from harzburgites, and 53 are from peridotites for which lithology was not described. The majority of clinopyroxenes (68%) are from the Southwest Indian Ridge (SWIR; n = 124) and Mid-Atlantic Ridge (MAR; n = 57), with additional data from the American-Antarctic Ridge (AAR; n = 9), Central Indian Ridge/Carlsberg Ridge (CIR; n = 18), East Pacific Rise (EPR; n = 8), Gakkel Ridge (GAK; n = 25), and Lena Trough (LT; n = 25) (Figure 2).

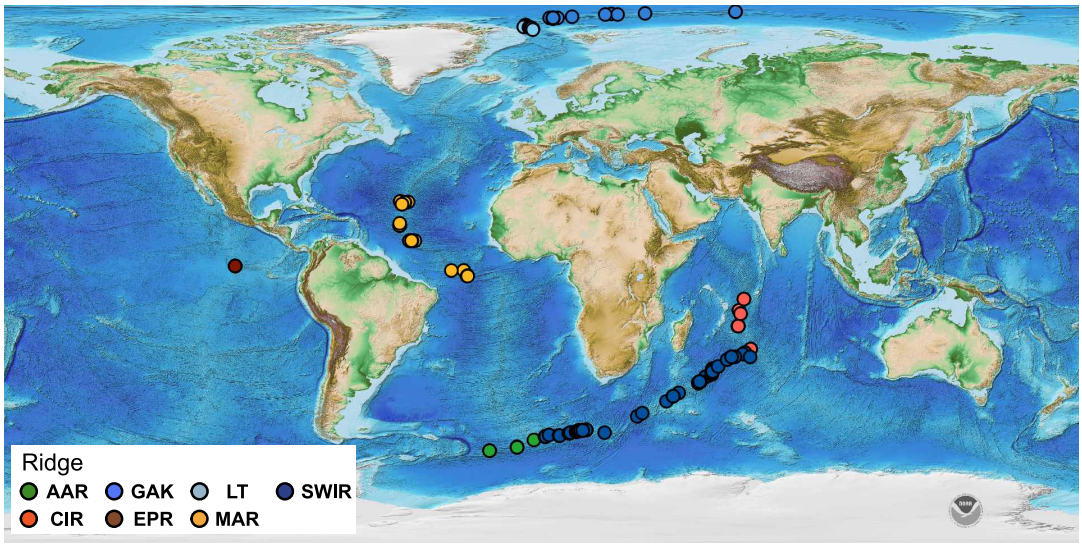

Figure 1: Global distribution of screened residual abyssal peridotites (n = 267). Ridge abbreviations are American-Antarctic Ridge (AAR), Central Indian Ridge/Carlsberg Ridge (CIR), East Pacific Rise (EPR), Mid-Atlantic Ridge (MAR), Gakkel Ridge (GAK), Lena Trough (LT), and Southwest Indian Ridge (SWIR). The topographic map is from Amante and Eakins (2009). Global distribution of un-screened residual abyssal peridotites (n = 1162) is shown in Supplementary Figure A1.

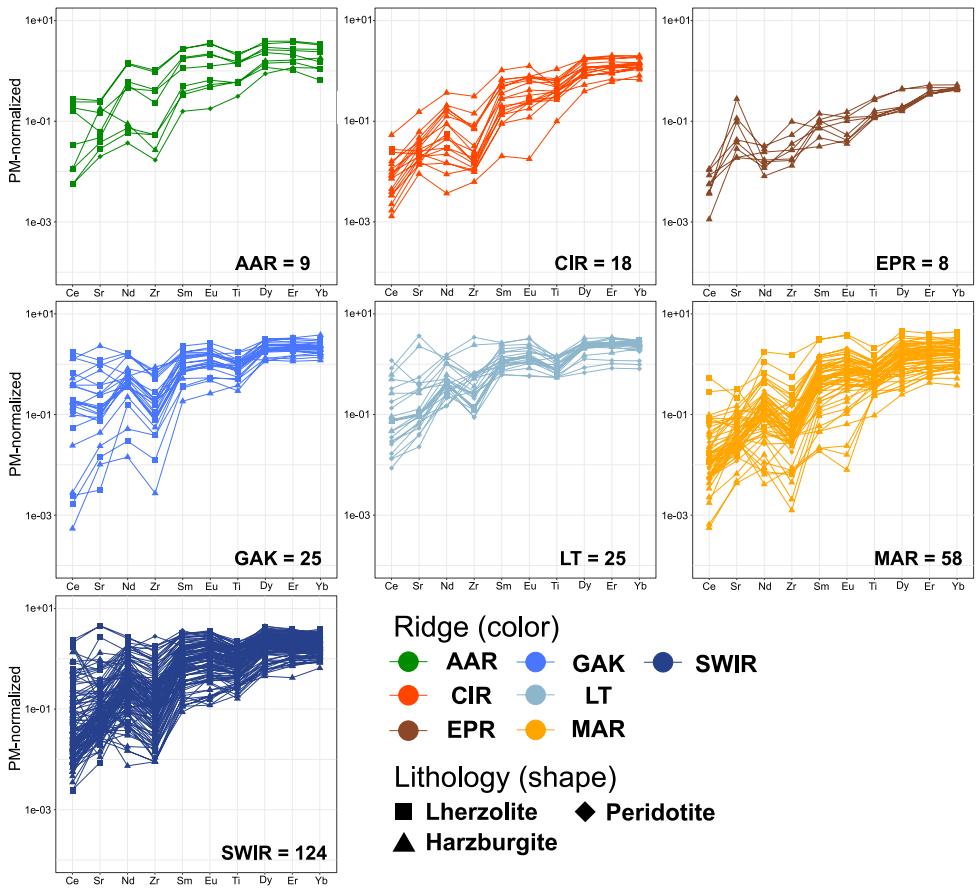

Figure 2: Variations in clinopyroxene trace element concentrations (REE, Sr, Zr and Ti) plotted by ridge for residual peridotites. All data (n = 267) are in situ analyses of clinopyroxene, normalized to primitive mantle (Sun and McDonough, 1989).

2.2.2 *Compositional data analysis (CoDA)*

Compositional data consist of a matrix of nonnegative, relative values with a constant sum (Aitchison, 1982; Egozcue et al., 2003; Greenacre, 2018). In the Earth sciences, whole-rock, and mineral chemical compositions are compositional data, and relevant for this study. Trace element compositions of clinopyroxenes are the parts of compositional data which is called subcomposition. Concentrations of various elements within a mineral are dependent on the concentrations of other elements in the mineral because the compositional data has a constant sum (i.e., values must sum to 100 wt.%). Therefore, n-dimensional data (where n = number of elements) are plotted on an $n-1$ dimensional space, as the concentration of one element is not an independent variable, and the potential for pseudo-correlations should be considered.

2.2.2.1 *Centered log-ratio transformation*

The filtered abyssal peridotite clinopyroxene trace element data ($n = 267$) were converted using centered log-ratio (CLR) transformation to conduct statistical analysis. Log-transformed ratios are key for the compositional and subcompositional data (Aitchison, 1982), as they emphasize relative magnitudes and variations in components rather than absolute values.

The CLR is performed by normalizing (centering) the log-transformed parts for each sample by its geometric mean. The log-transformation transforms compositional data (relative values with a constant sum) into multi-dimensional real space (Aitchison, 1982; Lawley, 2016), whereas normalizing to the geometric mean ensures that higher concentration elements (e.g., Ti in clinopyroxene) are not over-emphasized in further statistical analysis.

Given an element, x_i, within a total number of elements, D, geometric mean, g(x), the ith centered log-transformed data point z_i is calculated as follows:

$$z_i = \ln \frac{x_i}{g(x)} \tag{1}$$

(1) and geometric mean, g(x) is defined as the root of a total number of elements of the product of all elements as follows using the same notation as for Equation 1:

$$g(x) = \left(\Pi_i^D x_i\right)^{\frac{1}{D}} = \sqrt[D]{x(element)_1 \times x_2 \cdots \times x_D} \tag{2}$$

2.2.2.2 *Principal component analysis*

Principal component analysis (PCA) reduces the dimensionality of a data set while preserving as much information as possible (Greenacre, 2018). This is a commonly used method for determining the uncorrelated base vectors (i.e., combination of various CLR-transformed elements) that effectively account for the data by maximizing the variance along with the principal components. We conducted PCA on the log-transformed data to reduce the dimensionality of the data and chose PC1 and PC2

because the majority of the data can be described by only these two output vectors (PC1 and PC2) as described and discussed below. PCA on log-transformed data allows for identification of different groups of clinopyroxene compositions using k-means clustering. As a test for the necessity of performing CLR, we also applied PCA to the raw trace element data. This did not provide useful principal components as the concentration of Ti dominated the variance.

2.2.2.3 K-means clustering

K-means clustering is a classification method that divides multivariate data into a set of subgroups or clusters, where *k* is the number of clusters. Its objective is to minimize the average degree of scatter in each cluster, by minimizing the sum of squared distance of each data point from its cluster centers, starting from randomly assigned cluster centers. This method is an unsupervised approach solely based on a data set, and does not require prior information to identify the clusters.

We conducted *k*-means clustering using the PC1 and PC2 values derived from PCA. The number of clusters was chosen using the "elbow method". The variation (sum of squared distance from cluster centers) generally decreases as the number of clusters increases. However, there is an inflection point at which the rate of decrease in variation falls with increasing clusters—the so-called elbow. For our data set, this inflection point corresponds to $k = 4$ (Supplementary Figure A2), and so four clinopyroxene compositional groups are used. The results of k-means clustering are sensitive to the random starting assignments, so the process was repeated with 100 different random starting assignments. The result with the lowest sum of squared distance was selected to define clinopyroxene compositional groups.

2.2.3 Clinopyroxene trace element modeling

We modeled clinopyroxene compositions using open-system melting (Ozawa, 2001; Ozawa and Shimizu, 1995) to evaluate the multiple factors that can affect their geochemistry (
Table 1 and Supplementary Figure A3). The models were used to generate clinopyroxene compositions produced by fractional melting, nearly fractional melting, melt extraction followed by melt-rock reaction, and melting with a contribution from the garnet-stability field. The starting composition for all models was depleted MORB mantle (DMM) (Workman and Hart, 2005). Partition coefficients are from Kelemen et al. (2003) and Ozawa (2001) throughout. Melting modes and changes in the proportion of constituent phases from garnet-peridotite to spinel-peridotite follow Morishita et al. (2018).

Melting models applied to abyssal peridotites indicate that abyssal peridotites experience nearly fractional melting with low melt fractions retained in the source, rather than pure fractional melting (Brunelli et al., 2006; Ozawa, 2001). We modeled melt extraction using a variable retained melt fraction,

α, using α = 0.001, 0.005, 0.02 after Brunelli et al. (2006), in addition to one model using α = 0, corresponding to pure fractional melting (

Table 1).

Compositions of some abyssal peridotites are also consistent with some melt extraction in garnet-field melting prior to spinel-field melting (Hellebrand et al., 2002a). Following this, we modeled varying extents of garnet-field melting (0%, 1%, 5%, and 10%) prior to the onset of spinel-field melting.

We also modeled clinopyroxene compositions in peridotites which both undergo partial melting and react with melts, using parameters from Brunelli et al. (2014). We describe these models as melt-rock interaction models because the inducing melt reacts with the peridotite and causes further melting and depletion of the peridotite. We distinguish this from metasomatism (cf. Warren, 2016), because it results in a net depletion of fertile components, rather than a net addition of melt components. We modeled the reaction of peridotites after varying degrees of melt extraction in the spinel- and garnet-field with both All-MORB (Gale et al., 2013) and enriched melt compositions (formed by 1% partial melting in the garnet stability field).

Table 1: Melting conditions for partial melting models and melt-rock reactions models

Melting Model	Model	melt fraction (α)	spl-field melting (up to X%)	grt-field prior to spl-field melting
model1	fractional melting	0	8	0
model2	nearly fractional melting	0.001	8	0
model3	nearly fractional melting	0.005	10	0
model4	nearly fractional melting	0.02	16	0
model5	nearly fractional melting	0.001	8	1
model6	nearly fractional melting	0.02	14	1
model7	nearly fractional melting	0.001	8	5
model8	nearly fractional melting	0.02	14	5
model9	nearly fractional melting	0.001	6	10
model10	nearly fractional melting	0.02	14	10
Melt-Rock reaction Model	**Melt Composition**	**Starting material**	**Degrees of spl-melting of starting material**	**Degrees of grt-melting of starting material**
melt-rock1	All-MORB	DMM	0	0
melt-rock2	All-MORB	model2	8	0
melt-rock3	All-MORB	model4	10	0
melt-rock4	All-MORB	model5	8	1
melt-rock5	Enriched Melt	model2	8	0
melt-rock6	Enriched Melt	model4	10	0
melt-rock7	Enriched Melt	model5	8	1
melt-rock8	Enriched Melt	model7	8	5

2.3 Results

2.3.1 PCA & k-means clustering

84.2% of the variation in the data set is covered by the PC1 (57.9%) and PC2 (26.3%) values (Figure 3a). High PC1 values are generated primarily by high concentrations of the HREE and Ti, whereas PC1 generally decreases with increasing Ce, Zr, Nd, and Sr. High PC2 values are generated by high Sr, whereas low PC2 values correspond to high MREE (Sm and Eu). Clinopyroxene from harzburgites have greater compositional variation than those from lherzolites and peridotites, with higher maximum PC1 and PC2 values compared to lherzolite and peridotite (Figure 3b).

Samples from the EPR are characterized by high PC2 values, which are distinctive from other ridges (Figure 3c). Clinopyroxenes with high PC1 values (>6) are observed in GAK (D'Errico et al., 2016) and MAR (Harigane et al., 2016); clinopyroxenes with high PC2 values (>5) are observed in CIR (Hellebrand et al., 2002a) and MAR (Seyler et al., 2007).

Sixty-eight percentage of data are in clusters 2 & 3. Clusters 2 and 3 have similar PC2 values but cluster 2 has lower PC1 (Figure 3d). Cluster 1 (17% of data) is low in PC1 with relatively variable PC2. Cluster 4 (15% of data) is characterized by high PC2 values.

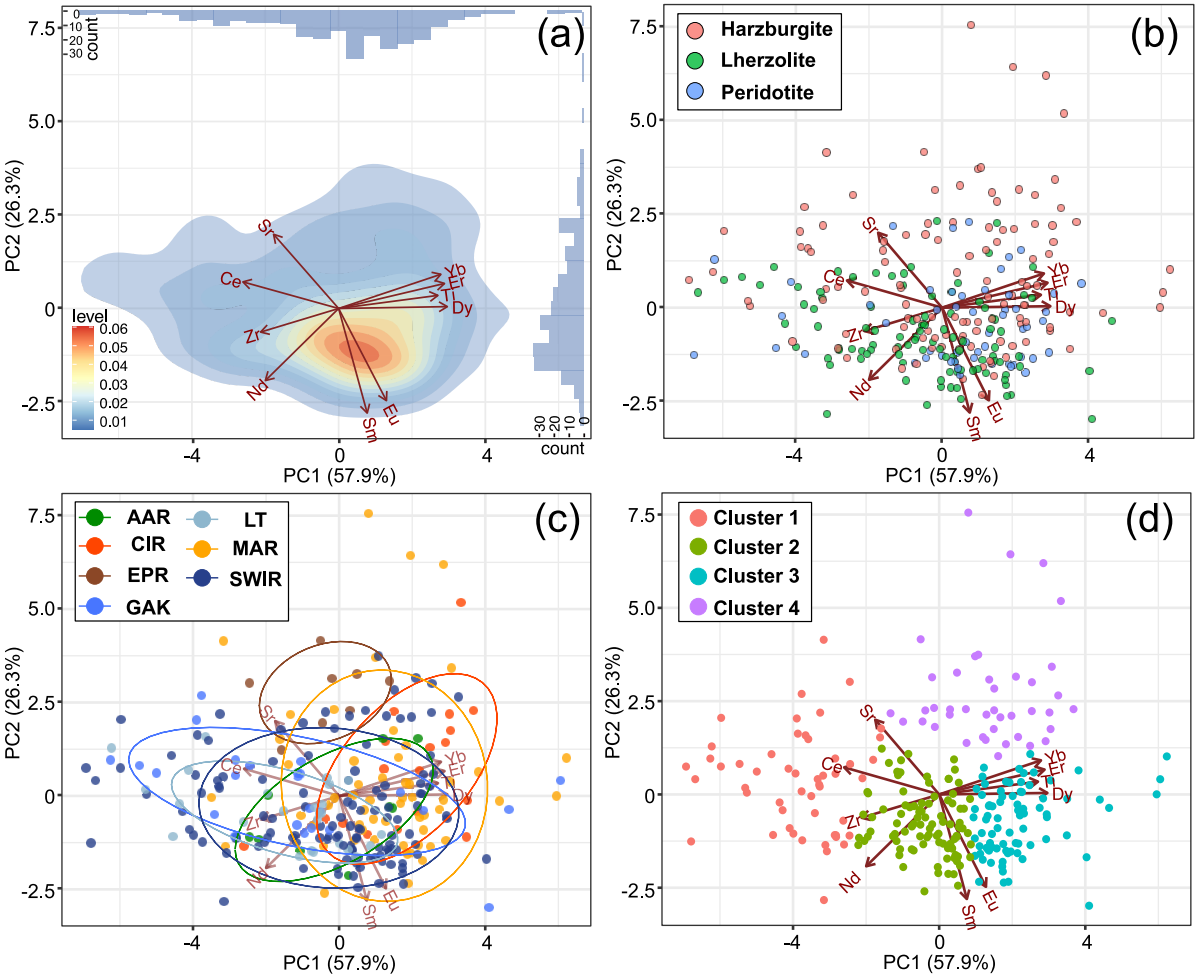

Figure 3: Principal component analysis (PCA) for clinopyroxene trace elements from residual abyssal peridotites. (a) Density plot of clinopyroxene PCA data. Remaining figures are PCA binary plots with samples grouped by (b) lithology, (c), ridges, and (d) k-means clustering. The ellipses in (b) are 68% (~1σ) confidence intervals.

2.3.2 Correlations between PCA & k-means clustering and clinopyroxene trace element compositions

Clusters 1–3 show similar variations in HREE abundances as shown. For example, by the interquartile ranges (IQR) of Yb from clusters 1–3 are between 0.60 and 1.38 ppm. However, they show different LREE abundances, demonstrating that LREE variations are the primary driver of variations in PC1 between clusters 1–3. For example, mean Ce values decrease from cluster 1 (1.08 ppm), to cluster 2 (0.12 ppm), to cluster 3 (0.02 ppm). Cluster 4 has a similar mean Ce concentration (0.02 ppm) to that of cluster 3. However, the mean Sr and Yb in cluster 4, are higher than and lower than that of cluster 3, respectively.

Correlations between PC1&2 values and clinopyroxene trace elements compositions are shown in Ce/Yb ratio and Sr/Nd ratio against PC1 & 2 values plots, respectively (Figure 4). PC1 value shows a negative correlation with Ce/Yb ratio (Figure 4a). Ce/Yb ratio falls from cluster 1 to cluster 3 but cluster 4 has a similar ratio to cluster 3. PC2 value shows a positive correlation with Sr/Nd ratio (Figure 4b). Cluster 4 has a high Sr/Nd ratio and PC2 value. Clusters 2 & 3 have similar Sr/Nd ratios and ratios are lower than that of cluster 4. Sr/Nd ratio of cluster 1 tends to be between those of cluster 4 and clusters 2 & 3. Variations in LREE(Ce)/HREE(Yb) ratios, HREE abundances, and Sr anomalies are therefore the primary drivers of PC1 and PC2 variation between the various clusters, and the clusters can be discriminated on a Sr/Nd against Ce/Yb plot (Figure 4c).

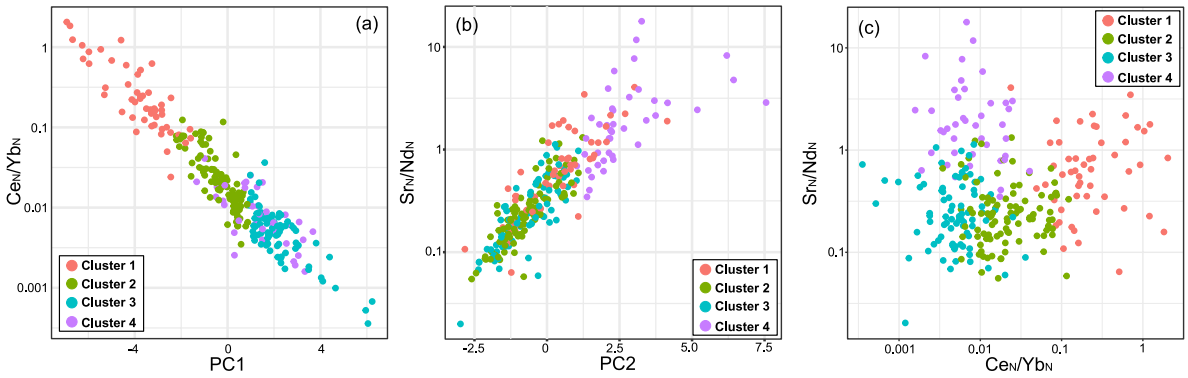

Figure 4: Primitive mantle (PM) normalized (Sun and McDonough, 1989) Ce/Yb ratio of clinopyroxenes versus PC1 value, (b) PM normalized Sr/Nd ratio of clinopyroxenes versus PC2 value, (c) Discrimination diagram for clinopyroxene trace elements compositions. PM normalized Sr/Nd ratio versus Ce/Yb ratio of clinopyroxenes from abyssal peridotites.

When plotted on primitive mantle (Sun and McDonough, 1989) normalized trace element patterns, clear differences can be seen between the groups defined by PCA and k-means clustering (Figure 5). Cluster 1 clinopyroxenes have high LREE/HREE ratios corresponding to flat trace element patterns. Cluster 2 has a moderate LREE/HREE ratio and shows more LREE-depleted patterns. Cluster 3 has a low LREE/HREE ratio and strong negative Zr anomalies. Cluster 4 shows distinctive patterns to all the other clusters, with low HREE abundances, positive Sr anomalies, and moderate LREE/HREE ratios.

We are careful to stress here that the variations between the groups are gradational, and the boundaries between the groups should not be interpreted as hard boundaries. For example, there are very clearly continuous changes between groups 1–3, and a few of the group 1 compositions have high PC2 values, showing some similarities to group 4. However, the *k*-means clustering provides an independent basis for grouping clinopyroxene compositions from a large, "noisy" data set. These clusters have distinct trace element patterns with a good degree of coherence within each cluster (Figure 5), and form the basis for further analysis (see Section 2.4).

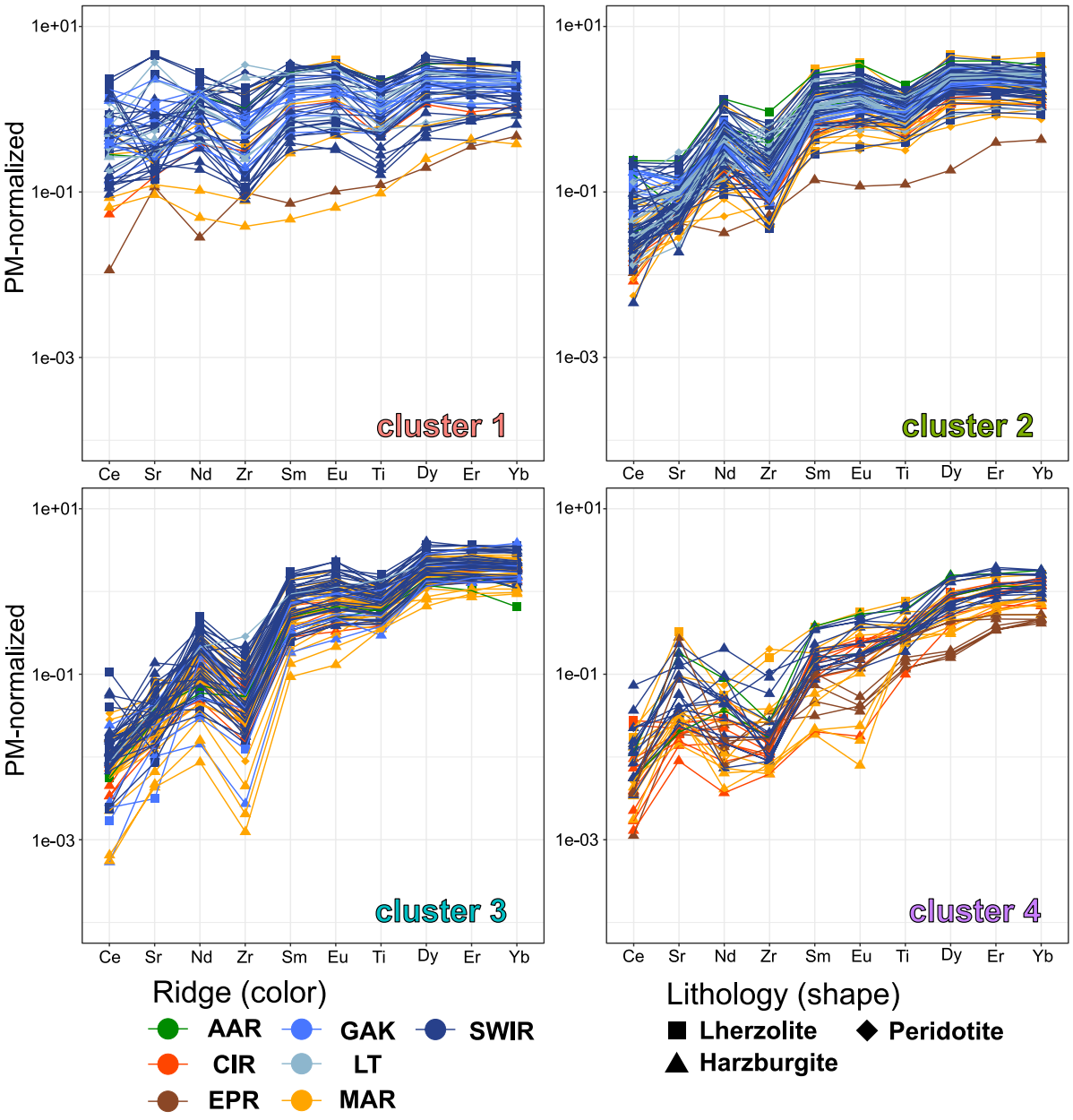

Figure 5: Primitive mantle normalized (Sun and McDonough, 1989) trace element patterns of clinopyroxenes in clusters 1–4 (a–d).

2.3.3 Modeled clinopyroxene compositions

Clinopyroxene compositions calculated from the partial melting models were plotted using the principal components derived from the natural clinopyroxene data (Figure 6). The modeled compositions produced by simple melting models without melt-rock reaction cover a similar area in PC1 and PC2 space to that of clusters 1–3. Degrees of partial melting positively correlate with PC1, due to the association of PC1 with LREE/HREE ratios (Section 2.4.1). Variations in the melt fraction retained in the source for near-fractional melting models generate variations in both PC1 and PC2, which increase at higher degrees of partial melting. Models with lower retained melt fractions (α = 0, 0.001–0.005) show larger changes in PC1 for a given degree of melting, with decreasing PC2 with increasing partial melting (Figure 6a). However, PC1 increases less, and PC2 components are more constant with increasing degrees of melting when melt fractions are high (α = 0.02). This decrease in PC1 variation corresponds to reduced LREE/HREE fractionation when retained melt fractions are high (Supplementary Figure A3), as the style of melting modeled tends away from pure fractional melting and more toward batch melting.

Garnet-field melting prior to spinel-field melting increases PC1 at the onset of spinel-field melting, but PC2 values are the same as for models without garnet-field melting (Figure 6b). Melt-rock interaction models are characterized by high PC2, similar to clinopyroxenes from cluster 4 (Figure 6c and 6d). PC1 and PC2 are both higher when the starting materials (peridotites before melt-rock reaction) are more depleted. When the same starting material reacts with enriched melt, it generates lower PC1 and higher PC2 than for reactions with MORB. PC1 and PC2 converge as reactions progress, as the reacting melt exerts an increasingly strong control on the modeled clinopyroxene compositions.

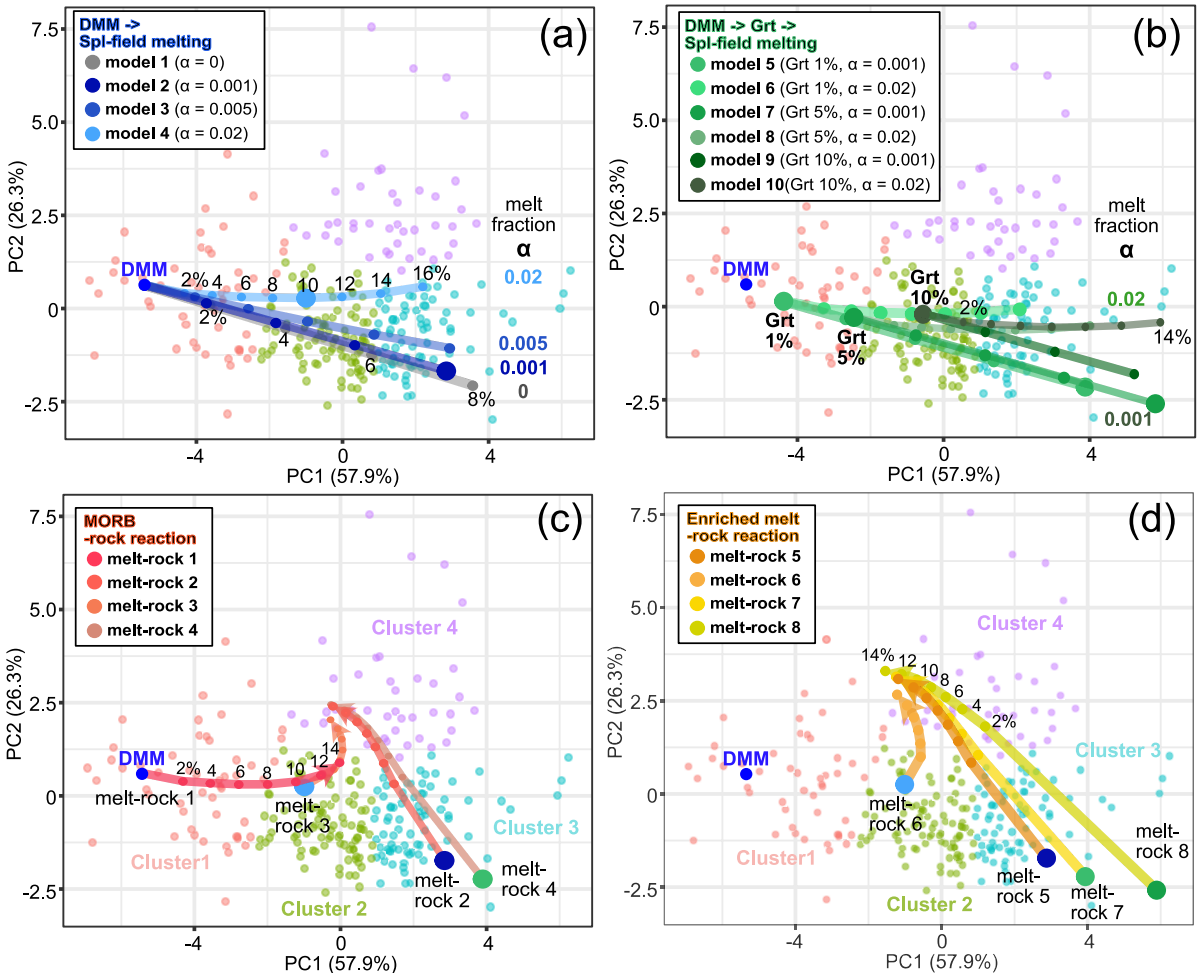

Figure 6: Principal component plots of modeled clinopyroxene compositions using the principal components derived from the natural clinopyroxene data. (a) Modeled clinopyroxene compositions obtained by spinel-field melting. Black numbers (e.g., 2%) show the degrees of melting and thick numbers show melt fraction α, (b) garnet-field melting prior to spinel-field melting. Thick black numbers show the degrees of melting in garnet-field prior to spinel-field, (c) modeled clinopyroxene compositions obtained by MORB melt-rock reactions. Starting materials are shown as larger circles, and (d) enriched melt-rock reactions. The setting of models is described in Table 1.

2.3.4 Correlations between clustering and mineral mode and major element compositions

We investigate whether clusters based on clinopyroxene compositions can be linked to differences in the major element and mineralogical composition of their host peridotites. Below, we focus on mineralogical and geochemical variables which have been used as indicators of the degree of partial melting (Arai, 1994; Hellebrand et al., 2002b, 2001).

Median modal clinopyroxene contents decrease in clusters 2–4 (Figure 7a). Cluster 4 has noticeably lower modal clinopyroxene than the other clusters, with a median value lower than any of the first quartiles for other clusters. Cluster 1 shows a wide range of modal clinopyroxene contents, but the maximum and third quartile values are higher than those of other clusters.

Median and quartile values for Na_2O in clinopyroxene systematically fall from cluster 1 to cluster 4 (Figure 7b). Concurrent with this decrease, the absolute compositional range in each cluster also decreases, as shown by falling IQRs.

Median TiO_2 in orthopyroxene also falls from clusters 2–4 (Figure 7c). Similar to modal clinopyroxene contents, TiO_2 in orthopyroxenes in cluster 1 shows a similar median value to that of cluster 2, but has a larger IQR and higher third quartile value.

Cr# of spinels shows the opposite relationship to the variables considered above, showing a systematic increase in median and quartile values from clusters 2–4 (Figure 7d). Cluster 4 has a larger IQR compared to other clusters. Cluster 1 has higher median and quartile values than those of cluster 2 and its IQR is also larger than those of clusters 2 and 3. A traditional Fo# olivine against Cr# of spinel plot therefore shows moderate correlations, Fo# and Cr# tend to be higher in cluster 4 followed by clusters 3 and 2 (Supplementary Figure A4).

Because the cluster analysis was performed on PC1 and PC2 data, the systematic variations observed in geochemical and mineralogical indicators of melting are linked with correlations between PC1, PC2, and these melting indicators. Modal clinopyroxene contents and incompatible elements (TiO_2, Na_2O, Al_2O_3) tend to show negative correlations with PC1 (Supplementary Figure A5). Spinels Cr# and olivine Fo# show positive correlations with PC1, although data for cluster 1 is widely scattered. Al_2O_3 contents in orthopyroxene show negative correlations with PC2 components, with cluster 4 showing the highest PC2 and lowest Al_2O_3.

Yb in clinopyroxene shows a correlation with Cr# of spinel (Figure 8), but Ce in clinopyroxene does not correlate with Cr# of spinel (Figure 8b) which are consistent with the results of previous studies (Hellebrand et al., 2001; Warren, 2016). As the correlation between clusters and Cr# is shown in Figure 7d, cluster 4 has high Cr# of spinel and low Yb in clinopyroxene followed by clusters 3 and 2. Cluster 1 shows variable compositions among the trend.

Cerium in clinopyroxene against Cr# of spinel plot shows clear compositional differences among clusters. Ce in clusters 2&3 clinopyroxenes tend to show a negative correlation with Cr#.

Clusters 4 has high Cr# of spinel but Ce in clinopyroxenes are similar to those of cluster 3. Cluster 1 clinopyroxenes have high Ce abundances but spinels have a large range of Cr#.

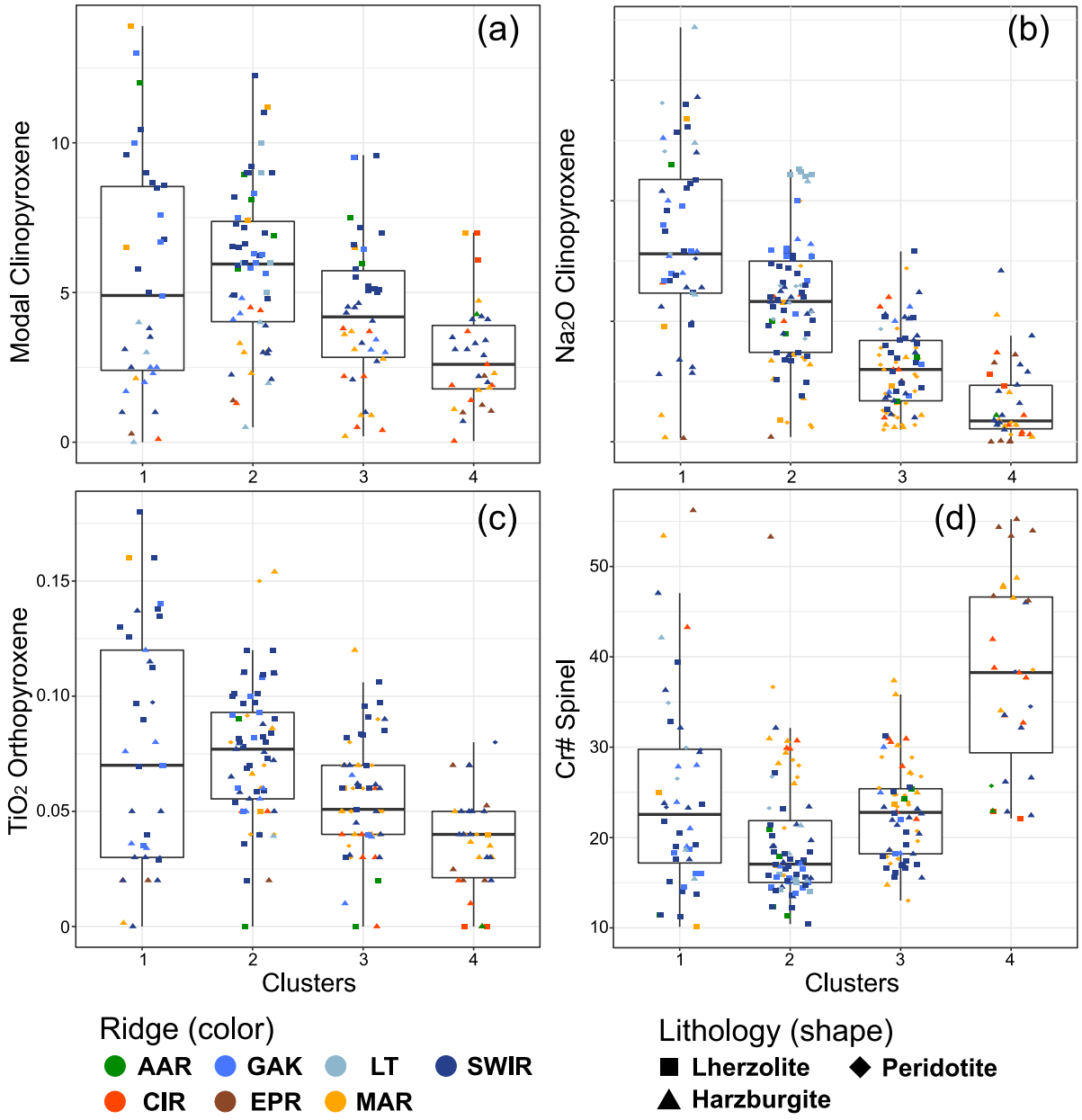

Figure 7: Correlations between clustering and mineral mode and major element compositions. Box plots showing variations in (a) Modal clinopyroxene, (b) Na_2O in clinopyroxene, (c) TiO_2 in orthopyroxene, and (d) Cr# of spinels from clusters 1–4. The upper and lower sides of each box represent the third and first quartiles of the observed values, with the median value shown as the horizontal line dividing the box. The vertical height of the box is the interquartile range (IQR).

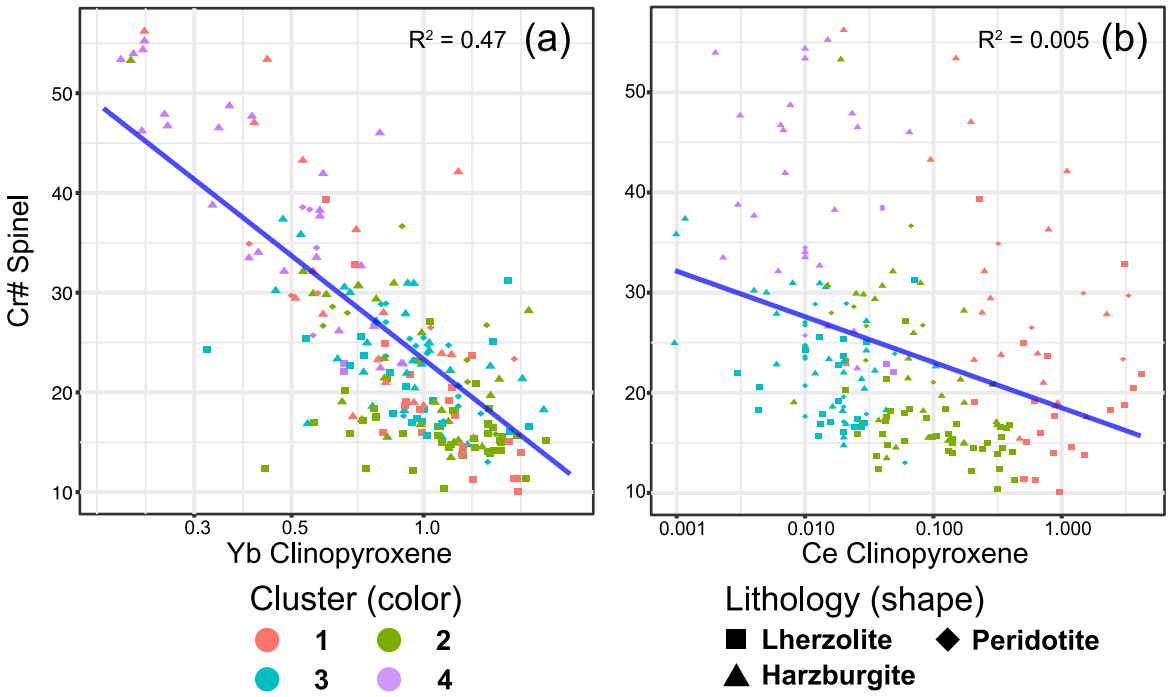

Figure 8: Correlations between Cr# of spinel and clinopyroxene trace elements compositions from clusters 1–4. Cr# of spinel versus (a) primitive mantle normalized (Sun and McDonough, 1989) Yb values, (b) PM normalized Ce values, The blue line was obtained by least-squares linear regressions (regression parameters shown in the upper right-hand corner).

2.4 Discussion

To summarize our results, clusters 1–3 (n = 226, 84.6% of the data) show progressive depletions in LREE/HREE (increasing PC1; Figure 5), and are associated with progressive decreases in modal clinopyroxene abundance, Na_2O in clinopyroxene, and TiO_2 in orthopyroxene their host peridotites (Figure 7). We therefore interpret that peridotites with clinopyroxene from clusters 1–3 are residues after partial melt extraction. However, peridotites with clinopyroxene from cluster 4 are the exception to a number of these trends. For example, cluster 4 clinopyroxenes show less fractionated LREE/HREE (Figure 5) than cluster 3 despite much higher spinel Cr#, lower modal clinopyroxene abundance, Na_2O in clinopyroxene, and TiO_2 in orthopyroxene in their host peridotites (Figure 7). They also have high PC2, which is otherwise only observed in our models involving melt-rock interaction (Figure 6c and 6d). We therefore interpret peridotites with clinopyroxene from cluster 4 to have experienced both partial melting and melt-rock interaction.

2.4.1 Controls on composition of cluster 1–3 residual peridotites

A comparison between the modeled clinopyroxene compositions and clinopyroxene clusters 1–3, shows that the majority of clinopyroxene compositions can be explained by spinel-field melting with retained melt fractions varying between $\alpha = 0.001$ and $\alpha = 0.02$ (Figure 6a) (Brunelli et al., 2006). However, some cluster 3 clinopyroxenes have particularly high PC1 at moderately high PC2, which may require that their host peridotites experienced some partial melt extractions in the garnet stability field. Spinel-field melting from DMM cannot reach such high PC1 and moderate PC2 without unreasonable amounts of melt extraction ($F > 16\%$) because clinopyroxene is exhausted after around 18% melt extraction. Cluster 3 clinopyroxenes with the highest PC1 components (>6) were collected from GAK and MAR and those show lowest REE abundances with negative Zr anomalies (D'Errico et al., 2016; Harigane et al., 2016). We interpret these peridotites as the most depleted residues that only experienced garnet- and spinel-field melting and this is consistent with the results of complex geochemical models (Harigane et al., 2016).

In summary, the variations in clinopyroxene composition in clusters 1–3 can be explained by differences in the degree of partial melting, the presence or absence of garnet-field melting prior to the onset of spinel-field melting, and the retained melt fraction during partial melting, as suggested by previous studies (Brunelli et al., 2006; Hellebrand et al., 2002b; Johnson and Dick, 1992; Morishita, 2015; Warren, 2016).

Mineral modes and mineral major element compositions show large compositional variations within each group (Figure 7), potentially suggesting that they are less sensitive to the degree of partial melt extraction and melt fraction compared to clinopyroxene trace elements or affected by different processes. However, Na_2O contents in clinopyroxenes appear similarly sensitive to the degree of partial melt extraction as clinopyroxene trace elements, as median and quantile values decrease in clusters 1–4.

2.4.2 Controls on composition cluster 4 depleted peridotites

Clinopyroxene compositions in cluster 4 are characterized by high PC2 at moderately high PC1, which corresponds to high LREE/HREE ratios for their level of HREE depletion, and positive Sr anomalies. The only models which produced such high PC2 values were melt-rock interaction models, so we infer that cluster 4 peridotites experienced melt-rock interaction.

A wide range of compositions can be produced by melt-rock reaction models using different degrees of melt depletion and different reacting melt compositions (Seyler et al., 2007; Seyler and Brunelli, 2018). Melt-rock reaction models between DMM that has not undergone melt extraction and MORB, show that it is difficult to reach simultaneously high PC1 and PC2 values without extensive

partial melt extraction before melt-rock interaction (Figure 6c). This suggests that cluster 4 clinopyroxenes may require partial melt extraction prior to melt-rock interaction to explain their compositions.

Differences in depletions and melt compositions are supported by mineral major elements. Cr# of spinels and Yb in clinopyroxenes show a negative correlation across all samples (Figure 8a and Figure 9a) and these elements have been used as indicators for degrees of melting (Hellebrand et al., 2001). Na_2O contents in clinopyroxenes are relatively constant with increasing spinel Cr# until spinel Cr# = 40 which supports differences in depletions (Figure 9b). High Cr# (>40) peridotites show various clinopyroxene Na_2O compositions. Na_2O contents in melt are high after low degrees of melting because most of the incompatible elements are partitioned into the first small melt fraction (Langmuir and Forsyth, 2007; Seyler and Brunelli, 2018). Therefore, wide ranges of Na_2O contents support requirements of different reacting melt compositions.

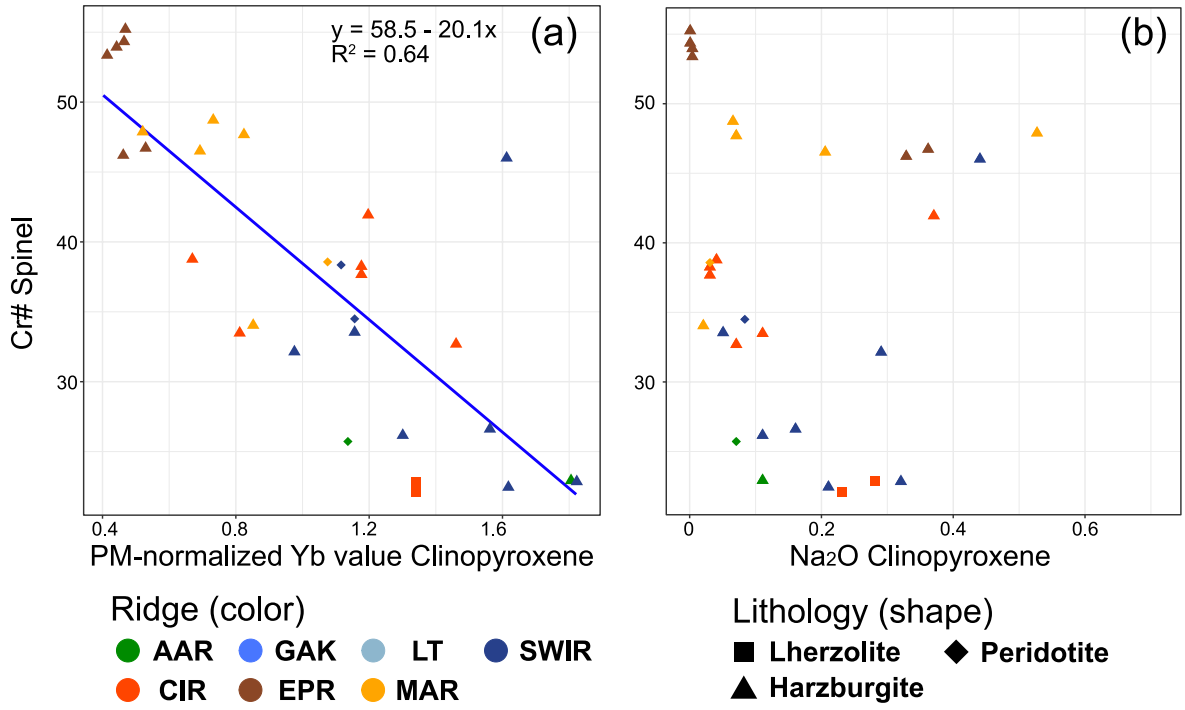

Figure 9: Correlations between Cr# of spinel and clinopyroxene major and trace elements compositions from cluster 4. Cr# of spinel versus (a) primitive mantle normalized (Sun and McDonough, 1989) Yb values, (b) Na_2O. The blue line was obtained by least-squares linear regressions (regression parameters shown in the upper right-hand corner).

Cluster 4 clinopyroxenes show positive Sr anomalies which we cannot reproduce in any of typical melting models (Figure 10a). One possible explanation arises from the serpentinized nature of abyssal peridotites, as serpentinization enriches fluid mobile elements such as Sr and Li (Morishita et al., 2009). However, consistent positive Sr anomalies are not observed in any of the other clusters,

despite the presence of serpentinized samples in these clusters. Alternatively, clinopyroxene with low HREE abundances, positive Sr anomalies and high LREE/ HREE ratios are observed in forearc peridotites (Figure 10b) (Birner et al., 2017; Parkinson et al., 1992). Clinopyroxene compositions from forearc peridotites from the Izu-Bonin-Mariana (IBM) arc were plotted using the principal components derived from the abyssal clinopyroxene data. IBM clinopyroxenes share the characteristics of high PC2 with cluster 4 (Figure 10c). We therefore speculate that cluster 4 peridotites could be recycled arc mantle materials (Bjerga et al., 2022; Urann et al., 2020), interacted with hydrous melts, and/or experienced hydrous melting at the mid-ocean ridge.

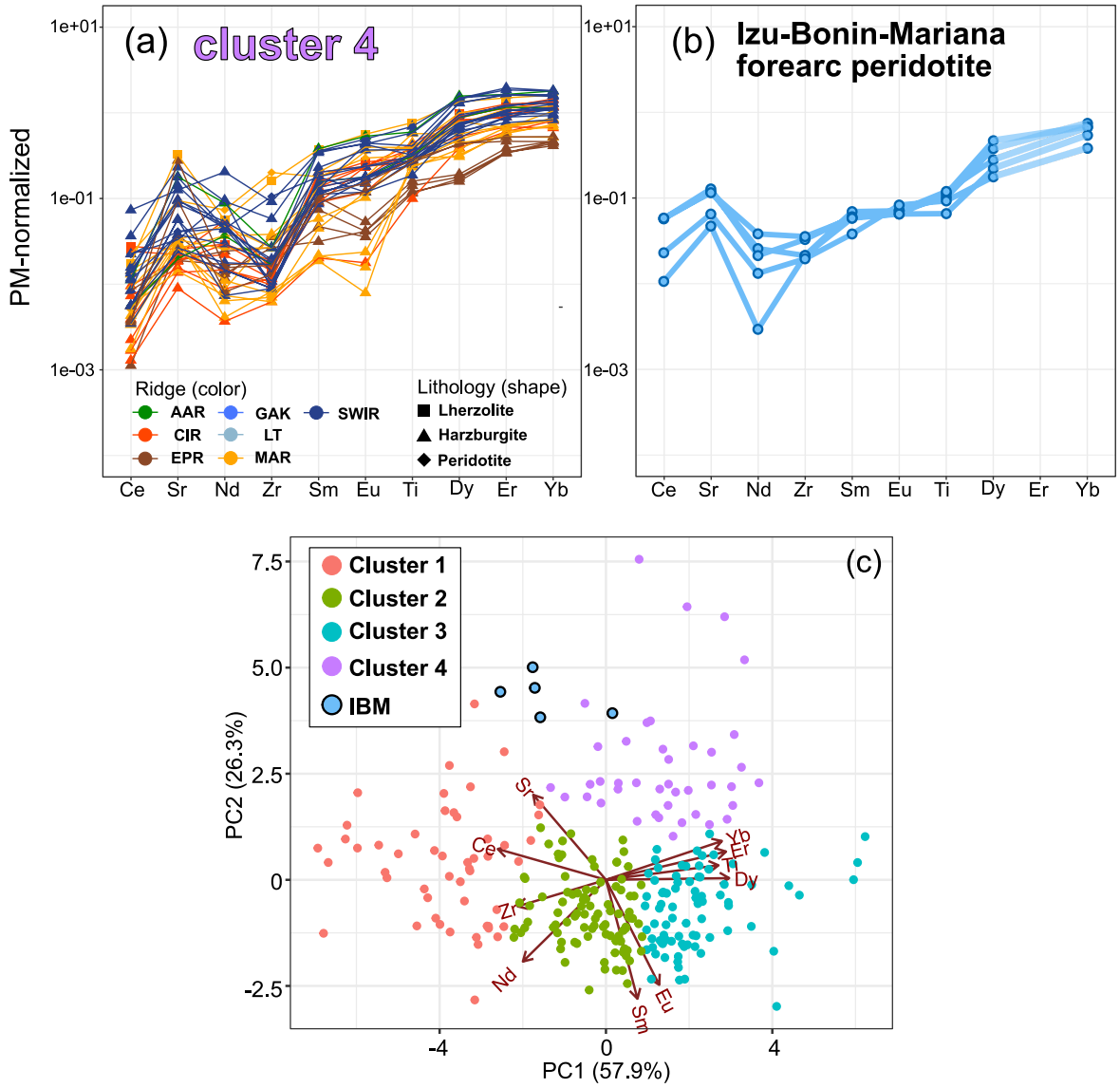

Figure 10: Comparisons of primitive mantle-normalized clinopyroxene trace elements compositions between (a) cluster 4 abyssal peridotite clinopyroxenes, (b) forearc peridotites from Izu-Bonin-Mariana arc (Parkinson et al., 1992), and (c) principal component plots of clinopyroxene from Izu-Bonin-Mariana forearc peridotite using the principal components derived from the abyssal clinopyroxene data.

2.4.3 Effects of cryptic metasomatism and refertilization

A potential objection to our interpretation of the cluster 4 clinopyroxene reflecting the effects of melt rock reaction is that their elevated Sr contents might reflect "cryptic" plagioclase metasomatism (Tamura et al., 2008; Warren and Shimizu, 2010). However, cluster 4 peridotites lack positive Eu anomalies which appear inconsistent with cryptic plagioclase metasomatism. To test this, we plotted data from metasomatized abyssal rocks including plagioclase impregnated peridotites (Warren, 2016) using the principal components derived from the residual abyssal clinopyroxene data. Clinopyroxene compositions from plagioclase impregnated peridotites and other metasomatized rocks tend to overlap clusters 1 and 2, or even plot outside the PC field defined by residual peridotites. This is largely due to their negative Sr anomalies and elevated LREE concentrations.

Critically, none of the metasomatized peridotite data show elevated PC2 values comparable to group 4 clinopyroxenes, in sharp contrast to forearc peridotites (Figure 10c). We therefore conclude that an origin as recycled arc mantle materials (Urann et al., 2020), interactions with hydrous melts, and/or the presence of hydrous melting at the mid-ocean ridge are the most likely explanations for cluster 4 clinopyroxenes.

Cluster 1 peridotites show large variations in mineral major element compositions (Figure 7) and Yb in clinopyroxenes negatively correlates with Cr# of spinel (Figure 8a). PC plots of clinopyroxene compositions from the metasomatized peridotites overlap cluster 1 clinopyroxenes (Figure 11). This large range of compositions and relative depletion of compatible elements suggests a potential role for refertilization (Warren, 2016).

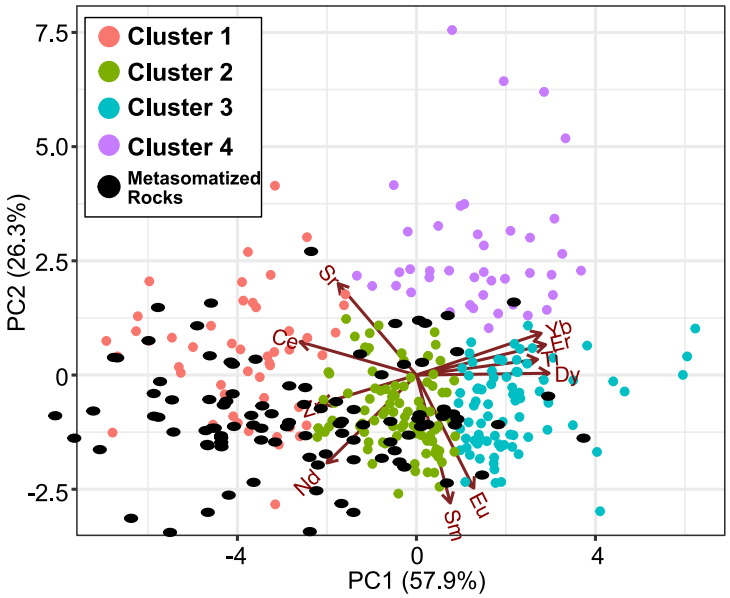

Figure 11: Principal component plots of clinopyroxene from metasomatized abyssal rocks (Warren, 2016) using the principal components derived from the abyssal clinopyroxene data.

2.4.4 Unique characteristics of peridotites from the fast-spreading East Pacific Rise?

Only depleted peridotites and chromitites have been sampled from the EPR (Arai and Matsukage, 1998; Dick and Natland, 1996). The Cr# of spinel from 35 EPR peridotites samples are available in our unscreened database (from Terevaka transform fault, Garrett transform fault and Hess Deep) and show depleted signatures, with median (Cr# = 52.5) and quartile values are much higher than those from other ridges (Figure 12). Furthermore, clinopyroxene from EPR peridotites has consistently high PC2, with the majority of samples falling in cluster 4 (Figure 3c). Although cluster 4 clinopyroxenes are observed in most ridges despite their different spreading rates (Supplementary Figure A6), the EPR is unusual in having such a high proportion of cluster 4 clinopyroxene. The few EPR samples in clusters 1 and 2 may reflect issues with separating groups from gradational data by k-means clustering, as these lie close to the boundaries between groups 1, 2, and 4.

Our modeling suggests that EPR clinopyroxene underwent high degrees of partial melting and melt-rock interaction as characterized by low HREE abundances and enriched LREE and Sr compared to the mantle beneath other ridges. Because amounts of clinopyroxene trace elements data are very limited (n = 8, 3% of the data), it remains unclear if these peridotites represent the composition of EPR mantle as a whole or an endmember composition of depleted peridotites that experienced melt-rock interaction. Further sampling of EPR abyssal peridotites is necessary to resolve the question and establish how depleted typical mantle is beneath fast-spreading ridges.

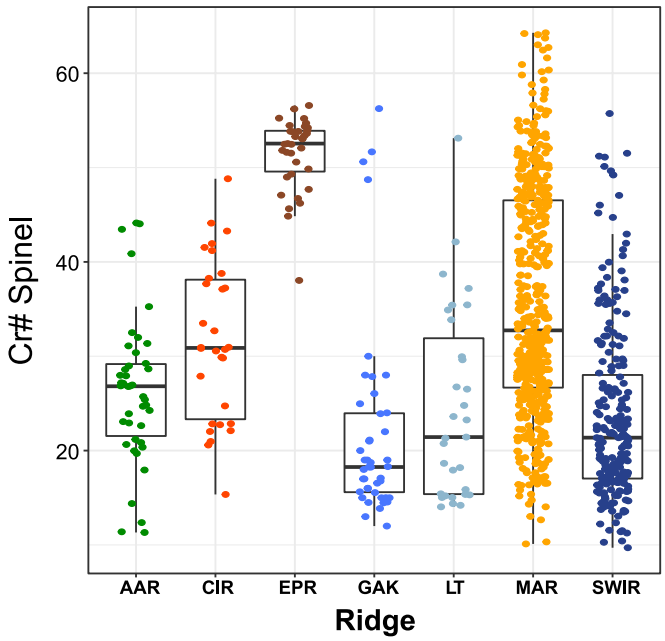

Figure 12: Boxplot of Cr# of spinel from the unfiltered abyssal peridotites database (n = 1,162).

2.4.5 Heterogeneous oceanic lithosphere

Clusters 1–4 are observed in most ridges (Supplementary Figure A6), consistent with compositionally heterogeneous abyssal peridotites on each ridge, as suggested in previous studies (Paquet et al., 2022; Rampone and Hofmann, 2012; Warren, 2016). The MAR consists of 56.5% (n = 657) of the unfiltered data (n = 1162), and has a Cr# range that covers the entire compositional range of other ridges (Cr# = 10–65) (Figure 12), potentially suggesting that the degree of compositional heterogeneity at ridges other than MAR is underestimated due to under sampling. Cluster 4 is not observed in GAK, though clinopyroxene-rare, low-HREE, and high LREE/HREE ratio harzburgites which are similar to characteristics of cluster 4 and have experienced similar melt-rock interactions are observed (D'Errico et al., 2016). Therefore, significant variability exists within each ridge, representing heterogeneities controlled by variable retained melt fraction, degree of partial melting, and melt-rock interaction.

2.5 Conclusion

We collated large database (n = 1162) of abyssal peridotite compositions and analyzed the clinopyroxene trace element data (n = 267) using statistical methods, CoDA and combined open-system melting models to investigate clinopyroxene compositional variation in abyssal peridotites.

Principal component analysis shows that 84.2% of the variation in the data set is covered by the PC1 (57.9%) and PC2 (26.3%) values and most abyssal clinopyroxene compositions from abyssal peridotites can be explained by the only 2-dimensional information. Ce/Yb ratio and Sr/Nd ratio are respectively primary drivers of PC1 and PC2 values.

K-means clustering using the PC1 and PC2 values classified clinopyroxene compositions into four clusters. Clusters 1–3, 84.6% of the data, show progressive depletions in LREE/HREE (increasing PC1), and are associated with decreases in modal clinopyroxene abundance, Na_2O in clinopyroxene, and TiO_2 in orthopyroxene and increases in Cr# of spinel their host peridotites. Cluster 4 clinopyroxenes, 15% of data, show less fractionated LREE/HREE, with low-HREE abundances and positive Sr anomalies. Peridotites with cluster 4 clinopyroxenes also show the most depleted signatures in their host peridotites, with the lowest modal clinopyroxene contents, Na_2O in clinopyroxene, and TiO_2 in orthopyroxene, and the highest spinel Cr#s.

We interpret that peridotites with clinopyroxene from clusters 1–3 are residues after partial melt extraction. The compositional variations in clusters 1–3 can be explained by differences in the degree of partial melting, the presence and/or absence of garnet-field melting prior to the onset of spinel-field melting, and the retained melt fraction during partial melting. But cluster 1 peridotites showing large variations in mineral major element compositions and Yb in clinopyroxenes negatively correlates with Cr# of spinel suggests a potential role for refertilization.

Clinopyroxene compositions in cluster 4 cannot be modeled by melt depletion alone and are only reconstructed in our models involving melt-rock interaction and suggest that the peridotites with clinopyroxene from cluster 4 have experienced both partial melting and melt-rock interaction. Positive Sr anomalies shown in cluster 4 clinopyroxenes cannot be reproduced in any of our melt-rock reaction models using reactions between variably depleted peridotites and either MORBs or enriched melts. However, low HREE abundances, positive Sr anomalies and high LREE/HREE ratios are observed in forearc peridotites, where they indicate fluid involvement. We therefore speculate that cluster 4 peridotites could be recycled arc mantle materials that interacted with hydrous melts, and/or experienced hydrous melting at the mid-ocean ridge.

Although clinopyroxene trace element data for East Pacific Rise samples are very limited (n = 8, 3% of the data), the majority of these peridotites contain cluster 4 clinopyroxene and show high Cr# of spinel (median = 52.5). The limited data availability means that it remains unclear if entire EPR mantle underwent similar depletion and melt-rock interaction or if this represents an endmember composition.

Cluster 1–4 clinopyroxenes are observed in most ridges, indicating significant compositional heterogeneity in abyssal peridotites on each ridge. Samples from the MAR comprise the majority of our data, and this ridge shows the greatest variability in Cr#, covering the entire compositional range of other ridges (Cr# = 10–65). This suggests that the degree of compositional heterogeneity at other ridges may be underestimated due to under sampling. The significant compositional variability within each ridge likely represents variations in the degree of partial melting, amount of garnet-field melting, retained melt fraction, and melt-rock interaction.

Chapter 3

3 Formation of ultra-depleted mantle peridotites and their relationship with boninitic melts: an example from the Kamuikotan unit, Hokkaido, Japan

3.1 Introduction

Ultra-depleted peridotites, which refer to peridotites that have undergone high degrees of partial melting, are an important end-member component of Earth's mantle (Xu et al., 2021). Due to their refractory physiochemical characteristics, ultra-depleted peridotites have the potential to contribute to continent stabilization (Scott et al., 2019), lithospheric mantle processes during subduction initiation (Parkinson and Pearce, 1998) and craton formation (Pearson et al., 2021). The formation of ultra-depleted peridotites may play an important role in oceanic crust formation during the early stages of the subduction zone development. However, this mechanistic link between subduction initiation has mainly been reconstructed by studies on volcanic rocks, i.e., tholeiite and boninite and by numerical modeling (Arculus et al., 2015; Ishizuka et al., 2020, 2011; Maunder et al., 2020). Ultra-depleted peridotites are, therefore, crucial to obtaining direct information on upper mantle conditions during subduction initiation.

Ultra-depleted peridotites include cratonic peridotites xenoliths (Pearson et al., 2021; Tomlinson and Kamber, 2021; Wittig et al., 2008), forearc peridotites (Birner et al., 2017; Day and Brown, 2021; Ichiyama et al., 2021), and peridotites from supra-subduction zone (SSZ) ophiolites (e.g., Guotana et al., 2017; le Roux et al., 2014). However, studies of ultra-depleted peridotites bodies with clinopyroxene-free (<1 vol.%) assemblages are very limited from the circum-Pacific belt (Figure 13). These include examples such as Papua New Guinea (e.g., Barrett et al., 2022), New Caledonia (e.g., Secchiari et al., 2020; Xu et al., 2021), Coast Range (e.g., Choi et al., 2008; Jean and Shervais, 2017), Anita peridotite massif (Czertowicz et al., 2016a; Scott et al., 2019), Shelting and Mainits zone, eastern Russia (Ishiwatari et al., 2004), and the Kamuikotan unit, Japan (Igarashi et al., 1985; Tamura et al., 1999).

The Takadomari and Horokanai (TH) complex from the Kamuikotan unit of Hokkaido in Japan is known for the occurrence of ultra-depleted peridotite bodies (Tamura et al., 1999). These peridotites are characterized by essentially clinopyroxene-free mineral assemblages, high olivine $Fo\#_{92–95}$ (=100*Mg/(Mg + Fe) atomic ratio) coupled with a high spinel $Cr\#_{0.60–0.91}$ (=Cr/(Cr + Al) atomic ratio). Because these peridotites lack clinopyroxene, which is generally the main budget of incompatible trace elements in peridotites, it is difficult to obtain their mineral trace elements compositions. However, recent studies show that trace element compositions of olivine and orthopyroxene do in fact record the formation and later metasomatic/metamorphic processes (e.g., Demouchy and Alard, 2021; Jean and Shervais, 2017; Nishio et al., 2022b; Scott et al., 2016). In this study, we examine olivine and orthopyroxene trace element compositions in addition to the petrography and mineral major element compositions from one of the clinopyroxene-free ultra-depleted peridotite bodies from the Kamuikotan unit. We also compare them with the clinopyroxene-free ultra-depleted bodies from the circum-Pacific belt for understanding the compositional systematics. Finally, we apply open-system melting models of Ozawa (2001), to assess both the degree of partial melting and the complex re-enrichment processes that occur in natural mantle peridotite.

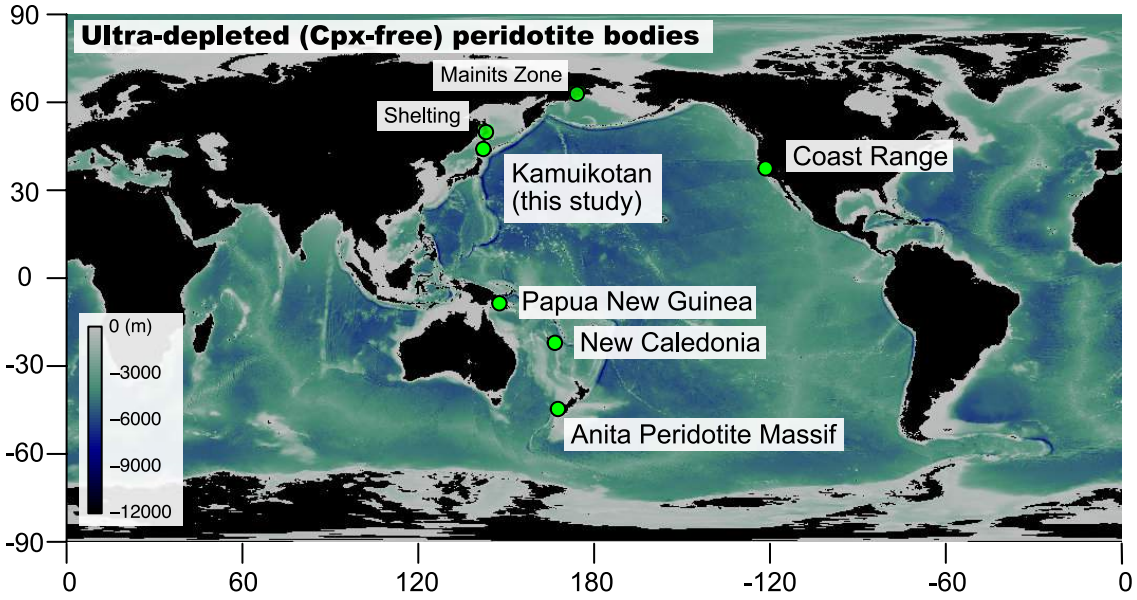

Figure 13: Distribution of the clinopyroxene-free ultra-depleted peridotite bodies in the circum-Pacific belt (Barrett et al., 2022; Choi et al., 2008b; Czertowicz et al., 2016b, 2016a; Ishiwatari et al., 2004; Jean et al., 2010; Jean and Shervais, 2017; Marchesi et al., 2009; Pirard et al., 2013; Secchiari et al., 2020b; Tamura et al., 1999; Ulrich et al., 2010; Xu et al., 2021). Compilation of mineral modes, major element and trace element compositions from these ultra-depleted peridotites are available at Zenodo (additional supporting information Table S1 of Nishio et al. (2023)) (https://doi.org/10.5281/zenodo.7263366). The topographic map is from Amante and Eakins (2009).

3.2 Geological and petrological background

The Kamuikotan unit is a tectonic mélange zone and distributed over 320 km from north to south within the Sorachi–Yezo terrane (Figure 14a; Takeshita et al., 2018; Ueda, 2010; Wallis et al., 2020). The Kamuikotan unit consists of ultramafic rocks and high-pressure and low-temperature metamorphic rocks. The Sorachi–Yezo terrane, including the Kamuikotan unit, consists of Late Jurassic to Early Cretaceous ophiolite, Horokanai ophiolite, to forearc basin (Ichiyama et al., 2012; Nagahashi and Miyashita, 2002; Sakakibara and Ota, 1994). The Horokanai ophiolite consists of ultramafic rocks (Kamuikotan unit; Tamura et al. (2024)), gabbros, amphibolites, basalts (Sorachi-Group) and sedimentary rocks (Figure 14b; Ishizuka, 1987, 1985). The Sorachi Group overlies the Horokanai ophiolite and represents an early Cretaceous submarine volcano-sedimentary sequence (Takashima et al., 2002). The Yezo Group overlies the Sorachi Group and comprises terrigenous sediments deposited in a forearc basin at the late Cretaceous (Takashima et al., 2004).

Ultramafic rocks are widely exposed throughout the Kamuikotan unit and in the mantle section of the Horokanai ophiolite (Figure 14a). Ultramafic rocks consist of serpentinites, peridotites, and minor amounts of chromitites and pyroxenites (Tamura et al., 1999; Walker et al., 2002). Peridotites with wide ranges of olivine Fo# (= 89–95), and spinel Cr# (= 0.18–0.92) have been interpreted to reflect various degrees of melt extraction (Arai et al., 1999; Harada and Arai, 1997; Kubo, 2002; Tamura et al., 1999; Tamura and Arai, 2006, 2005). Ultra-depleted peridotite bodies consisting mostly of harzburgite and dunite occur in the northern section (Shirikomadake, Takadomari, and Horokanai complex). These peridotites are characterized by high Cr# of spinel (0.60–0.91). In the southern section (Iwanaidake and Nukabira complex), depleted to fertile peridotites bodies are exposed: The Iwanaidake complex is dominated by depleted harzburgites with relatively high spinel Cr# (0.43–0.69) and the Nukabira complex is dominated by fertile lherzolites with low spinel Cr# (0.13–0.34; Tamura et al., 1999). The Nukabira fertile lherzolites with low spinel Cr# have LREE-depleted clinopyroxene compositions similar to those of residual abyssal peridotites (Tamura and Arai, 2006). These fertile lherzolites were therefore interpreted as residues after melt extraction under dry conditions. On the other hand, depleted harzburgites were interpreted as residues that experienced hydrous melting based on hydrous mineral inclusions within spinel, spinel/spinel-diopside lamellae in olivine, and/or relict fluid inclusions in olivine (Arai, 1978; Arai et al., 2021; Arai and Hirai, 1985; Hirai and Arai, 1987). Kubo (2002) suggested, based on geochemical modeling, that the depleted dunites in the Iwanaidake complex were formed by localized melting of the host harzburgite caused by an injection of hydrous melt.

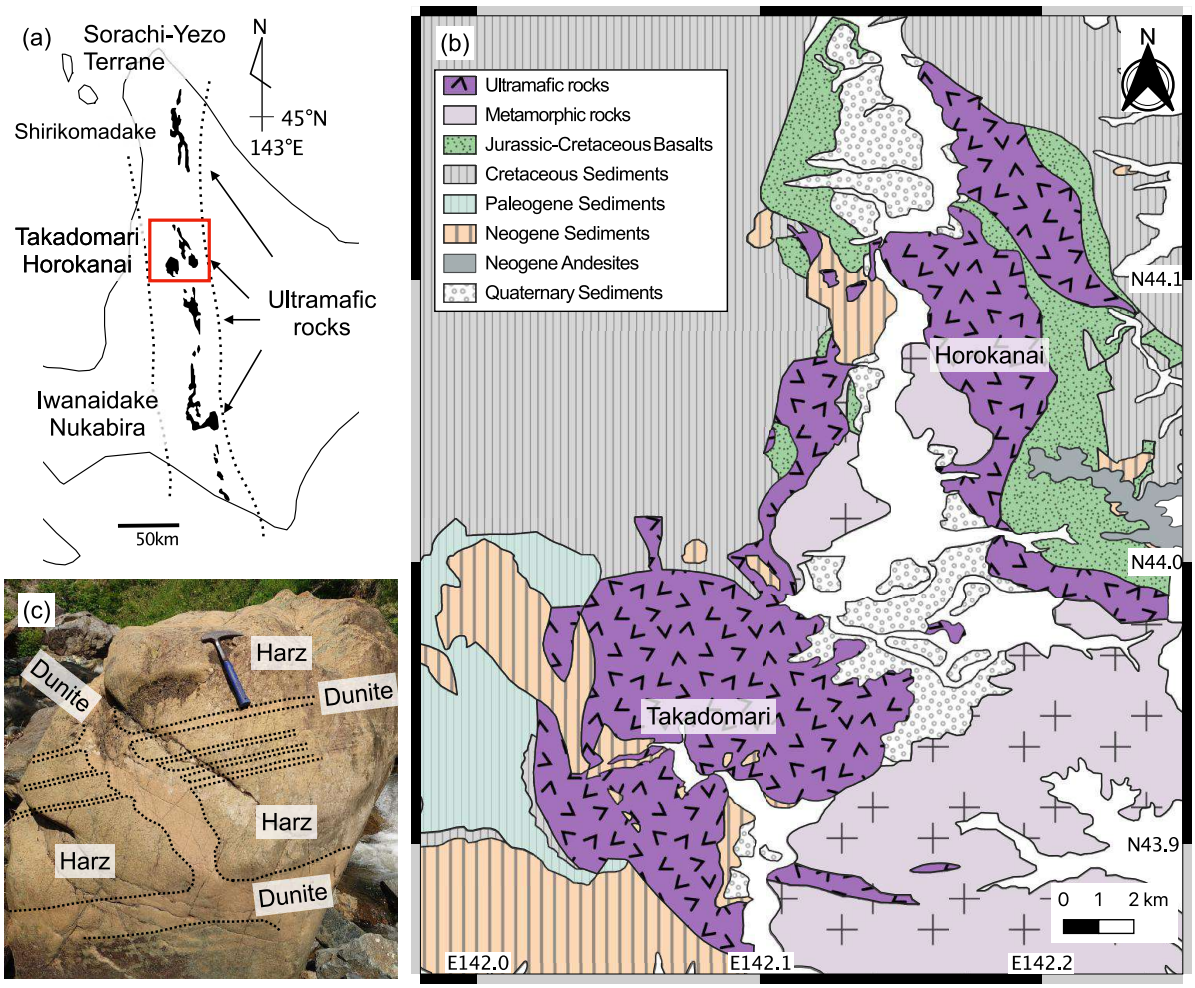

Figure 14: (a) Distribution of ultramafic rocks (black) in the Kamuikotan unit within the Sorachi-Yezo terrane, Hokkaido in Japan. The red squared area indicates the studied area (the Takadomari and the Horokanai complex). (b) Geological map of the Takadomari and Horokanai complex modified after Ishizuka (1985). (c) A representative field photograph of the harzburgite and dunite layers.

3.3 Petrographic characteristics of the Takadomari and the Horokanai (TH) ultramafic rocks

The Takadomari and Horokanai (TH) peridotites mostly consist of harzburgite and decimeter-thick dunite layers and veins are observed in the harzburgite (Figure 14c). Orthopyroxenite layers are rarely observed in the peridotites, however, when present, sometimes show layering structures (Ishizuka, 1985). Dunite consists of olivine (>99 vol.%), minor amounts of spinel (<1 vol.%), and/or orthopyroxene, and is extensively serpentinized (Figure 15a and Supplementary Figure A7). Spinel lamellae and relict fluid inclusions in olivine were reported in dunite (e.g., Arai et al., 2021). Harzburgites are less serpentinized

compared to dunite and consist of olivine (~84 vol.%), orthopyroxene (~15 vol.%), spinel (<1 vol.%), and/or amphibole (Figure 15b and Supplementary Figure A7). Rare grains of amphibole (edenite) are observed in harzburgites (Figure 15c). Spinel-hosted hydrous mineral inclusions, amphibole (hornblende) and Na-mica (aspidolite), were observed in dunite and harzburgite (Figure 15d).

Some inclusions within spinel are connected to interstitial serpentines by cracks. Those inclusions are mostly serpentine and phlogopite. Amphibole (tremolite) rarely rimmed orthopyroxenes in the harzburgites. We focus on the igneous process of the ultra-depleted peridotites in this study. Therefore, these alteration minerals, serpentine, and tremolite around orthopyroxene were excluded from the discussion.

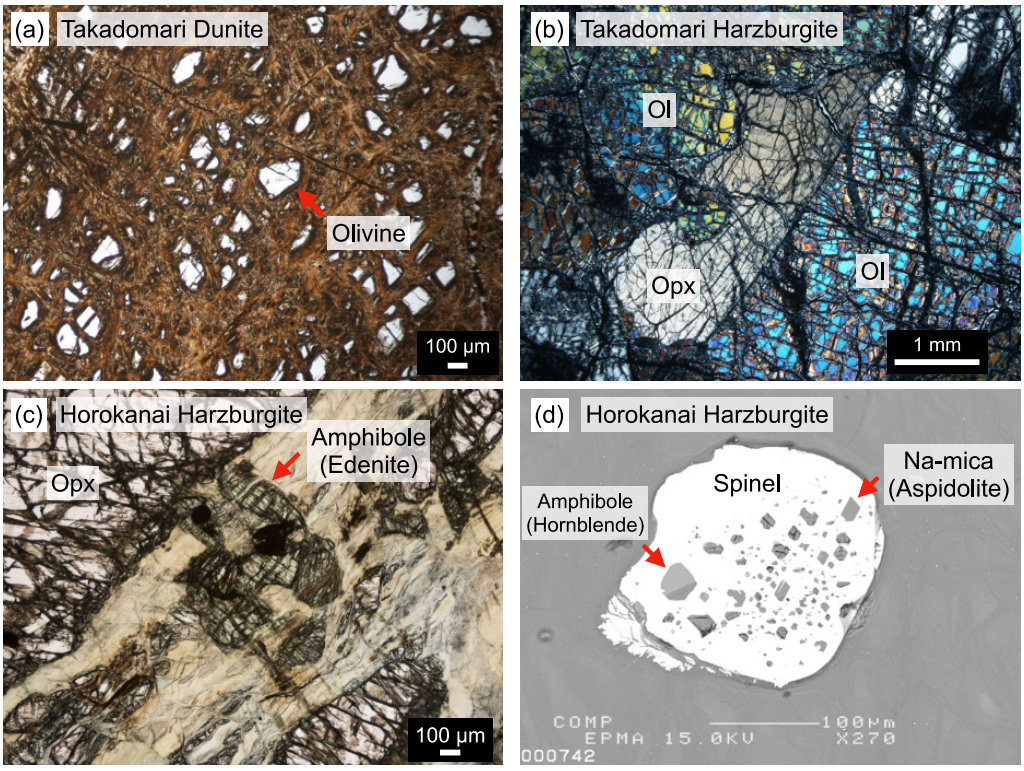

Figure 15: Photomicrograph and back-scattered electron images of the Takadomari and Horokanai peridotites. (a) Takadomari dunite, which is strongly serpentinized. (b) Takadomari harzburgite, which is less serpentinized relative to dunite. Large grains of orthopyroxene (Opx) and olivine (Ol) are observed. (c) Horokanai harzburgite, which rarely contains amphibole (Edenite) grains. (d) Spinel grain from the Horokanai harzburgite, which includes amphibole (Hornblende) and Na-mica (Aspidolite).

3.4 Analytical methods

Major element compositions of minerals in thirty-two peridotite samples were obtained using the JXA-8800 JEOL electron microprobe at Tokyo Institute of Technology and the compositions of mineral inclusions of spinel were obtained at the University of Tokyo. Analytical conditions were set at an accelerating voltage of 15 kV, 12 nA probe current, and a 3 μm beam spot for the analyses. Natural and synthetic mineral standards were used for calibration and JEOL software, using atomic-number–absorption–fluorescence (ZAF) corrections, was used for data reduction. In-house mineral standards, i.e., olivine, chromian spinel, diopside from Akizawa et al. (2021) were measured to monitor data quality.

Trace element compositions of olivine (eight samples), orthopyroxene (four samples), and amphibole (two samples) in peridotites were analyzed using a laser-ablation system (NewWave Research UP-213) coupled with an ICP-MS system (Agilent Technologies) at Kanazawa University. Each analysis was performed using a 90–100 μm ablation spot size for orthopyroxene and olivine and a 60 μm spot size for amphibole at a 6 Hz repetition rate. The analysis for amphibole inclusions in spinel was performed using a 15 μm ablation spot at a 5–6 Hz repetition rate. Standard glass NIST 612 (Jochum et al., 2011) was used for calibration with ^{29}Si as an internal standard, based on the Si content obtained by electron probe microanalysis (Longerich et al., 1996; Pearce et al., 1997). Details of the analytical method and data quality control were reported by (Morishita et al., 2005a, 2005b). Due to low trace element abundances in minerals, signals were carefully monitored for spikes or an increase in signals using elements such as B, Ba, Sr, Ba, Pb, Al, and Cr that indicate the presences of serpentine and/or spinel. Pre-ablation was conducted for a second at a 5–6 Hz repetition rate during every analysis to remove possible surface contamination.

3.5 Results: Mineral chemistry

Olivine Fo# and Cr# of spinel in the TH peridotites are high (92–95 and 0.60–0.91, respectively; Figure 16a). Olivine Fo# (93–95) and spinel Cr# (0.79–0.91) of dunites tend to be higher than those of harzburgites (Fo# = 92–93, Cr# = 0.60–0.88). Spinel TiO_2 contents are low (<0.1 wt. %) for all TH peridotites. Orthopyroxene from harzburgite is characterized by high Mg# (=Mg/(Mg+Fe) atomic ratio; 0.92–0.94) with low Al_2O_3, CaO and Cr_2O_3 contents (0.7–1.6 wt.%, 0.2–1.4 wt.% and 0.1–0.5 wt.%, respectively; Figure 16b). Amphibole inclusions in spinel are mostly hornblende, and amphibole grains in harzburgite were identified as edenite (Leake et al., 1997). Amphibole inclusions in the Takadomari dunite have slightly lower Na_2O contents (1.1–2.0 wt.%) compared to amphibole inclusions/grains (2.0–2.7 wt.%) of the Horokanai harzburgite (Figure 16c).

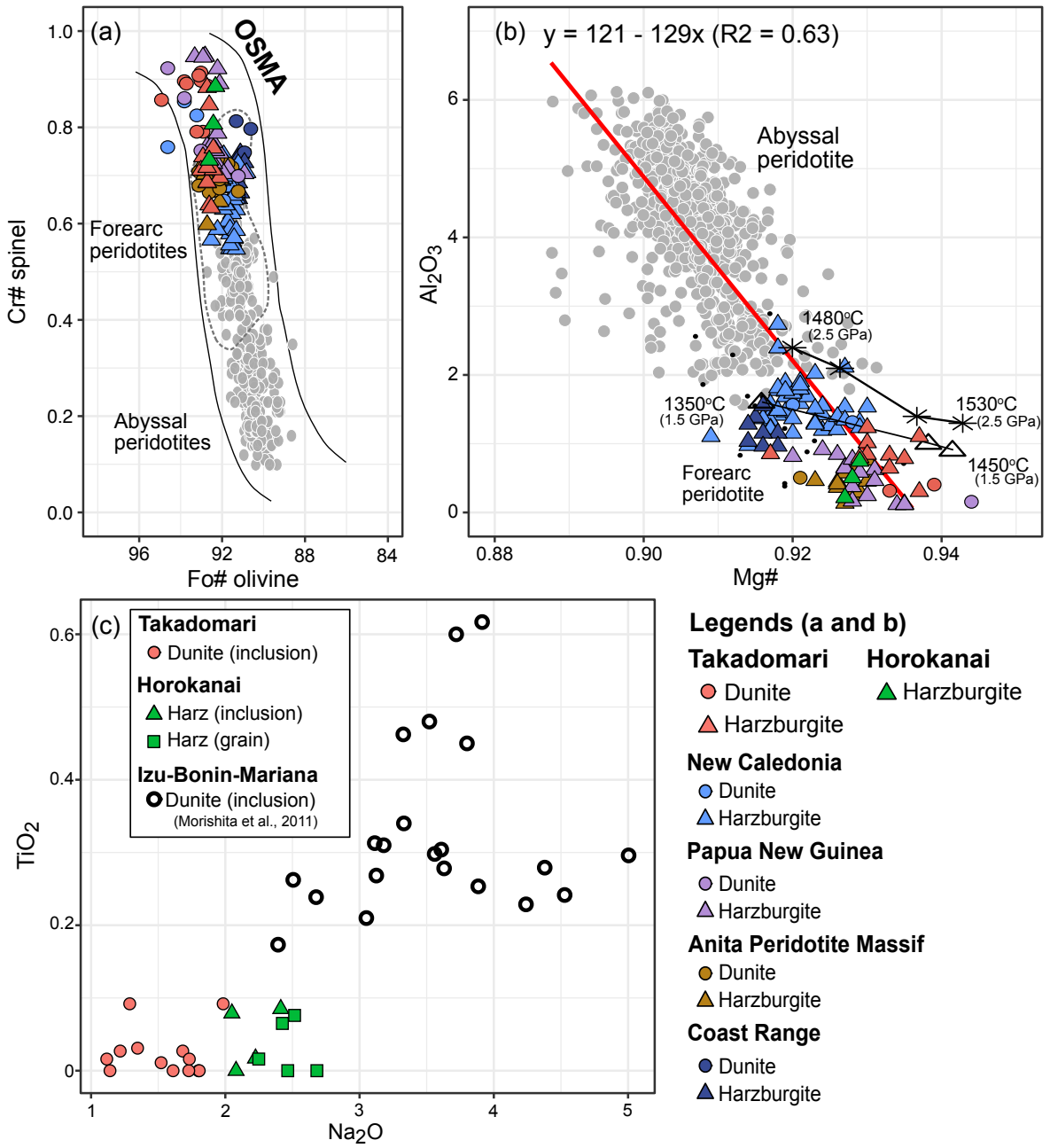

Figure 16: Mineral major element chemistry. (a) Relationship between Cr# of spinel and olivine Fo#. Olivine-spinel-mantle-array (OSMA: Arai, 1994). (b) Al_2O_3 wt.% versus Mg# of orthopyroxene. The black lines represent the composition of orthopyroxene obtained by the experimental study for the formation of ultra-depleted peridotite under hydrous conditions and the numbers denote the temperature and pressure for the experiments (Falloon and Danyushevsky, 2000). The red line was obtained by least-squares linear regressions using orthopyroxene from abyssal peridotites, forearc peridotites, and ultra-depleted peridotites (regression parameters shown in the upper left-hand corner). Compositional data of olivine, spinel, and orthopyroxene from forearc peridotites and abyssal peridotites are from Nishio et al. (2022a) and Parkinson and Pearce (1998). References of ultra-depleted peridotites are listed in Figure 13. (c) TiO_2 wt% versus Na_2O wt.% of amphibole grains and inclusions in spinel. The compositional data of amphibole inclusions of spinel in the Izu-Bonin-Mariana (IBM) forearc dunite are from Morishita et al. (2011).

We obtained abundances of six elements (Ca, Ti, Al, Y, Li, B) for olivine, four to five elements (Sr, Zr, Ti, Y, and/or Yb) for orthopyroxene, and seven elements (Ba, Nb, Ce, Sr, Zr, Ti, Y) for amphibole inclusions. Other elements such as rare earth elements (REE) were below the detection limit of analysis. Titanium in olivine (0.06–0.47 μg/g) of the TH peridotites show positive correlations with Ca (22–113 μg/g), Y (0.0002–0.0024 μg/g), Li (0.9–1.2 μg/g), and B (0.3–2.6 μg/g). The abundances of these elements in olivine of dunites are slightly higher than those of harzburgites except for Al. Al in dunitic olivine (1.5–4.1 μg/g) tends to be lower than those in harzburgitic olivine (2.8–6.2 μg/g). The Ti, Y, and Yb abundances in orthopyroxene of the TH harzburgite are very low (0.8–2.4 μg/g, 0.002–0.01 μg/g, and 0.007 μg/g, respectively) but Sr abundances in orthopyroxene are variable (0.01–0.2 μg/g; Figure 17a). Amphiboles are also low in REE. In particular, amphibole inclusions have lower abundances (example, Y: 0.2–0.3 μg/g) compared to amphibole grains (Y: 0.5–1.1 μg/g; Figure 17b).

Primitive mantle normalized patterns of orthopyroxenes of the TH harzburgites show Sr and Zr enrichments and Ti and Y depletions (Figure 17a) (Sun and McDonough, 1989). The trace element patterns and abundances are similar to orthopyroxenes from the circum-Pacific ultra-depleted harzburgites except for orthopyroxene from the Coast Range ultra-depleted harzburgites which have higher incompatible element concentrations (Jean et al., 2010). Orthopyroxene trace element abundances from the ultra-depleted peridotites are much lower than those in orthopyroxene from abyssal fertile–depleted peridotites (D'Errico et al., 2016; Morishita et al., 2009). Amphiboles of the TH peridotites show flat patterns with slightly enriched LREE and have similar characteristics to orthopyroxene which are enriched in Sr and/or Zr compared to Ti and Y abundance (Figure 17b). The TH amphiboles have lower abundances than amphiboles in dunite from Izu-Bonin-Mariana (IBM) forearc (Morishita et al., 2011).

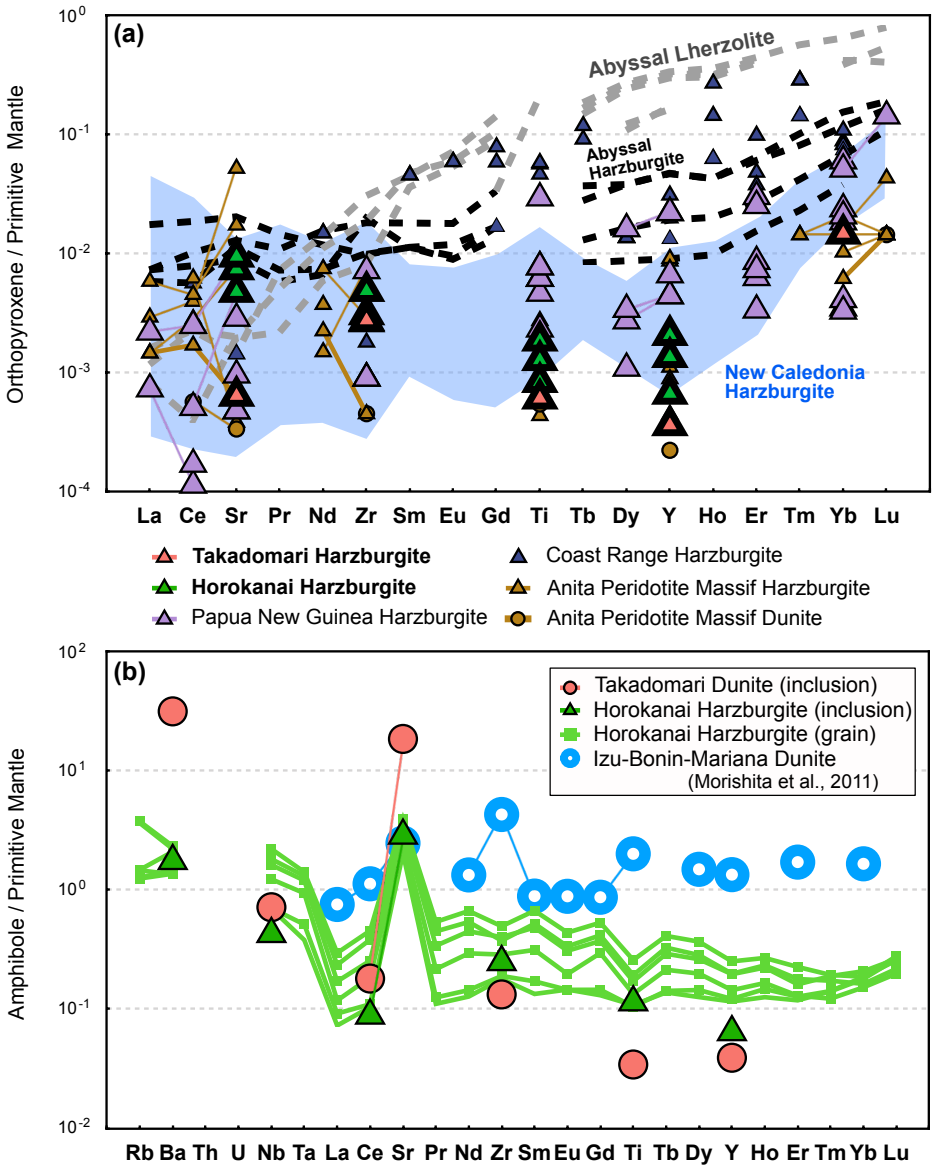

Figure 17: Primitive mantle-normalized trace element patterns of (a) orthopyroxene and (b) amphibole. (a) Grey and black dashed lines are the compositions of orthopyroxenes from abyssal lherzolites and harzburgite (D'Errico et al., 2016; Morishita et al., 2009). A blue colored field represents the orthopyroxene compositions from the New Caledonia ultra-depleted harzburgites. References of the ultra-depleted peridotites are listed in Fig. 1. (b) The light blue line is the composition of amphibole inclusion in spinel from IBM forearc dunite (Morishita et al., 2011). The primitive mantle value is from Sun and McDonough (1989).

3.6 Discussion

3.6.1 Geochemical characteristics of the TH harzburgites: the most depleted peridotites on Earth?

The origin of the TH harzburgites was interpreted as residual peridotites based on olivine Fo# (92–93) and Cr# (0.60–0.88) of spinel (Harada and Arai, 1997; Tamura et al., 1999), and the stratigraphic sequence of the ophiolite (Ishizuka, 1987). Here, we reassess the geochemical characteristics of the TH harzburgites based on the mineral major and trace element compositions combined with fractional melting models (Shaw, 1979).

Olivine Fo# and Cr# of spinel in the TH peridotites are similar to the circum-Pacific ultra-depleted harzburgites (Fo# = 91–93, Cr# = 0.48–0.95; Figure 16a). They plot within the chemical range expected for residual peridotite after partial melting of primitive mantle as indicated by the olivine-spinel-mantle-array (OSMA; Arai, 1994). High olivine Fo# and spinel Cr# contents in the peridotites suggest their origin as residues after high degrees of partial melting. The Mg# (0.92–0.94) of orthopyroxene of the TH harzburgite also display similar values to those from the circum-Pacific ultra-depleted peridotites (0.91–0.94) and tend to be higher than orthopyroxene in abyssal peridotites (0.89–0.93; Nishio et al., 2022a; Warren, 2016) and forearc peridotites (0.90–0.93; Parkinson and Pearce, 1998). The Al_2O_3 contents of orthopyroxenes in residual abyssal and forearc peridotites and the circum-Pacific ultra-depleted peridotites show a negative correlation with Mg# (R^2 = 0.63; Figure 16b). Amphibole grains and amphibole inclusions in spinel of the TH harzburgites have low TiO_2 and Na_2O contents (< 0.1 and 1.1–2.7 wt. %, respectively) but are high in Cr_2O_3 (>2.1 wt. %) compared to those in depleted dunites from IBM forearc (Figure 16c; Morishita et al., 2011).

These depleted signatures and systematics are consistent with the low Ti, Y, and Yb abundances in orthopyroxene and olivine from the TH harzburgites. The abundances are similar to those in olivine and orthopyroxene from the circum-Pacific ultra-depleted peridotites except for the Coast Range peridotites and lower than fertile–depleted residual peridotites (Figure 18; D'Errico et al., 2016; Lawley et al., 2020a; Morishita et al., 2009). We, therefore, conclude that the TH harzburgites are among the most depleted residual peridotites on Earth, which collectively, are found predominantly in SSZ ophiolites from the Western Pacific region (Figure 13).

We conducted a fractional melting model from a depleted-MORB mantle (DMM; Workman and Hart, 2005). Fractional melting is a process in which melt is formed in equilibrium with the residue and is instantaneously removed from the system during partial melting (Shaw, 1979). We used partition coefficients from Bizimis et al. (2000), Hellebrand et al. (2002a), McDade et al. (2003), and Ozawa (2001) and melting modes simplified from Kinzler and Grove (1992) and Parman and Grove (2004)

(0.05Spl + 0.45Opx + 0.75Cpx → 0.25Ol + 1Melt for clinopyroxene-bearing assemblage and 0.2Ol + 0.003Spl + 0.797Opx → 1Melt for clinopyroxene-free assemblage). We also tested the effect of fractional melting under pressure-temperature conditions of the garnet peridotite stability field following Morishita et al. (2018). We used melting modes simplified from Hellebrand et al. (2002a), and the mineral modes of the garnet peridotite were converted to that of spinel peridotite using the following reaction: 3Opx + 1Cpx + 1Spl = 4Grt + 1Ol (Takazawa et al., 1996). Details of melting mode, partition coefficients, and modeling results are provided Table S1 of additional supporting information of Nishio et al. (2023).

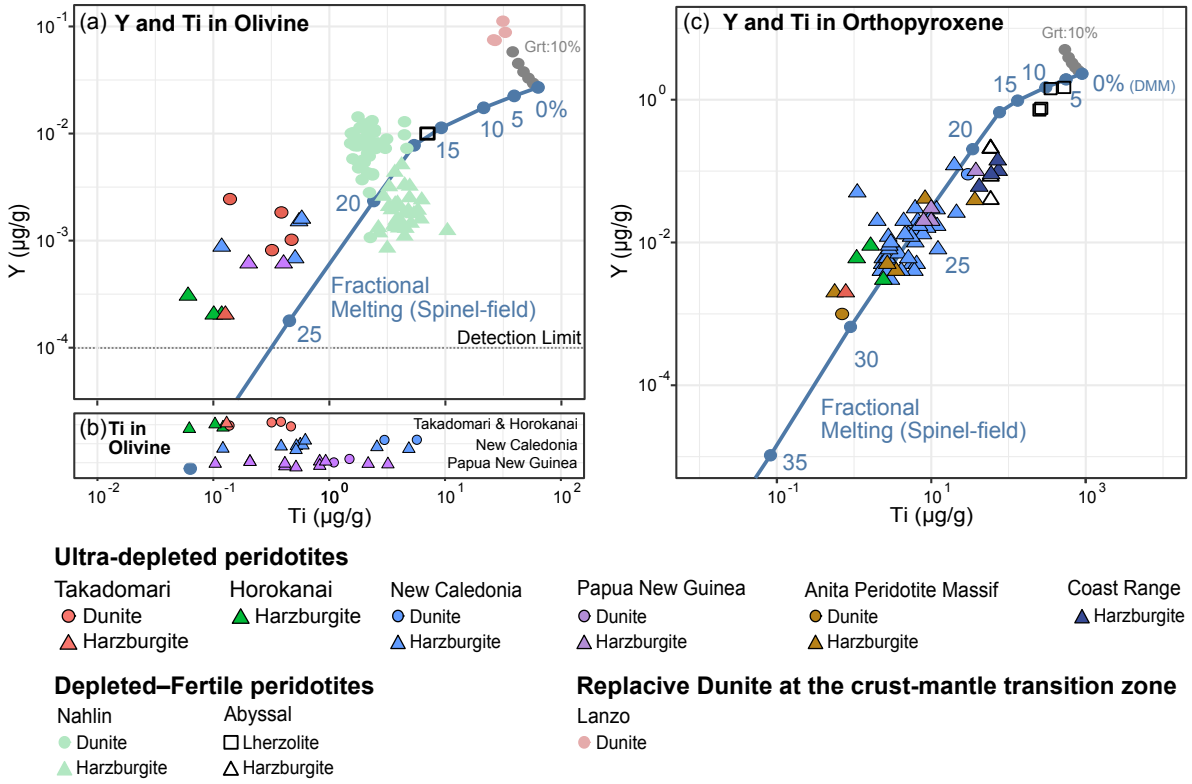

Figure 18: Y and Ti abundances in (a) olivine and (b) orthopyroxene. Blue solid lines were obtained by the spinel stability field fractional melting model and the numbers represent melting degrees. Grey points were obtained by the garnet stability field fractional melting model (0–10%). Light green plots are the compositions of olivine in relatively depleted peridotites from Nahlin ophiolite, Canada (Lawley et al., 2020a). The open square and triangle are the compositions of olivine in abyssal lherzolite and harzburgite (D'Errico et al., 2016; Morishita et al., 2009). Light red circles are the compositions of olivine in replacive dunites at the crust-mantle transition zone from Lanzo massif, Italy (Sanfilippo et al., 2017, 2014). References of the ultra-depleted peridotites are listed in Figure 13.

The fractional melting model shows that Ti and Y abundances in residual olivine and orthopyroxene decrease below those of DMM with increasing degree of melting (Figure 18). The melting trends are consistent with orthopyroxene compositions in the TH harzburgites and the circum-Pacific ultra-depleted peridotites. The fractional melting in the stability field of garnet peridotite (0–

10%) shows a decrease in Ti abundances but a slight increase in Y abundances with increasing degree of melting. Therefore, when peridotites undergo melting in the stability field of garnet peridotite prior to melting in the stability field of spinel peridotite, it requires higher melting degrees to deplete the Y in residues compared to the ones that experienced melting directly from DMM in the spinel stability field. Our fractional melting model suggests that the TH harzburgite and the circum-Pacific ultra-depleted peridotites are residues that went through at least 25% of melting from DMM in the spinel stability field.

Estimating the degree of partial melting shows how the fractional melting model most efficiently depletes incompatible elements in residues because fractional melting is a process that occurs if the melts had zero viscosity, or the mantle had infinite permeability. Melt fractions retained in the source, which result in less fractionation of incompatible elements in the source, should be considered. Therefore, it should be noted that the fractional melting model estimates the minimum degree of partial melting from the depletion of incompatible elements in the residual phases. In addition, estimating the exact degree is not easy because fractional melting models are particularly sensitive to minor differences in partition coefficients and melting modes for ultra-depleted peridotites, as noted by Scott et al. (2016). In any case, we emphasize that high degrees (>25%) of melting are necessary as a minimum requirement for the formation of the ultra-depleted harzburgites.

3.6.2 Melting processes for the formation of the TH harzburgites: influx melting obtained from the open-system melting model

The Ti and Y abundances in these peridotites show ultra-depleted signatures constrained by the fractional melting model (Figure 18). However, the enrichment of Sr and Zr compared to Y and Ti in orthopyroxene of the TH ultra-depleted peridotites cannot be reproduced by the fractional melting model, i.e., melting and melt extraction solely from the DMM source in both spinel and garnet stability fields (Figure 19a). This decoupling indicates that these peridotites underwent influx melting, in which fluid/melt flux are added into the system during partial melting and melt extraction (le Roux et al., 2014; Morishita et al., 2018; Tilhac et al., 2021).

We have conducted open-system melting model of Ozawa (2001) and Ozawa and Shimizu (1995) to constrain the melting conditions and account for the enriched Sr and Zr and depleted Ti and Y in orthopyroxene from the ultra-depleted peridotites. This open-system melting model formulated the input and output of elements during melting processes, which include flux (fluids/melts) input to the system as well as partial melting and melt extraction (an equation 33 for trace elements of Ozawa, 2001). Therefore, this model allows us to test more complex melting processes, such as fluid/melt influx melting and incongruent melting. Using this model, we have modeled influx melting and investigated starting source and flux compositions and other important parameters, which are critical melt fraction and influx rate. Critical melt fraction (α) is a parameter, at which the system becomes open to melt

separation and dimensionless influx rate (β) is a material influx rate relative to melting rate, which is the amount of material that flows into the system normalized by the amount of the source material. We used a melting mode under hydrous conditions (0.02Spl + 0.52Opx + 0.56Cpx → 0.1Ol + 1Melt) for the clinopyroxene-bearing assemblage from Bizimis et al. (2000) (Figure 19a: open-system melting after 0–17.3% of fractional melting). Except for the melting mode in the models in Figure 19a, partition coefficients and melting modes used in these models are the same as those for the fractional melting model. The slab fluid composition (Sr: 150 μg/g, Zr: 16 μg/g, Y and Ti: 0 μg/g) was also taken from Bizimis et al. (2000) as flux compositions. Details and results of models and parameters are provided in Table S3 of additional supporting information of Nishio et al. (2023).

Our models for influx melting with starting compositions formed after 17.3% (clinopyroxene-out) of fractional melting from DMM reproduced the enrichments of Sr and Zr and the depletions of Ti and Y in orthopyroxene, suggesting that ultra-depleted harzburgites experienced influx melting (Figure 19a). We conducted open-system melting model, i.e., influx melting with a low influx rate (ß = 0.05) and a low critical melt fraction (α = 0.01). It is interesting to note that the similar orthopyroxene compositions are also observed in other circum-Pacific ultra-depleted harzburgites. This indicates that influx melting is a common process among the circum-Pacific ultra-depleted peridotites, or at least in the mantle portion of many SSZ ophiolites.

Next, we investigated the influence of different parameters. We vary Zr concentration in flux, which is fluid in our model (Figure 19b), influx rate (Figure 19c), critical melt fraction (Figure 19d), Ti and Y concentrations in fluid (Figure 19e), and melting mode for testing multi-stages of melting (Figure 19a). Summary of the models are listed in Table 2.

Table 2: Summary of melting conditions and parameters used for geochemical models. Details of melting mode, partition coefficients and modeled olivine and orthopyroxene compositions are provided in TableS3 of additional supporting information of Nishio et al. (2023).

Figure	Parameters of open-system melting models						
	Starting material	Fluid (flux) composition				Influx rate	Critical melt fraction
		Sr (μg/g)	Zr (μg/g)	Ti (μg/g)	Y (μg/g)		
Figure 19a	•DMM •Residues after 5%, 10%, 15%, 17.3% of fractional melting from DMM	150	16	0	0	0.05	0.01
Figure 19b	•Residues after 17.3% of fractional melting from DMM	150	0.1–1000	0	0	0.05	0.01
Figure 19c	•Residues after 17.3% of fractional melting from DMM	150	16	0	0	0.01–1	0.01
Figure 19d	•Residues after 17.3% of fractional melting from DMM	150	16	0	0	0.05	0.001–0.05
Figure 19e	•Residues after 17.3% of fractional melting from DMM	150	16	0–1000	0–1000	0.05	0.01
Figure A8	•Residues after 17.3% of fractional melting from DMM	150–15000	0	0	0	0.05	0.01

Higher incompatible elements concentrations in fluid, as well as higher influx rate and critical melt fraction result in less fractionation of these elements in residual orthopyroxene. The compositional differences in fluid (Sr: 150–15000 μg/g and Zr: 0.1–1000 μg/g) cause the compositional difference in residual orthopyroxene in the logarithmic scale (Figure 19b and Supplementary Figure A8). The difference in influx rate (ß: 0.01–1) also causes compositional changes in orthopyroxene (Figure 19c). The first few degrees of influx melting (total degrees from DMM: 17.3–30%) show the largest compositional change in Sr and Zr abundances but the abundances converge in high melting degrees when fluid compositions and influx rates are constant. On the other hand, the difference in critical melt fraction (α = 0.001–0.05) does not affect Zr and Sr abundances in residual orthopyroxene (Figure 19d).

The Ti and Y abundances in residual orthopyroxene are less sensitive to fluid influx compared to Sr and Zr in our model. Compositional changes of Y and Ti abundances in residual orthopyroxene at the 40% degree of partial melting extent from DMM are not well documented when Y and Ti abundances in fluids are less than 10^3 times primitive mantle with an influx rate ß = 0.05 (Y: 0.01 μg/g, Ti: 10 μg/g in fluid; Figure 19e). On the other hand, Ti and Y abundances in residual orthopyroxene are more sensitive to critical melt fraction, which is retained in the system until melt is connected and removed from the source. High critical melt fractions result in less fractionation of Ti and Y depletions in orthopyroxene (Figure 19d).

Our parametric study indicates that fluid compositions and their influx rates exert primary control on Zr and Sr (and LREE) concentrations in residual orthopyroxene. Melting degrees and critical melt fractions exert primary control on Ti and Y concentrations in the residual orthopyroxene. High melting degrees with a low melt fraction are, therefore, key to depleting Ti, Y (and HREE) in the residue. The models show that the orthopyroxene compositions of the ultra-depleted peridotites can be reproduced when the fluid contains high Zr and Sr but low Y and Ti abundances with a low influx rate and a low critical melt fraction (10–100 μg/g for Zr and 150–1500 μg/g for Sr and <10 μg/g for Y and <1000 μg/g for Ti, ß = 0.05 and α = 0.01). The fluid composition in our model shares the characteristics of slab fluids with low Ti, Y, and HREE and high Sr, Zr, and LREE (Bizimis et al., 2000; Li et al., 2013). Therefore, we conclude that these ultra-depleted harzburgites were generated by high degrees (>30%) of slab-fluid influx melting.

Additionally, we tested the contribution of degrees of melt extraction before undergoing influx melting (two-stage melting model: residue after simple partial melting and extraction followed by influx melting expected in the subduction zone; e.g., Ishizuka et al., 2020). We compared influx melting with starting compositions formed after 5%, 10%, 15% and 17.3% of fractional melting from DMM and influx melting from DMM in the spinel stability field (Figure 19a). The models show that Zr and Sr concentrations in residual orthopyroxene converge at high degrees of melting (>30%) when fluid compositions and influx rates are constant. All models in Figure 19a can reproduce the orthopyroxene compositions. It is difficult to determine whether the ultra-depleted peridotites experienced partial melting prior to influx melting only based on the modeling results. However, the residual orthopyroxene

has slightly higher Ti and Y abundances when the starting material is more fertile prior to influx melting (Figure 19a). Higher trace element concentrations in fluids, influx rates and melt fractions also result in less depletion of the HREE in residual orthopyroxene (Figure 19b–e). Therefore, it is more likely that the relatively depleted composition of source peridotites prior to influx melting is a key factor in the formation of ultra-depleted harzburgites.

The TH amphiboles have lower TiO_2, Na_2O and HREE abundances with higher Cr_2O_3 contents compared to amphiboles of IBM forearc depleted dunite (Figure 16c and Figure 17b; Morishita et al., 2011). This is consistent with the ultra-depleted signatures shown in the co-existing mineral compositions. In addition, the TH amphiboles share the characteristics of the enriched Sr and Zr and depleted Ti and Y with orthopyroxene. The orthopyroxene compositions were only reproduced by influx melting as discussed above. Therefore, the high degree of influx melting possibly explains the presence of amphiboles and their compositions in the TH peridotites.

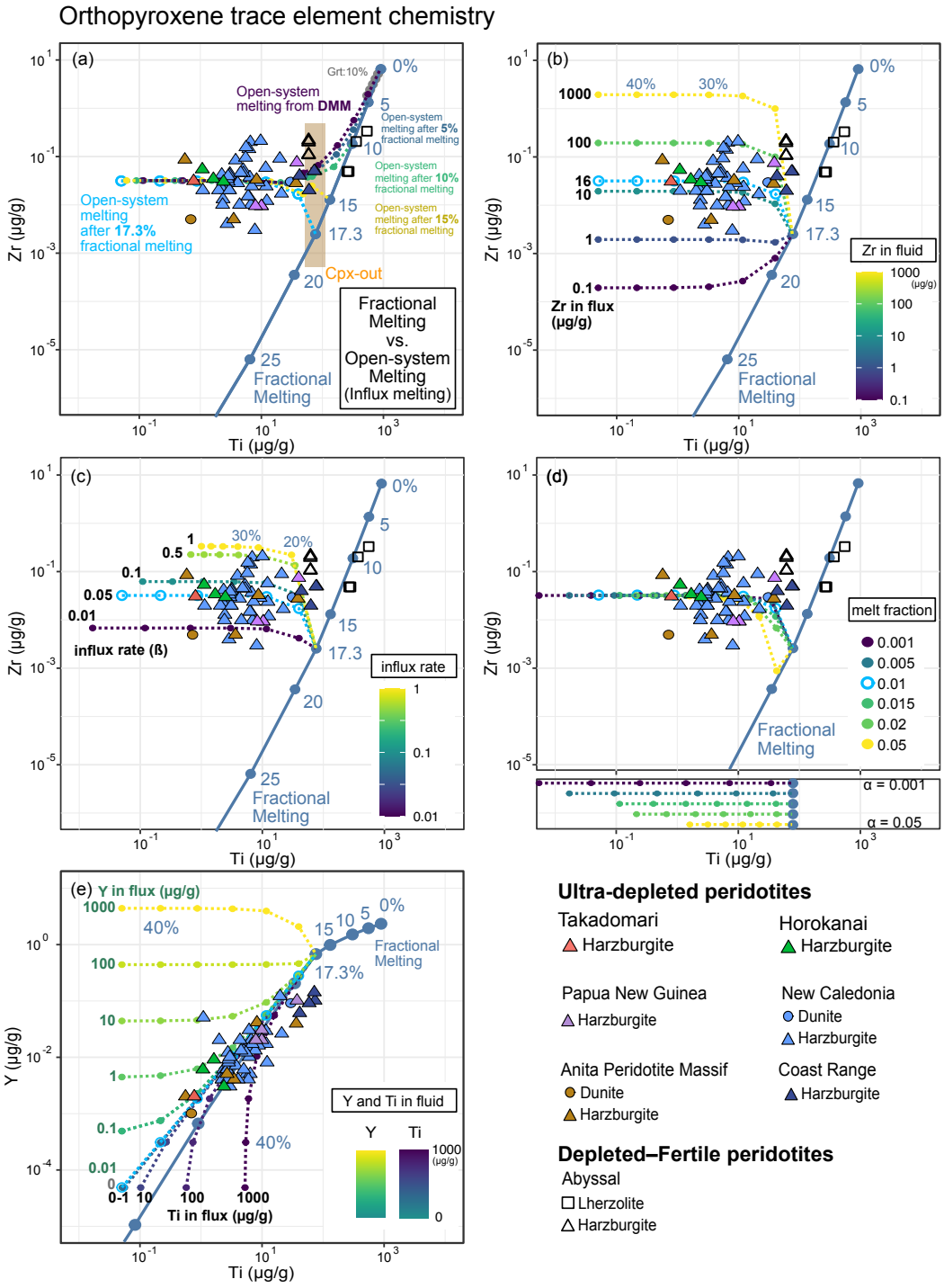

Figure 19: (a)–(d) Zr and Ti and (e) Y and Ti abundances in orthopyroxene. Orthopyroxene compositions from abyssal peridotites are from D'Errico et al. (2016). The blue solid line is the compositional trend reproduced by the spinel stability field fractional melting model. (a) Open-system melting model, i.e., influx melting, with starting compositions formed after 5–17.3% degrees of fractional melting from DMM (Workman and Hart, 2005) and from DMM. Grey points were obtained by the garnet stability field fractional melting model (0–10%). (b) Varying Zr abundance in fluid (=flux) ranging from 0.1–1000 µg/g, (c) varying influx rates ranging from 0.01–1, (d) varying melt fraction ranging from 0.001–0.05 and (e) varying Y and Ti abundances in fluid ranging from 0–1000 µg/g, respectively. References of the ultra-depleted peridotites are listed in Figure 13.

3.6.3 Origin of ultra-depleted dunites: melt-depleted peridotite interaction

The Ti and Ca (and Y) abundances in olivine decrease in abundance from abyssal lherzolite, moderately depleted peridotites, and ultra-depleted harzburgites (Barrett et al., 2022; Lawley et al., 2020a; Morishita et al., 2009; Secchiari et al., 2020b). This is consistent with the fractional melting model (Figure 18). However, these abundances in olivine are slightly higher in the TH dunites than those in the TH harzburgites although TH dunites tend to have higher olivine Fo# and Cr# of spinel. The TH dunites occur as layers or veins in host harzburgites (Figure 14c; Tamura et al., 1999). This suggests that the ultra-depleted dunites were produced by a process involving incongruent melting of orthopyroxene in the host harzburgite triggered by the introduction of hydrous melts (Kubo, 2002).

Dunite layers in the mantle sections containing slightly higher Ti in olivine compared to host harzburgites were also observed in ultra-depleted and depleted peridotites bodies and their origins were interpreted as a product of melt-rock interaction (Barrett et al., 2022; Lawley et al., 2020a). Olivine from the dunite layers in the mantle sections has much lower Ti, Ca and Y abundances than those in olivine from replacive dunites at the crust-mantle transition zone (Figure 16a). These replacive dunites at the crust-mantle transition zone were produced by melt-rock interaction with high melt/rock ratios and melt composition was suggested to be MORB (Kelemen et al., 1995; Sanfilippo et al., 2017, 2014). Although both dunites are products of melt-rock interaction, their compositional differences indicate that olivine trace element compositions in these dunites are controlled by the melt/rock ratio and by the compositions of the host residual peridotites and the melts. We, therefore, conclude that the TH ultra-depleted dunites are products of melt-rock interaction at low melt/rock ratios, and both rock, i.e., host peridotites and melts were depleted in incompatible elements.

3.6.4 Petrogenesis of ultra-depleted peridotite and their link to boninites

Boninites are characterized by enrichments in Sr and Zr and depletions in Ti and Y (Figure 20; Umino et al., 2015). The instantaneous fractional melts, which are in equilibrium with ultra-depleted residual harzburgites, reproduced by our open-system melting model, i.e., influx melting, show similar characteristics to boninite. However, trace elements abundances in the melts are lower than those in boninite (Figure 20a). The models show that these abundances in the instantaneous fractional melts reproduced by influx melting from DMM are higher at low melting degrees; however, these abundances in the instantaneous fractional melts are lower at higher melting degrees compared to those in boninites (Figure 20a). Therefore, when our influx melting model reproduces the ultra-depleted orthopyroxene compositions, the instantaneous fractional melts are more depleted than boninites. In our model, the enriched Sr and Zr in boninites were only reproduced when these abundances in fluids are very high (Sr: >1500 μg/g, Zr: >1000 μg/g) or high influx rate (ß >0.5). These indicate that boninites are rather

accumulated melt and/or fractionated melt from the instantaneous fractional melt. Another possible explanation is that the instantaneous fractional melts experienced inputs of slab fluids/melts in a later process before erupting as boninites.

We also calculated melts in equilibrium with amphiboles using the partition coefficients from (Ozawa, 2001) and Shimizu et al. (2017). Although the formation of spinel-hosted inclusions is controversial, it allows us to estimate the melt compositions involved in the system (e.g., Arai et al., 2022; Rospabé et al., 2021; Tamura et al., 2014). The calculated melts equilibrated with the TH amphiboles are more depleted compared to the melt equilibrated with amphibole from the IBM forearc dunite (Morishita et al., 2011). The calculated melts characterized by low HREE abundance and positive Sr anomalies are similar to those of high-Si boninite which is one of the most high-field strength elements and heavy REE depleted melts (Figure 20b; Umino et al., 2018, 2015). Findings from the mineral chemistry and modeling suggest that the TH and the circum-Pacific clinopyroxene-free ultra-depleted peridotites are residues after extraction of high-Si boninitic melts.

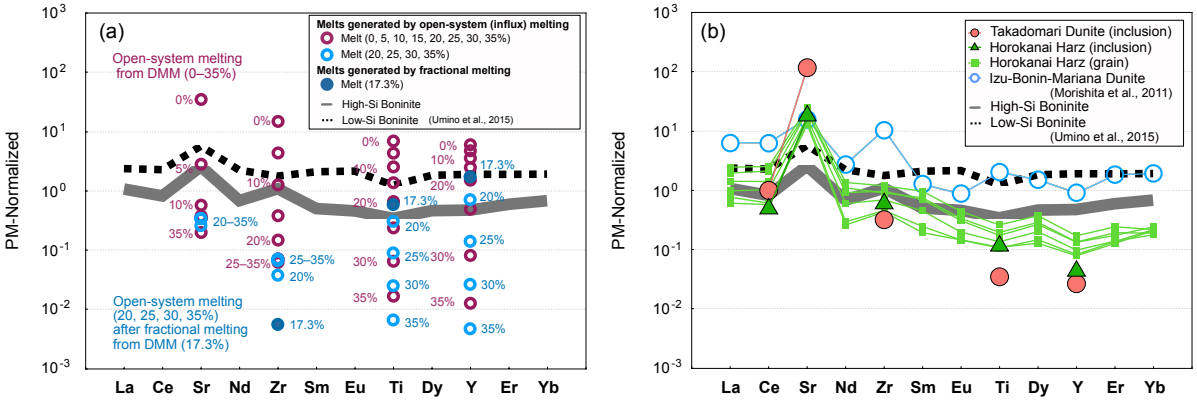

Figure 20: (a) Primitive mantle-normalized patterns of the instantaneous fractional melts estimated from the open-system melting model, i.e., influx melting. The purple plots are the instantaneous fractional melt compositions generated by influx melting from the DMM source which did not experience fractional melting before the influx melting (the purple-colored model in Figure 19a). Blue plots are instantaneous fractional melts compositions generated by 17.3% degree of fractional melting from DMM. Light blue plots are the instantaneous fractional melts generated by influx melting (20–35%: the total melting degrees from DMM) with starting compositions formed after 17.3% of fractional melting from DMM (the light blue colored model in Figure 19a). (b) the calculated melts in equilibrium with amphibole grains and inclusions using the amphibole-melt partition coefficients from Ozawa (2001) and Shimizu et al. (2017). The black dotted and grey solid lines are the representative patterns of low-Si boninite and high-Si boninite, respectively (Umino et al., 2015). The blue line is the pattern of amphibole inclusion in spinel from the IBM forearc dunite (Morishita et al., 2011). The primitive mantle value is from Sun and McDonough (1989).

Low-pressure and high-temperature conditions were constrained for the formation of high-Si boninite (0.8 GPa, 1430ºC; Umino et al., 2015). High Mg# and low Al_2O_3 contents in orthopyroxene of the TH harzburgite also suggest high-temperature conditions. Orthopyroxene compositions from the ultra-depleted peridotites are consistent with those from depleted harzburgites at high temperatures (>1350 ºC) and under hydrous conditions constrained by the experimental study (Figure 16b; Falloon and Danyushevsky, 2000; Parman and Grove, 2004). Therefore, high temperature (>1350 ºC) and continuous supply of fluids are key to the formation of ultra-depleted peridotites and boninitic magma.

The TH ultra-depleted peridotite body occurs in the northern part of the Kamuikotan unit. In contrast, the fertile-depleted peridotite bodies characterized by middle to low spinel Cr# occur in the southern part, i.e., the Nukabira and Iwanaidake complex (Figure 14a). The Nukabira peridotite body consisting mostly of fertile-lherzolite is interpreted as residual peridotite after some extent of melt extraction under dry conditions (Tamura and Arai, 2006). These distributions and geochemical features of the TH ultra-depleted peridotites and fertile peridotites can be explained as mantle materials during subduction initiation (Ishizuka et al., 2011). Fertile-lherzolites from the southern part might be residues after extraction of tholeiitic melts (forearc basalt: FAB after Reagan et al. (2010)) as a result of decompression melting with a low influx in the earliest stage of subduction (Stage 1 in Figure 21a). Although no boninite has been reported from the studied area, we speculate that the TH ultra-depleted harzburgites are residues after extraction of high-Si boninitic melts as a result of slab-fluid influx melting (Stage 2 in Figure 21a). Dunite layers are observed within both ultra-depleted harzburgites and fertile lherzolites. These dunites are products of melt-rock interactions (Figure 21b). Compositional differences and mineral assemblage of dunites, and associated lithology reflects the differences in the compositions of melts and host peridotites (Tamura et al., 1999).

The ultra-depleted–fertile peridotites bodies are distributed in the Kamuikotan unit more than 100 km-scale. Other circum-Pacific ultra-depleted peridotites bodies also occur with depleted–fertile peridotites bodies at a similar scale (Figure 13; Barrett et al., 2022; Choi et al., 2008a, 2008b; Secchiari et al., 2020a; Xu et al., 2022). This commonality suggests that the distribution of ultra-depleted–fertile peridotite bodies in the mantle was probably >100 km-scale.

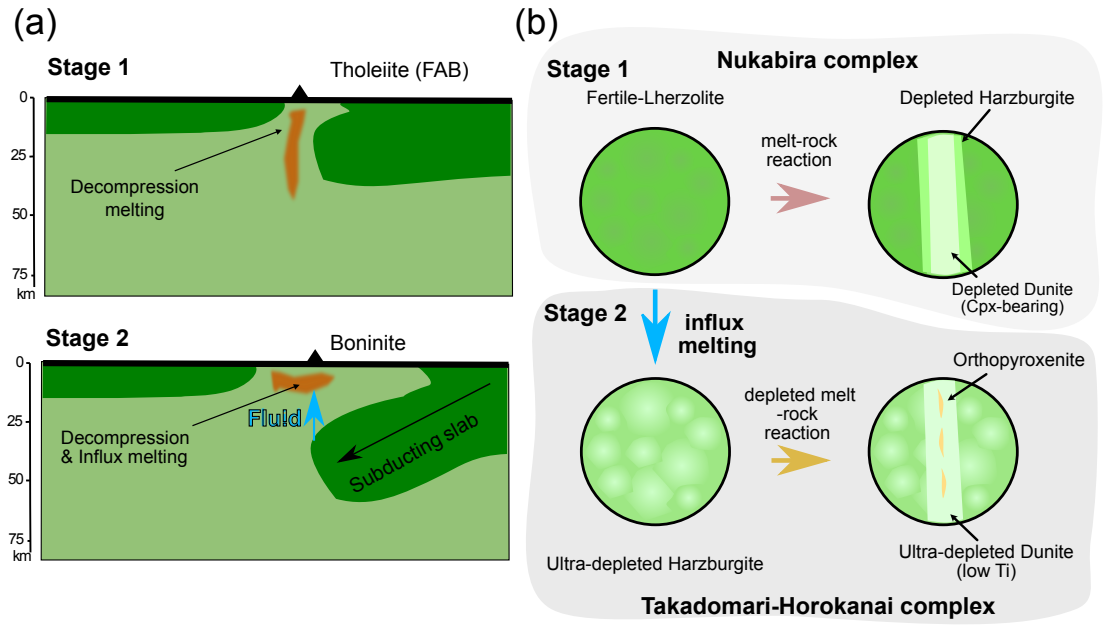

Figure 21: (a) Schematic illustrations for the evolution of subduction zone modified from Ishizuka et al. (2011). (b) Schematic illustrations for the formation of the ultra-depleted peridotites in the Kamuikotan unit modified from (Tamura et al., 1999). Fertile lherzolites from the Nukabira complex can be regarded as residues of decompression melting in stage 1. This melting is thought to be caused by the extension associated with slab sinking and counterflow of asthenospheric mantle. On the other hand, ultra-deplete peridotites from the Takadomari and Horokanai complex can be regarded as residues of decompression and slab-fluid influx melting which formed boninites. Then, the residual lherzolites and harzburgites reacted with melts respectively. Interactions between melts and residues produced dunites and wall peridotites (harzburgites) in the Nukabira complex. The reaction formed ultra-depleted dunites and orthopyroxenites in the Takadomari and Horokanai complex.

3.7 Conclusion

Peridotites from the Takadomari and the Horokanai (TH) complex have high olivine Fo# (92–95), Cr# (0.60–0.91) of spinel, and Mg# (0.92–0.94) of orthopyroxene. On the other hand, these peridotites have low Al_2O_3 contents (0.7–1.6 wt.%) in orthopyroxene and low Ti and Y abundances in olivine and orthopyroxene. These geochemical signatures suggest that the harzburgites are residues after large extents of melt extraction and among the most depleted peridotites on Earth.

The Takadomari and Horokanai peridotites include rare amphibole and/or amphibole inclusions in spinel. Orthopyroxene and amphibole in the ultra-depleted harzburgites show enriched Zr and Sr (LREE) and depleted Ti and Y (HREE) abundances. This decoupling in orthopyroxene was reproduced by the open-system melting model, i.e., influx melting, and it suggests that ultra-depleted peridotites formed after high degrees (>30%) of slab-fluid influx melting with a low influx rate and critical melt fraction.

The Ti abundance in olivine is slightly higher in the dunite layers or veins than those in ultra-depleted harzburgites but much lower than dunites associated with fertile–depleted peridotites. These suggest that the ultra-depleted dunites are a product of depleted melt-depleted peridotite interaction.

The instantaneous fractional melts equilibrated to ultra-depleted residues produced by the open-system melting model, i.e., influx melting and melts equilibrated to amphiboles share the characteristic of enriched Zr and Sr and depleted Ti and Y with boninites. But the instantaneous fractional melts have lower abundances compared to boninites. These indicate that ultra-depleted harzburgites are residues after extractions of depleted boninitic melts. Boninites are probably accumulated melt during the melting processes or fractionated melt from the instantaneous fractional melt. The boninitic melt composition and high Mg# and low Al_2O_3 contents in orthopyroxene of the TH harzburgite indicate the melting under high-temperature conditions (>1350℃).

Distributions of the fertile lherzolites in the south and the ultra-depleted peridotites in the north can be explained as mantle materials during subduction initiation. We speculate that the fertile lherzolites are residues after the extraction of tholeiitic melts and the ultra-depleted harzburgites are residues after the extraction of boninitic melts. A continuous supply of fluids and high temperature are the key to the formation of ultra-depleted peridotites and boninites at subduction initiation.

Chapter 4

4 Metasomatic modification of the Mesoarchean Ulamertoq ultramafic body, Southern West Greenland

4.1 Introduction

Archean geodynamics and crustal differentiation are central topics in Earth sciences (Korenaga, 2013; Palin et al., 2020). These studies are usually based mainly on granitoid and supracrustal rocks, while petrologic studies of Archean ultramafic rocks are rather limited (Friend and Nutman, 2011; Ishikawa et al., 2017; Rollinson, 2007; Shirey and Richardson, 2011; Wilde et al., 2001). Ultramafic rocks are ubiquitously exposed, in small outcrops, within the Archean geological units of southern West (SW) Greenland. These ultramafic bodies have been studied to understand the ancient mantle conditions and geochemical development of early Earth (Fischer-Gödde et al., 2020). However, the origin of the ultramafic rocks remains controversial: the two main origins suggested by different studies are as residues after partial melting in the mantle (Friend et al., 2002; Friend and Nutman, 2011; van de Löcht et al., 2020, 2018) or cumulates of mafic minerals from primitive mantle-derived melts (Aarestrup et al., 2021; Garde, 1997; Garde et al., 2020; McIntyre et al., 2021, 2019; Szilas et al., 2018; Waterton et al., 2022; Zemeny et al., 2023; Zhang et al., 2023). The controversy over the origin of these Archean ultramafic rocks is, in large part, a function of the significant metasomatic and metamorphic overprints that have modified their primary igneous features, both mineralogically and geochemically, as documented in this paper. It is essential to carefully evaluate the lithologic and compositional variation of these ultramafic rocks to decipher the geochemical evolution of early Earth.

The Ulamertoq ultramafic body is one of the largest bodies in the Mesoarchean Akia terrane of SW Greenland (Figure 22). We document the common occurrence of hydrous mineral-rich metasomatic rocks at the boundary between ultramafic body and the granitoid country rocks. Ultramafic rocks far from the contact with granitoid rocks contain less hydrous minerals, i.e., they are less metasomatized. Therefore, the Ulamertoq ultramafic body is the best candidate for investigating the lithologic and compositional variations within the Archean ultramafic bodies of the Akia terrane.

Here, we report petrographic characteristics as well as mineral and whole-rock chemistry of a suite of samples from the Ulamertoq ultramafic body and demonstrate that multi-stage metamorphism and metasomatism are recorded by the ultramafic rocks. This secondary modification of the protolith has to be considered when discussing the origin of the ultramafic rocks in the Archean crust of SW Greenland.

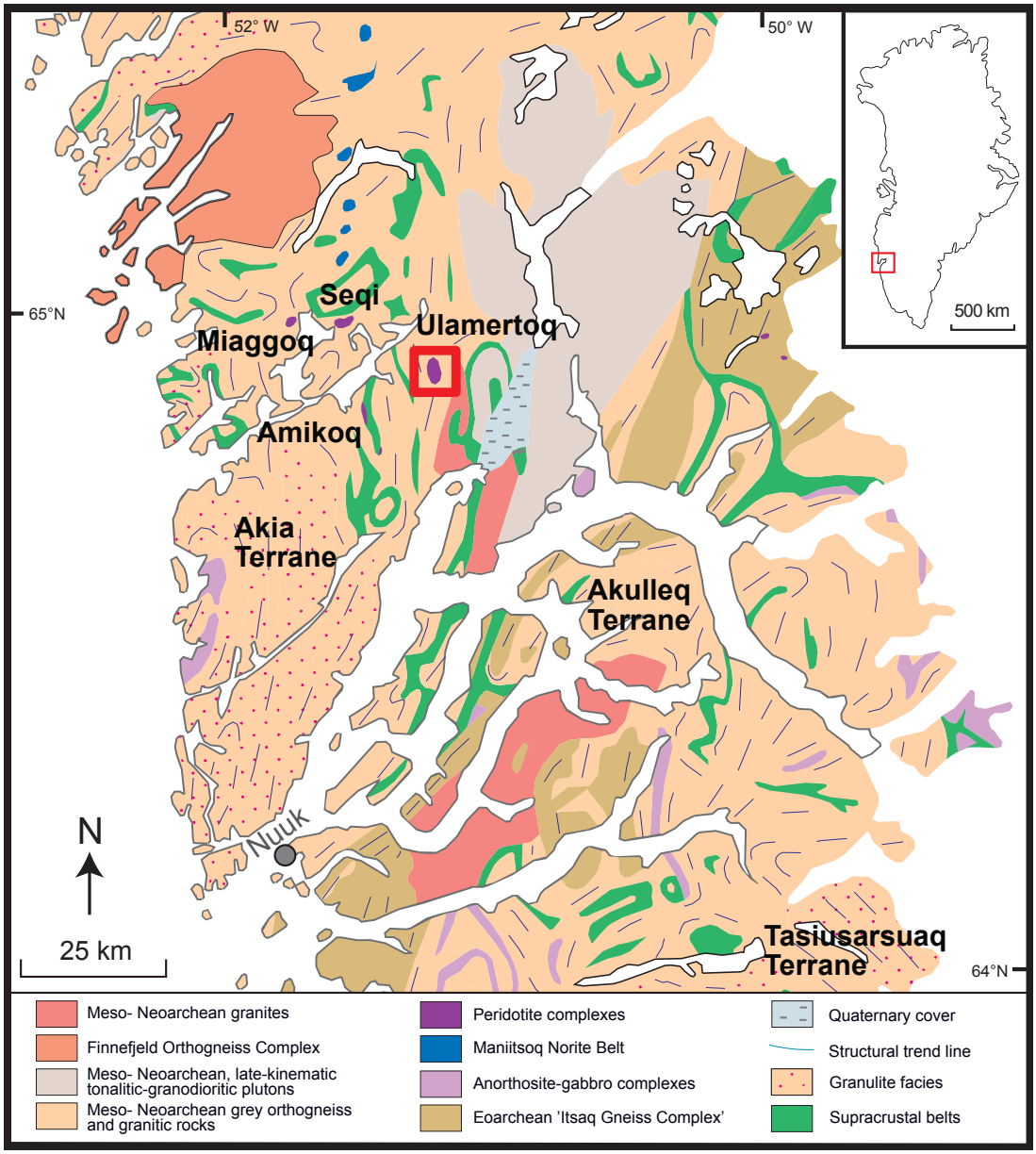

Figure 22: Geological map modified after Szilas et al. (2018) of Nuuk region, showing the Ulamertoq ultramafic body and some similar complexes, including the Fiskefjord area bodies such as Seqi, Amikoq, Miaggoq.

4.2 Regional geology

4.2.1 Akia terrane

Part of the North Atlantic Craton is exposed in SW Greenland (Figure 22). The region is subdivided, from north to south, into the 3.22–2.97 Ga Akia terrane, the 2.85–2.83 Ga Akulleq terrane and the 2.92–2.86 Ga Tasiusarsuaq terrane by their ages and degree of metamorphism (Friend et al., 1988; Friend and Nutman, 2005; Komiya et al., 1999). Our study focusses on the Akia terrane, dominated by 3.22–3.18 Ga dioritic and 3.07–2.97 Ga tonalite–trondhjemite–granodiorite (TTG) orthogneisses (Garde, 1990; Garde et al., 2000; Gardiner et al., 2019). Minor amounts of supracrustal rocks and mafic–ultramafic rocks are also exposed (Szilas et al., 2017, 2015; Waterton et al., 2020a).

The geologic history of the Akia terrane is still debated. One model assumes that the presence of the TTG gneiss indicates evolutions in an arc setting (Garde, 2007; Garde et al., 2020, 2000; Windley and Garde, 2009). On the other hand, a recent alternate theory suggests the development of TTG gneisses via stagnant-lid tectonics. Zircon Hf-isotope compositions and U–Pb ages suggest the incorporation of Eoarchean mafic crust in the formation of the Mesoarchean TTG (Gardiner et al., 2019) and phase-equilibrium modeling for the rocks is consistent with a high geothermal gradient (Yakymchuk et al., 2020). Subsequently or simultaneously, 2.99– 2.97 Ga low-pressure granulite-facies metamorphism was recorded in the gneisses and granitic sheets, which intruded the ultramafic body and were associated with the metamorphism(Garde, 1997). Later, high-temperature metamorphism at 2.8–2.7 Ga, suggested from the supracrustal belt of the Akia terrane, was coincident with the tectonic assembly of the Nuuk region (Kirkland et al., 2018a). Younger metamorphic events at 2.63 and 2.54 Ga are recorded in neoblastic apatite and zircon overgrowths (Kirkland et al., 2018b) and in titanite (Kirkland et al., 2020).

The Akia terrane also has been regarded as an important and controversial area due to the impact hypothesis at 3 Ga from the Maniitsoq structure in the north of the terrane (Figure 22) (Garde et al., 2020, 2013, 2012; Gardiner et al., 2019; Yakymchuk et al., 2021).

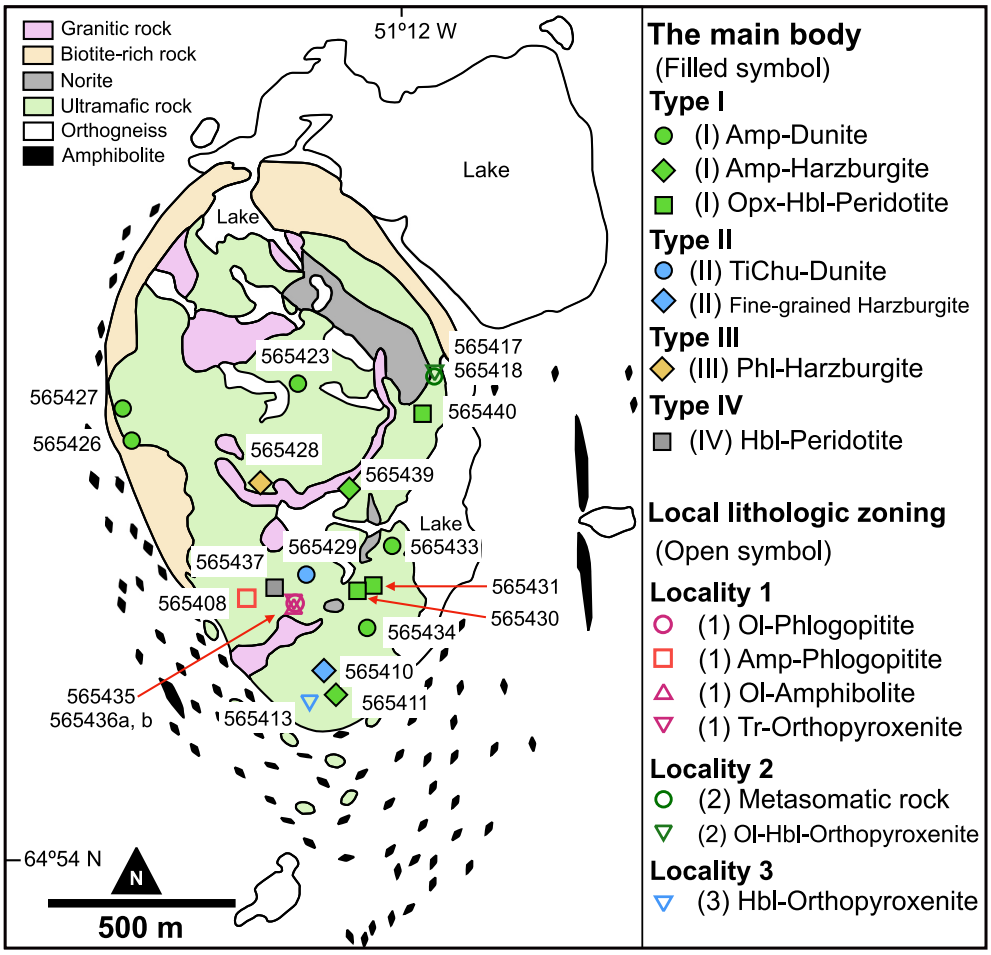

Figure 23: Detailed map of the Ulamertoq ultramafic body modified after Garde (1997), showing ultramafic rocks surrounded by orthogneiss and cut by granites. The numbers represent sample numbers. Biotite-rich rocks occur between the ultramafic body and surrounding orthogneiss and were firstly described as metasediment (Garde, 1997). Our study suggests that the origin of this lithology should be reconsidered and thus we denote this lithology as biotite-rich rock.

4.2.2 Ulamertoq ultramafic body

Several ultramafic and mafic bodies occur within the orthogneiss in the Akia terrane (Garde, 1997). The Ulamertoq ultramafic body is the largest ultramafic body, 1 × 1.5 km in area, occurring within the amphibolite–granulite facies orthogneiss (Figure 23 and Figure 24a) (Garde, 1997; Guotana et al., 2018; Nishio et al., 2022b, 2019). Similar large ultramafic lenses such as the Seqi, Amikoq and Miaggoq bodies have been observed in the Fiskefjord area (Figure 22) (Garde, 1997; Szilas et al., 2018, 2015, 2014). Small ultramafic lenses (a few to tens of metres long) occur surrounding the Ulamertoq ultramafic body (Figure 23). Zircons from the granitic sheets intruding the ultramafic body and zircons from a large olivine porphyroblast in the Seqi dunite give U–Pb ages of ~2.97 Ga, constraining the minimum age of the ultramafic bodies (Garde, 1997; Szilas et al., 2018; Whyatt et al., 2020).

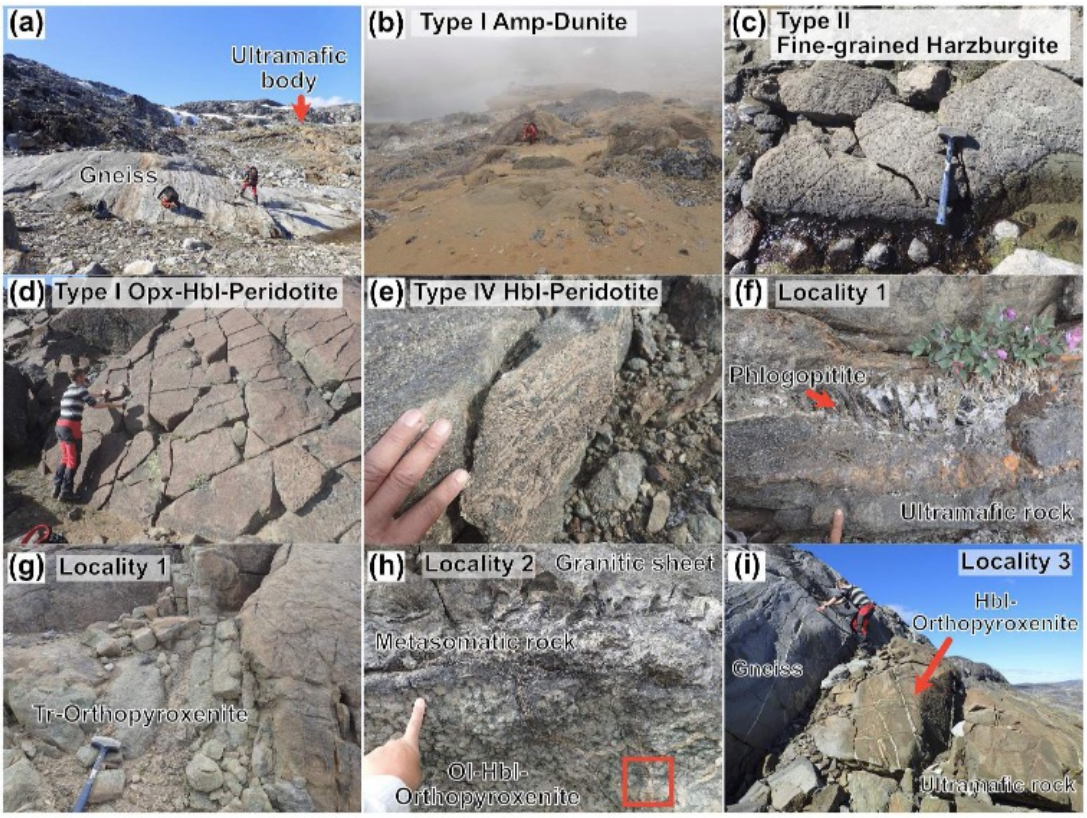

Figure 24: Representative field photographs of the Ulamertoq ultramafic rocks. (a) Relationships between ultramafic rocks and orthogneiss; (b) Type I, amphibole- bearing dunite (Amp-Dunite); (c) Type II, fine-grained harzburgite. Surface protrusions are composed of aggregates of fine-grained orthopyroxenes; (d) Type I, orthopyroxene and amphibole-rich peridotite (Opx-Hbl-Peridotite) with characteristic red-coloured weathered surface; (e) Type IV, spinifex-like textured hornblende-bearing peridotite (Hbl-Peridotite) showing olivine (yellowish part) and amphibole (greenish part); (f) Locality 1 hydrous mineral-rich layers along the boundary of country rocks; (g) Locality 1 dike-like tremolite-orthopyroxenite (Tr-Orthopyroxenite) along the boundary; (h) Locality 2 olivine-hornblende-bearing orthopyroxenite (Ol-Hbl-Orthopyroxenite) intruded by a granitic sheet. Red square shows a centimetre-scale granitic apophysis where metasomatic rocks were collected. Photos and simplified sketch are shown in Supplementary Figure A10; Locality 3 hornblende-bearing orthopyroxenite veins (Hbl-Orthopyroxenite) near the contact with surrounding orthogneiss.

4.3 Analytical methods

Element-distribution images of the entire thin section for samples was obtained by a micro x-ray fluorescence (XRF) using a Bruker M4-Tornado at the Geological Survey of Japan. The measurements were performed using 50 kV accelerating voltage and 600 μA probe current, with a 25-μm diameter beam spot. A mineral phase distribution image was generated using ImageJ software (Nguyen et al., 2018; Schneider et al., 2012). The modal abundances of minerals were determined from the images and confirmed via point counting (2000–4000 per thin section).

A total of 21 samples were selected for whole-rock major and trace element analysis. They were cut using a diamond saw and then washed in an ultrasonic bath to avoid contamination. Ultramafic rocks require quartz dilution for XRF because the elevated Mg concentration can cause crystallization in the glass bead. Therefore, a separate aliquot was prepared for inductively coupled plasma mass spectrometry (ICP–MS) and was ground in a steel mill. Whole-rock major and trace element analyses were acquired from the geochemical laboratory at GeoAnalytical Lab, Washington State University, USA, using procedures involving flux-fusing of rock powders followed by applying standard XRF and ICP–MS methods. The full analytical procedures are described by Johnson et al. (1999). The XRF data have detection limits of ~20 ppm, and the ICP–MS analysis accurately measured most trace elements to ~0.5 ppm.

The major element compositions of minerals from 13 samples of the main ultramafic rocks and 7 samples of the country rock lithologies were obtained by the JXA-8800 JEOL electron micro- probe at Kanazawa University in Japan. Analytical conditions were 20 kV accelerating voltage, 20 nA probe current and a 3-μm diameter beam spot. Natural and synthetic mineral standards were prepared for calibration. JEOL software using atomic-number–absorption–fluorescence (ZAF) corrections was used for data reduction. In-house mineral standards (olivine, chromian spinel, diopside and K-feldspar) were measured to monitor data quality.

Trace element abundances of major phases (orthopyroxene and amphibole) in ultramafic rocks were determined using a laser-ablation system (GeoLas Q-plus, MicroLas) coupled with an ICP–MS system (Agilent 7500s, Technologies, Santa Clara) at Kanazawa University. Each analysis was performed using a 90–100- μm diameter ablation spot for orthopyroxene and a 60-μm spot for amphibole at a 6 Hz repetition rate. Standard glass NIST 612 was used for calibration with Si as an internal standard, based on the SiO_2 content obtained by electron probe microanalysis (Longerich et al., 1996; Pearce et al., 1997). Details of the analytical method and data quality control were given by (Morishita et al., 2005a, 2005b).

Pseudosection modeling was performed using Perple_X 6.9.0 (Connolly, 2009) and the thermodynamic dataset (Holland and Powell, 1998, updated in 2002). Solid–solution models used in this study are the same as those used by Endo et al. (2015) and listed in the supplementary materials.

4.4 Petrographic descriptions

The Ulamertoq ultramafic body consists mainly of dunite, harzburgite and orthopyroxene–amphibole-rich peridotite (Figure 24b-e). These lithologies are not distributed systematically. The body was intruded by numerous small (decameter-to-centimeter scale) felsic rocks that are not shown in Figure 23 due to their small size. Local hydrous mineral-rich lithologic zoning and associated orthopyroxenites occur over limited extents (meter-to-millimeter scale), but most frequently occur at the boundary

between the ultramafic body and decameter-to-centimeter scale felsic rocks (Figure 24f–i). The lithologic zonation is of a smaller scale compared with the main body of ultramafic rocks that comprise dunite, harzburgite and orthopyroxene–amphibole- rich peridotite (Figure 24b-e).

Dunites typically occur far from granitic sheets and orthogneisses (± local hydrous mineral-rich zone) (Figure 24b). Harzburgite is identified by its uneven weathered surface, with orthopyroxene standing proud of the surface (Figure 24c). The orthopyroxene– amphibole-rich peridotite has a weathered reddish surface (Figure 24d). Rare hornblende-bearing peridotite, showing spinifex-like texture on the weathered surface, occurs as vein-like structures in other ultramafic rocks (Figure 24d). Norites occur in the northern part of the ultramafic body (Figure 23) (Garde, 1997), and rare chromitite layers occur in the main body (Guotana et al., 2018).

Since local hydrous mineral–orthopyroxene-rich lithologies are likely to have variable degrees of effect on the main ultramafic body, we first describe the local lithologic zoning in three representative localities in order to identify the main body ultramafic rocks that are far from the boundaries. The nomenclature of the ultramafic rocks follows that of Streckeisen (1976) and Giovanardi et al. (2018). The mineral abbreviations are from Whitney and Evans (2010).

4.4.1 Local lithologic zoning

Local lithologic zonation (metre-to-millimetre scale) related to felsic rocks (decimetre-to-centimetre scale) can be classified into two types. The first displays systematic mineral zoning in phlogopite-, amphibole-lithologies and orthopyroxenite from the country rock to the main body. Such lithologies were collected from south of the body near dunite (Locality 1) and north of the body near orthopyroxene and amphibole-rich peridotite (Locality 2) (Figure 23). The other lithology comprises orthopyroxenite veins or networks, not associated with phlogopitite layers and is collected near the boundary between harzburgite and orthogneiss (Locality 3).

Table 3: Petrographic description of the local lithologies

Rock Type	Ol	Opx	Amp	Phl	Other
Locality 1 near dunite					
Ol/Amp-Phlogopitite	○/-	-	-/Tr, Ath	○	Spl, Mag, Tlc, Sulphide
Ol-Amphibolite	○	-	Tr	○	Spl, Mag, Chl, Sulphide
Tr-Orthopyroxenite	-	○	Tr	-	Spl, Mag, Tlc, Sulphide
Locality 2 near Opx-Hbl-Peridotite					
Metasomatic rock	-	○	Ed, Act, Hbl, Ath	○	Zrn, Ilm, Rt, Tlc, Spl
Ol-Hbl-Orthopyroxenite	○	○	Hbl	-	Spl
Locality 3 near harzburgite					
Hbl-Orthopyroxenite	○	○	Hbl	-	Cpx, Spl

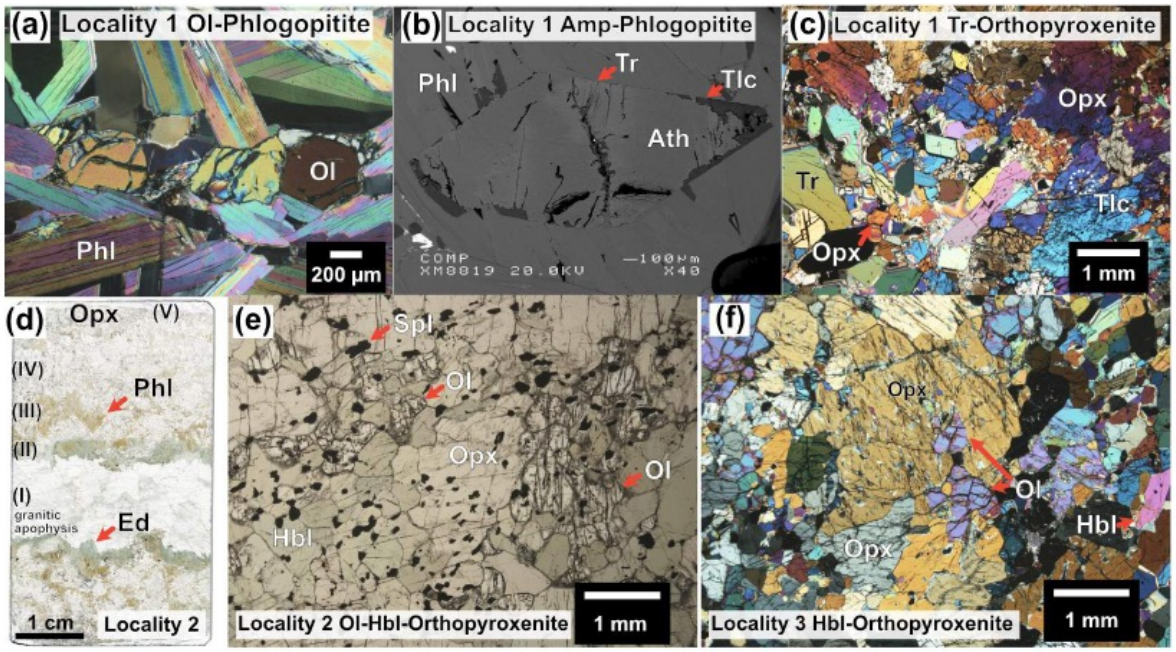

Figure 25: Microphotographs and back-scattered electron (BSE) images of the local lithologies. (a) Olivine (Ol) in phlogopite (Phl)-rich matrix of Locality 1 Ol-Phlogopitite; (b) occurrence of anthophyllite (Ath) partly replaced by or replacing tremolite (Tr). Talc (Tlc) rimmed in Locality 1 Amp-Phlogopitite; (c) coarse- grained orthopyroxene (Opx) with spinel (Spl) grains in Locality 1 Tr-Orthopyroxenite (Figure 24g). Talc is observed at the grain boundary of orthopyroxene and along the cleavages; (d) whole thin section of Locality 2 lithologic zoning along centimeter-scale granitic apophysis (Figure 24h); (e) small olivine and spinel grains are observed within orthopyroxene and amphibole of Locality 2 Ol-Hbl-Orthopyroxenite (Figure 24h); (f) poikilitic orthopyroxene containing olivine grains in Locality 3 Hbl-Orthopyroxenite (Figure 24i). Amphibole is observed along the vein.

4.4.1.1 Hydrous mineral-rich layers and related orthopyroxenite: Locality 1

Lithologic zonation (meter-to-centimeter scale) at Locality 1 near dunite consists of olivine- and/or amphibole-bearing phlogopitite (Figure 24f), olivine-amphibolite towards dunitic rocks and tremolite-orthopyroxenite occurs as a dike-like intrusion near the boundary (Figure 24g). We refer to these lithologies as Ol-Phlogopitite and Amp-Phlogopitite, Ol-Amphibolite and Tr-Orthopyroxenite, respectively (

Table 3). Ol-Phlogopitite and Ol-Amphibolite were continuously sampled, although Amp-Phlogopitite and dike-like Tr- Orthopyroxenite were separately sampled.

Olivine grains are observed as discrete inclusions in Ol-Phlogopitite (Figure 25a). The modal abundance of olivine increases towards and adjacent to the Ol-Amphibolite. Amphibole of Amp-Phlogopitite is anthophyllite with tremolitic domains and lamellae, especially near cleavages. Talc commonly occurs bordering anthophyllite (Figure 25b). Magnetite and a few sulphide minerals are also observed in both types of phlogopitites. The Ol-Amphibolite is characterized by abundant amphibole

and comprises amphibole, olivine and phlogopite. Olivine contains numerous magnetite inclusions, and phlogopite occurs in small amounts near the Ol-Phlogopitite. Tr-Orthopyroxenite has orthopyroxene- and amphibole-dominant portions. The orthopyroxene occurs as lager grains containing numerous spinel inclusions where orthopyroxene is dominant and as inclusion-free small grains within the amphibole-rich portions (Figure 25c). Talc is observed at the grain boundary of orthopyroxene and along the cleavages (Supplementary Figure A9). Olivine is not observed in Tr-Orthopyroxenite.

4.4.1.2 Hydrous mineral-rich layers along granitic apophysis and related orthopyroxenite: Locality 2

Lithologic zoning is observed symmetrically along a centimeter-scale granitic apophysis originating from a decameter-thick intrusive granitic sheet comprising plagioclase and quartz near orthopyroxene and amphibole-rich peridotites (Supplementary Figure A10). We discerned five different lithologic subzones (millimeter-scale) along the centimeter-scale granitic apophysis towards ultramafic body based on mineral assemblage (Figure 25d): subzone (i) granitic apophysis; (ii) edenite with accessory zircon, rutile and apatite (edenite includes plagioclase and is vertically aligned with the apophysis); (iii) actinolite, hornblende, anthophyllite and phlogopite with accessory rutile, apatite and spinel, where actinolite and hornblende show anthophyllite lamellae; (iv) anthophyllite with accessory rutile, apatite and spinel; and (v) orthopyroxene and spinel.

Olivine–hornblende-bearing orthopyroxenite (Ol-Hbl-Orthopyroxenite), associated with the decameter-thick granitic rock (Figure 24h; Supplementary Figure A10), consists of orthopyroxene, amphibole and dark-greenish spinel with a minor amount of olivine (Figure 25e). Olivine grains are included in large orthopyroxene grains (locally crystallographically continuous) and/or are surrounded by a fine-grained amphibole aggregate. Orthopyroxene seams surrounding olivine are also observed.

4.4.1.3 Orthopyroxenite vein or network near surrounding orthogneiss: Locality 3

Hornblende-bearing orthopyroxenite (meter-to-centimeter scale) occurs as veins or networks (Hbl-Orthopyroxenite) in the harzburgitic rock near the border with the orthogneiss (Figure 24i). Mineralogical zoning from both the orthopyroxene-rich center and amphibole-rich margins is commonly observed along the veins.

Orthopyroxene with poikilitic texture includes isolated olivine grains that are crystallographically continuous (Figure 25f). Clinopyroxene and amphibole are observed as blebs in the poikilitic orthopyroxenes.

4.4.2 The main body ultramafic rocks

After observing the local lithologic zoning, we collected samples representing lithologic variations in the main body far from the local lithologic zonings. We classified the main body ultramafic rocks into four types of ultramafic rocks based on mineral assemblage, modal abundance and chemical characteristics as discussed below (Table 4): Type I amphibole-bearing dunite (Amp-Dunite), amphibole-bearing harzburgite (Amp-Harzburgite) and orthopyroxene and amphibole-rich peridotite (Opx-Hbl-Peridotite) (Figure 24b and d); Type II titanian clinohumite-bearing dunite (TiChu-Dunite) and harzburgite characterized by fine-grained orthopyroxene aggregates (Fine-grained Harzburgite) (Figure 24c); Type III phlogopite-bearing harzburgite (Phl-Harzburgite); and Type IV spinifex-like textured hornblende-peridotite (Hbl-Peridotite) (Figure 24e).

Table 4: Modal proportions for the ultramafic rocks from the Ulamertoq main body. 'n' = number of samples.

Rock Type	Type	Ol	Opx	Amp	Spinel	Other (<1 %)
Amp-Dunite (n=4)	Type I	88-92	3-6	3-5	2-4	Chl, Mag
Amp-Harzburgite (n=2)	Type I	65-69	29	4-6	3	Chl, Mag
Opx-Hbl-Peridotite (n=3)	Type I	45-50	25-30	25-26	<5	Chl, Mag, Sulphide
TiChu-Dunite (n=1)	Type II	95	2-4	-	1-2	TiChu, Ilm, Mag, Chl
Fine-grained Harzburgite (n=1)	Type II	72	25	-	3	Chl, Mag
Phl-Harzburgite (n=1)	Type III	70	20	<1	<1	Phl (10%), Sulphide (<1)
Hbl-Peridotite (n=1)	Type IV	72	-	25	<1	Sulphide, Phl

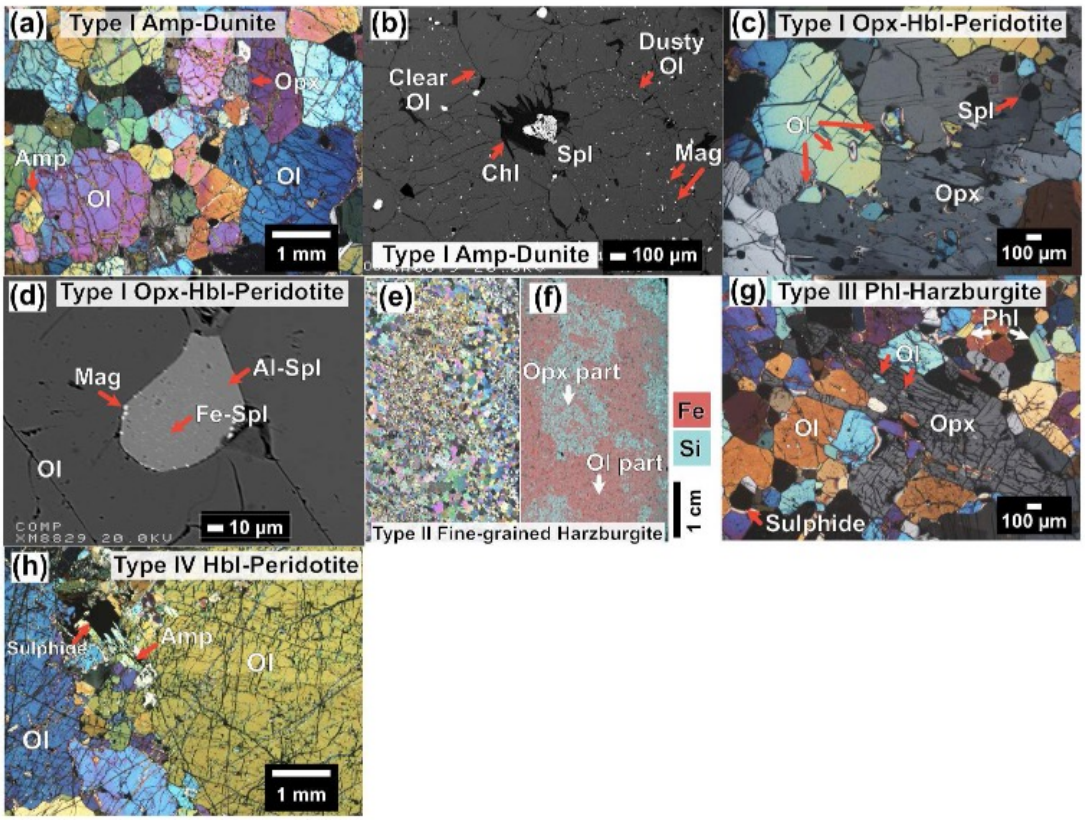

Figure 26: Microphotographs and BSE images of the Ulamertoq main body ultramafic rocks. (a) Fine-grained orthopyroxene (Opx) and amphibole (Amp) with olivine (Ol) of Type I Amp-Dunite (Figure 24b); (b) olivine presents two distinctive petrographic features of Type I Amp-Dunite: dusty olivine (Dusty Ol) containing magnetite (Mag) inclusions and clear olivine (Clear Ol) without or less inclusions. Spinel (Spl) is surrounded by chlorite (Chl); (c) poikilitic orthopyroxene includes olivine of Type I Opx-Hbl-Peridotite (Figure 24d). Olivine grains indicated by arrows are optically continuous; (d) spinel presents two phases: Fe-rich tiny grains (Fe-Spl; light-grey phases) in Al-rich spinel (Al-Spl) of Type I Opx-Hbl-Peridotite. Magnetites (bright phases) are observed in the rim of spinel; (e) image of whole thin section of Type II fine-grained harzburgite. Fine-grained orthopyroxene-dominant parts protrude on weathered surface (Figure 24c); (f) combined x-ray intensity map of Si and Fe showing the distribution of orthopyroxene (light blue) and olivine (light red); (g) orthopyroxene presents a poikilitic texture including olivine grains of Type III Phl-Harzburgite. Phlogopite (Phl) and sulphide are fine grains; (h) amphibole is observed at the grain boundary of large olivine grains (~1 cm) of Type IV Hbl-Peridotite (Figure 24e). Sulphide is observed associated with amphibole.

4.4.2.1 Type I: amphibole-bearing dunite and harzburgite and orthopyroxene-amphibole-rich peridotite (Amp-Dunite, Amp-Harzburgite, Opx-Hbl-peridotite)

Type I rocks, especially dunites, are the most common lithologies in the study area. Amp-Dunite and Amp-Harzburgite are characterized by the presence of notable amounts of amphibole and orthopyroxene (Table 4; Supplementary Figure A11). They have an equigranular texture (Figure 26a) with 1–2-mm olivines that are dusty in appearance from tiny magnetite inclusions or with clear olivine (Figure 26b). Orthopyroxene is generally fine-grained (~200 µm across) but also rarely shows poikilitic texture.

Amphibole occurs as subhedral ~200-μm grains. Spinel has chlorite aureoles (Figure 26b). The modal abundances of orthopyroxene and amphibole in the dunite are broadly similar, but amphibole is less abundant in harzburgite (Table 4; Supplementary Figure A11).

Opx-Hbl-Peridotite mainly comprises olivine, orthopyroxene and amphibole with minor amounts of spinel and sulphide minerals (Table 4; Supplementary Figure A11). The modal abundances of orthopyroxene and amphibole are similar. Olivine occurs as resorbed grains and locally isolated grains included by poikilitic orthopyroxene are crystallographically continuous (Figure 26c). Spinel occurs mostly as dark-greenish inclusions in silicate minerals and is separated into Fe-rich and Al-rich phases and is commonly surrounded by magnetite (Figure 26d). Ni-sulphide is observed but is rare.

4.4.2.2 Type II: titanian clinohumite-bearing dunite and fine-grained orthopyroxene-aggregate-bearing harzburgite (TiChu-Dunite, fine-grained harzburgite)

TiChu-Dunite characterized by the presence of titanian clinohumite (TiChu) has an equigranular texture (Nishio et al., 2019). Olivine occurs either as >1-mm grains that appear dusty because of many magnetite inclusions or as <1-mm grains that are clear (without opaque inclusions). Minor amounts of small (~200 μm) orthopyroxene occur as discrete grains. Modal abundances of orthopyroxene and spinel are 2–4 vol.% and 1–2 vol.%, respectively (Table 4). Spinel is commonly surrounded by chlorite. TiChu is in contact with the dusty olivine, and ilmenite is found sporadically near the contact. Further details are given by Nishio et al. (2019).

Fine-grained harzburgite is characterized by fine-grained orthopyroxene-rich aggregates, resulting in the olivine- and orthopyroxene- dominant portions (Figure 26e and f) while amphibole and phlogopite are absent. The orthopyroxene-dominant portion comprises fine-grained aggregates of orthopyroxene and minor olivine. The olivine is larger (~1 mm) and dustier in the olivine-dominant portions than in the orthopyroxene-dominant portions. Spinel is surrounded by chlorite.

4.4.2.3 Type III: phlogopite-bearing harzburgite (Phl-Harzburgite)

Phl-Harzburgite is characterized by the presence of phlogopite (~10 modal %) (Table 4). All mineral phases are relatively finer (<1 mm) than the other samples. Ni-sulphide is often associated with phlogopite. One amphibole grain was observed next to sulphide mineral. Olivine is fine-grained (<1 mm). Orthopyroxene displays a poikilitic texture including olivine grains that show crystallographic continuity (Figure 26g).

4.4.2.4 Type IV: spinifex-like textured hornblende-peridotite (Hbl-peridotite)

Hbl-Peridotite occurs as a dike-like intrusion of several tens of centimeters in thickness and its volume is likely very minor. The weathered surface is characterized by a spinifex-like texture (Figure 24c). It is

composed mainly of olivine and amphibole (Table 4). Phlogopite, chlorite and Ni-sulphides are observed as accessory minerals. Olivine grains are larger (>2 cm) relative to other ultramafic-rock samples. Small amphibole and phlogopite grains are observed as inclusions within olivine (Figure 26h). Euhedral amphibole (~500 μm) and sulphide minerals are observed along the olivine grain boundaries.

4.5 Whole-rock major and trace element chemistry

4.5.1 Local lithologic zoning

Orthopyroxenites are dominated by orthopyroxene and amphibole. The compositions have lower MgO and higher SiO_2 and CaO contents compared with those in the main body ultramafic rocks (Figure 27a and b). The compositions reflect the abundant orthopyroxene and amphibole assemblages. Locality 1 Tr-Orthopyroxenite has similar Al_2O_3 and Cr contents as those in nearby dunite (Figure 27c and d). Locality 2 Ol-Hbl-Orthopyroxenite has high Al_2O_3 and TiO_2 contents. Locality 3 Hbl-Orthopyroxenite has high CaO and TiO_2 contents compared with those in the main body ultramafic rocks. The high CaO content in Locality 3 Hbl-Orthopyroxenite reflects the presence of amphibole and clinopyroxene. Locality 1 Ol- Phlogopitite has slightly higher MgO and Ni contents and lower SiO_2 and K_2O contents than those in Amp-Phlogopitite (Supplementary Table S1 of Nishio et al. (2022b)), and both phlogopitites are low in TiO_2. Ol-Amphibolite rock shows higher CaO and lower Cr contents than other main body rocks.

Orthopyroxenites and Locality 1 Ol-Amphibolite show flat rare-earth element (REE) patterns (Figure 28a). Trace element chemistries of orthopyroxenites tend to reflect those of amphiboles. Locality 1 Tr-Orthopyroxenite and Ol-Amphibolite show strong negative Ti, Zr and Sr anomalies (Figure 28b). Locality 2 Ol-Hbl-Orthopyroxenite has negative Sr anomalies but no Zr or Ti anomalies. Locality 3 Hbl-Orthopyroxenite shows a different pattern characterized by positive Zr and Sr anomalies. Locality 1 Ol/Amp-Phlogopitites shows a low abundance of trace elements with positive anomalies of Eu, Ti, Zr, Sr, U and Rb (Figure 28b).

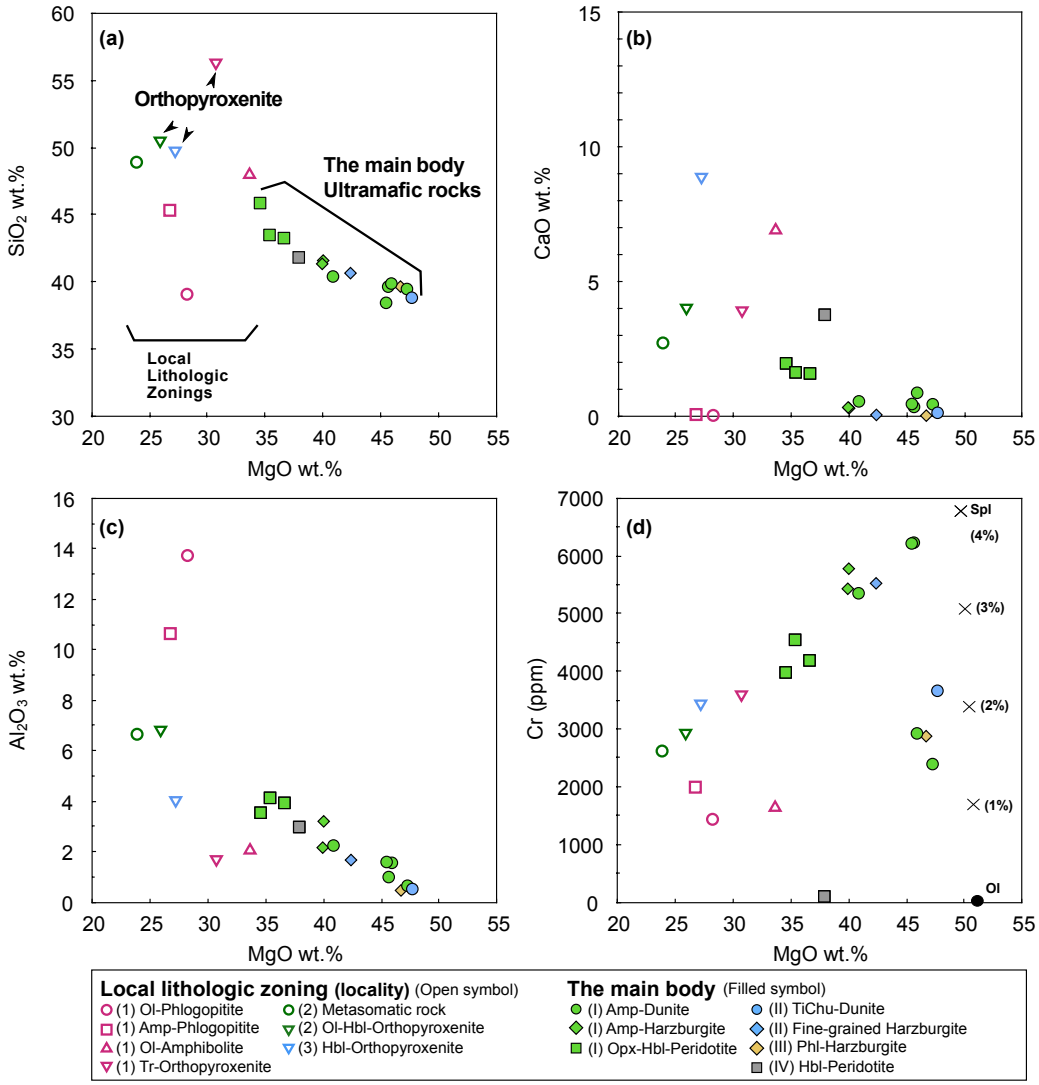

Figure 27: Whole-rock chemistry of the Ulamertoq main body ultramafic rocks and local lithologic zonation. (a) SiO_2 wt.% vs MgO wt.%; (b) CaO wt.% vs MgO wt.%; (c) Al_2O_3 wt.% vs MgO wt.%; (d) Cr (ppm) vs MgO wt.%. Black-coloured crosses show the calculated composition of the representative spinel addition (1–4 vol.%) to the representative olivine composition of dunite.

4.5.2 The main body ultramafic rocks

The whole-rock MgO contents of the main body ultramafic rocks show negative correlations with SiO_2, Al_2O_3, CaO and TiO_2 contents. The MgO contents also negatively correlate with the modal abundances of orthopyroxene and/or amphibole except for Type IV Hbl-Peridotite, which has high CaO and high TiO_2 contents (Figure 27a–c; Supplementary Table S1 of Nishio et al. (2022b)). The CaO contents in Type I ultramafic rocks including amphibole are slightly higher than those in amphibole-free Type II and amphibole-rare III ultramafic rocks.

The Cr contents of the main body ultramafic rocks vary depending on the modal abundance of spinel, although the Cr content in Type IV Hbl-Peridotite is distinctively low (Figure 27) The Ni content shows a positive correlation with the MgO content (Supplementary Table S1 of Nishio et al. (2022b)).

Types I–III ultramafic rocks have similar chondrite-normalized REE patterns and primitive mantle-normalized trace element patterns. They show negative Eu anomalies with slightly enriched light-REE (LREE) (Figure 28c). As modal abundances of orthopyroxene and/or amphibole increase, REE abundance increases from Phl-Harzburgite, TiChu-Dunite and Amp-Dunite to fine-grained harzburgite, Amp-Harzburgite and Opx-Hbl-Peridotite. They show negative Sr and Eu anomalies. Fine-grained harzburgite and Amp-Harzburgite also show positive Zr anomalies (Figure 28d). The trace element chemistry of Type IV Hbl-Peridotite is different from that of the other types. It is characterized by high REE and trace element abundances with a slight sigmoidal REE pattern and a negative Zr anomaly (Figure 28c and d).

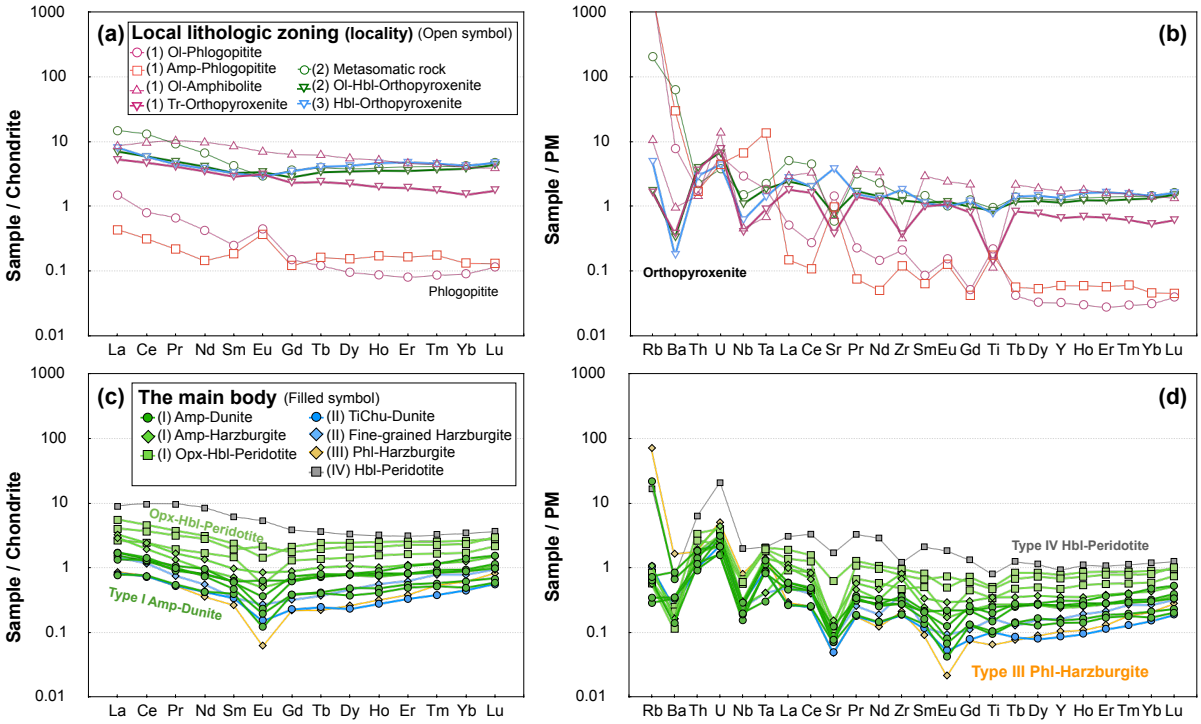

Figure 28: Chondrite-normalised REE and primitive mantle-normalised trace element patterns of the whole-rock chemistry. (a) REE and (b) trace element patterns of the local lithologic zonings; (c) REE and (d) trace element patterns of the main body ultramafic rocks. Chondrite and primitive mantle values are from Sun and McDonough (1989).

4.6 Mineral major and trace element chemistry

4.6.1 Major element compositions

4.6.1.1 Olivine

Forsterite [Fo#=100×Mg / (Mg+Fe^{2+})] and NiO contents of the olivine are high in TiChu-Dunite and Amp-Dunite followed by fine-grained harzburgite, Amp-Harzburgite and Opx-Hbl-Peridotite among Types I and II (Figure 29a). The Fo# has a negatively correlation with the modal abundance of orthopyroxene and/or amphibole (Supplementary Figure A12). The MnO content shows a negative correlation with Fo# (Supplementary Table S2 of Nishio et al. (2022b)). Olivine of TiChu-Dunite and Amp-Dunite has the highest Fo# (92.6–93.3) and NiO content (0.34–0.45 wt.%) among the Ulamertoq bodies. The Fo# (89.0– 90.9) and NiO contents (0.18–0.33 wt.%) of olivine in fine-grained harzburgite and Amp-Harzburgite are lower than those in olivine of dunites but higher than olivine Fo# (87.1–87.6) and NiO contents (0.21–0.33 wt.%) of Opx-Hbl-Peridotite.

The olivine compositions of Types III and IV differ in that they have low NiO content (Figure 29b). Olivine of Phl-Harzburgite has high Fo# (92.3–92.8) and low NiO contents (0.17–0.26 wt.%). Hbl-Peridotite has Fo# (88.7–89.5) and low NiO content (0.13–0.17 wt.%).

The olivine compositions of Localities 1–3 lithologies are different from place to place but are similar to those of the main body ultramafic rocks (Figure 29b). The NiO content (0.37–0.43 wt.%) in olivine of Locality 1 Ol-Amphibolite and Ol-Phlogopitite overlaps that in olivine of nearby dunite. Fo# shows a systematic compositional trend: as one moves away from the main body dunite, the Fo# of Locality 1 Ol-Amphibolite slightly decreases towards the adjacent Ol-Phlogopitite (from 92.8 to 92). Olivine of Locality 2 Ol-Hbl-Orthopyroxenite has the lowest Fo# (84.9–85.9) and NiO contents (0.22–0.29 wt.%). The contents are similar but slightly lower than those in olivine of nearby Opx-Hbl-Peridotite. Olivine from Locality 3 Hbl-Orthopyroxenite has a similar Fo# (89.5–90.1) to that in olivine of nearby harzburgites, but the NiO content (0.30–0.38 wt.%) is slightly higher.

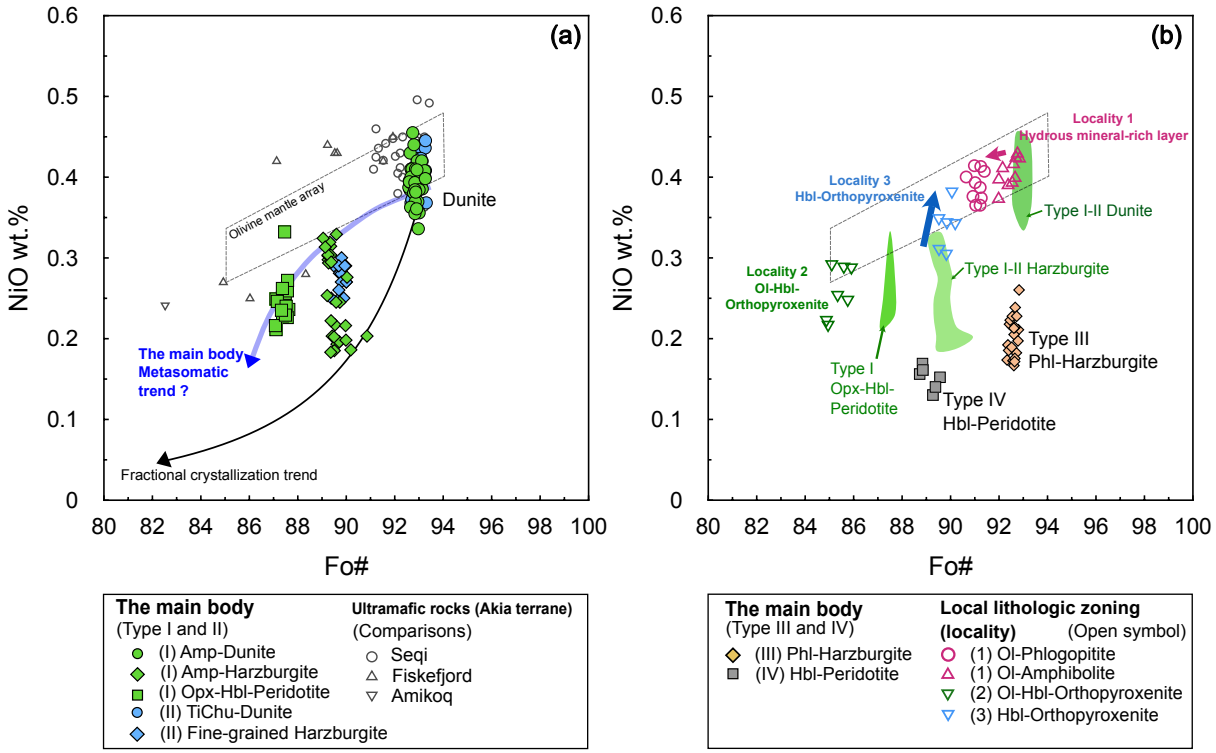

Figure 29: NiO content vs Fo# in olivine from the Ulamertoq ultramafic rocks. The dashed compositional area of olivine mantle array is from (Takahashi et al., 1987). (a) Olivine compositions of the main body Types I and II ultramafic rocks. Olivine compositions of ultramafic rocks from the Akia terrane are also shown (Aarestrup et al., 2020; Szilas et al., 2018, 2015). The metasomatic trend is from Cordier et al. (2015) and Gordeychik et al. (2020). The black solid arrow represents the fractionation trend reproduced by Rayleigh fractionation calculation using partition coefficients from Matzen et al. (2013); (b) olivine compositions of the main body Types III and IV ultramafic rocks and Localities 1–3 lithologies. Purple solid arrow represents metasomatic modification related to the formation of phlogopite at Locality 1 near dunite. Blue solid arrow represents the metasomatic modification related to the formation of orthopyroxenite vein at Locality 3. Green compositional areas are those of the main body Types I and II ultramafic rocks.

4.6.1.2 Spinel

Most spinels from the main body and the local lithologic zones are surrounded by chlorite and have Fe-rich compositions (Supplementary Table S2 of Nishio et al. (2022b)). The spinel cores of the main body ultramafic rocks have low Cr# [Cr / (Cr + Al)] (0.11–0.34) and low Mg# [Mg / (Mg+Fe^{2+})] (0.54–0.73). The spinel composition of Type I Amp-Dunite varies from the core to the Fe-rich rim; meanwhile, spinel from other peridotites (Type I Amp-Harzburgite and Opx-Hbl-Peridotite and Type II fine-grained harzburgite) separated into two phases—Al-rich (Cr# < 0.3) and Fe-rich portions. Spinel within Type II TiChu-Dunite is rich in Cr and Fe. Spinel in Type III Phl-Harzburgite has a low Al_2O_3 content and is rich in Fe and Cr.

The spinel from Locality 1 Tr-Orthopyroxenite is also Fe- and Cr-rich, whereas that of Locality 2 Ol-Hbl-Orthopyroxenite has higher Al_2O_3 content (up to 58.2 wt.%). Cr# of spinel inclusions in orthopyroxene from subzone (v) along a granitic apophysis is 0.35–0.53.

4.6.1.3 Orthopyroxene

Orthopyroxene is characterised by low Cr_2O_3 (<0.3 wt.%) and CaO (<0.4 wt.%) contents and the varied Mg# (0.84–0.93) and Al_2O_3 (<3.25 wt.%; Figure 30a–c). Between Types I and II rocks, Mg# negatively correlates with the modal abundance of orthopyroxene and/or amphibole, in the same way as olivine Fo# (Supplementary Figure A12). The Mg# is high in TiChu-Dunite and Amp-Dunite (0.92–0.93) followed by fine-grained harzburgite and Amp-Harzburgite (0.88–0.90) and Opx-Hbl-Peridotite (0.87–0.88). The Al_2O_3 and Cr_2O_3 contents show a negative correlation (Figure 30a). Orthopyroxene of Type III Phl-Harzburgite shows high Mg# (0.93) but very low Al_2O_3 content (<0.1 wt.%) (Figure 30a and b).

The Mg# systematics of orthopyroxene of the local lithologic zonation mirrors that of olivine Fo#, in that the Mg# is high in Locality 1 lithologies and is progressively less in Locality 3 and Locality 2 lithologies. Orthopyroxene of Locality 1 Tr-Orthopyroxenite has Mg# (0.93) and low Al_2O_3 content (<1.0 wt.%) (Figure 30b). Inclusion-rich orthopyroxene has slightly higher Cr_2O_3 (0.18–0.27 wt.%) and lower CaO contents (<0.13 wt.%) compared with inclusion- free orthopyroxene, which contains Cr_2O_3 (<0.15 wt.%) and CaO contents (0.06–0.25 wt.%) (Figure 30c, Supplementary Table S2 of Nishio et al. (2022b)). The Al_2O_3 (2.48–2.86 wt.%), Cr_2O_3 (0.01–0.10 wt.%) and CaO contents (0.19–0.36 wt.%) of the porphyroblastic orthopyroxene of Locality 2 Ol-Hbl-Orthopyroxenite are similar to those in orthopyroxene of the main body Type I and II rocks, but the Mg# (0.85) is lower. The orthopyroxene seams surrounding olivine of Locality 2 Ol-Hbl-Orthopyroxenite are very poor in Al_2O_3 (<0.4 wt.%), CaO (<0.1 wt.%) and Cr_2O_3 (<0.6 wt.%) contents (Supplementary Table S2 of Nishio et al. (2022b)). Orthopyroxene of Locality 3 Hbl-Orthopyroxenite has Mg# (0.90–0.91) and Al_2O_3 content (1.17–1.40 wt.%) with a slightly wider range of Cr_2O_3 (<0.16 wt.%) and CaO (0.21–0.38 wt.%) contents.

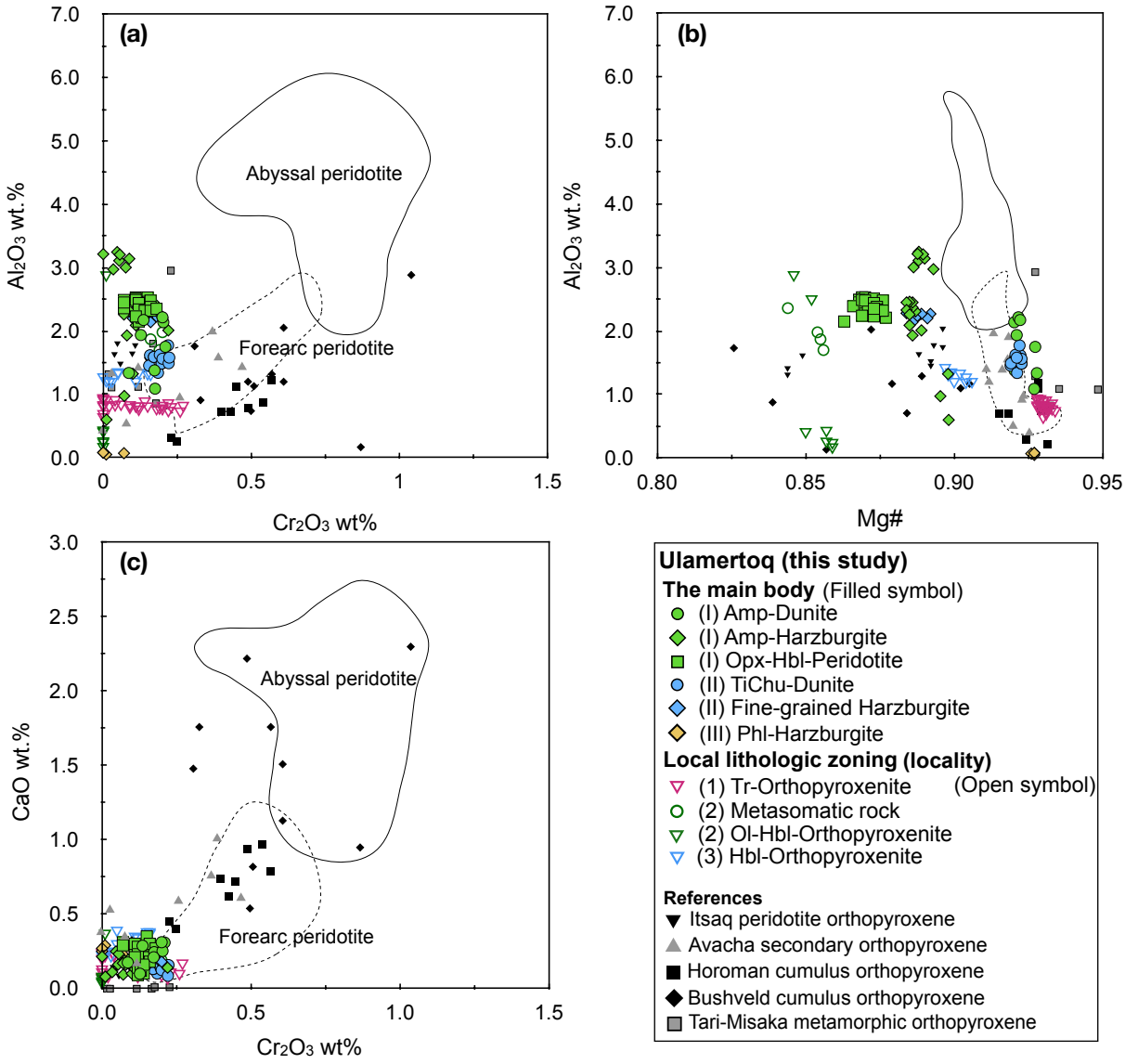

Figure 30: Major element chemistry of orthopyroxene. (a) Al_2O_3 wt. % vs Cr_2O_3 wt. %; (b) Al_2O_3 wt. % vs Mg#; (c) CaO wt. % vs Cr_2O_3 wt. % plots of orthopyroxenes. Composition of orthopyroxenes in peridotites shown for comparison are from the Itsaq area of southern West Greenland (Friend et al., 2002), secondary orthopyroxenes in mantle xenolith from Avacha volcano (Ishimaru et al., 2007), cumulus orthopyroxene from the Horoman peridotite and Bushveld complexes (Matsufuji et al., 2006; Sharpe and Hulbert, 1985) and metamorphic orthopyroxene from the Tari–Misaka complex (Arai, 1974). Compositional fields of primary orthopyroxene in abyssal peridotites and forearc peridotites are from Parkinson and Pearce (1998) and Warren (2016). More comparisons with orthopyroxene in ultramafic rocks are shown in Supplementary Figure A13.

4.6.1.4 Amphibole

Amphibole is observed in Type I (Amp-Dunite, Amp-Harzburgite and Opx-Hbl-Peridotite) and Type IV (Hbl-Peridotite), but rarely observed in Type III (Phl-Harzburgite). The composition of amphibole is tremolitic to hornblendic in Amp-Dunite. It is hornblendic in Amp-Harzburgite, Opx-Hbl-Peridotite and Hbl-Peridotite. Tremolitic amphibole occurs in Phl-Harzburgite (Figure 31a) using the

classifications of Leake et al. (2004, 1997). The Mg# of amphibole is high in Amp-Dunite (0.93–0.95), followed by Amp- Harzburgite (0.89) and Opx-Hbl-Peridotite (0.87–0.90) (Figure 31b). The systematics of amphibole Mg# variability follows that of coexisting olivine Fo# and Mg# in orthopyroxene. TiO_2 and Al_2O_3 contents in amphiboles of Type I rocks show a positive correlation (Figure 31c). Amphibole of Amp-Dunite is tremolitic with low TiO_2 (0.18–0.50 wt.%) and Al_2O_3 (3.19–7.47 wt.%). Amphibole of Amp-Harzburgite is hornblendic and has slightly higher TiO_2 (0.60– 0.77 wt.%) and Al_2O_3 contents (7.60–9.74 wt.%) than Opx-Hbl-Peridotite (0.28–0.61 wt.% for TiO_2, 7.36–9.32 wt.% for Al_2O_3). Tremolite of Type III Phl-Harzburgite presents high Mg# (0.97), with low TiO_2 (0.03 wt.%) and Al_2O_3 contents (0.07 wt.%) (Figure 31b and c). The composition of the amphibole of Type IV Hbl-Peridotite is hornblendic to tremolitic with Mg# (0.88–0.93) and TiO_2 (0.22–0.60 wt.%) and Al_2O_3 (3.45–10.01 wt.%) contents but is poor in NiO (<0.05 wt.%) and Cr_2O_3 (<0.04 wt.%) contents (Supplementary Table S2 of Nishio et al. (2022b)).

Amphibole within the lithologies collected from boundaries of the body has various chemical compositions. The Mg# is high in Locality 1 followed by Localities 3 and 2 lithologies. The composition of calcic amphibole is tremolitic in Locality 1, edenitic to hornblendic and actinolitic in Locality 2, and hornblendic in Locality 3 Hbl-Orthopyroxenite (Figure 31a and b). Amphibole of the Locality 1 lithologies is characterized by high Mg# (0.93–0.96) and low TiO_2 (<0.1 wt.%) contents (Figure 31b and c). Amphibole in subzone (i) granitic apophysis of Locality 2 metasomatic rocks has low Mg# (0.59) and high TiO_2 content (0.65 wt.%) (Supplementary Table S2 of Nishio et al. (2022b)). Edenite in subzone (ii) has low Mg# (0.72–0.74), low TiO_2 (<0.16 wt. %) and high Al_2O_3 (11.91–11.83 wt.%) contents. TiO_2 and Al_2O_3 contents are positively correlated in actinolite to horn- blende of Locality 2 metasomatic rock and Ol-Hbl-Orthopyroxenite (Figure 31c). The amphibole of Locality 3 Hbl-Orthopyroxenite has lower Al_2O_3 (6.50–8.07 wt.%) and TiO_2 (0.26–0.38 wt.%) contents compared with those in amphibole of Amp-Harzburgite (Figure 31c).

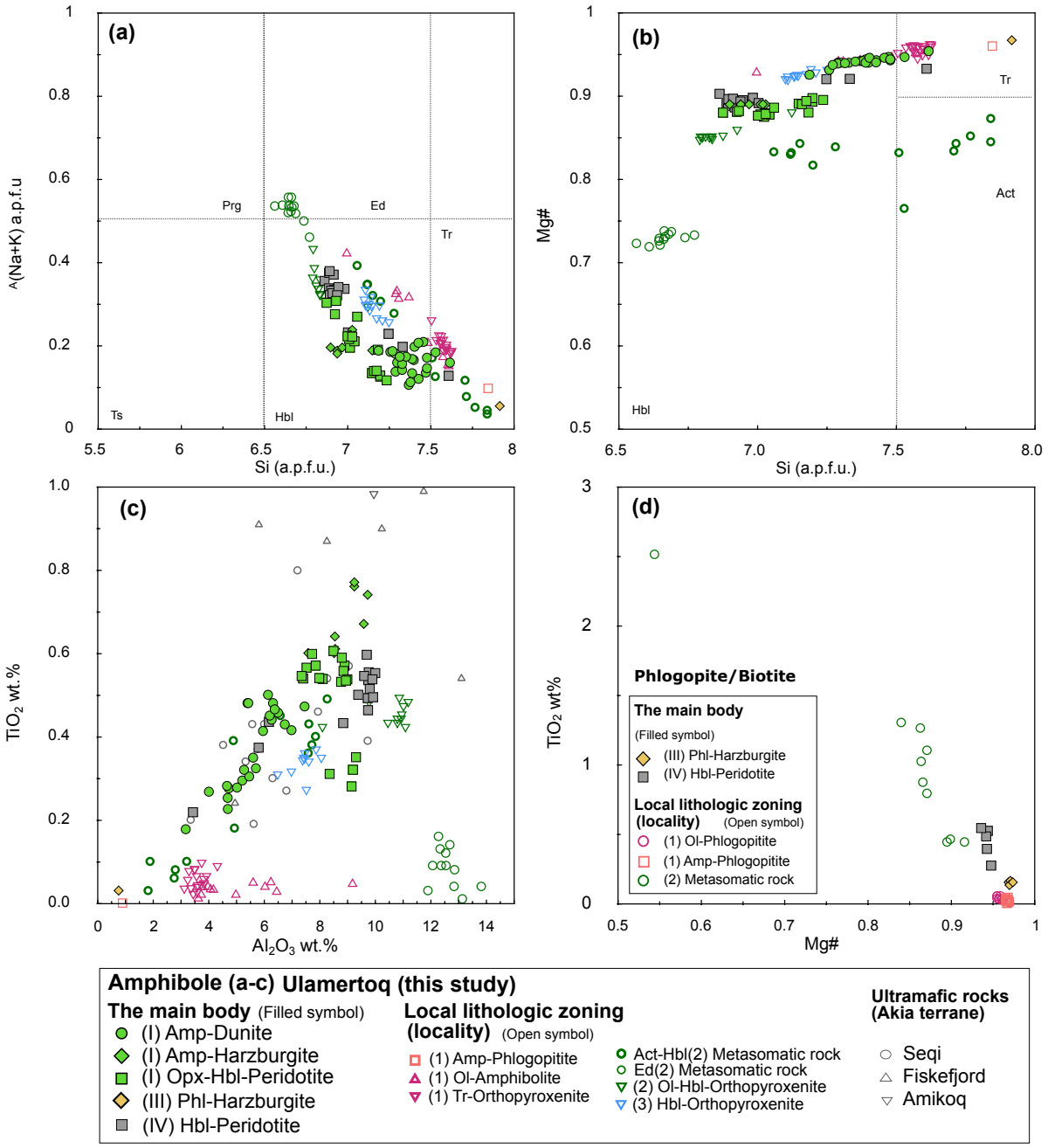

Figure 31: Major element chemistry of amphibole and phlogopite. (a) Classification of amphiboles of the Ulamertoq ultramafic rocks based on ^{A}(Na + K) atoms per formula unit (a.p.f.u.) and Si a.p.f.u. (Leake et al., 1997); (b) classification of amphiboles of the Ulamertoq ultramafic rocks based on Mg# and Si a.p.f.u.; (c) TiO_2 wt. % vs Al_2O_3 wt. % of amphiboles the Ulamertoq ultramafic rocks and ultramafic rocks from the Akia terrane (Aarestrup et al., 2020; Szilas et al., 2018, 2015); (d) TiO_2 wt. % vs Mg# plot of phlogopite/biotite.

4.6.1.5 Phlogopite and biotite

Mg# in phlogopite shows a negative correlation with TiO_2 content (Figure 31d). Phlogopites in Type III Phl-Harzburgite show high Mg# (0.97) and low TiO_2 (0.14–0.17 wt.%) contents. Phlogopite inclusions

in olivine in Type IV Hbl-Peridotite have slightly low Mg# (0.94–0.95) and high TiO_2 contents (0.28–0.55 wt.%).

Phlogopite of Locality 1 Ol/Amp-Phlogopitite is low in TiO_2 content (<0.06 wt.%) but high Mg# (0.95–0.97). The Mg# increases towards Locality 1 Ol-Amphibolite against the decrease of Fo# in coexisting olivine. The composition of phlogopite of Locality 2 metasomatic rock is variable as well as that of amphibole. It shows the wide range of Mg# (0.82–0.92) and TiO_2 content (0.45–1.31 wt.%). Biotite inclusions in subzone (i) a granitic apophysis of Locality 2 metasomatic rocks have high TiO_2 content (2.52 wt.%) and low Mg# (0.54).

4.6.2 Trace element compositions

4.6.2.1 Orthopyroxene

Chondrite-normalized REE and primitive mantle-normalized trace element patterns of orthopyroxenes of the main body ultramafic rocks display negative Sr and/or Eu anomalies and positive Zr and Ti anomalies except for Type III Phl-Harzburgite (Figure 32a and b). The middle to heavy REEs (MHREE) abundance of orthopyroxene can be distinguished by the presence of coexisting amphibole. The MHREE abundance of orthopyroxene that coexists with amphibole of Type I rocks is lower than that of orthopyroxenes of Types II and III rocks that are amphibole free or rare. Trace element compositions of orthopyroxene of Type III Phl-Harzburgite are different from the other types as shown by their major element compositions, which is characterized by negative Zr, Ti, Eu and Sr anomalies (Figure 32b).

The orthopyroxenes of Localities 1–3 orthopyroxenites show positive Ti and Zr anomalies, but a positive Sr anomaly is shown only by orthopyroxene of Locality 3 Hbl-Orthopyroxenite (Figure 32d). The orthopyroxene of Localities 1–3 orthopyroxenites shows a negative correlation between HREE abundance and Mg#. High

Mg# (0.93) orthopyroxene of Locality 1 Tr-Orthopyroxenite has the low HREE abundance. The low Mg# (0.85) orthopyroxene of Locality 2 Ol-Hbl-Orthopyroxenite has the high HREE abundance. Mg# (0.90) and HREE abundance in orthopyroxene of Locality 3 Hbl-Orthopyroxenite are between those of Locality 1 high Mg# Tr-Orthopyroxenite and Locality 2 low Mg# Ol-Hbl-Orthopyroxenite. Overall, the systematics of the HREE abundance in orthopyroxenes correlate negatively with the Mg# of coexisting amphibole. The HREE abundance in orthopyroxenes also corresponds to the systematics of olivine Fo# in the nearby main body ultramafic rocks (Figure 23).

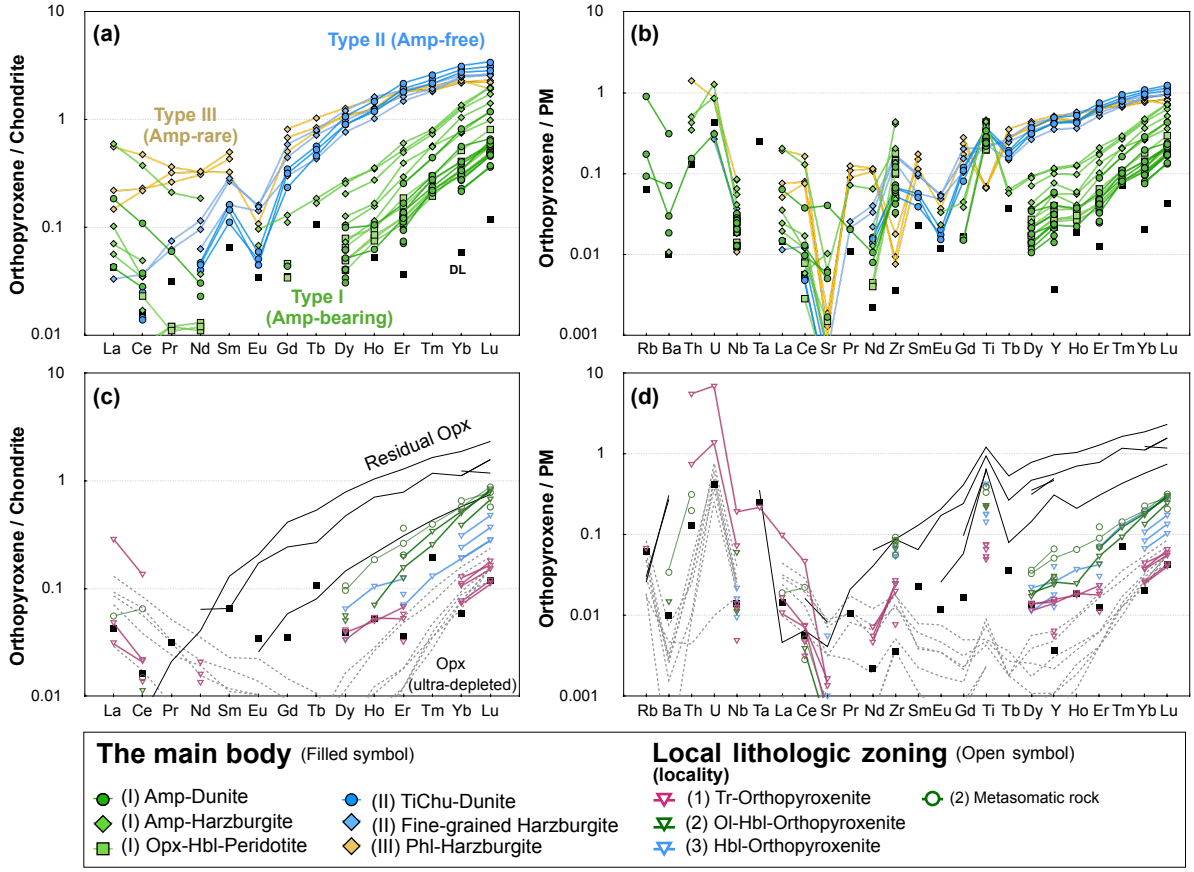

Figure 32: Chondrite-normalized REE and primitive mantle-normalized trace element patterns of orthopyroxene. (a) REE and (b) trace element patterns of orthopyroxene of the main body Types I–III ultramafic rocks; (c) REE and (d) trace element patterns of orthopyroxene from Locality 1 Tr-Orthopyroxenite, Locality 2 Metasomatic rock, Ol-Hbl-Orthopyroxenite and Locality 3 Hbl-Orthopyroxenite. Black lines (in Figure 32c and d) are representative REE and trace element compositions of residual orthopyroxene (D'Errico et al., 2016; Jean and Shervais, 2017; Morishita et al., 2009; Scott et al., 2016) and orthopyroxene in a supra subduction zone ultra-depleted peridotite (Xu et al., 2021). Black squares represent the detection limit (DL). Chondrite and primitive mantle values are from Sun and McDonough (1989).

4.6.2.2 Amphibole

Amphibole is the main reservoir of incompatible trace elements in Types I and IV ultramafic rocks. Amphibole from the main body ultramafic rocks is characterized by slight LREE-enriched patterns with negative Sr, Ti and Zr anomalies and/or Eu anomalies except for Type IV Hbl-Peridotite (Figure 33a and b). The REE abundance in amphibole, which strongly depends on the major element composition, is lower in tremolite than in hornblende. The abundance is higher in amphibole within the Amp-Harzburgite followed by Opx-Hbl-Peridotite and Amp-Dunite among Type I (Figure 33a). REE abundance shows positive correlations with Al_2O_3 content and negative correlations with Mg# and SiO_2 contents.

Chondrite-normalized REE patterns of amphibole from Localities 1–3 orthopyroxenites show flat patterns (Figure 33c). HREE tends to be more abundant in amphibole of Locality 2 Ol-Hbl-Orthopyroxenite than in those of Locality 3 Hbl-Orthopyroxenite and Locality 1 Tr-Orthopyroxenite, conforming to the systematics of orthopyroxene (Figure 33c), negatively correlated with Mg#. Amphiboles of Localities 1 and 2 lithologies present negative Ti, Zr and Sr anomalies; however, amphibole of Locality 3 Hbl-Orthopyroxenite shows positive Zr and Sr anomalies (Figure 33d).

Amphibole coexisting with phlogopite shows various trace element compositions (Figure 33e and f). Tremolite from Locality 1 Amp-Phlogopitite shows LREE-enriched patterns with a negative Eu anomaly (Figure 33e and f). Edenite shows a positive Eu anomaly with a LREE-enriched pattern. Actinolite has a flat pattern with HREE abundance. Hornblende in contact with phlogopite of Locality 2 shows a high REE abundance and a negative Eu anomaly (Figure 33e and f).

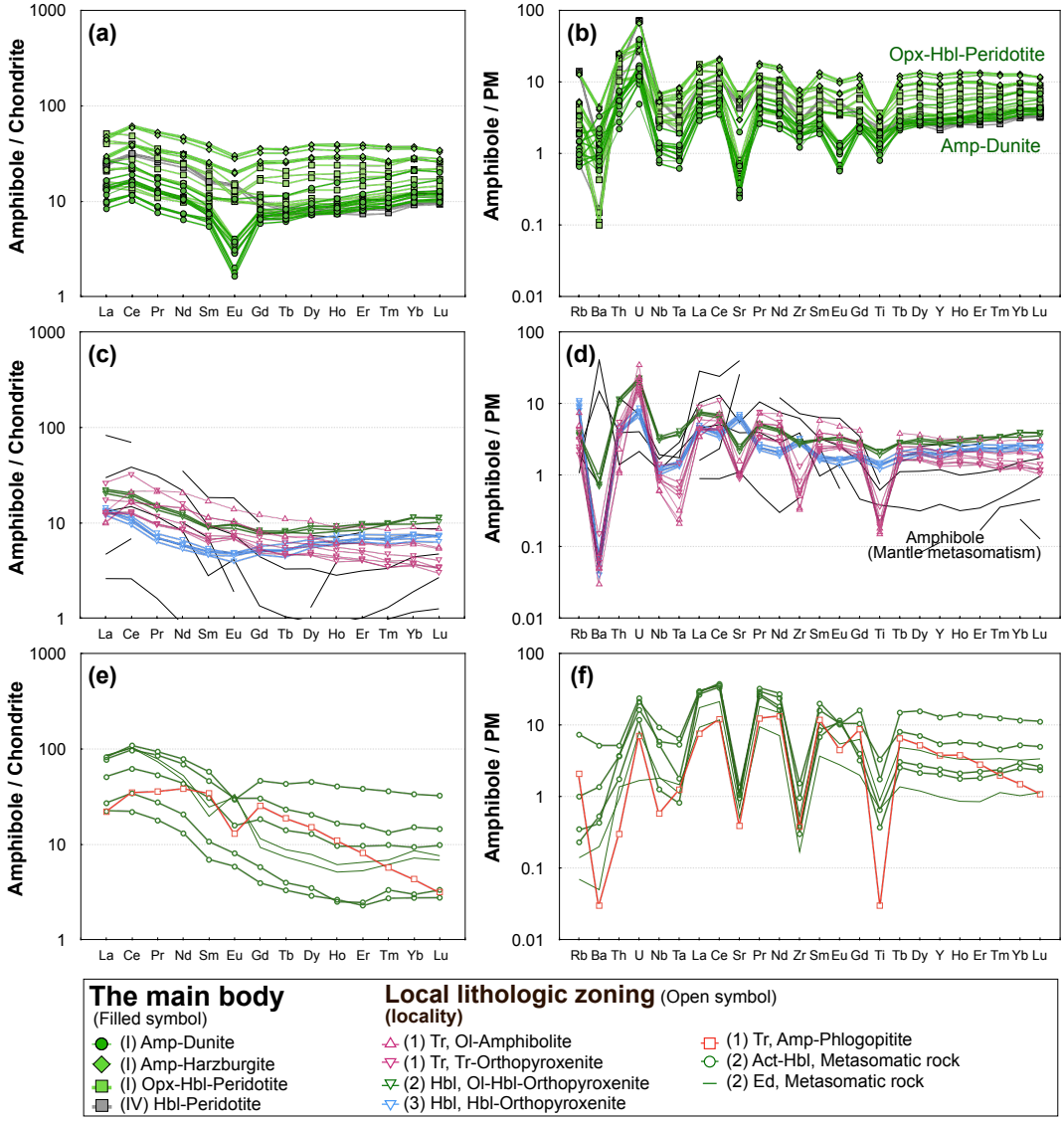

Figure 33: Chondrite-normalized REE and primitive mantle-normalized trace element patterns of amphibole. (a) REE and (b) trace element patterns of amphibole from the main body Type I ultramafic rocks and Type IV Hbl-Peridotite; (c) REE and (d) trace element patterns of amphibole of Localities

1–3 orthopyroxenites and Locality 1 Ol-Amphibolite. Black lines are trace element compositions of amphibole formed by mantle metasomatism (Grégoire et al., 2001; Ishimaru and Arai, 2008; Pearson and Nowell, 2002); (e) REE and (f) trace element patterns of amphibole of Locality 1 Amp-Phlogopitite and Locality 2 Metasomatic rock. Chondrite and primitive mantle values are from Sun and McDonough (1989).

4.7 Discussion

Here, we first discuss the origin of hydrous mineral- and/or orthopyroxene-rich ultramafic rocks (local lithologic zoning), which occur preferentially along the boundary between the ultramafic body and the surrounding host orthogneiss/granitic sheet, focusing on local metasomatic activity. We then examine the effect of more diffuse metasomatism in the main body ultramafic rocks at Ulamertoq. The origin and history of the main body ultramafic rocks are finally discussed.

4.7.1 Local metasomatism: origin of hydrous mineral-rich layers and related orthopyroxenite

Local metasomatism can be classified into two processes (Table 5): that discussed in this section—the formation of hydrous mineral-rich layers and related orthopyroxenites (Localities 1 and 2) and the formation of orthopyroxenite veins (Locality 3), discussed in the next section.

Table 5: Geochemical characteristics of the local lithologic zoning

Lithology	Hydrous mineral-rich layers and Orthopyroxenites		Orthopyroxenite veins
Locality	Locality 1	Locality 2	Locality 3
Protolith (Ultramafic rock)	Dunite	Opx-Hbl-Peridotite	Harzburgite
Olivine	High Fo# Decreasing towards Ol-Phlogopitite (92.8→90)	Low Fo# (84.9–85.9)	Middle Fo# (89.5–90.1) with slightly high NiO (0.30–0.38 wt.%)
Orthopyroxene in Orthopyroxenite	High Mg# (0.93) Low HREE abundance	Low Mg# (0.85) High HREE abundance	Middle Mg# (0.90–0.91) Middle HREE abundance
Amphibole in Orthopyroxenite	High Mg# (0.96) Low TiO_2 (<0.1 wt.%) Low HREE abundance	Low Mg# (0.85) High HREE abundance	Middle Mg# (0.92–0.93) Middle HREE abundance Positive Sr and Zr anomalies

Systematic mineral zoning in phlogopite-, amphibole- and orthopyroxene-rich lithologies from the country rock to the main body is observed in many places and described as Locality 1 and Locality 2. The presence of olivine (Figure 25a) and the high Cr and NiO contents (Figure 27d) in Locality 1 Ol-Phlogopitite and Locality 2 Ol-Hbl-Orthopyroxenite suggest that the protoliths of these lithologies were the main body ultramafic rocks. Locality 1 Ol-Phlogopitite occurs adjacent to Ol-Amphibolite, whereas

Tr-Orthopyroxenite occurs dike-like near the boundary (Figure 24g) and these lithologies are poor in Ti (Figure 28b and Figure 31c). The formation of the lithologies can be explained by multiple infiltrations of metasomatic agents originating from similar sources, in which there is a systematic change in chemical composition of the metasomatic agent as metasomatism proceeds.

The modal abundance, size and Fo# of olivine in locality 1 Ol-Amphibolite decrease towards the adjacent Ol-Phlogopitite (Figure 29b). Phlogopites can be formed by consuming olivine via reaction with a fluid (Fluid I) that also introduces alkali elements, Al_2O_3, SiO_2 and CaO (Arai and Takahashi, 1989; T. B. Grant et al., 2014). The formation of phlogopitite via this reaction, likely driven by fluid infiltration from the surrounding granite, increased the Na_2 O/K_2O ratio and CaO in the residual fluid (Fluid II). The Ol-Amphibolite was formed by the reaction of olivine and Fluid II.

Low-Cr_2O_3-CaO orthopyroxene in Locality 1 Tr-Orthopyroxenite (Figure 30c) suggests that the orthopyroxenites were formed by the reaction between olivine and high-SiO_2 fluid, again introduced from the granitic country rocks. The optically continuous fine-grained olivine grains included in the low-Cr_2O_3-CaO orthopyroxene of Locality 2 Ol-Hbl-Orthopyroxenite are consistent with this metasomatic origin (Figure 30c).

Amphibole, phlogopite, orthopyroxene and relic olivine in Locality 1 lithologies have higher Mg# (Figure 29b and Figure 30b) but distinctively lower TiO_2 contents and HREE abundance (Figure 31c–d and Figure 32c) than those of Locality 2 lithologies. Locality 1 high Mg# lithologies were collected near high Mg# dunites, while Locality 2 low Mg# lithologies were collected near low Mg# Opx-Hbl-Peridotite (Table 5). The Mg# systematics and difference of TiO_2 contents between these localities suggest that they reflect the compositional difference of the main body ultramafic rocks at each locality and the invading metasomatic fluids. The mineral chemical systematics also indicate that local lithological zonation was generated subsequent to the formation of metasomatic rocks formed within the main body.

The Ti abundance in phlogopite of Locality 1 ultramafic rocks is much lower than Ti in mantle metasomatic phlogopite (typically ~5000 ppm) produced by mantle metasomatism (Pearson and Nowell, 2002), indicating that the metasomatic processes considered here are distinct from mantle metasomatism.

Amphiboles (edenite) in the subzone (ii) of Locality 2 metasomatic rocks contain plagioclase and zircon and are free of Cr-rich phases, while hydrous minerals in subzones (iii) and (iv) contain detectable Cr_2O_3 and spinel inclusions are observed. The presence of chromian phases suggests the original contact between the granitic intrusive apophysis and the ultramafic parent rock was between subzones (ii) and (iii).

Metasomatic mineral zoning of hydrous mineral-rich layers and orthopyroxenites are commonly observed along the boundary between ultramafic rocks and intrusive granitic sheets/orthogneisses in other localities (Faithfull et al., 2018; Gargiulo et al., 2013; Marocchi et al., 2010, 2009; Su et al., 2016; Uno et al., 2017). Similar hydrous mineral-rich layers have been reported from the Seqi ultramafic body in the Akia terrane (Whyatt et al., 2020) and were interpreted as local reaction products between dunite

and SiO_2-rich fluid derived from a granitic sheet. Extending these observations to Ulamertoq, the formation of phlogopite, amphibole and orthopyroxene and their associated geochemical mostly likely resulted from metasomatism related to the ingress and systematic compositional change of metasomatic fluid from the granitic intrusion.

4.7.2 Local metasomatism: origin of Hbl-Orthopyroxenite veins and vein networks

Symmetric mineral zoning characterized by amphibole-rich margins and orthopyroxene-rich centers is observed in Locality 3 Hbl-Orthopyroxenite (Figure 25f). Large orthopyroxene grains contain optically continuous olivine grains coupled with low-Cr_2O_3–CaO contents (Figure 25i and Figure 30c). The NiO contents in discrete olivine grains are higher compared with those in olivine of harzburgites (Figure 29b). These petrological and mineralogical characteristics indicate an origin of orthopyroxene by replacement of olivine in the ultramafic rock via a reaction with an orthopyroxene-saturated metasomatic agent (Endo et al., 2015).

Amphibole within Locality 3 Hbl-Orthopyroxenite exhibits positive Sr and Zr anomalies, which are distinct from those of the lithologies in the Ulamertoq body (Figure 33d; Table 5). The distinctive characteristics suggest that the metasomatic agents that produced Locality 3 Hbl-Orthopyroxenite are different from those which formed Localities 1 and 2 metasomatic rocks and the main body.

4.7.3 Effect of metasomatism on lithologic variations in the main body: is orthopyroxene primary or metasomatic?

Here we discuss metasomatic effects on the main body ultramafic rocks by considering Types I−III separately from Type IV spinifex-like textured Hbl-Peridotite because of the differences in occurrence, the geochemical characteristics, and the lack of orthopyroxene.

Orthopyroxene is a common component of the main body ultramafic rocks, except for those of Type IV. The orthopyroxenes of the main body ultramafic rocks commonly form aggregates of small grains (Figure 26e) and are characterized by poikilitic texture, including olivine grains (Figure 26c and g), and often contain dark-green spinels (Figure 26c). The petrographic characteristics are similar to secondary orthopyroxenes (Berno et al., 2020), rather than orthopyroxene porphyroclasts in typical peridotites, such as ultramafic xenoliths in volcanic rocks, from ultramafic ophiolite sequences, or abyssal peridotites (Morishita et al., 2009).

The low Cr_2O_3 orthopyroxene in the main body ultramafic rocks is different from orthopyroxene from abyssal peridotites recovered from mid-ocean ridges (Warren, 2016) and forearc settings (Parkinson and Pearce, 1998) as well as being distinct from ultramafic cumulates (Figure 30; Supplementary Figure A13) (Barnes et al., 2016; Matsufuji et al., 2006; Sharpe and Hulbert, 1985). The

negative Sr and/or Eu anomalies in Ulamertoq orthopyroxenes are also different from residual orthopyroxene from mantle peridotites that do not show negative Eu and Sr anomalies (Figure 32b) (D'Errico et al., 2016; Scott et al., 2016; Xu et al., 2021).

Instead, low-CaO–Cr_2O_3 and negative correlations between Cr_2O_3, Mg# and Al_2O_3 of orthopyroxene are consistent with the characteristics observed in secondary orthopyroxene formed by the reaction between a dunitic rock and orthopyroxene-saturated melt (Berno et al., 2020). Low-CaO–Cr_2O_3 orthopyroxenes are similar to metasomatic orthopyroxene observed in sub-arc peridotite xenoliths that underwent SiO_2-rich fluid/melt metasomatism in arc setting (Figure 30a and c) (Arai et al., 2004; Ishimaru et al., 2007; Ishimaru and Arai, 2008).

Our study emphasises that orthopyroxene in the main body ultra- mafic rocks is a later reaction product rather than the primary igneous phase. It is noteworthy that the compositions of orthopyroxene in ultramafic rocks interpreted as cumulates from the Mesoarchean Akia terrane (Aarestrup et al., 2020; McIntyre et al., 2021; Szilas et al., 2018, 2015) and also ultramafic rocks interpreted as mantle residues from the Eoarchean Itsaq gneiss (Friend et al., 2002) are similar to those of orthopyroxene in the Ulamertoq body (Figure 30; Supplementary Figure A13). Hence, the origins and chemical signatures carried by the Archean ultramafic rocks from SW Greenland should be considered in the context of metasomatism that has involved significant mass transport into these bodies from the surrounding country rocks.

4.7.4 Multiple metasomatic events and agents: evidence based on chemical compositions of orthopyroxene and amphibole

Multiple metasomatic events comprising different metasomatic agents are required based on the differences in trace element compositions of orthopyroxene ± amphibole in the main body ultramafic rocks. We focus our discussion on hornblende because tremolite in the same samples likely formed later at lower temperatures.

Orthopyroxene in the main body ultramafic rocks can be geochemically classified into three types (Figure 32a and b; Table 6): Type I orthopyroxene has low REE abundances and coexists with amphibole in Amp-Dunite, Amp-Harzburgite and Opx-Hbl-Peridotite; Type II orthopyroxene has high REE abundances with Eu negative anomalies in the TiChu-Dunite and fine-grained harzburgite; and Type III orthopyroxene has high REE abundances with negative anomalies of Eu and high-field strength elements (HFSEs) in Phl-Harzburgite.

Orthopyroxene and coexisting amphibole are characterised by the negative anomalies of Sr and Eu (Figure 32b and Figure 33b). No clear textural evidence of replacement of Type I orthopyroxene by amphibole or vice versa was observed. These geochemical and textural features suggest that Type I orthopyroxene and amphibole formed in the same metasomatic event. The metasomatic formation of

both orthopyroxene and amphibole in ultramafic rocks had also been reported from an experimental study of the interaction between peridotite and interaction with hydrous basalt melt (Wang et al., 2021).

The calculated REE composition of melts in equilibrium with amphibole from Type I ultramafic rocks, using partition coefficients (Shimizu et al., 2017), are similar to regional norites (Waterton et al., 2020a) and TTG gneiss (Gardiner et al., 2019) from the Akia terrane (Figure 34; Supplementary Figure A14). The metasomatic agents that formed orthopyroxene and amphibole in Type I ultramafic rocks were probably derived from surrounding crustal materials. As the equilibrated melts show negative Eu anomalies (Figure 34a), the negative Eu and Sr anomalies of orthopyroxene (Figure 32b) and amphibole (Figure 33b) indicate that the metasomatic melts were derived from sources affected by plagioclase fractionation or residual plagioclase.

Table 6: Geochemical systematics of the main body ultramafic rock

Lithology	Dunite		Harzburgite		Opx-Hbl-Peridotite	Phl-Harzburgite
	Amp-Dunite Type I	TiChu-Dunite Type II	Amp-Harzburgite Type I	Fine-grained Harzburgite Type II	Opx-Hbl-Peridotite Type I	Phl-Harzburgite Type III
Modal abundance of opx and/or amp	Low (3–10 %)		Middle (25–33 %)		High (54–56%)	Middle (20% + Phl 10%)
Olivine	Fo# negatively correlates with the modal abundance of orthopyroxene and/or amphibole.					High Fo# with low NiO
Low-CaO–Cr_2O_3 Orthopyroxene	Mg# negatively correlates with the modal abundance of orthopyroxene and/or amphibole. Mg# correlate with Al_2O_3 negatively and Cr_2O_3 positively.					Low-CaO–Cr_2O_3 Al_2O_3
Amphibole (Type I)	High Mg# (0.93–0.95)	-	Low Mg# (0.89)	-	Middle Mg# (0.87–0.90)	High (Tremolite)
Modal amp/opx ratio	1	-	<1	-	1	-
Orthopyroxene Trace elements	Low-HREE Negative Sr anomalies	High-HREE Negative Eu and Sr anomalies	Low-HREE Negative Sr anomalies	High-HREE Negative Eu and Sr anomalies	Low-HREE Negative Sr anomalies	High-HREE Negative Eu, Sr, Ti, Zr anomalies
Amphibole Trace elements	Low-REE Negative Eu and Sr anomalies	-	High-REE Negative Eu and Sr anomalies	-	Middle-REE Negative Eu and Sr anomalies	(Tremolite)
Whole-rock Mg/Si ratio Al/Si ratio	Mg/Si ratio decreases but Al/Si ratio increases as the modal abundance of orthopyroxene and/or amphibole.					High Mg/Si Low Al/Si
Whole-rock REE	REE abundance increases as the modal abundance of orthopyroxene and/or amphibole.					Low REE

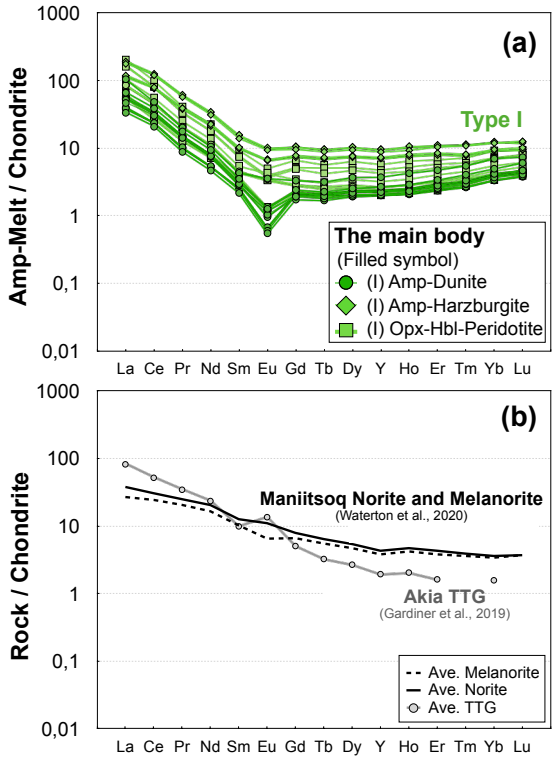

Figure 34: (a) REE + Y compositions of melts in equilibrium with amphibole in Type I ultramafic rocks. Calculations were carried out using amphibole/melt partition coefficients (Shimizu et al., 2017); (b) average REE + Y compositions of crustal rocks from Akia terrane, melanorite, orthopyroxene-rich norite, (Ave. Melanorite; n=19) and norite (Ave. Norite; n=27) from Maniitsoq region (Waterton et al., 2020a) and of TTG gneiss (Ave. TTG; n = 7) (Gardiner et al., 2019). The patterns of all the data of crustal rocks are shown in Supplementary Figure A14.

The systematic variations in major element mineral chemistry and modal abundances of orthopyroxene and amphibole (Table 6) can be explained by differences in the melt/rock ratio and water content during the interaction between hydrous melt and ultramafic rocks.

It is striking that the trace element patterns of orthopyroxene and/or amphibole in Types I and II have similar characteristics with negative Sr and/or Eu anomalies and positive Zr and Ti anomalies (Figure 32b), although no amphibole is observed in Type II ultramafic rocks. The REE abundance of orthopyroxene in Type II rocks is higher than that of orthopyroxene in Type I, whereas modal orthopyroxene is lower in Type II TiChu-Dunite than in Type I rocks. These relationships can be explained by a small-amount addition of metasomatic minerals from a fractionated metasomatic agent after the formation of Type I ultramafic rocks or via the reaction of similar source rocks with different water contents.

The composition of Type III Phl-Harzburgite is distinct from other rock-types (Table 6). It is characterized by a high modal abundance of phlogopite and orthopyroxene with very low Al_2O_3 (Figure 30a), relatively high LREE and negative anomalies of HFSE (Figure 32b). The metasomatic agent

related to Phl-Harzburgite was most probably different to that of other types or to the fractionated metasomatic agents that formed Type I.

Formation of the orthopyroxene in amphibole-free Type II rocks showing high HREE abundance with negative Sr and Eu anomalies by the reaction between dunitic cumulate and melt in the late-magmatic stage is still possible if the metasomatic norite melt formed in the same igneous event. However, the genesis and age of norites and their relationship with the regional ultramafic rocks such as those considered here remain enigmatic (Aarestrup et al., 2021; Garde, 1997; Garde et al., 2013; Waterton et al., 2020a). The cataclastic structure of the Finnefjeld gneisses in the northern part of the terrane and the Ni-sulphide mineralization in the Maniitsoq norite have been interpreted as having formed from the reworking of Akia TTG gneiss in conjunction with events caused by a giant bolide impact before 3.0 Ga (Garde et al., 2020, 2014, 2013, 2012). Yakymchuk et al. (2021) recently tested the impact hypothesis; their results are incompatible with the interpretation of a giant bolide impact.

Waterton et al. (2020) interpreted the ~3 Ga Maniitsoq norites to be the result of mixing of ultramafic rocks and TTG. The Ulamertoq norite, >50 km away from the Finnefjeld gneiss, does not contain Ni-sulphide and shows plagioclase-orthopyroxene assemblage which is different from those of the Maniitsoq norite. The origin of norites in our study area is, however, beyond the scope of this study but is needed for a better understanding of the evolution of the ultramafic-mafic complex and the possible role of a giant bolide impact.

4.7.5 Implications of metasomatic modification for the compositional variation in the Ulamertoq ulatramafic body

Discussion of the origin of ultramafic rocks requires consideration of the fact that orthopyroxene and amphibole in the main body ultramafic rocks are not primary igneous phases. Here, we discuss the extent to which the modal metasomatism associated with the introduction of these phases also modified the 'primary' olivine Fo# and whole-rock compositions. Samples with the same Fo# but varying the NiO content of the olivine will be discussed in the next section.

As the modal abundance of metasomatic orthopyroxene and amphibole increases, the Fo# of olivine decreases from TiChu-Dunite and Amp-Dunite to fine-grained harzburgite and Amp-Harzburgite and then Opx-Hbl-Peridotite among Types I and II rocks (Table 6; Supplementary Figure A12). The systematics of olivine in Types I and II are best explained as a metasomatic trend rather than a trend generated by magmatic fractional crystallisation (Antonicelli et al., 2020; Berno et al., 2020; Cordier et al., 2015). The metasomatic origin of this trend is supported by experiments that show that Fo# and NiO contents of olivine decrease as the reaction between peridotite and basalt progresses (Wang et al., 2016, 2013).

Metasomatic modification observed in Locality 3 Hbl-Orthopyroxenite, generated increasing olivine NiO occurs at constant Fo# (Figure 29b). This modification is not plausible for the main body ultramafic rocks because olivine compositions in the olivine- and orthopyroxene-dominant zone of fine-grained harzburgite are identical. Although we cannot exclude the possibility that the olivine chemistry of some peridotites still reflects original compositions, it seems unlikely to be the solely a result of primary igneous processes.

It has been suggested that geochemical correlations between Mg/Si and Al/Si ratios of whole-rock compositions of Archean ultramafic rocks from SW Greenland are similar to those of residual peridotites (Figure 35) (Friend et al., 2002; Friend and Nutman, 2011; van de Löcht et al., 2020, 2018), although the inability of this plot in distinguishing mantle vs cumulate peridotite has been shown by both (McIntyre et al., 2019; Waterton et al., 2022). The whole-rock compositions of the main Ulamertoq body ultramafics span the entire chemical range of Archean ultramafic rocks from SW Greenland. Among the Ulamertoq samples, TiChu-Dunite, Amp-Dunite and Phl-Harzburgite have high Mg/Si and low Al/Si ratios, while Opx-Hbl-Peridotites have low Mg/Si and high Al/Si ratios (Figure 35). The geochemical trend of whole-rock compositions in SW Greenland Archean ultramafic rocks can be generated simply by the addition of metasomatic minerals to dunitic rocks rather than partial melting, i.e., all the dispersion on the Mg/Si vs Al/Si diagram is a function of the degree of metasomatism.

The bulk geochemical variation in SW Greenland peridotites as a whole can be explained by metasomatic addition of material derived from local crustal rocks, as demonstrated by the mixing line between dunitic and regional noritic rocks (Waterton et al., 2020a) or TTG (Gardiner et al., 2019) assuming that the crustal rocks represent the metasomatic melt compositions (Figure 35). Metasomatic features of the mineral chemistry and whole-rock chemistry of the Ulamertoq ultramafic rocks are comparable to the Mesoarchean ultramafic rocks in the Fiskefjord area indicating that those ultramafic bodies experienced a similar metasomatic history and that they could be fragments of the large ultramafic complex as suggested by McIntyre et al. (2021).

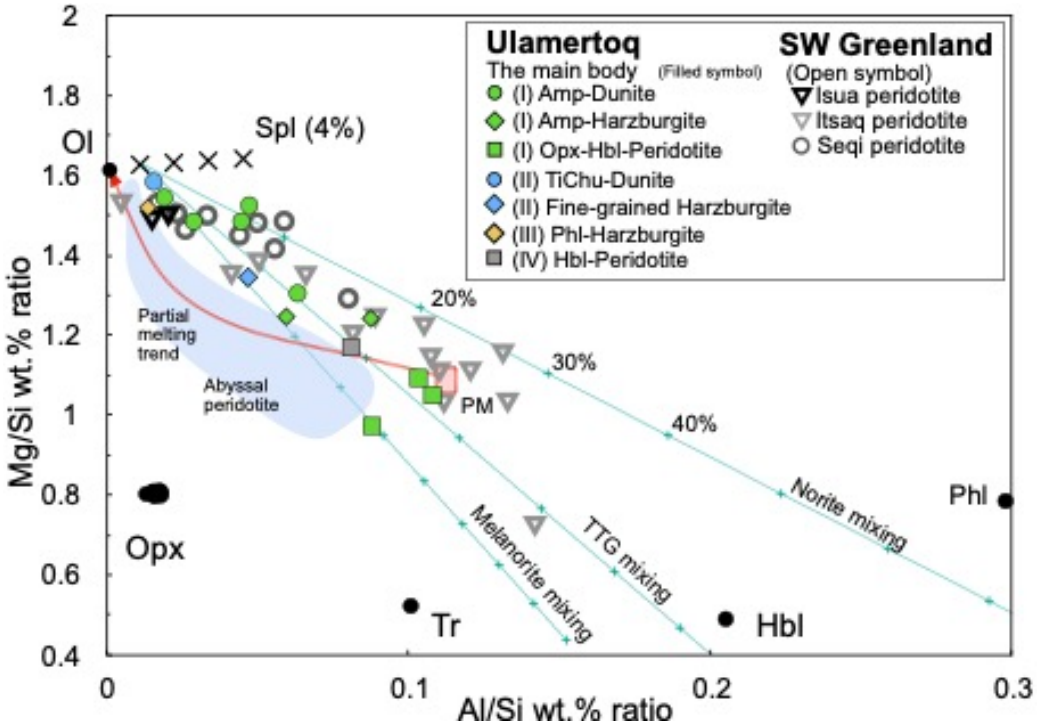

Figure 35: Whole-rock Mg/Si wt.% ratio vs Al/Si wt.% ratio chemistry. Representative mineral compositions are from the main body ultramafic rocks. Black-colored crosses show the calculated composition of the representative spinel addition (1–4 vol.%) to the representative olivine composition of Amp- Dunite. Green-colored lines show mixing trends between the composition of dunitic rock (Ol 99%, Spl 1%) and average compositions of norite (n = 45), melanorite, orthopyroxene-rich norite (n = 19) (Waterton et al., 2020a) or TTG gneiss (n=7) (Gardiner et al., 2019) from Akia terrane and crosses with percentages indicate the amount of crustal mixing into dunite. Primitive mantle (PM; red square) is from Sun & McDonough (1989). Partial melting trend (red-colored dotted line) is from Rollinson (2007). Compositional area of abyssal peridotites (blue colored area) from Niu (2004). Seqi ultramafic cumulates (Szilas et al., 2018) and peridotites of the Itsaq and Isua area (Friend et al., 2002; Friend and Nutman, 2011) from SW Greenland were respectively interpreted as cumulate and mantle residues. See Waterton et al. (2022) for alternative interpretation.

4.7.6 A note of caution in deciphering the igneous features of the Ulamertoq ultramafic rocks

Our study of a Mesoarchean ultramafic body in the Akia terrane, SW Greenland, has shown that most whole-rock chemistry and mineral compositions were modified by metasomatism to compositions that diverge significantly from their primary igneous compositions. The metasomatic alteration experienced by the Ulamertoq body is a common feature in all ultramafic bodies across SW Greenland. Therefore, it is crucial to try to define any primary igneous signatures offered by this or similar ultramafic bodies from the least-metasomatized peridotites, in order to best constrain their origin and the information they might provide about the Mesoarchean mantle from which the primary melts were derived.

From the petrological and geochemical features discussed above, it is clear that dunite containing minimal orthopyroxene or hydrous minerals are expected to be the least-metasomatized

ultramafic rocks in the Ulamertoq ultramafic body and by extension, in other regional ultramafic bodies. Within the Ulamertoq body, dunites varieties such as Type I Amp-Dunite and Type II TiChu-Dunite, have high olivine Fo# (~93) (Figure 29a) and low Cr# (0.25–0.4) of spinel. The high Fo# and low Cr# of these rocks are inconsistent with depleted residual peridotite, such as forearc peridotites have high Fo# (~91) and Cr# (>0.6) (Morishita et al., 2011); ultra-depleted dunite xenoliths from the sub-continental lithospheric mantle of North Atlantic Craton after a high degree of partial melting have high Fo# (92.0–93.7) and Cr# (up to 0.96) (Bernstein et al., 2006). Therefore, the origin of the Ulamertoq dunite (olivine: 99–96% + spinel: 1–4%) is best explained by cumulative origin.

From our above discussion, it is clear that the TiChu-Dunite not likely of pristine igneous origin but instead originated by deserpentinization of a serpentinite or heavily serpentinized ultramafic (Nishio et al., 2019), although the range in NiO content and Fo# in TiChu-Dunite are much smaller than those of olivine in highly serpentinized/deserpentinized dunite from the Eoarchean Isua Supracrustal Belt (Dymek et al., 1988b, 1988a; Friend and Nutman, 2011; Guotana et al., 2022) that are not likely to represent mantle melt residues either (Waterton et al., 2022).

4.7.7 The evolution and pressure–temperature history of the Ulamertoq ultramafic body

Here we constrain pressure–temperature (P–T) conditions (Figure 36; see Supplementary Figure A15 for details) and summarize the complex evolution of the Mesoarchean Ulamertoq ultramafic rocks from SW Greenland (Figure 37).

4.7.7.1 Earliest stages: magmatism and metamorphism

Based on the geochemical and petrological characteristics of the least metasomatized ultramafic rocks, a cumulative origin is most likely. The magmatic age of the Ulamertoq ultramafic rocks was not constrained, but a preliminary Re–Os age of ~3.3 Ga was suggested from the Seqi ultramafic rock which is near the Ulamertoq body and shares similar geochemical and petrological signatures (Szilas et al., 2016).

It is notable that hydration (serpentinization) and subsequent dehydration (deserpentinization) processes likely occurred, at ~800° C–900° C and < 2 GPa, as documented by the TiChu-bearing dunite (Nishio et al., 2019). Because only one dunite sample contains TiChu, it is not possible to determine whether the hydration–dehydration event is local or widespread in the Ulamertoq ultramafic body though it seems unlikely that only one small segment of the body was hydrated. TiChu and associated petrographic features were observed in one of the least-metasomatized dunites, indicating that the hydration-dehydration processes possibly occurred before the main metasomatism that affected the main body (Figure 37).

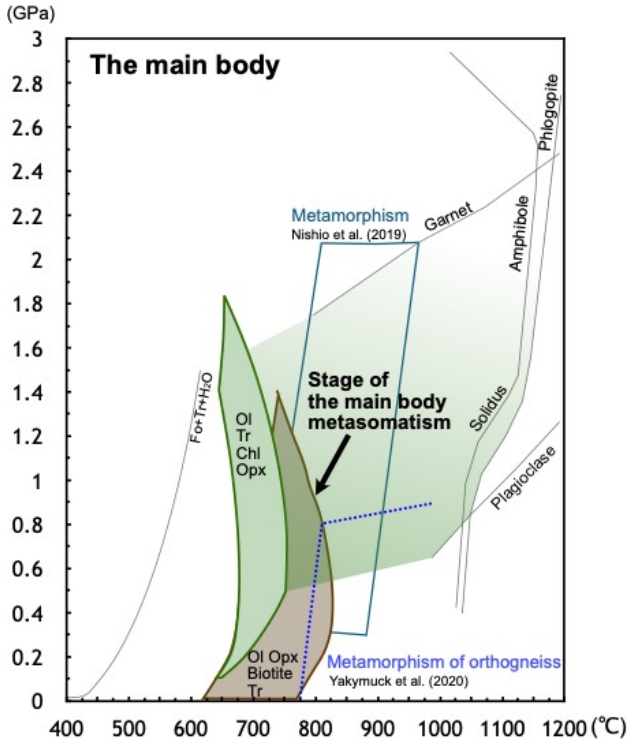

Figure 36: Possible P–T conditions for the Ulamertoq ultramafic rocks. The stage of the main body metasomatism took place under granulite to amphibolite facies conditions. Later retrograde conditions constrained by pseudosections modeling of Type I Amp-Dunite, sample 565423 and Type III Phl-Harzburgite sample 565428. Details about pseudosection modeling are in the supplementary material. The field of metamorphism recorded in TiChu-Dunite is from Nishio et al. (2019). The stability field of amphibole and phlogopite is from Conceiçao and Green (2004).

4.7.7.2 Main body metasomatism

We estimate the P–T condition of the major minerals of the main body based on experimental data and pseudosection modeling for Type I peridotites. The primary lithology comprising the main body ultramafic rocks—likely a dunite—experienced variable metasomatism forming the olivine-spinel-orthopyroxene-hornblende assemblage that constitutes peridotites of Type I (Figure 37). No garnet or plagioclase is observed in the ultramafic rocks, indicating that they were formed within the spinel peridotite stability field. Amphibole is stable <1125 ºC at 2.5 GPa in metasomatized depleted peridotite compositions (Conceiçao and Green, 2004), indicating that amphibole (± phlogopite) in Type I peridotites could be stable even under granulite-facies conditions in the Ulamertoq ultramafic rocks (Figure 36) as discussed below.

Type I Amp-Dunite (565423) and Type III Phl-Harzburgite (565428) are characterized by olivine-spinel-orthopyroxene-tremolite-chlorite and olivine-spinel-orthopyroxene-phlogopite-tremolite assemblages. The P–T pseudosection constrained the conditions from 650 ºC to 750 ºC at <1.8 GPa for Type I Amp-Dunite and 650 ºC to 850 ºC at <1.5 GPa for Type III Phl-Harzburgite (Supplementary

Figure A15). Since chlorite is usually found surrounding spinel, the estimated P–T conditions for Type I Amph-Dunite are interpreted as retrograde P–T conditions. It is noted that low-pressure granulite-facies metamorphism is recorded in the surrounding TTG gneiss, to at least 800ºC, at pressures <0.8 GPa. (White et al., 2017; Yakymchuk et al., 2020).

4.7.7.3 Local metasomatism

Two processes of local metasomatism are recorded in the Ulamertoq peridotites: formation of hydrous mineral-rich layers (+ related orthopyroxenites) and orthopyroxenite veins (Figure 36).

Phlogopitites and metasomatic phlogopite−amphibole rocks (Localities 1 and 2) contain anthophyllite and talc. The stable field of anthophyllite and talc in ultramafic compositions is limited to temperatures <750ºC and pressures <1.2 GPa (Chernosky et al., 1985). Application of the plagioclase−hornblende geothermometer for Locality 2 metasomatic rocks related to a centimeter-scale granitic apophysis indicates the occurrence of reaction at ~650ºC (Holland and Blundy, 1994). Such P–T conditions are consistent with those estimated for the hydrous mineral-rich layers related to the 2.97 Ga granitic intrusions in the Seqi body (Szilas et al., 2018; Whyatt et al., 2020). The field relationships of Locality 1 lithologies with low-TiO_2 signatures indicate that the protoliths and the source of the metasomatic agents are very similar. Talc is observed at the grain boundaries of orthopyroxenes and along the cleavages in Tr-Orthopyroxenite (Supplementary Figure A9) suggesting that talc is a retrograde phase.

The Ca-in-orthopyroxene thermometer, applied to Locality 3 Hbl-Orthopyroxenite (Brey and Köhler, 1990) suggests equilibration temperatures of ~950ºC. Because Hbl-Orthopyroxenite occurs as veins or vein-networks up to metre-scale, the temperature conditions estimated by orthopyroxene thermometry probably represent local, not the ambient conditions.

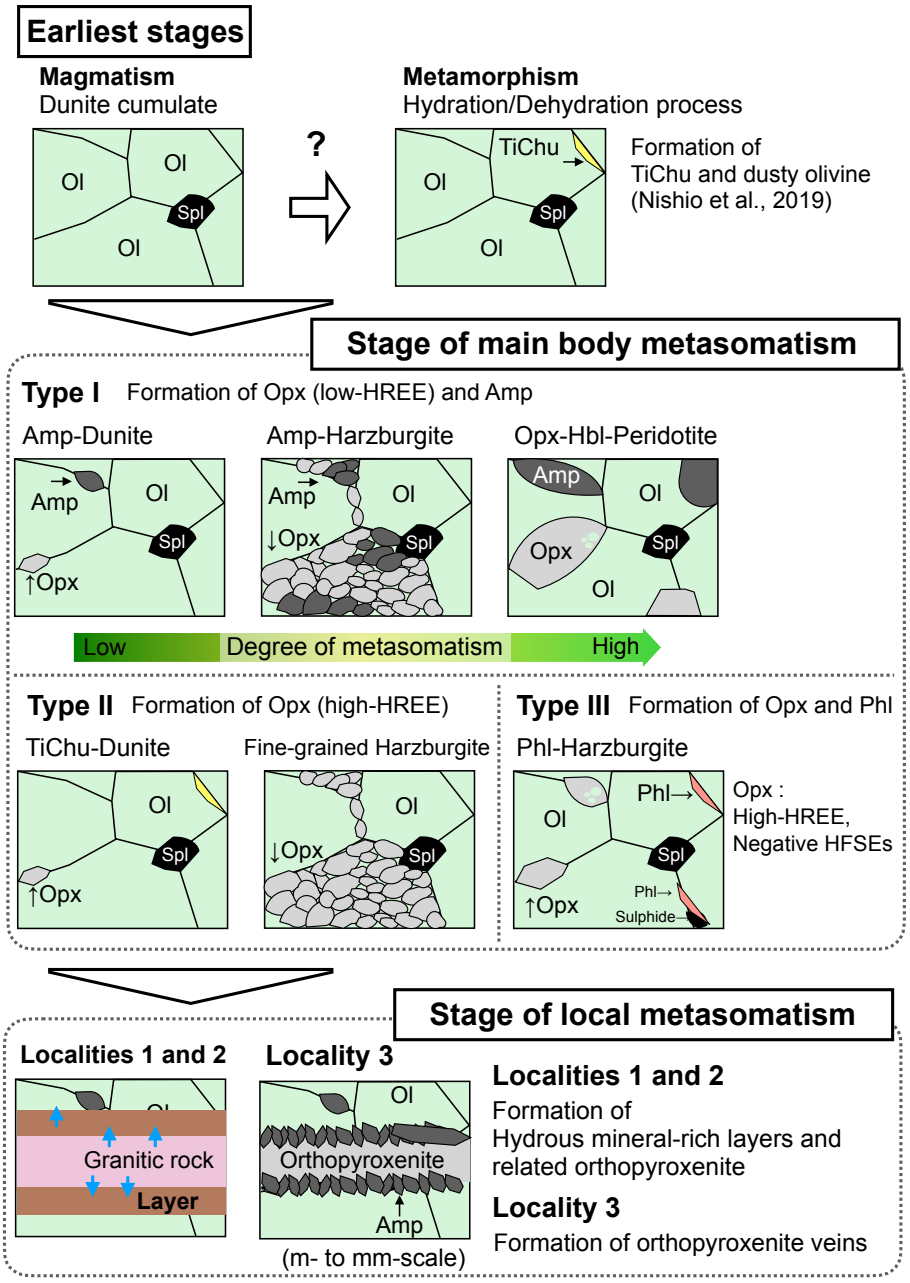

Figure 37: Schematic illustration of the evolution of the Mesoarchean Ulamertoq ultramafic rocks. The origin of the ultramafic rocks is most probably cumulative, from mantle-derived melts. One of the least-metasomatized dunites contains titanian clinohumite (TiChu). TiChu-Dunite records a hydration/dehydration process (Nishio et al., 2019). The extent of the area that may have been affected by this metamorphism of hydration/dehydration is still unknown, but the metamorphism probably occurred before the following metasomatic events. The stage of main body metasomatism is a major event. It formed secondary orthopyroxene and/or hydrous minerals in the main body ultramafic rocks. The metasomatism was probably caused by surrounding crustal rocks (norite or orthogneiss). It is noteworthy that most of the orthopyroxene in the main body formed by this metasomatism. However, we cannot rule out the possibility that the orthopyroxene in Type II (amphibole-free peridotites) is a product of cumulus-melt reaction in the late magmatic stage. Finally, local metasomatism occurred on the meter-to-millimeter scale related to numerous late granitic intrusions from the surrounding orthogneiss. The stage of the local metasomatisms has two types, (a) the formation of hydrous mineral-rich layers and associated orthopyroxenite (e.g. Localities 1 and 2) and (b) the formation of orthopyroxenite veins (e.g. Locality 3).

4.8 Conclusion

The petrology and mineral chemistry of the largest Mesoarchean body—the Ulamertoq ultramafic rocks—from SW Greenland demonstrate that the body was formed by cumulate igneous processes, in the crust and that it experienced multi-stage metasomatic and metamorphic events related to interaction with the surrounding crustal rocks. These events strongly modified the primary compositions as follows.

Meter-to-millimeter scale local metasomatic zonation formed near the boundaries with country rock orthogneiss and invading granitic sheets. The lithologies formed mostly from multiple infiltration event involving metasomatic agents that evolved in their composition. The compositions of the resulting metasomatic lithologies reflect the compositional differences of close to the main body ultramafic rocks. The local metasomatic activity is the latest event recorded in the mineralogical evolution of the Ulamertoq body, occurring after metasomatism of the main body ultramafic rocks.

The metasomatism affecting the main body occurred under granulite-to-amphibolite facies conditions. Tremolite-bearing peridotite and phlogopite-bearing harzburgite record later retrograde conditions at 650ºC –750ºC and < 1.8 GPa and 650◦ C–850ºC and < 1.5 GPa, respectively. We conclude that the geochemical and lithologic variations in the Ulamertoq ultramafic body resulted primarily from the secondary addition of orthopyroxene ± hydrous minerals to cumulative dunitic protoliths by metasomatic agents derived the surrounding crust.

Titanian clinohumite and related mineral assemblages in the least-metasomatized sample and magnetite inclusions in olivine in some samples suggest that the ultramafic body probably experienced hydration (serpentinization) followed by dehydration (deserpentinization) processes at ~800ºC –900ºC and < 2 GPa before the main metasomatic events (Nishio et al., 2019).

Most of the Archean ultramafic bodies from SW Greenland are small and have comparable mineral assemblages and chemistry to the peridotites from Ulamertoq, indicating that they experienced significant metasomatic modification. The lithological and compositional variations are observed not only in the Archean ultramafic rocks of SW Greenland but also other ultramafic bodies exposed in crustal materials. Therefore, it is critical to account for the extensive interaction of these ultramafic bodies with crustal rocks when interpreting the geochemical signatures of these rocks.

Chapter 5

5 Komatiitic layered intrusions as a missing complement to depleted cratonic mantle

5.1 Introduction

Archean to Proterozoic layered intrusions represent major igneous plumbing systems are crucial to understanding early Earth magmatism (Kamber and Tomlinson, 2019; Latypov et al., 2013; Yao et al., 2021). Ultramafic rocks, including chromitite from layered intrusions, are products of early crystallization from primitive parental magmas (Yudovskaya et al., 2015). However, constraining the parental magma composition of these layered intrusions remains challenging. Both boninitic and komatiitic parental magmas have been suggested, respectively implying subduction zone or plume settings (e.g., Barnes, 1989; Godel et al., 2011; Mondal et al., 2019; Yao et al., 2021). Therefore, the parental magma composition of these layered intrusions is crucial for understanding the geodynamics of early Earth.

Spinel in chromitite and host ultramafic rocks is a useful petrological indicator of igneous, metamorphic, and metasomatic processes (Arai, 1994; Barnes and Roeder, 2001; Irvine, 1965; Staddon et al., 2021). Chromitite is less susceptible to alteration compared to peridotite, which makes it a good indicator for identifying parental magma compositions, although its formation process is still controversial.

Ultramafic rocks are ubiquitously exposed within the Archean geological units of southern West (SW) Greenland. Although these ultramafic rocks often undergone metamorphism and metasomatism (e.g., Guotana et al., 2022; Nishio et al., 2022b), they provide clues to the condition of the early Earth's mantle, crust, and tectonics (Friend et al., 2002; van de Löcht et al., 2018; Waterton et al., 2022; Zemeny et al., 2023; Zhang and Szilas, 2024).

One of the oldest known chromitites occurs in the Ujaragssuit Nunât layered body from SW Greenland (Appel et al., 2002; Chadwick and Crewe, 1986; Coggon et al., 2015, 2013; Fischer-Gödde et al., 2020; Rollinson et al., 2002). Rollinson et al. (2002) analyzed spinel compositions across various lithologies from the Ujaragssuit body, and identified a wide range of spinel compositions reflecting igneous and metamorphic processes. They interpreted the body to be part of layered intrusion formed

from a high- Mg and Cr magma. However, the exact nature of the parental magma, whether boninitic or komatiitic, remains elusive.

We present spinel major and trace element and whole-rock PGE compositions from the Ujaragssuit ultramafic body in order to constrain both primary igneous and secondary metamorphic and metasomatic processes. We apply independent component analysis to a large database of spinel compositions from different parental magmas and tectonic settings to identify key geochemical discriminators between different parental magma types. Finally, we apply this discrimination scheme to Ujaragssuit compositions and compiled data on other Archean to Proterozoic layered intrusion chromitites to investigate their parental magma compositions and tectonic settings.

5.2 Geological setting

Part of the North Atlantic Craton (NAC) is exposed in SW Greenland (Figure 38a) (Friend et al., 1988), where numerous ultramafic rocks are sparsely distributed within Archean gneisses in SW Greenland (e.g., Chadwick and Crewe, 1986; Dymek et al., 1988). The Ujaragssuit ultramafic body is 100 m x 600 m and consists mostly of peridotite and chromitite (Figure 38b and c). The body is hosted by the >3.8 Ga gneiss and is crosscut by 2.97 Ga granitic intrusions (Chadwick and Crewe, 1986; Crewe, 1984). Field observation and spinel major element compositions suggest that the body is part of a layered igneous complex and underwent amphibolite-facies metamorphism (Appel et al., 2002; Rollinson et al., 2002).

The geochronology of this body remains controversial. The body was previously thought to preserve a mantle depletion Os isotopic model age of 4.1 Ga and experienced later -3.7 Ga and -2.8 Ga metamorphisms based on Os and Pb isotopic works, spinel chemistry, and field relationship (Coggon et al., 2013; Rollinson et al., 2002). However, a recent study has suggested 3.2 Ga igneous age and subsequent metamorphism at 2.97 Ga based on U-Pb ages and Hf model ages of zircon found from chromitites (Sawada et al., 2023). In either case, the Ujaragssuit body contains one of the oldest chromitites on Earth.

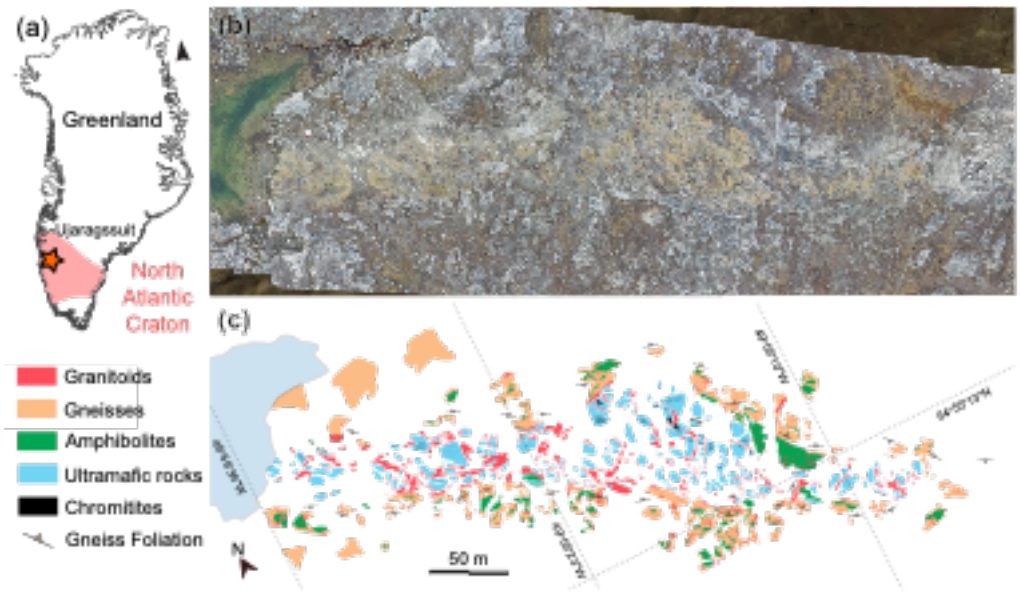

Figure 38: (a) Location of the Ujaragssuit Nunât (Ujaragssuit) layered body in Greenland. (b) Drone image and (c) a detailed geological map of the Ujaragssuit intrusion.

5.3 Sample occurrence and petrography

5.3.1 Occurrence

The ultramafic rocks are surrounded by orthogneiss; however, we did not observe that ultramafic rocks are in direct contact with orthogneiss. Instead, ultramafic rocks are separated and wrapped by 0.1 m to 10 m wide granitoid sheets (Figure 38b, c and Supplementary Figure A16).

The ultramafic body is mainly composed of amphibole and/or phlogopite-peridotite which are dunite alternating to peridotite. Based on mineral assemblages and chemistry, we grouped these into amphibole-peridotite (Amp-Peridotite) and phlogopite-peridotite (Phl-Peridotite). Chromitites occur as massive pods or thin layers hosted by Phl-Peridotites. Massive chromitites are 0.5–3 m thick and are observed in the northern part of the body (Figure 38b and c). Layered chromitites are 1–20 cm thick and are observed in the western part (Figure 38b and c). The host lithology of layered chromitite gradually changes from spinel-rich Phl-Peridotite to spinel-poor Amp-Peridotite in cm–m size away from the chromitite layer (Supplementary Figure A16).

Various younger lithologies are observed in cm–m size associated with the granitoid sheets (Supplementary Figure A16). These are orthopyroxenites, hydrous mineral-rich layers, and amphibolites that sometimes contain corundum. Orthpyroxenites often occur as veins crosscutting the main

peridotites. The hydrous mineral-rich layers consist of the phlogopite zone, anthophyllite zone, and talc-carbonate zone from granitoid to peridotite. The hydrous mineral-rich rocks between chromitites and granitoid sheets are green-colored amphibole rocks.

5.3.2 Petrography

Massive chromitite consists of spinel (average 92 vol.%) with the interstitial presence of phlogopite, chlorite, and/or talc. Ni-sulfide mineral is rarely observed. Layered chromitite consists of spinel (30–93 vol.%), phlogopite, chlorite, and/or olivine. Spinel in chromitite is generally homogeneous (Figure 39a).

Phl-Peridotite mainly consists of olivine, spinel, and phlogopite, with minor amounts of amphibole, chlorite, orthopyroxene, and talc. Phlogopite is often associated with spinel (Figure 39b). Amp-Peridotite mainly consists of olivine, spinel, and amphibole with minor amounts of orthopyroxene, phlogopite, and chlorite. Phl-Peridotite generally contains homogeneous spinel, but Amp-Peridotite contains heterogeneous spinel, which shows both Al-rich and Fe-rich phases (Figure 39c). The texture and proportions of these two phases vary between spinel grains, even within a single Amp-Peridotite sample. Spinel from one layered chromitite occurring near a granitoid sheet is also heterogeneous and shows multiple phases (Figure 39d).

Cross-cutting orthopyroxenites consist mainly of orthopyroxene and amphibole. Spinel in these samples exhibit variable textures: spinel from orthopyroxenite veins that crosscut Amp-Peridotite tends to be heterogeneous (Figure 39e), while spinel from orthopyroxenite that cross-cuts Phl-Peridotite tends to exhibit Fe-rich compositions. Talc-carbonate rock, occurring between peridotites and granitoid sheets, contains a minor amount of Fe-rich spinel (Figure 39f). Green-amphibole rock, occurring between chromitite and granitoid rock, is dominated by amphibole and spinel with minor amount of phlogopite (Figure 39g).

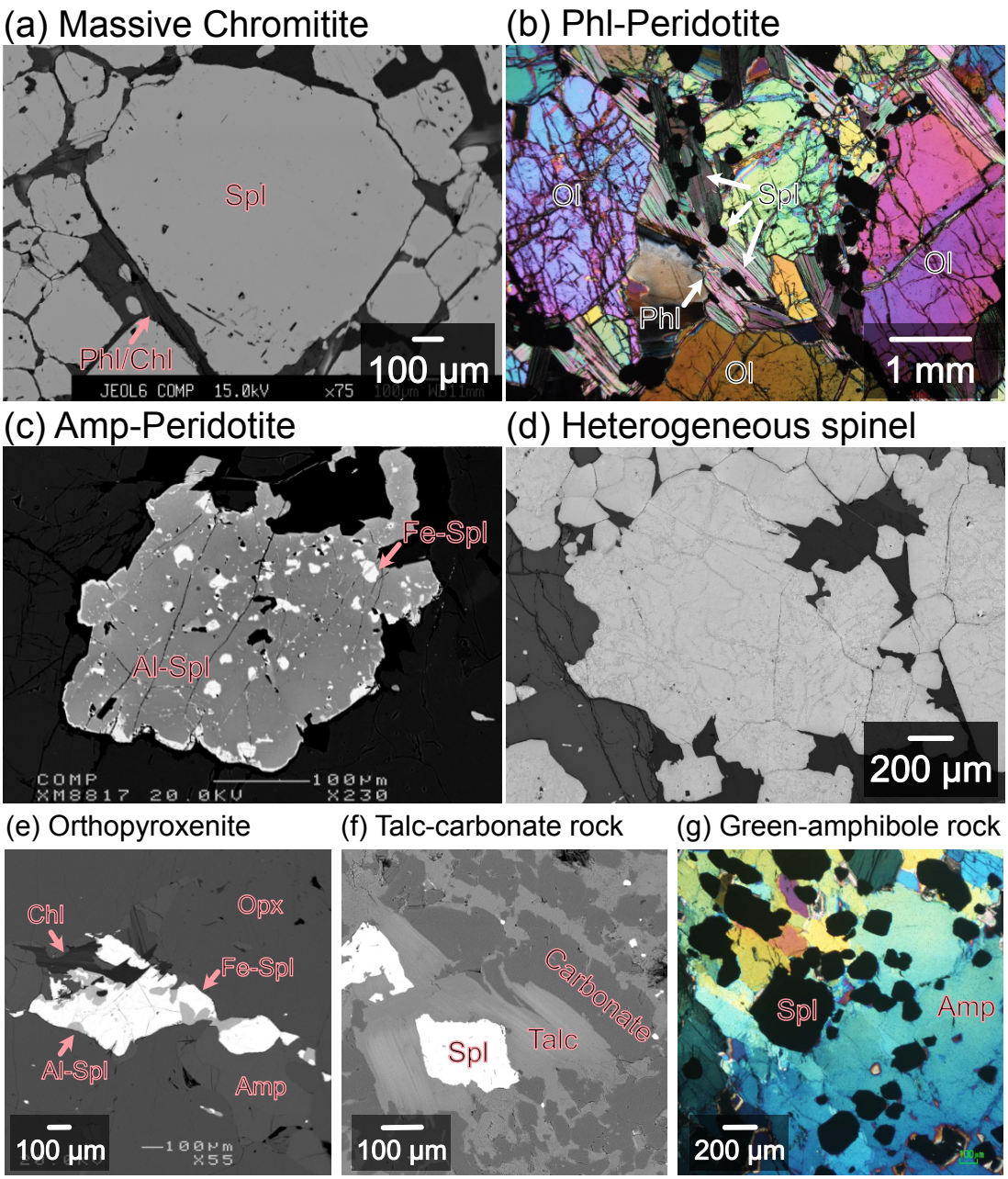

Figure 39: Photomicrographs of the Ujaragssuit ultramafic rocks. (a) Spinel (Spl) and interstitial phlogopite/chlorite (Phl/Chl) in massive chromitite. (b) Phlogopite peridotite (Phl-Peridotite), which hosts chromitite, consisting of olivine (Ol), and spinel associated with phlogopite. (c) Heterogeneous spinel from amphibole peridotite (Amp-Peridotite) showing Al-rich phase (Al-Spl) and Fe-rich phase (Fe-Spl). (d) Heterogeneous spinel from one layered chromitite, which occurs near granitoid sheet, showing complex texture and multiple phases. (e) Spinel from orthopyroxenite vein cutting Amp-Peridotite showing Al-rich phase and Fe-rich phase which often surrounded by chlorite. (f) Spinel from talc-carbonate rock. (g) Abundant spinel grains in the green-amphibole rock.

5.4 Methods

Major element compositions of minerals were analyzed for 37 samples using electron probe microanalyzers, a JEOL JXA-8800 at Kanazawa University, and a JEOL JXA-8200 at the University of Copenhagen. Trace element compositions of spinel were analyzed for 6 chromitite samples using 193 nm ArF excimer laser ablation-inductively coupled plasma-mass spectrometry (LA-ICPMS, Agilent 7900 equipped with Teledyne Photon Machines Analyte Excite) at the University of Copenhagen. Whole-rock platinum-group element (PGE) compositions for 19 samples were obtained at Université du Québec à Chicoutimi by NiS-FA pre-concentration and measurement by ICPMS (Thermo Elemental X7 series; Thermo Fisher Scientific). Full details of the analytical methods and representative data are available in supplementary information 8.4.

5.5 Results

5.5.1 Spinel major element compositions

Spinel from massive chromitite is grouped into two clusters (Figure 40a and b). One cluster contains low $Fe^{3+}/(Fe^{3+}+Cr+Al)$ (0.11 ± 0.01, average ± 2*standard deviation) and high Mg# [=Mg/(Mg+Fe^{2+})] (0.45 ± 0.07). It also shows high Cr# [=Cr/(Cr+Al)] (0.73 ± 0.04) and low TiO_2 (0.24 ± 0.14 wt.%). The other cluster has higher $Fe^{3+}/(Fe^{3+}+Cr+Al)$ (0.21 ± 0.02) and TiO_2 (0.34 ± 0.34 wt.%), and lower Mg# (0.32 ± 0.04) and Cr# (0.67 ± 0.08) than those of the low $Fe^{3+}/(Fe^{3+}+Cr+Al)$ cluster.

Spinel from layered chromitite shows high $Fe^{3+}/(Fe^{3+}+Cr+Al)$ (0.28 ± 0.06), TiO_2 (0.58 ± 0.24 wt.%), and Cr# (0.76 ± 0.12) and low Mg# (0.25 ± 0.08) (Figure 40a and b). The heterogeneous spinel-bearing layered chromitite has distinctive spinel compositions although we were not able to obtain the compositions of the separate phases due to the ubiquitous nature and small size of the multiple spinel phases. The mixed spinel compositions show low $Cr/(Fe^{3+}+Cr+Al)$ (0.36 ± 0.11) and form a linear array on a trivalent ternary plot ranging from 0.18 to 0.75 for $Fe^{3+}/(Fe^{3+}+Cr+Al)$ (Figure 40a and b).

Spinel from peridotite exhibits variable compositions (Figure 40c and d). Phl-Peridotite, which hosts chromitite, has high $Cr/(Fe^{3+}+Cr+Al)$ (>0.5) spinel akin to those from layered chromitite. Spinel from Phl-Peridotite shows wide ranges of $Fe^{3+}/(Fe^{3+}+Cr+Al)$ (0.27 ± 0.16), TiO_2 (0.58 ± 0.24 wt.%) and Cr# (0.8 ± 0.16), with low Mg# (0.21 ± 0.16). Phl-Peridotite sometimes contain Fe-rich spinel, which has high $Fe^{3+}/(Fe^{3+}+Cr+Al)$ (0.73 ± 0.1) with very low Mg# (0.05 ± 0.02). One Phl-Peridotite sample which does not host chromitite has different spinel composition which shows low $Cr/(Fe^{3+}+Cr+Al)$ (0.43 ± 0.02) and Cr# (0.55 ± 0.02). Spinel in Amp-Peridotite is separated into an Fe-rich phase

[Fe^{3+}/(Fe^{3+}+Cr+Al) = 0.72 ± 0.14] and an Al-rich phase [Fe^{3+}/(Fe^{3+}+Cr+Al) = 0.12 ± 0.04] within single grains. Both phases have low Cr/(Fe^{3+}+Cr+Al) (0.25 ± 0.12).

Orthopyroxenite also shows a wide range of spinel compositions (Figure 40e and f). Spinel from orthopyroxenite occurring near chromitite-hosting Phl-Peridotite shows high Fe^{3+}/(Fe^{3+}+Cr+Al) (0.6 ± 0.2) and Cr/(Fe^{3+}+Cr+Al) (0.37 ± 0.18). Spinel from the orthopyroxenite cutting the Phl-Peridotite which does not host chromitite shows slightly lower Cr/(Fe^{3+}+Cr+Al) (0.33 ± 0.06) than those occurring near chromitite-hosting Phl-Peridotite. Orthopyroxenite cutting or occurring near Amp-Peridotite contain inhomogeneous spinel, similar to those seen in the Amp-Peridotite. This spinel shows low Cr/(Fe^{3+}+Cr+Al) (0.16 ± 0.14).

Spinel in green-amphibole rock has similar Fe^{3+}/(Fe^{3+}+Cr+Al) (0.11 ± 0.02) to spinel from the host massive chromitite, but it has higher Cr# (0.81 ± 0.04) with lower Mg# (0.10 ± 0.08) than spinel from the host chromitite (Figure 40e and f). The talc-carbonate rock sample is adjacent to Phl-Peridotite (Supplementary Figure A16). Spinel in talc-carbonate rock has a magnetite composition [Fe^{3+}/(Fe^{3+}+Cr+Al) = 0.93], while spinel in the adjacent Phl-Peridotite has a similar Cr/(Fe^{3+}+Cr+Al) (0.51) to spinel from Phl-Peridotite but higher Fe^{3+}/(Fe^{3+}+Cr+Al) (0.44).

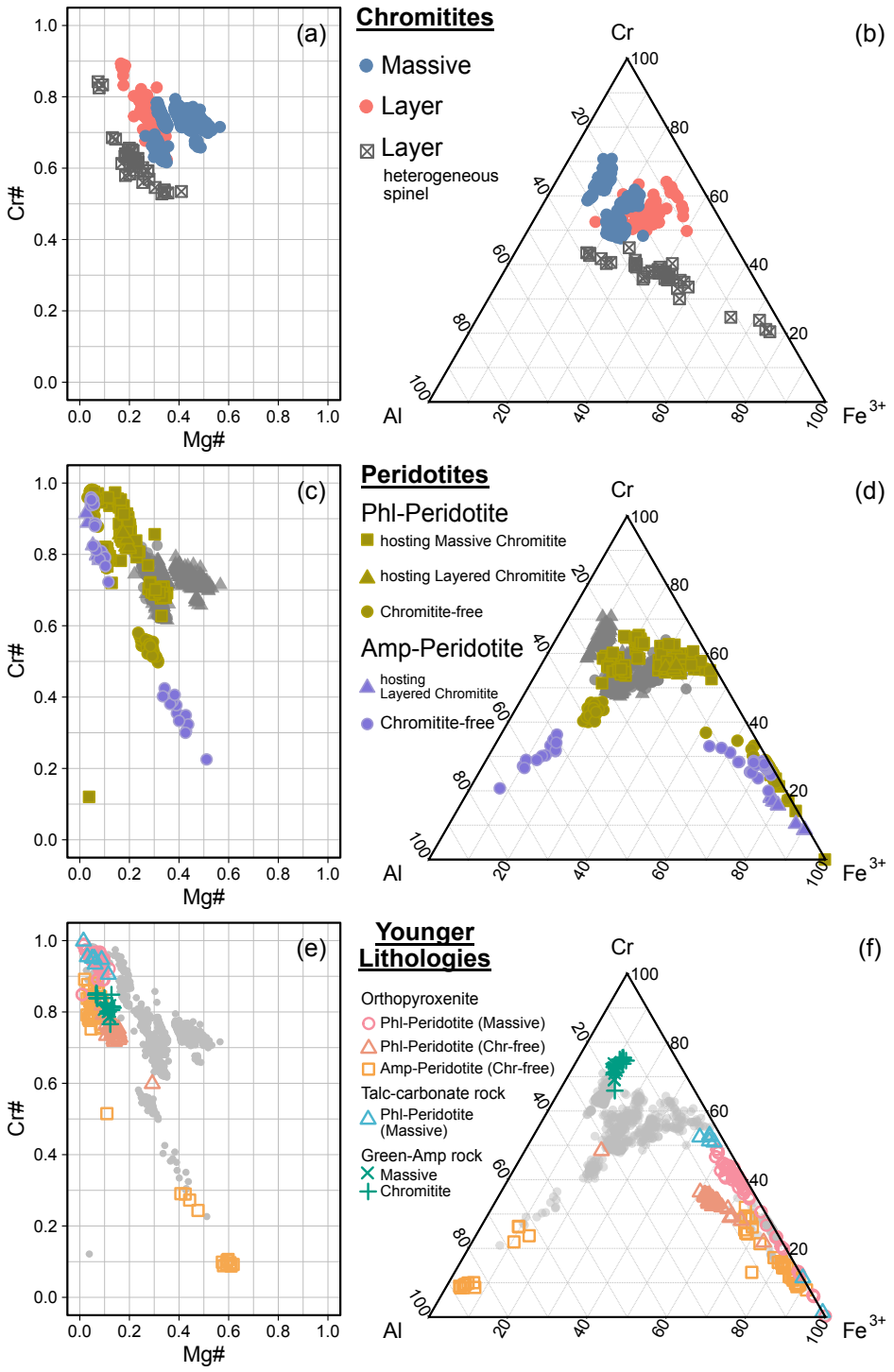

Figure 40: Spinel Cr# [=Cr/(Cr+Al)] against Mg# [=Mg/(Mg+Fe)] and ternary plots. (a, b) Spinel from massive and layered chromitite, (c, d) spinel from Phl-Peridotite, and Amp-Peridotite. Gray points are spinel compositions from chromitite except for heterogeneous layered chromitite. (e, f) spinel from younger lithologies. For orthopyroxenite, Phl-Peridotite (Massive) representing for orthopyroxenite occurring near Phl-Peridotite hosting massive chromitites, Phl-Peridotite (Chr-free) representing for orthopyroxenite occurring near Phl-Peridotite which does not host chromitites, Amp-Peridotite (Chr-free) representing orthopyroxenite occurring near Amp-Peridotite which does not host chromitite. Light gray points are spinel compositions from chromitite and peridotite except for inhomogeneous layered chromitite.

5.5.2 Spinel trace element compositions

We analyzed Ga, Ti, Ni, Zn, Co, Mn, V, and Sc in spinel from 6 chromitite samples. Spinel generally contains over 1000 ppm of Ti (1368–2517 ppm), Ni (797–1294 ppm), Zn (1281–3170 ppm) and Mn (2297–3063 ppm) while exhibiting relatively lower concentrations of Ga (30–41 ppm), V (493–940 ppm), and Sc (4–5 ppm).

When we normalized our spinel data using spinel composition from mid-ocean ridge basalt (MORB) (Pagé and Barnes, 2009), Ga, Ti, Ni, and Sc show similar values to MORB spinel, but Zn, Co, and Mn show elevated values (Figure 41a). Zn shows a clear positive correlation with $Fe^{3+}/(Fe^{3+}+Cr+Al)$ (Figure 41a). Ti also shows a positive correlation with $Fe^{3+}/(Fe^{3+}+Cr+Al)$ but chromitite which has high Cr# - Mg# - low $Fe^{3+}/(Fe^{3+}+Cr+Al)$ spinel shows constant Ti. V in spinel remains consistent regardless of differences in major element composition except for one sample which has high spinel $Fe^{3+}/(Fe^{3+}+Cr+Al)$.

5.5.3 Whole-rock PGE compositions

Chondrite (Fischer-Gödde et al., 2010) normalized PGE patterns of chromitite shows high Ir, Ru, and Rh, but low Pt and Pd values (Figure 41b). Most peridotites have similar PGE patterns with low Ir, Ru, and Rh but high Pt and Pd values (Figure 41b). Two peridotite samples show different patterns that are low in Pt and Pd. Orthopyroxenite shows various patterns, one shows a similar pattern to peridotite, one has low Ir values, and one has high Pt value.

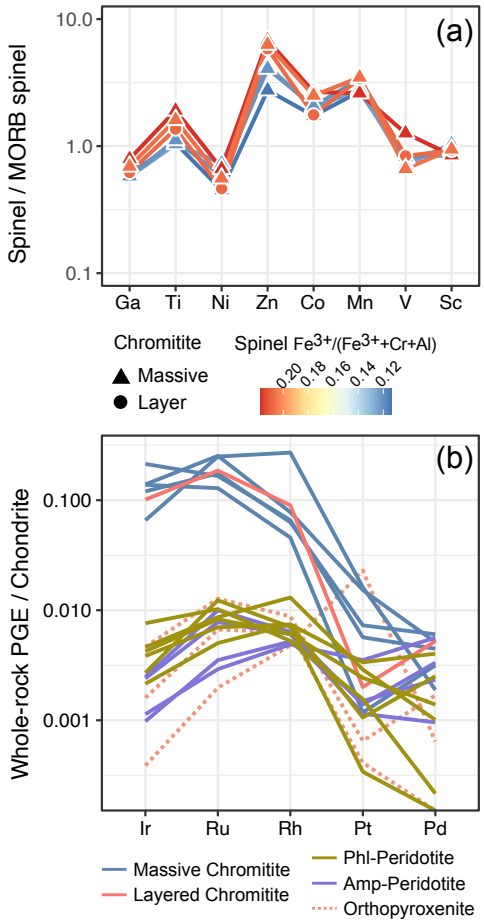

Figure 41: Spinel trace element and whole-rock PGE data. (a) mid-ocean ridge basalt (MORB) spinel-normalized (Pagé and Barnes, 2009) spinel trace element patterns from massive and layered chromitite. Color scale indicates spinel $Fe^{3+}/(Fe^{3+} + Cr + Al)$. (b) Chondrite-normalized (Fischer-Gödde et al., 2010) PGE patterns for chromitite, peridotite and orthopyroxenite.

5.6 Discussion

Due to the amphibolite-facies metamorphism displayed in the region (Rollinson et al., 2002), and the occurrence of numerous younger cross-cutting lithologies, it is highly likely that the spinel composition has undergone some degrees of modification. We therefore first discuss the influence of metasomatic and metamorphic overprints on the spinel compositions, before using the least modified spinel compositions to address the origins of the chromitite.

5.6.1 Younger metamorphic/metasomatic modification

Orthopyroxenite often occurs as a vein crosscutting the main peridotite. Spinel Cr/(Fe^{3+}+Cr+Al) is higher from orthopyroxenite occurring near chromitite-hosting Phl-Peridotite, than either orthopyroxenite occurring Phl-Peridotite without chromitite or orthopyroxenite adjacent to Amp-Peridotite (Figure 40f). Amp-Peridotite and orthopyroxenite occurring near Amp-Peridotites contain inhomogeneous spinel (Figure 39). These systematic differences suggest that spinel textures and spinel Cr/(Fe^{3+}+Cr+Al) primarily depend on their host peridotite compositions. Similar orthopyroxenite occurrences in other Archean ultramafic bodies also show Mg# and HREE systematics that reflect their host peridotite compositions (Nishio et al., 2022b). This suggests that the orthopyroxenites largely inherit the Cr/(Fe^{3+}+Cr+Al) of their host peridotite (protolith) during the secondary formation of orthopyroxenite.

Spinel in the peridotite adjacent to the talc-carbonate rock shows similar Cr/(Fe^{3+}+Cr+Al) to those from Phl-Peridotite but more enriched in the magnetite component (Figure 40f). Spinel from talc-carbonate rock has a magnetite composition. Therefore, either primary spinel compositions were oxidized and modified to a magnetite composition, or spinel became unstable and was replaced by magnetite during the formation of hydrous mineral-rich layers. The association of these layers with cross-cutting granitoids suggests these resulted from the reaction between peridotite and fluid originating from the intrusive granitoid sheets (Nishio et al., 2022b).

Spinel in green-amphibole rock shows higher Cr# and lower Mg# than those in the host massive chromitite (Figure 40f). This indicates that Cr# and Mg# were increased during the formation of the amphibole. We therefore conclude that spinel from these younger lithologies records a variety of metasomatic and metamorphic processes, but does not preserved primary igneous processes.

5.6.2 Older metamorphic/metasomatic modification

5.6.2.1 Secondary formation of phlogopite and amphibole

Spinel composition in peridotite and chromitite tends to vary depending on its co-occurrence with phlogopite and/or amphibole (Figure 40). The formation of these hydrous minerals is key to understanding whether how the observed diverse spinel compositions reflect secondary overprinting.

Phlogopite is an interstitial phase in the massive chromitites that lack olivine (Figure 39a). Phlogopite is also generally associated with spinel, either within the layered chromitites or in Phl-Peridotites adjacent to massive or layered chromitites (Figure 39b). By contrast, amphibole is generally observed in peridotites further from chromitite contacts, with the exception of the green amphibole rock. Both phlogopite and amphibole have low TiO_2 contents (<1 wt.%, Rollinson et al., 2002). This is distinct to igneous phlogopite and amphibole, which generally have high TiO_2 contents (>1 wt.%) and crystallize

after olivine and spinel (Bucholz et al., 2014; Itano et al., 2021). Therefore, we suggest that these hydrous minerals were formed during metamorphism, likely through consuming preexisting olivine and/or orthopyroxene (Rollinson et al., 2002).

Spinel mode gradationally decreases from the layered chromitite, Phl-Peridotite to Amp-Peridotite on a cm–m scale in one occurrence (Supplementary Figure A16). This, along with the association of phlogopite with chromitites, may suggest that the formation of either amphibole or phlogopite during metamorphism is governed by the spinel mode in the protolith. Al is relatively immobile during metamorphism, so we suggest that spinel acts as a local Al-source during metasomatic alteration of the protoliths, such that chromitites and peridotites with abundant spinel produce Al-rich phlogopite when reacted with metamorphic fluids. By contrast, spinel-poor peridotites have insufficient Al to produce phlogopite, and Al-poor compositions favor the formation of amphibole as a hydrous mineral (Grant et al., 2014). The metamorphic assemblage therefore in part reflects primary modal differences in the protoliths. However, in the entire intrusion scale, a clear correlation between spinel mode and hydrous mineral mode are not shown. This suggests that both diversity in the original mineral modal abundances, and differences in both the extent of metasomatism and composition of metasomatic agents (Nishio et al., 2022b), caused the diversity in mineral assemblage and composition in the Ujaragssuit intrusion.

5.6.2.2 Modification of spinel composition in Amp-Peridotite

Spinel in Amp-Peridotite is characterized by inhomogeneous spinel showing Al-rich and Fe-rich phases (Figure 39c). The heterogeneous spinel is also observed in one layered chromitite and orthopyroxenite near Amp-Peridotite (Figure 39d and e). $Cr/(Fe^{3+}+Cr+Al)$ in spinel from Amp-Peridotite is low and almost equivalent between contiguous phases of each grain (Figure 40d). The compositional immiscibility of two/multi-phase spinel in the ultramafic rocks are frequently reported, they all agree that these were not formed during the igneous process (Ahmed et al., 2008; Colás et al., 2020; Loferski and Lipin, 1983; Tamura and Arai, 2005).

Previous studies interpreted that spinel composition shows two trends (Appel et al., 2002; Rollinson et al., 2002): one shows a trend from high Cr spinel in massive chromitite to Fe-phase of inhomogeneous spinel in Amp-Peridotite. The other shows a trend from high Cr spinel to Al-phase of inhomogeneous spinel in Amp-Peridotite. These Al-rich and Fe-rich spinel compositions are compositions of Fe-phases and Al-phases in a single grain (Figure 39c). If these compositional variations show magmatic trends, spinel is expected to have high TiO_2 contents (Barnes and Roeder, 2001). However, spinel in the Ujaragssuit body is low in TiO_2 (average 0.48 wt.%). Therefore, it is unlikely to that these trends are magmatic. The subsolidus exsolution due to compositional immiscibility is most likely to be the origin of the inhomogeneous spinel and these spinel compositional variations were attributed to secondary processes during metamorphism and/or metasomatism.

5.6.2.3 *Modification of spinel composition in Phl-Peridotite*

Total Fe in spinel and silicate minerals mode show an increase from massive chromitite to layered chromitite and Phl-Peridotite while spinel Cr/(Fe^{3+}+Cr+Al) remains constant (Figure 40b and d). This can be attributed to subsolidus Mg-Fe^{2+} exchange, which depends on the silicate/spinel ratio. Higher silicate/spinel ratios result in lower Mg# in spinel. Fe^{3+} also increases in correlation with Fe^{2+}. This suggests that Fe^{2+} contents in spinel were increased due to Mg-Fe^{2+} exchange and the increased Fe^{2+} was subsequently oxidized to Fe^{3+} during the metasomatism. Therefore, the metasomatic hydrous agent which caused the formation of phlogopite also appears to have oxidized spinel. We conclude that spinel compositions in layered chromitite and Phl-Peridotite are also affected by metamorphic and metasomatic overprints.

5.6.3 *Origin of the Ujaragssuit ultramafic intrusion*

5.6.3.1 *Primary igneous composition preserved in massive chromitite*

Although all of the Ujaragssuit ultramafic rocks experienced metamorphic and metasomatic overprints, spinel from massive chromitite has low Fe^{3+}/(Fe^{3+}+Cr+Al), and high Mg# and Cr#. We interpret this to indicate that the effect of secondary modification is minimal (Rollinson et al., 2002), and that the massive chromitite spinel major element compositions were least affected by metamorphism.

The trace element composition of spinel is sensitive to differences in parental magma composition and formation tectonics (e.g., González-Jiménez et al., 2014). However, trace element compositions should be used with care because divalent cations such as Zn and Mn have relatively high diffusion rates and are susceptible to modification during metamorphism (e.g., Colás et al., 2020; Staddon et al., 2021). In the Ujaragssuit chromitite, spinel Zn concentrations increase with Fe^{3+}/(Fe^{3+}+Cr+Al) (Figure 41a). This suggests that this element, and potentially other divalent cations, may have been modified during metasomatism and metamorphism. In contrast, Ti, V^{3+} and V^{4+} have lower diffusion rates and are expected to be less susceptible to disturbance (Sievwright et al., 2020). Spinel from massive chromitite, which retains low Fe^{3+}/(Fe^{3+}+Cr+Al) and high Mg# and Cr#, has indeed constant V and Ti concentrations (Figure 41a). The PGE patterns in Ujaragssuit chromitite samples are also relatively constant (Figure 41b) and do not show clear correlations with spinel Fe^{3+}/(Fe^{3+}+Cr+Al). Ti, V, and PGE composition from massive chromitites therefore also appear to preserve igneous compositions.

5.6.4 Classifying the Ujaragssuit chromitite using a multivariate statistical analysis

Here we re-evaluate the origin of the Ujaragssuit chromitite using multivariate statistical analysis (Itano et al., 2023; Nishio et al., 2022a). We conducted independent component analysis (ICA) on log-transformed spinel major element compositions to reduce the dimensionality of dataset while preserving as much information as possible. Log-transformation is an important step for the treatment of compositional data as they emphasize relative magnitudes and variations in components rather than absolute values.

We collected the spinel data (spinel major and trace elements and whole-rock PGE compositions) in high-Cr chromitite (spinel Cr# > 0.6) hosted by ultramafic rock from the Archean to Proterozoic layered intrusions, from mantle section of supra-subduction zone (SSZ) ophiolites, and spinel from komatiite, picrite and boninite (Figure 42). We collated spinel major element data (n = 7611), comprising our dataset (n = 3369) and Barnes and Roeder (2001)'s boninitic and komatiitic spinel dataset (n = 4242). For our dataset, we excluded data that have either lower Mg# (<0.4) or higher $Fe^{3+}/(Fe^{3+} + Cr + Al)$ ratio (>0.16) because these likely reflect metamorphic processes. Many komatiites have also undergone metamorphism, which resulted in their spinel composition being enriched in Fe (Barnes and Roeder, 2001). Therefore, we also excluded spinel data that have either lower MgO (<5 wt.%) or higher $Fe^{3+}/(Fe^{3+} + Cr + Al)$ ratio (>0.16) from Barnes and Roeder (2001)'s dataset. We then screened to include only spinel data for the elements TiO_2, Fe_2O_3, FeO, MgO, Al_2O_3, and Cr_2O_3. This is because these were the only elements analyzed for most samples in the database and compositional data statistical analysis cannot be performed on a dataset with missing values. This screening results in 4732 remaining spinel analyses. The method and references for compiled data are given in supplementary information 8.4 and Figure A17.

ICA, a statistical method, reveals sources and factors underlying the distribution of multivariate observations. In geochemical applications of ICA, source materials and processes with independent geochemical signatures can be identified as ICs (IC1, IC2, etc). ICs are chosen to describe the largest amount of variability in the data. The results of the ICA identify that IC1 is mainly controlled by varying MgO/TiO_2 at a similar Cr# (Figure 42 and Supplementary Figure A18). This implies that MgO and TiO_2 contents are important variables to classify high Cr# chromitites, in line with previous findings (Barnes and Roeder, 2001).

Spinel from the Ujaragssuit massive chromitites shows similar IC1 values to those of other layered intrusion chromitites, on the other hand, IC1 shows a clear difference from those of SSZ ophiolite chromitites (Figure 42a). Indeed, MgO content distinguishes between spinel from layered intrusion chromitites and SSZ ophiolite chromitites (Figure 42b). Spinel from layered intrusion chromitites generally have lower MgO compared to those from SSZ ophiolite chromitites, as previously identified (Barnes and Roeder, 2001). For high-Mg and Cr magma such as komatiite, olivine crystalizes

before spinel (e.g., Yao et al., 2021). The MgO in parental magma is therefore consumed by olivine crystallization before the crystallization of spinel. This low MgO indicates that chromitite from the ultramafic (dunitic) layers of layered intrusions were a product of the crystallization of olivine and spinel with the subsequent mechanical sorting of spinel leading to the chromitite formation (Barnes et al., 2023). The observed Ni negative anomaly in potentially supports the hypothesis of co-crystallization with olivine (Figure 41a).

ICA, therefore, correctly classifies the Ujaragssuit chromitites as having formed in a layered intrusion, consistent with previous work (Rollinson et al., 2002).

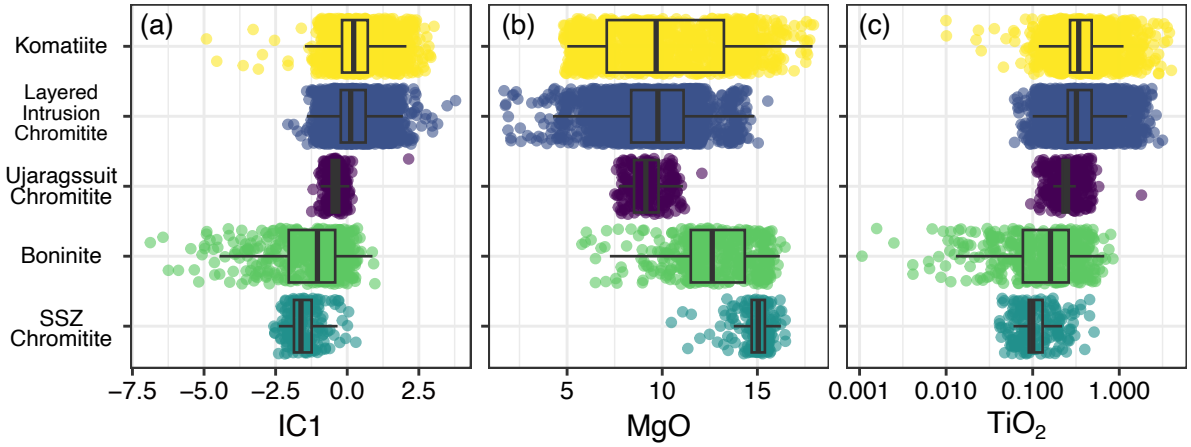

Figure 42: Compiled spinel major elements data for high Cr# chromitites. (a) Independent Component value (IC1) obtained by independent component analysis of spinel major element compositions. (b) MgO contents (c) TiO_2 contents. Compiled data and all references are given in the supplementary information 8.4.

5.6.5 Archean to Proterozoic layered intrusion chromitites originated from komatiitic magma

5.6.5.1 Komatiitic parental magma for the formation of the layered intrusion

The average IC1 values also distinguish komatiitic spinel (average IC1 = 0.36) from boninitic spinel (ave. IC1 = -1.41) (Figure 42a), which strongly reflects the difference in TiO_2 contents at similar Cr#s (Figure 42c). Komatiitic spinel generally has higher TiO_2 contents (ave. 0.47 wt.%) compared with boninitic spinel (ave. 0.17 wt.%). Welch t-test, which is a statistical test to determine whether there is a difference between the means of komatiitic spinel and boninitic spinel, shows a very low-p value (<0.001). This suggests a significant difference between the means of komatiitic spinel and boninitic spinel and TiO_2 contents (ave. 0.4 wt.%) are indeed useful to refer the parental magma composition (e.g., Barnes and Roeder, 2001).

The average TiO_2 content (0.4 wt.%) in spinel from layered intrusion chromitites including the Ujaragssuit chromitites generally has similar TiO_2 contents at similar Cr#s to komatiitic spinel (Figure 42c). However, 68% of layered intrusions have spinel with TiO_2 contents (0.1–0.4 wt.%), overlapping with 63.8% of komatiitic spinel and 66% of boninitic spinel (Figure 42c). This highlights the need for caution when identifying parental magmas based solely on spinel major element compositions. Therefore, we investigated the differences between komatiite and boninite using spinel trace element compositions and PGE abundances.

Based on the screened Barnes and Roeder (2001)'s dataset, Ti and V concentrations in tend to demonstrate the differences between komatiitic spinel with higher Ti (median 3104 ppm, 1st quantile value 1678 ppm, 3rd quantile value 3476 ppm) and lower V (median 1009 ppm, 1st quantile value 798 ppm, 3rd quantile value 1679 ppm) and boninitic spinel with lower Ti (median 1618 ppm, 1st quantile value 1198 ppm, 3rd quantile value 1977 ppm) and higher V (median 1155 ppm, 1st quantile value 883 ppm, 3rd quantile value 1359 ppm) (Figure 43a). Characteristics of komatiitic spinel aligns more closely with layered intrusions as well as the result of ICA. However, most spinel V_2O_3 contents obtained by EPMA were obtained without the correction (Staddon et al., 2021) and the data is scattered. Therefore, further study on spinel Ti-V systematics using LAICPMS is necessary.

Based on LA-ICPMS obtained data, Ti and V contents are able to distinguish spinel from layered intrusion chromitite from spinel from Izu-Bonin-Mariana (IBM) arc boninite (Pagé and Barnes, 2009) and picrite (Park et al., 2017). However, Ti-V systematics of Archean and Proterozoic layered intrusions are similar to spinel from komatiite (Barnes et al., 2023) and from Troodos low-Si boninite (Hu et al., 2023). This confirms that the overlapping between komatiitic spinel and boninitic spinel based solely on the major elements were caused by the similarity between undeleted low-Si boninite and komatiite.

Ti-V systematics can be explained by considering the behavior of Ti and V during mantle melting and whole rock Ti-V systematics for these different magma types (Shervais, 2022). Vanadium has variable cation states (V^{2+}, V^{3+}, V^{4+}, V^{5+}), making its partitioning sensitive to varying redox conditions (Mallmann and O'Neill, 2009). In peridotite, its partition coefficient decreases in more oxidized conditions. Partial melts from more oxidized peridotite sources are therefore expected to have higher V with a correspondingly lower Ti/V ratio. Ti/V ratio of komatiites (average = 15.7, n = 37; Sossi et al. (2016)) is generally higher than that of IBM boninites (average = 7.99, n = 150; Ishizuka et al. (2020)), consistent with studies showing that IBM boninites are indeed more oxidized magmas (Brounce et al., 2021). By contrast, the Troodos boninites were recently argued not to have originated from oxidized mantle (Hu et al., 2023). This is consistent with the Ti/V systematics: IBM boninitic spinel exhibits lower Ti/V ratios than the Troodos boninitic spinel (Figure 43a). Therefore, spinel Ti/V ratios appear to reflect the redox conditions of their parental komatiite and boninite magmas (Nicklas et al., 2019; Shervais, 1982). We conclude that boninites formed at nascent arcs from the oxidized mantle cannot be the parental magma of layered intrusion chromitites.

The PGE patterns of layered intrusion chromitite hosted by peridotite show high Ir, and Ru with low Rh, Pt, and Pd values (Figure 43b). These patterns resemble komatiitic and picritic spinel more than boninitic spinel including IBM and Troodos, that show lower Ir with high Rh values (e.g., Pagé and Barnes, 2016; Park et al., 2017). This is consistent with the higher abundance of Ir in komatiite (2 ± 0.15 ppb, n = 271; Waterton et al. (2021)) compared to IBM boninite (0.1– 0.18 ppb, n = 3; Woodland et al. (2002)).

Our comprehensive investigation of spinel compositions reveals that Cr#, Ti, V, and Ir are important petrological indicators and the parental magma compositions of the Archean to Proterozoic layered intrusion chromitite are more consistent with a komatiitic magma source. This conclusion applies even to chromitites that were previously interpreted to have a boninitic origin (e.g., Mondal et al., 2019). We conclude that the major Archean to Proterozoic layered intrusions studied here most probably originated from komatiitic magma in a plume setting. Modern-style plate subduction was not necessary for their formation.

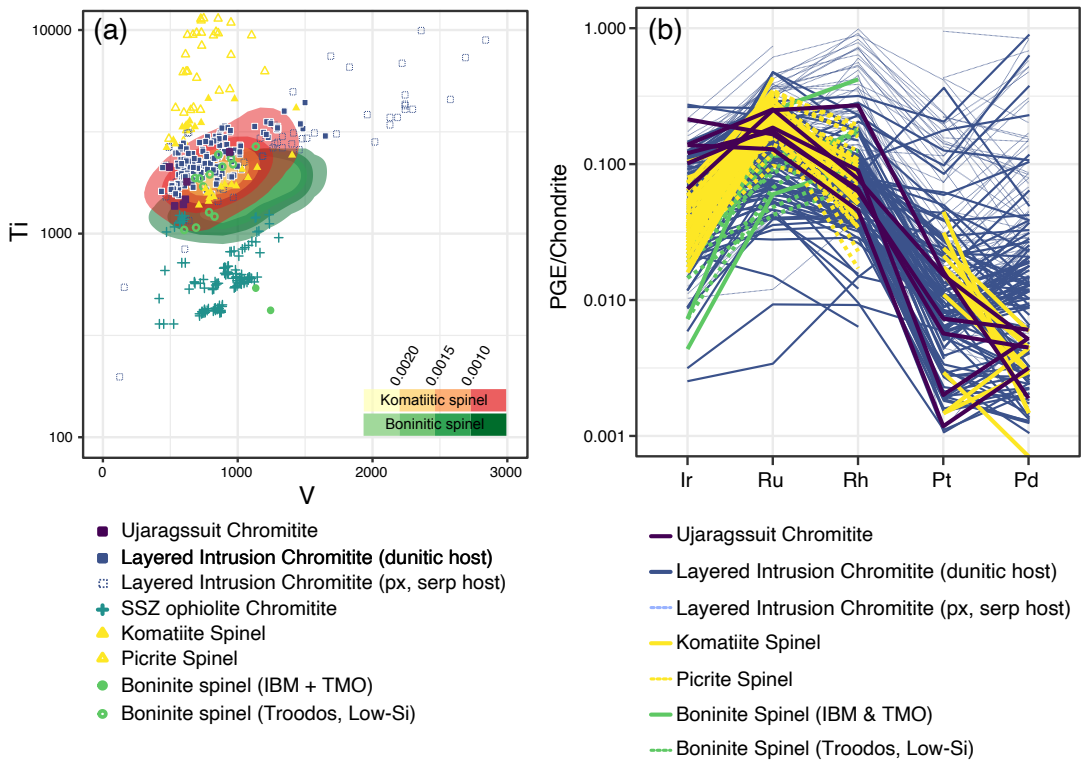

Figure 43: Compiled spinel trace elements, and whole-rock PGE data, for high Cr# chromitites. (a) Ti and V concentrations (ppm) in spinels. Kernel densities for komatiitic spinel and boninitic spinel were obtained from the screened dataset of Barnes and Roeder (2001). (b) Chondrite-normalized (Fischer-Gödde et al., 2010) PGE patterns. Layered intrusion chromitite (dunitic host) is chromitite from dunitic layer. Layered intrusion chromitite (px, serp host) is chromitite from pyroxene-rich peridotite, pyroxenite layer or serpentinite layer.

5.6.5.2 Layered intrusions as the surviving remnants of the missing komatiites

Mafic-ultramafic rocks are thought to dominate the early Earth crust (Kamber, 2015), and most of them were destroyed due to later metamorphism and burial due to their higher density compared to felsic crust (Johnson et al., 2016). Recent studies suggested that metamorphism of komatiite played important roles as sources and in water storage for TTG (tonalite–trondhjemite–granodiorite) formation, gold deposits, and H_2 production (Tamblyn et al., 2023; Tamblyn and Hermann, 2023; Yu et al., 2023). These indicate komatiitic magmas must been far more common than indicated in the preserved rock record.

Most Cratons contain komatiite, but its occurrence is heterogeneous (e.g., Waterton and Arndt, 2024). In Slave Craton and North Atlantic Craton where no komatiite has been reported, komatiitic spinel was recently found (Haugaard et al., 2021) and we now recognized the Ujaragssuit intrusion as representing a komatiitic layered intrusion, respectively. Therefore, komatiitic rocks are commonality among craton.

Formation tectonics of the cratonic mantle remains enigmatic (e.g., Pearson et al., 2021). Recently, it has been suggested that cratonic peridotite was formed by the melting and reaction with komatiite/basalt in the deeper mantle (Tomlinson and Kamber, 2021; Walsh et al., 2023). The model requires a 50:50 proportion of peridotite and komatiite, and the lack of komatiite occurrences was indicated (Kamber and Tomlinson, 2019). This is also problematic for plume models of komatiite melting columns 100s of km long, high extents of melting (Waterton and Arndt, 2024).

Archean ultramafic rocks often occur with lens-shaped bodies surrounded by TTG gneisses (e.g., Guice et al., 2022; Szilas et al., 2018) and recent geochemical studies suggested that most of them are cumulates (e.g., Waterton et al., 2022; Zemeny et al., 2023; Zhang et al., 2023; Zhang and Szilas, 2024). Komatiite–ultramafic cumulate body of Proterozoic Winnipegosis Komatiite belt is also located in the Archean TTG gneiss (Waterton et al., 2020b). With the present example of the komatiitic affinity of the Ujaragssuit body, we propose that similar lower crustal ultramafic intrusions help explain some portions of the missing komatiitic magmas in the rock record of Greenland, and elsewhere.

We conclude that layered intrusions containing high-Cr chromitites are products from komatiitic magma that failed eruption but survived later destructions and may serve as the missing complements to depleted cratonic peridotites. Komatiitic magma in a plume setting is possibly a crucial factor for the formation of TTG and depleted mantle peridotites as well as mafic-ultramafic rocks, i.e., cratonization.

5.7 Conclusion

The Ujaragssuit ultramafic layered intrusion is known for containing one of the oldest chromitite occurrences on Earth. The intrusion has undergone various metamorphic and metasomatic overprints.

Peridotites and chromitites in the Ujaragssuit intrusion are less modified compared to the younger lithologies, but these still contain secondary hydrous minerals and modified spinel compositions. Spinel from massive chromitite has low Fe and high Cr#, with consistent Ti and V contents, and consistent whole-rock PGE patterns. We interpret these massive chromitite to be the samples that best approximate igneous compositions.

We collated a large database of chromitite spinel compositions and whole-rock PGE data from Archean to Proterozoic layered intrusions, supra-subduction zone ophiolites, and spinel data from komatiite and boninite to constrain the parental magma compositions. Our statistical analysis distinguishes between spinel from layered intrusion chromitites, including the Ujaragssuit chromitite, and SSZ ophiolite chromitites, consistent with previous interpretations that the Ujaragssuit body is a part of layered intrusion.

High spinel Cr#, high Ti/V, and high whole-rock Ir contents of layered intrusion chromitites, are best explained by the parental magma of Archean to Proterozoic layered intrusions being komatiitic magmas. This indicates that the tectonic setting in which layered intrusion formed was most likely a plume setting, and not a modern-style subduction zone.

Links of layered intrusion, komatiite, TTG, and depleted cratonic mantle peridotite indicate that layered intrusions are survived and missing complements to depleted cratonic mantle and komatiitic magma played crucial role in the formation of TTG and depleted mantle peridotite as well as mafic-ultramafic rocks.

6 Synthesis

6.1 Summary

I studied ultramafic rocks from different setting and ages focusing on mineral chemistry to contribute to a nuanced understanding of the diversity and heterogeneity of the Earth's mantle.

Composition of the oceanic lithosphere changes as a result of plate tectonics, with formation occurring at mid-ocean ridges and subsequent subduction. I performed multivariate statistical analyses and geochemical modeling on a large database of clinopyroxene trace elements from residual abyssal peridotites for understanding processes in the oceanic mantle beneath the mid-ocean ridges. Our study suggests that 85% of the residual abyssal peridotite samples can be explained by residues that melted to varying degrees during the melting process, and the last group, 15% of the samples, can be the product of melting and melt-rock reaction. Our study identified that the most depleted residual abyssal peridotites experienced ~17% degrees of partial melting collected from GAK and MAR (D'Errico et al., 2016; Harigane et al., 2016). But the studied ultra-depleted peridotites from supra-subduction zone ophiolites experienced greater degrees (>30%) of partial melting than the depleted residual abyssal peridotites. The formation conditions of ultra-depleted peridotites are different from those of abyssal peridotites. They formed under high temperature, low pressure, and hydrous conditions during subduction initiation. The variations in oceanic mantle peridotites indicates that the degree of partial melting and melt extractions are the primary control, but the presence/absence of garnet-field melting, retained melt fraction, fluids, and melt-rock interaction also contribute to their variation.

The Archean Ulamertoq ultramafic rocks from SW Greenland show lithological and geochemical variations from depleted dunite to fertile peridotite. These variations are mainly the result of the later metasomatic and metamorphic overprinting on the cumulative dunitic protolith and/or the result of the crystallization sequence from dunite to peridotite but not the result of the partial melting exhibited by the oceanic mantle peridotites. The ultramafic rocks of the Ujaragssuit also mostly show similar lithological and geochemical variations as the result of metamorphic and metasomatic overprinting. However, the massive chromitites preserve the igneous compositions. Statistical analysis on a large database of chromitite spinel compositions suggests that the parental magma of Archean to Proterozoic layered intrusions including the Ujaragssuit intrusion, being komatiitic magmas rather than boninitic magmas. This indicates that the tectonic setting in which layered intrusion formed was most likely a plume setting, and not a modern-style subduction zone. Links of layered intrusion, komatiite, TTG, and depleted cratonic mantle peridotite indicate that layered intrusions are survived and missing complements to depleted cratonic mantle and komatiitic magma played crucial role in the formation of TTG and depleted mantle peridotite as well as mafic-ultramafic rocks.

6.2 Future work

- **Pacific plate**: Based on our statistical analysis on the large database of abyssal peridotites, we confirmed that samples from the EPR are limited (n = 49, 4% of the unscreened data and n = 8, 3% of the screened clinopyroxene trace elements data). Clinopyroxene composition from the EPR peridotites shows low HREE abundances and enriched LREE. This characteristic is also observed in the Petit-spot mantle xenolith, representing the uppermost part of the pacific plate (Mikuni et al., 2022). Geochemical modeling suggests that the low HREE and enriched LREE are the results of the high degrees of partial melting and melt-rock interaction. Therefore, we may not have obtained the residual abyssal peridotites from the Pacific plate that experienced only partial melting and melt extraction, that are crucial material to understanding the fast-spreading mid-ocean ridge mantle. Further study of the East Pacific Rise and mantle xenoliths captured by the petit-spot volcanic rocks (Hirano et al., 2006; Mikuni et al., 2022), will help us better understand about the mid-ocean ridge mantle.
- **Evolution of mantle during subduction initiation**: During subduction initiation, the first volcanism, forearc basalt (Reagan et al., 2010), forms by the decompression melting without the input of slab fluid and subsequently boninite forms by the slab-fluid influx melting under high temperature condition leaving the depleted to ultra-depleted peridotites (e.g., Whattam, 2023a, 2023b). Supra-subduction zone ophiolites are generally identified by the depleted signature of mantle harzburgites, linking the relationship with those volcanic rocks. However, the formation and the role of basal fertile lherzolites occurring in supra-subduction zone ophiolites remain unclear (Takazawa et al., 2003; Wu et al., 2022). Their origin has been interpreted as either residue at the earliest stage of the subduction initiation or residue formed at the mid-ocean ridges. The study of these lherzolites is therefore important to understanding the formation of ophiolites and the evolution of mantle such as redox states during subduction initiation (Birner et al., 2017). The depleted–fertile peridotite bodies from the Kamuikotan unit would be the material to tackle these questions.
- **Formation of the lithospheric mantle of the North Atlantic Craton**: Ultra-depleted cratonic mantle peridotite xenoliths occur in Greenland and its mineral chemistry differs from modern abyssal and arc peridotites (e.g., Bernstein et al., 2006). These ultra-depleted peridotites are mostly spinel-bearing dunites and are thought to be less modified cratonic mantle xenoliths. In Chapters 4 and 5, we examined the Archean ultramafic bodies formed from komatiitic magmas, which may be related to the formation of cratonic lithosphere. Study of these xenoliths focusing on mineral trace and volatiles element compositions is necessary for a better understanding of craton formation.

7 References

Aarestrup, E., Jørgensen, T.R.C., Armitage, P.E.B., Nutman, A.P., Christiansen, O., Szilas, K., 2020. The Mesoarchean Amikoq Layered Complex of SW Greenland: Part 1. Constraints on the *P-T* evolution from igneous, metasomatic and metamorphic amphiboles. Mineral Mag 1–78. https://doi.org/10.1180/mgm.2020.68

Aarestrup, E., McDonald, I., Armitage, P.E.B., Nutman, A.P., Christiansen, O., Szilas, K., 2021. The Mesoarchean Amikoq Layered Complex of SW Greenland: Part 2. Geochemical evidence for high-Mg noritic plutonism through crustal assimilation. Mineral Mag 1–64. https://doi.org/10.1180/mgm.2021.44

Ahmed, A.H., Helmy, H.M., Arai, S., Yoshikawa, M., 2008. Magmatic unmixing in spinel from late Precambrian concentrically-zoned mafic–ultramafic intrusions, Eastern Desert, Egypt. Lithos 104, 85–98. https://doi.org/10.1016/J.LITHOS.2007.11.009

Aitchison, J., 1982. The Statistical Analysis of Compositional Data. Journal of the Royal Statistical Society: Series B (Methodological) 44, 139–160. https://doi.org/10.1111/J.2517-6161.1982.TB01195.X

Akizawa, N., 2023. Thermochemical state of the oceanic lithosphere constrained from oceanic mantle peridotites. Japanese Magazine of Mineralogical and Petrological Sciences 52, 230204. https://doi.org/10.2465/GKK.230204

Akizawa, N., Früh-Green, G.L., Tamura, A., Tamura, C., Morishita, T., 2020. Compositional heterogeneity and melt transport in mantle beneath Mid-Atlantic Ridge constrained by peridotite, dunite, and wehrlite from Atlantis Massif. Lithos 354–355, 105364. https://doi.org/10.1016/j.lithos.2019.105364

Akizawa, N., Ohara, Y., Okino, K., Ishizuka, O., Yamashita, H., Machida, S., Sanfilippo, A., Basch, V., Snow, J.E., Sen, A., Hirauchi, K. ichi, Michibayashi, K., Harigane, Y., Fujii, M., Asanuma, H., Hirata, T., 2021. Geochemical characteristics of back-arc basin lower crust and upper mantle at final spreading stage of Shikoku Basin: an example of Mado Megamullion. Prog Earth Planet Sci 8, 1–24. https://doi.org/10.1186/S40645-021-00454-3

Alapieti, T.T., Kujanpaa, J., Lahtinen, J.J., Papunen, H., 1989. The Kemi stratiform chromitite deposit, northern Finland. Economic Geology 84, 1057–1077. https://doi.org/10.2113/GSECONGEO.84.5.1057

Amante, C., Eakins, B.W., 2009. ETOPO1 arc-minute global relief model : procedures, data sources and analysis. NOAA technical memorandum NESDIS NGDC 24, 1–25. https://doi.org/10.7289/V5C8276M

Antonicelli, M., Tribuzio, R., Liu, T., Wu, F.-Y., 2020. Contaminating melt flow in magmatic peridotites from the lower continental crust (Rocca d'Argimonia sequence, Ivrea–Verbano Zone). European Journal of Mineralogy 32, 587–612. https://doi.org/10.5194/ejm-32-587-2020

Appel, C.C., Appel, P.W.U., Rollinson, H.R., 2002. Complex chromite textures reveal the history of an early Archaean layered ultramafic body in West Greenland. Mineral Mag 66, 1029–1041. https://doi.org/10.1180/0026461026660075

Arai, S., 1994. Characterization of spinel peridotites by olivine-spinel compositional relationships: Review and interpretation. Chem Geol 113, 191–204. https://doi.org/10.1016/0009-2541(94)90066-3

Arai, S., 1978. Chromian spinel lamellae in olivine from the Iwanai-dake peridotite mass, Hokkaido, Japan. Earth Planet Sci Lett 39, 267–273. https://doi.org/10.1016/0012-821X(78)90202-9

Arai, S., 1974. "Non-calciferous" orthopyroxene and its bearing on the petrogenesis of ultramafic rocks in Sangun and Joetsu zones. The Journal of the Japanese Association of Mineralogists, Petrologists and Economic Geologists 69, 343–353. https://doi.org/10.2465/ganko1941.69.343

Arai, S., Hirai, H., 1985. Relics of H2O fluid inclusions in mantle-derived olivine. Nature 1985 318:6043 318, 276–277. https://doi.org/10.1038/318276a0

Arai, S., Hoshikawa, C., Miura, M., Ando, J., Ishimaru, S., Mochizuki, N., Tamura, A., 2021. Dehydrogenation of deep-seated hydrous olivine in "black-colored" dunites of arc origin. Lithos 384–385, 105967. https://doi.org/10.1016/j.lithos.2021.105967

Arai, S., Matsukage, K., 1998. Petrology of a chromitite micropod from Hess Deep, equatorial Pacific: a comparison between abyssal and alpine-type podiform chromitites. Lithos 43, 1–14. https://doi.org/10.1016/S0024-4937(98)00003-6

Arai, S., Prichard, H.M., Matsumoto Ichiro, Fisherf, P.C., 1999. Platinum–Group Minerals in Podiform Chromitite from the Kamuikotan Zone, Hokkaido, Northern Japan. Resource Geology 49, 39–47. https://doi.org/10.1111/J.1751-3928.1999.TB00030.X

Arai, S., Takada, S., Michibayashi, K., Kida, M., 2004. Petrology of peridotite xenolihs from Iraya volcano, Philippines, and its implication for dynamic mantle-wedge processes. Journal of Petrology 45, 369–389. https://doi.org/10.1093/petrology/egg100

Arai, S., Takahashi, N., 1989. Formation and compositional variation of phlogopites in the Horoman peridotite complex, Hokkaido, northern Japan: implications for origin and fractionation of metasomatic fluids in the upper mantle. Contributions to Mineralogy and Petrology 101, 165–175. https://doi.org/10.1007/BF00375303

Arai, S., Tamura, A., Miura, M., Morishita, T., 2022. Origin of spinel-hosted mineral inclusions in mantle peridotite from Setogawa in the Circum-Izu Massif Serpentine Belt, central Japan: Implications for the chromitite genesis. Ore Geol Rev 140, 104422. https://doi.org/10.1016/J.OREGEOREV.2021.104422

Arculus, R.J., Ishizuka, O., Bogus, K.A., Gurnis, M., Hickey-Vargas, R., Aljahdali, M.H., Bandini-Maeder, A.N., Barth, A.P., Brandl, P.A., Drab, L., do Monte Guerra, R., Hamada, M., Jiang, F., Kanayama, K., Kender, S., Kusano, Y., Li, H., Loudin, L.C., Maffione, M., Marsaglia, K.M., McCarthy, A., Meffre, S., Morris, A., Neuhaus, M., Savov, I.P., Sena, C., Tepley III, F.J., van der Land, C., Yogodzinski, G.M., Zhang, Z., 2015. A record of spontaneous subduction initiation in the Izu–Bonin–Mariana arc. Nature Geoscience 2015 8:9 8, 728–733. https://doi.org/10.1038/ngeo2515

Asimow, P.D., Dixon, J.E., Langmuir, C.H., 2004. A hydrous melting and fractionation model for mid-ocean ridge basalts: Application to the Mid-Atlantic Ridge near the Azores. Geochemistry, Geophysics, Geosystems 5, 1–16. https://doi.org/10.1029/2003GC000568

Ballard, S., Pollack, H.N., 1988. Modern and ancient geotherms beneath southern Africa. Earth Planet Sci Lett 88, 132–142. https://doi.org/10.1016/0012-821X(88)90052-0

Barnes, S., Jones, S., 2013. Deformed Chromitite Layers in the Coobina Intrusion, Pilbara Craton, Western Australia. Economic Geology 108, 337–354. https://doi.org/10.2113/ECONGEO.108.2.337

Barnes, S.J., 1989. Are Bushveld U-type parent magmas boninites or contaminated komatiites? Contributions to Mineralogy and Petrology 101, 447–457. https://doi.org/10.1007/BF00372218/METRICS

Barnes, S.J., Mansura, E.T., Maier, W.D., Prevec, S.A., 2023. A comparison of trace element concentrations in chromite from komatiites, picrites, and layered intrusions: Implications for the formation of massive chromite layers. Can J Earth Sci 60, 97–132. https://doi.org/10.1139/CJES-2022-0064/ASSET/IMAGES/CJES-2022-0064_F24.JPG

Barnes, S.J., Mole, D.R., le Vaillant, M., Campbell, M.J., Verrall, M.R., Roberts, M.P., Evans, N.J., 2016. Poikilitic Textures, Heteradcumulates and Zoned Orthopyroxenes in the Ntaka Ultramafic Complex, Tanzania: Implications for Crystallization Mechanisms of Oikocrysts. Journal of Petrology 57, 1171–1198. https://doi.org/10.1093/petrology/egw036

Barnes, S.J., Roeder, P.L., 2001. The Range of Spinel Compositions in Terrestrial Mafic and Ultramafic Rocks. Journal of Petrology 42, 2279–2302. https://doi.org/10.1093/petrology/42.12.2279

Barrett, N., Jaques, A.L., González-Álvarez, I., Walter, M.J., Pearson, D.G., 2022. Ultra-Refractory Peridotites of Phanerozoic Mantle Origin: the Papua New Guinea Ophiolite Mantle Tectonites. Journal of Petrology 63. https://doi.org/10.1093/PETROLOGY/EGAC014

Berno, D., Tribuzio, R., Zanetti, A., Hémond, C., 2020. Evolution of mantle melts intruding the lowermost continental crust: constraints from the Monte Capio–Alpe Cevia mafic–ultramafic sequences (Ivrea–Verbano Zone, northern Italy). Contributions to Mineralogy and Petrology 175, 1–28. https://doi.org/10.1007/s00410-019-1637-8

Bernstein, S., Hanghøj, K., Kelemen, P.B., Brooks, C.K., 2006. Ultra-depleted, shallow cratonic mantle beneath West Greenland: Dunitic xenoliths from Ubekendt Ejland. Contributions to Mineralogy and Petrology 152, 335–347. https://doi.org/10.1007/s00410-006-0109-0

Birner, S.K., Cottrell, E., Warren, J.M., Kelley, K.A., Davis, F.A., 2021. Melt addition to mid-ocean ridge peridotites increases spinel Cr# with no significant effect on recorded oxygen fugacity. Earth Planet Sci Lett 566, 116951. https://doi.org/10.1016/J.EPSL.2021.116951

Birner, S.K., Cottrell, E., Warren, J.M., Kelley, K.A., Davis, F.A., 2018. Peridotites and basalts reveal broad congruence between two independent records of mantle fO2 despite local redox heterogeneity. Earth Planet Sci Lett 494, 172–189. https://doi.org/10.1016/J.EPSL.2018.04.035

Birner, S.K., Warren, J.M., Cottrell, E., Davis, F.A., Kelley, K.A., Falloon, T.J., 2017. Forearc Peridotites from Tonga Record Heterogeneous Oxidation of the Mantle following Subduction Initiation. Journal of Petrology 58, 1755–1780. https://doi.org/10.1093/PETROLOGY/EGX072

Bizimis, M., Salters, V.J.M., Bonatti, E., 2000. Trace and REE content of clinopyroxenes from supra-subduction zone peridotites. Implications for melting and enrichment processes in island arcs. Chem Geol 165, 67–85. https://doi.org/10.1016/S0009-2541(99)00164-3

Bjerga, A., Stubseid, H.H., Pedersen, L.E.R., Beinlich, A., Pedersen, R.B., 2022. A Highly Depleted and Subduction-Modified Mantle Beneath the Slow-Spreading Mohns Ridge. Geochemistry, Geophysics, Geosystems 23, e2022GC010585. https://doi.org/10.1029/2022GC010585

Bodinier, J.L., Godard, M., 2014. Orogenic, Ophiolitic, and Abyssal Peridotites. Treatise on Geochemistry: Second Edition 3, 103–167. https://doi.org/10.1016/B978-0-08-095975-7.00204-7

Bonatti, E., 1968. Ultramafic Rocks from the Mid-Atlantic Ridge. Nature 219, 363–364. https://doi.org/10.1038/219363a0

Boyd, F.R., 1973. A pyroxene geotherm. Geochim Cosmochim Acta 37, 2533–2546. https://doi.org/10.1016/0016-7037(73)90263-9

Boyd, F.R., Gumeyt, J.J., Richardson, S.H., 1985. Evidence for a 150–200-km thick Archaean lithosphere from diamond inclusion thermobarometry. Nature 315, 387–389. https://doi.org/10.1038/315387a0

Brey, G.P., Köhler, T., 1990. Geothermobarometry in Four-phase Lherzolites II. New Thermobarometers, and Practical Assessment of Existing Thermobarometers. Journal of Petrology 31, 1353–1378. https://doi.org/10.1093/PETROLOGY/31.6.1353

Brounce, M., Reagan, M.K., Kelley, K.A., Cottrell, E., Shimizu, K., Almeev, R., 2021. Covariation of Slab Tracers, Volatiles, and Oxidation During Subduction Initiation. Geochemistry, Geophysics, Geosystems 22, e2021GC009823. https://doi.org/10.1029/2021GC009823

Brown, M., Johnson, T., 2018. Secular change in metamorphism and the onset of global plate tectonics. American Mineralogist 103, 181–196. https://doi.org/10.2138/AM-2018-6166/PDF

Brunelli, D., Paganelli, E., Seyler, M., 2014. Percolation of enriched melts during incremental open-system melting in the spinel field: A REE approach to abyssal peridotites from the Southwest Indian Ridge. Geochim Cosmochim Acta 127, 190–203. https://doi.org/10.1016/J.GCA.2013.11.040

Brunelli, D., Seyler, M., Cipriani, A., Ottolini, L., Bonatti, E., 2006. Discontinuous Melt Extraction and Weak Refertilization of Mantle Peridotites at the Vema Lithospheric Section (Mid-Atlantic Ridge). Journal of Petrology 47, 745–771. https://doi.org/10.1093/PETROLOGY/EGI092

Bucholz, C.E., Jagoutz, O., Schmidt, M.W., Sambuu, O., 2014. Phlogopite- and clinopyroxene-dominated fractional crystallization of an alkaline primitive melt: petrology and mineral chemistry of the Dariv Igneous Complex, Western Mongolia. Contributions to Mineralogy and Petrology 167, 994. https://doi.org/10.1007/s00410-014-0994-6

Cawood, P.A., Chowdhury, P., Mulder, J.A., Hawkesworth, C.J., Capitanio, F.A., Gunawardana, P.M., Nebel, O., 2022. Secular Evolution of Continents and the Earth System. Reviews of Geophysics 60, e2022RG000789. https://doi.org/10.1029/2022RG000789

Chadwick, B., Crewe, M.A., 1986. Chromite in the early Archean Akilia association (ca. 3,800 m.y.), Ivisartoq region, inner Godthabsfjord, southern west Greenland. Economic Geology. https://doi.org/10.2113/gsecongeo.81.1.184

Chaudhuri, T., Mazumder, R., Arima, M., 2015. Petrography and geochemistry of Mesoarchaean komatiites from the eastern Iron Ore belt, Singhbhum craton, India, and its similarity with 'Barberton type komatiite.' Journal of African Earth Sciences 101, 135–147. https://doi.org/10.1016/J.JAFREARSCI.2014.09.014

Chernosky, J. v, Day, H.W., Caruso, L.J., 1985. Equilibria in the system MgO–SiO2–H2O: experimental determination of the stability of Mg-anthophyllite. American Mineralogist 70, 223–236.

Choi, S.H., Mukasa, S.B., Shervais, J.W., 2008a. Initiation of Franciscan subduction along a large-offset fracture zone: Evidence from mantle peridotites, Stonyford, California. Geology 36, 595–598. https://doi.org/10.1130/G24993A.1

Choi, S.H., Shervais, J.W., Mukasa, S.B., 2008b. Supra-subduction and abyssal mantle peridotites of the Coast Range ophiolite, California. Contributions to Mineralogy and Petrology 156, 551–576. https://doi.org/10.1007/S00410-008-0300-6/FIGURES/9

Coggon, J.A., Luguet, A., Fonseca, R.O.C., Lorand, J.P., Heuser, A., Appel, P.W.U., 2015. Understanding Re-Os systematics and model ages in metamorphosed Archean ultramafic rocks: A single mineral to whole-rock investigation. Geochim Cosmochim Acta 167, 205–240. https://doi.org/10.1016/j.gca.2015.07.025

Coggon, J.A., Luguet, A., Nowell, G.M., Appel, P.W.U., 2013. Hadean mantle melting recorded by southwest Greenland chromitite 186 Os signatures. Nat Geosci 6, 871–874. https://doi.org/10.1038/ngeo1911

Colás, V., Subías, I., González-Jiménez, J.M., Proenza, J.A., Fanlo, I., Camprubí, A., Griffin, W.L., Gervilla, F., O'Reilly, S.Y., Escayola, M.F., Colás, V., Subías, I., González-Jiménez, J.M., Proenza, J.A., Fanlo, I., Camprubí, A., Griffin, W.L., Gervilla, F., O'Reilly, S.Y., Escayola, M.F., 2020. Metamorphic fingerprints of Fe-rich chromitites from the Eastern Pampean Ranges, Argentina. Boletín de la Sociedad Geológica Mexicana 72. https://doi.org/10.18268/BSGM2020V72N3A080420

Conceiçao, R. v., Green, D.H., 2004. Derivation of potassic (shoshonitic) magmas by decompression melting of phlogopite+pargasite lherzolite. Lithos 72, 209–229. https://doi.org/10.1016/J.LITHOS.2003.09.003

Connolly, J.A.D., 2009. The geodynamic equation of state: What and how. Geochemistry, Geophysics, Geosystems 10, n/a-n/a. https://doi.org/10.1029/2009GC002540

Cordier, C., Sauzeat, L., Arndt, N.T., Boullier, A.M., Batanova, V., Barou, F., 2015. Metasomatism of the lithospheric mantle immediately precedes kimberlite eruption: New evidence from olivine composition and microstructures. Journal of Petrology 56, 1775–1796. https://doi.org/10.1093/petrology/egv054

Crewe, M.A., 1984. A textural study of Archaean peridotites; Ujaragssuit nunât, Ivisârtoq region, southern West Greenland. Rapport Grønlands Geologiske Undersøgelse 120, 70–74. https://doi.org/10.34194/RAPGGU.V120.7860

Czertowicz, T.A., Scott, J.M., Waight, T.E., Palin, J.M., van der Meer, Q.H.A., le Roux, P., Münker, C., Piazolo, S., 2016a. The Anita Peridotite, New Zealand: Ultra-depletion and Subtle Enrichment in Sub-arc Mantle. Journal of Petrology 57, 717–750. https://doi.org/10.1093/PETROLOGY/EGW001

Czertowicz, T.A., Toy, V.G., Scott, J.M., 2016b. Recrystallisation, phase mixing and strain localisation in peridotite during rapid extrusion of sub-arc mantle lithosphere. J Struct Geol 88, 1–19. https://doi.org/10.1016/J.JSG.2016.04.011

Datta, P., Mukherjee, R., Mondal, S.K., Lingadevaru, M., 2021. Origin of Ni-Cu-(PGE + Au) sulfides in late-Archean komatiitic suite of rocks in the Shankaraghatta belt, Western Dharwar Craton (India). Ore Geol Rev 138, 104375. https://doi.org/10.1016/J.OREGEOREV.2021.104375

Day, J.M.D., Brown, D.B., 2021. Ancient melt-depletion in fresh to strongly serpentinised Tonga Trench peridotites. Journal of Petrology. https://doi.org/10.1093/PETROLOGY/EGAB088

Demouchy, S., Alard, O., 2021. Hydrogen, trace, and ultra-trace element distribution in natural olivines. Contributions to Mineralogy and Petrology 176, 26. https://doi.org/10.1007/s00410-021-01778-5

D'Errico, M.E., Warren, J.M., Godard, M., 2016. Evidence for chemically heterogeneous Arctic mantle beneath the Gakkel Ridge. Geochim Cosmochim Acta 174, 291–312. https://doi.org/10.1016/j.gca.2015.11.017

Dick, H.J.B., 1989. Abyssal peridotites, very slow spreading ridges and ocean ridge magmatism. Geological Society, London, Special Publications 42, 71–105. https://doi.org/10.1144/GSL.SP.1989.042.01.06

Dick, H.J.B., Natland, J.H., 1996. Late-Stage Melt Evolution and Transport in the Shallow Mantle beneath the East Pacific Rise. Proceedings of the Ocean Drilling Program, 147 Scientific Results. https://doi.org/10.2973/ODP.PROC.SR.147.007.1996

Diener, J.F.A., Powell, R., White, R.W., Holland, T.J.B., 2007. A new thermodynamic model for clino- and orthoamphiboles in the system Na2O–CaO–FeO–MgO–Al2O3–SiO2–H2O–O. Journal of Metamorphic Geology 25, 631–656. https://doi.org/10.1111/J.1525-1314.2007.00720.X

Dilek, Y., Furnes, H., 2014. Ophiolites and Their Origins. Elements 10, 93–100. https://doi.org/10.2113/GSELEMENTS.10.2.93

Dymek, R.F., Boak, J.L., Brothers, S.C., 1988a. Titanian chondrodite- and titanian clinohumite-bearing metadunite from the 3800 Ma Isua supracrustal belt, West Greenland: chemistry, petrology, and origin. Am. Mineral.; (United States) 73:5–6.

Dymek, R.F., Brothers, S.C., Schufferies, C.M., 1988b. Petrogenesis of Ultramafic Metamorphic Rocks from the 3800 Ma Isua Supracrustal Belt, West Greenland. Journal of Petrology 29, 1353–1397. https://doi.org/10.1093/petrology/29.6.1353

Egozcue, J.J., Pawlowsky-Glahn, V., Mateu-Figueras, G., Barceló-Vidal, C., 2003. Isometric Logratio Transformations for Compositional Data Analysis. Math Geol 35, 279–300. https://doi.org/10.1023/A:1023818214614

Endo, S., Mizukami, T., Wallis, S.R., Tamura, A., Arai, S., 2015. Orthopyroxene-rich Rocks from the Sanbagawa Belt (SW Japan): Fluid–Rock Interaction in the Forearc Slab–Mantle Wedge Interface. Journal of Petrology 56, 1113–1137. https://doi.org/10.1093/petrology/egv031

Faithfull, J.W., Dempster, T.J., MacDonald, J.M., Reilly, M., EIMF, 2018. Metasomatism and the crystallization of zircon megacrysts in Archaean peridotites from the Lewisian complex, NW Scotland. Contributions to Mineralogy and Petrology 173, 99. https://doi.org/10.1007/s00410-018-1527-5

Falloon, T.J., Danyushevsky, L. v., 2000. Melting of Refractory Mantle at 1·5, 2 and 2·5 GPa under Anhydrous and H2O-undersaturated Conditions: Implications for the Petrogenesis of High-Ca Boninites and the Influence of Subduction Components on Mantle Melting. Journal of Petrology 41, 257–283. https://doi.org/10.1093/PETROLOGY/41.2.257

Fischer-Gödde, M., Becker, H., Wombacher, F., 2010. Rhodium, gold and other highly siderophile element abundances in chondritic meteorites. Geochim Cosmochim Acta 74, 356–379. https://doi.org/10.1016/J.GCA.2009.09.024

Fischer-Gödde, M., Elfers, B.-M., Münker, C., Szilas, K., Maier, W.D., Messling, N., Morishita, T., Van Kranendonk, M., Smithies, H., 2020. Ruthenium isotope vestige of Earth's pre-late-veneer mantle preserved in Archaean rocks. Nature 579, 240. https://doi.org/10.1038/s41586-020-2069-3

Friedrich, B.M., Marques, J.C., Olivo, G.R., Frantz, J.C., Joy, B., Queiroz, W.J.A., 2020. Petrogenesis of the massive chromitite layer from the Jacurici Complex, Brazil: evidence from inclusions in chromite. Miner Depos 55, 1105–1126. https://doi.org/10.1007/S00126-019-00917-0/FIGURES/14

Friend, C.R.L., Bennett, V.C., Nutman, A.P., 2002. Abyssal peridotites >3,800 Ma from southern West Greenland: Field relationships, petrography, geochronology, whole-rock and mineral chemistry of dunite and harzburgite inclusions in the Itsaq Gneiss Complex. Contributions to Mineralogy and Petrology 143, 71–92. https://doi.org/10.1007/s00410-001-0332-7

Friend, C.R.L., Nutman, A.P., 2011. Dunites from Isua, Greenland: A ca. 3720 Ma window into subcrustal metasomatism of depleted mantle. Geology 39, 663–666. https://doi.org/10.1130/G31904.1

Friend, C.R.L., Nutman, A.P., 2005. New pieces to the Archaean terrane jigsaw puzzle in the Nuuk region, southern West Greenland: steps in transforming a simple insight into a complex regional tectonothermal model. J Geol Soc London 162, 147–162. https://doi.org/10.1144/0016-764903-161

Friend, C.R.L., Nutman, A.P., McGregor, V.R., 1988. Late Archaean terrane accretion in the Godthåb region, southern West Greenland. Nature 335, 535–538. https://doi.org/10.1038/335535a0

Frisby, C., Bizimis, M., Mallick, S., 2016. Seawater-derived rare earth element addition to abyssal peridotites during serpentinization. Lithos 248–251, 432–454. https://doi.org/10.1016/J.LITHOS.2016.01.025

Furnes, H., De Wit, M., Dilek, Y., 2014. Four billion years of ophiolites reveal secular trends in oceanic crust formation. Geoscience Frontiers 5, 571–603. https://doi.org/10.1016/J.GSF.2014.02.002

Gale, A., Dalton, C.A., Langmuir, C.H., Su, Y., Schilling, J.G., 2013. The mean composition of ocean ridge basalts. Geochemistry, Geophysics, Geosystems 14, 489–518. https://doi.org/10.1029/2012GC004334

Garde, A.A., 2007. A mid-Archaean island arc complex in the eastern Akia terrane, Godthåbsfjord, southern West Greenland. J Geol Soc London 164, 565–579. https://doi.org/10.1144/0016-76492005-107

Garde, A.A., 1997. Accretion and evolution of an Archaean high-grade grey gneiss–amphibolite complex: the Fiskefjord area, southern West Greenland. Geology of Greenland Survey Bulletin Vol. 177, 115pp.

Garde, A.A., 1990. Thermal granulite-facies metamorphism with diffuse retrogression in Archaean orthogneisses, Fiskefjord, southern West Greenland. Journal of Metamorphic Geology 8, 663–682. https://doi.org/10.1111/j.1525-1314.1990.tb00494.x

Garde, A.A., Dyck, B., Esbensen, K.H., Johansson, L., Möller, C., 2014. The Finnefjeld domain, Maniitsoq structure, West Greenland: Differential rheological features and mechanical homogenisation in response to impacting? Precambrian Res 255, 791–808. https://doi.org/10.1016/J.PRECAMRES.2014.06.022

Garde, A.A., Friend, C.R., Nutman, A.P., Marker, M., 2000. Rapid maturation and stabilisation of middle Archaeancontinental crust: the Akia terrane, southern WestGreenland. Geology of Greenland Survey Bulletin Vol. 47, pp. 1–27.

Garde, A.A., McDonald, I., Dyck, B., Keulen, N., 2012. Searching for giant, ancient impact structures on Earth: The Mesoarchaean Maniitsoq structure, West Greenland. Earth Planet Sci Lett 337–338, 197–210. https://doi.org/10.1016/j.epsl.2012.04.026

Garde, A.A., Pattison, J., Kokfelt, T.F., McDonald, I., Secher, K., 2013. The norite belt in the Mesoarchaean Maniitsoq structure, southern West Greenland: Conduit-type Ni-Cu mineralisation in impact-triggered, mantle-derived intrusions? Geological Survey of Denmark and Greenland Bulletin 45–48.

Garde, A.A., Windley, B.F., Kokfelt, T.F., Keulen, N., 2020. Archaean Plate Tectonics in the North Atlantic Craton of West Greenland Revealed by Well-Exposed Horizontal Crustal Tectonics, Island Arcs and Tonalite-Trondhjemite-Granodiorite Complexes. Front Earth Sci (Lausanne) 8, 526. https://doi.org/10.3389/feart.2020.540997

Gardiner, N.J., Kirkland, C.L., Hollis, J., Szilas, K., Steenfelt, A., Yakymchuk, C., Heide-Jørgensen, H., 2019. Building Mesoarchaean crust upon Eoarchaean roots: the Akia Terrane, West Greenland. Contributions to Mineralogy and Petrology 174, 20. https://doi.org/10.1007/s00410-019-1554-x

Gargiulo, M.F., Bjerg, E.A., Mogessie, A., 2013. Spinel group minerals in metamorphosed ultramafic rocks from Río de las tunas belt, central Andes, Argentina. Geologica Acta 11, 133–148. https://doi.org/10.1344/105.000001836

Garuti, G., Proenza, J.A., Zaccarini, F., 2007. Distribution and mineralogy of platinum-group elements in altered chromitites of the Campo Formoso layered intrusion (Bahia State, Brazil): Control by magmatic and hydrothermal processes. Mineral Petrol 89, 159–188. https://doi.org/10.1007/S00710-006-0141-9/METRICS

Giovanardi, T., Freddo, I., Mazzucchelli, M., 2018. Filling the gap in the classification of phlogopite-bearing ultramafic rocks. Journal of Geology 126, 361–370. https://doi.org/10.1086/697244

Godel, B., Barnes, S.J., Maier, W.D., 2011. Parental magma composition inferred from trace element in cumulus and intercumulus silicate minerals: An example from the Lower and Lower Critical Zones of the Bushveld Complex, South-Africa. Lithos 125, 537–552. https://doi.org/10.1016/J.LITHOS.2011.03.010

González-Jiménez, J.M., Camprubí, A., Colás, V., Griffin, W.L., Proenza, J.A., O'Reilly, S.Y., Centeno-García, E., García-Casco, A., Belousova, E., Talavera, C., Farré-de-Pablo, J., Satsukawa, T., 2017. The recycling of chromitites in ophiolites from southwestern North America. Lithos 294–295, 53–72. https://doi.org/https://doi.org/10.1016/j.lithos.2017.09.020

González-Jiménez, J.M., Griffin, W.L., Proenza, J.A., Gervilla, F., O'Reilly, S.Y., Akbulut, M., Pearson, N.J., Arai, S., 2014. Chromitites in ophiolites: How, where, when, why? Part II. The crystallization of chromitites. Lithos 189, 140–158. https://doi.org/10.1016/J.LITHOS.2013.09.008

González-Jiménez, J.M., Locmelis, M., Belousova, E., Griffin, W.L., Gervilla, F., Kerestedjian, T.N., O'Reilly, S.Y., Pearson, N.J., Sergeeva, I., 2015. Genesis and tectonic implications of podiform chromitites in the metamorphosed ultramafic massif of Dobromirtsi (Bulgaria). Gondwana Research 27, 555–574. https://doi.org/10.1016/J.GR.2013.09.020

González-Jiménez, J.M., Proenza, J.A., Gervilla, F., Melgarejo, J.C., Blanco-Moreno, J.A., Ruiz-Sánchez, R., Griffin, W.L., 2011. High-Cr and high-Al chromitites from the Sagua de Tánamo district, Mayarí-Cristal ophiolitic massif (eastern Cuba): Constraints on their origin from mineralogy and geochemistry of chromian spinel and platinum-group elements. Lithos 125, 101–121. https://doi.org/10.1016/J.LITHOS.2011.01.016

Gordeychik, B., Churikova, T., Shea, T., Kronz, A., Simakin, A., Wörner, G., 2020. Fo and Ni Relations in Olivine Differentiate between Crystallization and Diffusion Trends. Journal of Petrology. https://doi.org/10.1093/petrology/egaa083

Grambling, N.L., Dygert, N., Boring, B., Jean, M.M., Kelemen, P.B., 2022. Thermal History of Lithosphere Formed Beneath Fast Spreading Ridges: Constraints From the Mantle Transition Zone of the East Pacific Rise at Hess Deep and Oman Drilling Project, Wadi Zeeb, Samail Ophiolite. J Geophys Res Solid Earth 127, e2021JB022696. https://doi.org/10.1029/2021JB022696

Grant, Thomas B., Milke, R., Wunder, B., 2014. Experimental reactions between olivine and orthopyroxene with phonolite melt: implications for the origins of hydrous amphibole + phlogopite + diopside bearing metasomatic veins. Contributions to Mineralogy and Petrology 168, 1–18. https://doi.org/10.1007/S00410-014-1073-8/FIGURES/8

Grant, T. B., Milke, R., Wunder, B., Wirth, R., Rhede, D., 2014. Experimental study of phlogopite reaction rim formation on olivine in phonolite melts: Kinetics, reaction rates, and residence times. American Mineralogist 99, 2211–2226. https://doi.org/10.2138/am-2014-4821

Greenacre, M., 2018. Compositional Data Analysis in Practice, 1st ed, Chapman and Hall/CRC. Chapman and Hall/CRC. https://doi.org/10.1201/9780429455537

Grégoire, M., McInnes, B.I.A., O'Reilly, S.Y., 2001. Hydrous metasomatism of oceanic sub-arc mantle, Lihir, Papua New Guinea: Part 2. Trace element characteristics of slab-derived fluids. Lithos 59, 91–108. https://doi.org/10.1016/S0024-4937(01)00058-5

Guice, G.L., Miocevich, S.R., Hughes, H.S.R., McDonald, I., Goodenough, K.M., Ackerson, M.R., MacDonald, J.M., Faithfull, J.W., 2022. Origin of ultramafic–mafic bodies on the Isles of Lewis and Harris (Scotland, UK): Constraints on the Archean–Paleoproterozoic evolution of the Lewisian Gneiss Complex, North Atlantic Craton. Precambrian Res 369, 106523. https://doi.org/10.1016/J.PRECAMRES.2021.106523

Guotana, J.M., Morishita, T., Nishio, I., Tamura, A., Mizukami, T., Tani, K., Harigane, Y., Szilas, K., Pearson, D.G., 2022. Deserpentinization and high-pressure (eclogite-facies) metamorphic features in the Eoarchean

ultramafic body from Isua, Greenland. Geoscience Frontiers 13, 101298. https://doi.org/10.1016/J.GSF.2021.101298

Guotana, J.M., Morishita, T., Yamaguchi, R., Nishio, I., Tamura, A., Tani, K., Harigane, Y., Szilas, K., Pearson, D.G., 2018. Contrasting textural and chemical signatures of chromitites in the mesoarchaean ulamertoq peridotite body, southern west Greenland. Geosciences (Switzerland) 8. https://doi.org/10.3390/geosciences8090328

Guotana, J.M.R., Payot, B.D., Dimalanta, C.B., Ramos, N.T., Faustino-Eslava, D. V., Queaño, K.L., Yumul, G.P., 2017. Petrological and geochemical characteristics of the Samar Ophiolite ultramafic section: implications on the origins of the ophiolites in Samar and Leyte islands, Philippines. Int Geol Rev 60, 401–417. https://doi.org/10.1080/00206814.2017.1336944

Harada, T., Arai, S., 1997. The Application of Detrital Chromian Spinel Chemistry to Geochemical Survey of Chromite Deposit Examples of the Kamuikotan Tectonic Belt. Shigen-Chishitsu 47, 201–209. https://doi.org/10.11456/SHIGENCHISHITSU1992.47.201

Harigane, Y., Abe, N., Michibayashi, K., Kimura, J.I., Chang, Q., 2016. Melt-rock interactions and fabric development of peridotites from North Pond in the Kane area, Mid-Atlantic Ridge: Implications of microstructural and petrological analyses of peridotite samples from IODP Hole U1382A. Geochemistry, Geophysics, Geosystems 17, 2298–2322. https://doi.org/10.1002/2016GC006429

Harigane, Y., Michibayashi, K., Morishita, T., Tamura, A., Hashimoto, S., Snow, J.E., 2022. Deformation beneath Gakkel Ridge, Arctic Ocean: From mantle flow to mantle shear in a sparsely magmatic spreading zone. Tectonophysics 822, 229186. https://doi.org/10.1016/J.TECTO.2021.229186

Haugaard, R., Waterton, P., Ootes, L., Pearson, D.G., Luo, Y., Konhauser, K., 2021. Detrital chromites reveal Slave craton's missing komatiite. Geology 49, 1079–1083. https://doi.org/10.1130/G48840.1

Helffrich, G.R., Wood, B.J., 2001. The Earth's mantle. Nature 412, 501–507. https://doi.org/10.1038/35087500

Hellebrand, E., Snow, J.E., Dick, H.J.B., Hofmann, A.W., 2001. Coupled major and trace elements as indicators of the extent of melting in mid-ocean-ridge peridotites. Nature 410, 677–681. https://doi.org/10.1038/35070546

Hellebrand, E., Snow, J.E., Hoppe, P., Hofmann, A.W., 2002a. Garnet-field Melting and Late-stage Refertilization in 'Residual' Abyssal Peridotites from the Central Indian Ridge. Journal of Petrology 43, 2305–2338. https://doi.org/10.1093/PETROLOGY/43.12.2305

Hellebrand, E., Snow, J.E., Mühe, R., 2002b. Mantle melting beneath Gakkel Ridge (Arctic Ocean): abyssal peridotite spinel compositions. Chem Geol 182, 227–235. https://doi.org/10.1016/S0009-2541(01)00291-1

Herzberg, C., Condie, K., Korenaga, J., 2010. Thermal history of the Earth and its petrological expression. Earth Planet Sci Lett 292, 79–88. https://doi.org/10.1016/J.EPSL.2010.01.022

Hesse, K.T., Gose, J., Stalder, R., Schmädicke, E., 2015. Water in orthopyroxene from abyssal spinel peridotites of the East Pacific Rise (ODP Leg 147: Hess Deep). Lithos 232, 23–34. https://doi.org/10.1016/J.LITHOS.2015.06.011

Hirai, H., Arai, S., 1987. H2OCO2 fluids supplied in alpine-type mantle peridotites: electron petrology of relic fluid inclusions in olivines. Earth Planet Sci Lett 85, 311–318. https://doi.org/10.1016/0012-821X(87)90041-0

Hirano, N., Takahashi, E., Yamamoto, J., Abe, W., Ingle, S.P., Kaneoka, I., Hirata, T., Kimura, J.I., Ishii, T., Ogawa, Y., Machida, S., Suyehiro, K., 2006. Volcanism in response to plate flexure. Science (1979) 313, 1426–1428. https://doi.org/10.1126/SCIENCE.1128235/SUPPL_FILE/HIRANO.SOM.PDF

Hoare, B.C., Tomlinson, E.L., Kamber, B.S., 2022. Evidence for a very thick Kaapvaal craton root: Implications for equilibrium fossil geotherms in the early continental lithosphere. Earth Planet Sci Lett 597, 117796. https://doi.org/10.1016/J.EPSL.2022.117796

Hofmann, A.W., 2014. Sampling Mantle Heterogeneity through Oceanic Basalts: Isotopes and Trace Elements. Treatise on Geochemistry: Second Edition 3, 67–101. https://doi.org/10.1016/B978-0-08-095975-7.00203-5

Holland, T., Blundy, J., 1994. Non-ideal interactions in calcic amphiboles and their bearing on amphibole-plagioclase thermometry. Contributions to Mineralogy and Petrology 116, 433–447. https://doi.org/10.1007/BF00310910

Holland, T.J.B., Powell, R., 1998. An internally consistent thermodynamic data set for phases of petrological interest. Journal of Metamorphic Geology 16, 309–343. https://doi.org/10.1111/j.1525-1314.1998.00140.x

Hu, W.J., Zhou, M.F., Ribeiro, J.M., Malpas, J., Wu, Y.D., Bai, Z.J., 2023. The Redox State of Incipient Oceanic Subduction Zones: An Example From the Troodos Ophiolite (Cyprus). J Geophys Res Solid Earth 128, e2022JB025008. https://doi.org/10.1029/2022JB025008

Hyvärinen, A., Oja, E., 2000. Independent component analysis: algorithms and applications. Neural Networks 13, 411–430. https://doi.org/10.1016/S0893-6080(00)00026-5

Ichiyama, Y., Ishiwatari, A., Kimura, J.I., Senda, R., Kawabata, H., Tatsumi, A.Y., 2012. Picrites in central Hokkaido: Evidence of extremely high temperature magmatism in the late jurassic ocean recorded in an accreted oceanic plateau. Geology 40, 411–414. https://doi.org/10.1130/G32752.1

Ichiyama, Y., Tsujimori, T., Fryer, P., Michibayashi, K., Tamura, A., Morishita, T., 2021. Temporal and spatial mineralogical changes in clasts from Mariana serpentinite mud volcanoes: Cooling of the hot forearc-mantle at subduction initiation. Lithos 105941. https://doi.org/10.1016/j.lithos.2020.105941

Igarashi, T., Kaloh, T., Niida, K., 1985. The Takadomari Serpentinites in the Kamuikotan Ophiolite Belt, Hokkaido, Japan. Jour. Fac. Sci., Hokkaido Univ. 21, 305–319.

Irvine, T.N., 1965. Chromian spinel as a petrogenetic indicator: Part 1. Theory. Can J Earth Sci 2, 648–672. https://doi.org/10.1139/E65-046

Ishikawa, A., Suzuki, K., Collerson, K.D., Liu, J., Pearson, D.G., Komiya, T., 2017. Rhenium-osmium isotopes and highly siderophile elements in ultramafic rocks from the Eoarchean Saglek Block, northern Labrador, Canada: implications for Archean mantle evolution. Geochim Cosmochim Acta 216, 286–311. https://doi.org/10.1016/J.GCA.2017.07.023

Ishimaru, S., Arai, S., 2008. Calcic amphiboles in peridotite xenoliths from Avacha volcano, Kamchatka, and their implications for metasomatic conditions in the mantle wedge. Geological Society, London, Special Publications 293, 35–55. https://doi.org/10.1144/SP293.3

Ishimaru, S., Arai, S., Ishida, Y., Shirasaka, M., Okrugin, V.M., 2007. Melting and Multi-stage Metasomatism in the Mantle Wedge beneath a Frontal Arc Inferred from Highly Depleted Peridotite Xenoliths from the Avacha Volcano, Southern Kamchatka. Journal of Petrology 48, 395–433. https://doi.org/10.1093/petrology/egl065

Ishiwatari, A., Sokolov, S.D., Vysotskiy, S. v., 2004. Petrological diversity and origin of ophiolites in Japan and Far East Russia with emphasis on depleted harzburgite. Geol Soc Spec Publ 218, 597–617. https://doi.org/10.1144/GSL.SP.2003.218.01.30

Ishizuka, H., 1987. Igneous and metamorphic petrology of the horokanai ophiolite in the kamuikotan zone, hokkaido, japan: synthetic thesis. Memoirs of the Faculty of Science, Kochi University. Ser. E, Geology 8, 1–70.

Ishizuka, H., 1985. Prograde Metamorphism of the Horokanai Ophiolite in the Kamuikotan Zone, Hokkaido, Japan. Journal of Petrology 26, 391–417. https://doi.org/10.1093/PETROLOGY/26.2.391

Ishizuka, O., Tani, K., Reagan, M.K., Kanayama, K., Umino, S., Harigane, Y., Sakamoto, I., Miyajima, Y., Yuasa, M., Dunkley, D.J., 2011. The timescales of subduction initiation and subsequent evolution of an oceanic island arc. Earth Planet Sci Lett 306, 229–240. https://doi.org/10.1016/j.epsl.2011.04.006

Ishizuka, O., Taylor, R.N., Umino, S., Kanayama, K., 2020. Geochemical Evolution of Arc and Slab Following Subduction Initiation: a Record from the Bonin Islands, Japan. Journal of Petrology 61. https://doi.org/10.1093/PETROLOGY/EGAA050

Itano, K., Morishita, T., Nishio, I., Guotana, J.M., Ogusu, Y., Ishizuka, O., Tamura, A., 2021. Petrogenesis of amphibole-rich ultramafic rocks in the Hida metamorphic complex, Japan: Its role in arc crust differentiation. Lithos 404–405, 106440. https://doi.org/10.1016/J.LITHOS.2021.106440

Itano, K., Takehara, M., Horie, K., Iizuka, T., Nishio, I., Morishita, T., 2023. A long-lived mafic magma reservoir: Zircon evidence from a hornblende peridotite in the Hida Belt, Japan. Geology. https://doi.org/10.1130/G51560.1

Itano, K., Ueki, K., Iizuka, T., Kuwatani, T., 2020. Geochemical Discrimination of Monazite Source Rock Based on Machine Learning Techniques and Multinomial Logistic Regression Analysis. Geosciences (Basel) 10, 63. https://doi.org/10.3390/geosciences10020063

Iwamori, H., Yoshida, K., Nakamura, H., Kuwatani, T., Hamada, M., Haraguchi, S., Ueki, K., 2017. Classification of geochemical data based on multivariate statistical analyses: Complementary roles of cluster, principal component, and independent component analyses. Geochemistry, Geophysics, Geosystems 18, 994–1012. https://doi.org/10.1002/2016GC006663

Jean, M.M., Shervais, J.W., 2017. The distribution of fluid mobile and other incompatible trace elements in orthopyroxene from mantle wedge peridotites. Chem Geol 457, 118–130. https://doi.org/10.1016/j.chemgeo.2017.03.017

Jean, M.M., Shervais, J.W., Choi, S.H., Mukasa, S.B., 2010. Melt extraction and melt refertilization in mantle peridotite of the Coast Range ophiolite: An LA-ICP-MS study. Contributions to Mineralogy and Petrology 159, 113–136. https://doi.org/10.1007/S00410-009-0419-0/FIGURES/11

Jochum, K.P., Stoll, B., Herwig, K., Willbold, M., Hofmiann, A.W., Amini, M., Aarburg, S., Abouchami, W., Hellebrand, E., Mocek, B., Raczek, I., Stracke, A., Alard, O., Bouman, C., Becker, S., Dücking, M., Brätz, H., Klemd, R., De Bruin, D., Canil, D., Cornell, D., De Hoog, C.J., Dalpé, C., Danyushevshy, L., Eisenhauer, A., Gao, Y., Snow, J.E., Groschopf, N., Günther, D., Latkoczy, C., Guillong, M., Hauri, E.H., Höfer, H.E., Lahaye, Y., Horz, K., Jacob, D.E., Kasemann, S.A., Kent, A.J.R., Ludwig, T., Zack, T., Mason, P.R.D., Meixner, A., Rosner, M., Misawa, K., Nash, B.P., Pfänder, J., Premo, W.R., Sun, W.D., Tiepolo, M., Vannucci, R., Vennemann, T., Wayne, D., Woodhead, J.D., 2006. MPI-DING reference glasses for in situ microanalysis: New reference values for element concentrations and isotope ratios. Geochemistry, Geophysics, Geosystems 7, 2008. https://doi.org/10.1029/2005GC001060

Jochum, K.P., Weis, U., Stoll, B., Kuzmin, D., Yang, Q., Raczek, I., Jacob, D.E., Stracke, A., Birbaum, K., Frick, D.A., Günther, D., Enzweiler, J., 2011. Determination of Reference Values for NIST SRM 610–617 Glasses Following ISO Guidelines. Geostand Geoanal Res 35, 397–429. https://doi.org/10.1111/J.1751-908X.2011.00120.X

Johnson, D.M., Hooper, P.R., Conrey, R.M., 1999. XRF Analysis of Rocks and Minerals for Major and Trace Elements on a Single Low Dilution Li-tetraborate Fused Bead. GeoAnalytical Laboratory, Washington State University, Pullman, WA 99 164.

Johnson, K.T.M., Dick, H.J.B., 1992. Open system melting and temporal and spatial variation of peridotite and basalt at the Atlantis II Fracture Zone. J Geophys Res Solid Earth 97, 9219–9241. https://doi.org/10.1029/92JB00701

Johnson, K.T.M., Dick, H.J.B., Shimizu, N., 1990. Melting in the oceanic upper mantle: an ion microprobe study of diopsides in abyssal peridotites. J Geophys Res 95, 2661–2678. https://doi.org/10.1029/JB095iB03p02661

Johnson, T.E., Brown, M., Goodenough, K.M., Clark, C., Kinny, P.D., White, R.W., 2016. Subduction or sagduction? Ambiguity in constraining the origin of ultramafic–mafic bodies in the Archean crust of NW Scotland. Precambrian Res 283, 89–105. https://doi.org/10.1016/J.PRECAMRES.2016.07.013

Jorgenson, C., Higgins, O., Petrelli, M., Bégué, F., Caricchi, L., 2022. A Machine Learning-Based Approach to Clinopyroxene Thermobarometry: Model Optimization and Distribution for Use in Earth Sciences. J Geophys Res Solid Earth 127, e2021JB022904. https://doi.org/10.1029/2021JB022904

Kamber, B.S., 2015. The evolving nature of terrestrial crust from the Hadean, through the Archaean, into the Proterozoic. Precambrian Res 258, 48–82. https://doi.org/10.1016/J.PRECAMRES.2014.12.007

Kamber, B.S., Tomlinson, E.L., 2019. Petrological, mineralogical and geochemical peculiarities of Archaean cratons. Chem Geol 511, 123–151. https://doi.org/10.1016/J.CHEMGEO.2019.02.011

Kelemen, P.B., Hirth, G., Shimizu, N., Spiegelman, M., Dick, H.J.B., 1997. A review of melt migration processes in the adiabatically upwelling mantle beneath oceanic spreading ridges. Philosophical Transactions of the Royal Society of London. Series A: Mathematical, Physical and Engineering Sciences 355, 283–318. https://doi.org/10.1098/RSTA.1997.0010

Kelemen, P.B., Shimizu, N., Salters, V.J.M., 1995. Extraction of mid-ocean-ridge basalt from the upwelling mantle by focused flow of melt in dunite channels. Nature 1995 375:6534 375, 747–753. https://doi.org/10.1038/375747a0

Kelemen, P.B., Yogodzinski, G.M., Scholl, D.W., 2003. Along-Strike Variation in the Aleutian Island Arc: Genesis of High Mg# Andesite and Implications for Continental Crust. Geophysical Monograph Series 138, 223–276. https://doi.org/10.1029/138GM11

Khatun, S., Mondal, S.K., Zhou, M.F., Balaram, V., Prichard, H.M., 2014. Platinum-group element (PGE) geochemistry of Mesoarchean ultramafic–mafic cumulate rocks and chromitites from the Nuasahi Massif, Singhbhum Craton (India). Lithos 205, 322–340. https://doi.org/10.1016/J.LITHOS.2014.07.013

Kimura, J.I., Gill, J.B., van Keken, P.E., Kawabata, H., Skora, S., 2017. Origin of geochemical mantle components: Role of spreading ridges and thermal evolution of mantle. Geochemistry, Geophysics, Geosystems 18, 697–734. https://doi.org/10.1002/2016GC006696

Kimura, T., Ozawa, K., Kuritani, T., Iizuka, T., Nakagawa, M., 2020. Thermal state of the upper mantle and the origin of the Cambrian-Ordovician ophiolite pulse: Constraints from ultramafic dikes of the Hayachine-Miyamori ophiolite. American Mineralogist 105, 1778–1801. https://doi.org/10.2138/AM-2020-7160

Kinzler, R.J., Grove, T.L., 1992. Primary magmas of mid-ocean ridge basalts 1. Experiments and methods. J Geophys Res 97, 6885–6906. https://doi.org/10.1029/91JB02840

Kirkland, C.L., Yakymchuk, C., Gardiner, N.J., Szilas, K., Hollis, J., Olierook, H., Steenfelt, A., 2020. Titanite petrochronology linked to phase equilibrium modelling constrains tectono-thermal events in the Akia Terrane, West Greenland. Chem Geol 536, 119467. https://doi.org/10.1016/j.chemgeo.2020.119467

Kirkland, C.L., Yakymchuk, C., Hollis, J., Heide-Jørgensen, H., Danišík, M., 2018a. Mesoarchean exhumation of the Akia terrane and a common Neoarchean tectonothermal history for West Greenland. Precambrian Res 314, 129–144. https://doi.org/10.1016/j.precamres.2018.06.004

Kirkland, C.L., Yakymchuk, C., Szilas, K., Evans, N., Hollis, J., McDonald, B., Gardiner, N.J., 2018b. Apatite: a U-Pb thermochronometer or geochronometer? Lithos 318–319, 143–157. https://doi.org/10.1016/j.lithos.2018.08.007

Komiya, T., Maruyama, S., Hirata, T., Yurimoto, H., Nohda, S., 2004. Geochemistry of the oldest MORB and OIB in the Isua Supracrustal Belt, southern West Greenland: Implications for the composition and temperature of early Archean upper mantle. Island Arc 13, 47–72. https://doi.org/https://doi.org/10.1111/j.1440-1738.2003.00416.x

Komiya, T., Maruyama, S., Masuda, T., Nohda, S., Hayashi, M., Okamoto, K., 1999. Plate tectonics at 3.8-3.7 Ga: Field evidence from the Isua Accretionary Complex, southern West Greenland. Journal of Geology 107, 515–554. https://doi.org/10.1086/314371

Korenaga, J., 2020. Plate tectonics and surface environment: Role of the oceanic upper mantle. Earth Sci Rev 205, 103185. https://doi.org/10.1016/J.EARSCIREV.2020.103185

Korenaga, J., 2013. Initiation and Evolution of Plate Tectonics on Earth: Theories and Observations. Annu Rev Earth Planet Sci 41, 117–151. https://doi.org/10.1146/annurev-earth-050212-124208

Kubo, K., 2002. Dunite Formation Processes in Highly Depleted Peridotite: Case Study of the Iwanaidake Peridotite, Hokkaido, Japan. Journal of Petrology 43, 423–448. https://doi.org/10.1093/petrology/43.3.423

Laarman, J., 2014. A Detailed Metallogenic Study of the McFaulds Lake Chromite Deposits, Northern Ontario. The University of Western Ontario, Electronic Thesis and Dissertation Repository.

Langmuir, C.H., Forsyth, D.W., 2007. Mantle melting beneath mid-ocean ridges. Oceanography 20, 78–89. https://doi.org/10.5670/OCEANOG.2007.82

Langmuir, C.H., Klein, E.M., Plank, T., 1992. Petrological Systematics of Mid-Ocean Ridge Basalts: Constraints on Melt Generation Beneath Ocean Ridges, in: Mantle Flow and Melt Generation at Mid-Ocean Ridges, Geophysical Monograph Series. pp. 183–280. https://doi.org/https://doi.org/10.1029/GM071p0183

Latypov, R., O'Driscoll, B., Lavrenchuk, A., 2013. Towards a model for the in situ origin of PGE reefs in layered intrusions: Insights from chromitite seams of the Rum Eastern Layered Intrusion, Scotland. Contributions to Mineralogy and Petrology 166, 309–327. https://doi.org/10.1007/S00410-013-0876-3/FIGURES/11

Lawley, C., 2016. Compositional symmetry between Earth's crustal building blocks. Geochem Perspect Lett 2, 117–126. https://doi.org/10.7185/GEOCHEMLET.1612

Lawley, C., Kjarsgaard, B., Jackson, S., Yang, Z., Petts, D., Roots, E., 2018. Trace metal and isotopic depth profiles through the Abitibi cratonic mantle. Lithos 314–315, 520–533. https://doi.org/10.1016/J.LITHOS.2018.06.026

Lawley, C., McCafferty, A.E., Graham, G.E., Huston, D.L., Kelley, K.D., Czarnota, K., Paradis, S., Peter, J.M., Hayward, N., Barlow, M., Emsbo, P., Coyan, J., San Juan, C.A., Gadd, M.G., 2022. Data–driven prospectivity modelling of sediment–hosted Zn–Pb mineral systems and their critical raw materials. Ore Geol Rev 141, 104635. https://doi.org/10.1016/J.OREGEOREV.2021.104635

Lawley, C., Pearson, D.G., Waterton, P., Zagorevski, A., Bédard, J.H., Jackson, S.E., Petts, D.C., Kjarsgaard, B.A., Zhang, S., Wright, D., 2020a. Element and isotopic signature of re-fertilized mantle peridotite as determined by nanopowder and olivine LA-ICPMS analyses. Chem Geol 536, 119464. https://doi.org/10.1016/j.chemgeo.2020.119464

Lawley, C., Petts, D.C., Jackson, S.E., Zagorevski, A., Pearson, D.G., Kjarsgaard, B.A., Savard, D., Tschirhart, V., 2020b. Precious metal mobility during serpentinization and breakdown of base metal sulphide. Lithos 354–355, 105278. https://doi.org/10.1016/J.LITHOS.2019.105278

le Roux, V., Dick, H.J.B., Shimizu, N., 2014. Tracking flux melting and melt percolation in supra-subduction peridotites (Josephine ophiolite, USA). Contributions to Mineralogy and Petrology 168, 1–22. https://doi.org/10.1007/s00410-014-1064-9

Leake, B.E., Woolley, A.R., Arps, C.E.S., Birch, W.D., Gilbert, M.C., Grice, J.D., Hawthorne, F.C., Kato, A., Kisch, H.J., Krivovichev, V.G., Linthout, K., Laird, J., Mandarino, J.A., Maresch, W. v, Nickel, E.H., Rock, N.M.S., Schumacher, J.C., Smith, D.C., Stephenson, N.C.N., Ungaretti, L., Whittaker, E.J.W., Youzhi, G., 1997. Nomenclature of amphiboles; report of the subcommittee on amphiboles of the International

Mineralogical Association, Commission on New Minerals and Mineral Names. The Canadian Mineralogist 35, 219–246.

Leake, B.E., Woolley, A.R., Birch, W.D., J. Burke, E.A., Ferraris, G., Grice, J.D., Hawthorne, F.C., Kisch, H.J., Krivovichev, V.G., Schumacher, J.C., N. Stephenson, N.C., W. Whittaker, E.J., 2004. Nomenclature of amphiboles: additions and revisions to the International Mineralogical Association's amphibole nomenclature. Mineral Mag 68, 209–215. https://doi.org/10.1180/0026461046810182

Li, W., Soustelle, V., Jin, Z., Li, H., Chen, T., Tao, C., 2017. Origins of water content variations in the suboceanic upper mantle: Insight from Southwest Indian Ridge abyssal peridotites. Geochemistry, Geophysics, Geosystems 18, 1298–1329. https://doi.org/10.1002/2016GC006767

Li, Y.-B., Kimura, J.-I., Machida, S., Ishii, T., Ishiwatari, A., Maruyama, S., Qiu, H.-N., Ishikawa, T., Kato, Y., Haraguchi, S., Takahata, N., Hirahara, Y., Miyazaki, T., 2013. High-Mg Adakite and Low-Ca Boninite from a Bonin Fore-arc Seamount: Implications for the Reaction between Slab Melts and Depleted Mantle. Journal of Petrology 54, 1149–1175. https://doi.org/10.1093/PETROLOGY/EGT008

Loferski, P.J., Lipin, B.R., 1983. Exsolution in metamorphosed chromite from the Red Lodge District, Montana. American Mineralogist 68, 777–789.

Longerich, H.P., Jackson, S.E., Günther, D., 1996. Laser ablation inductively coupled plasma mass spectrometric transient signal data acquisition and analyte concentration calculation. J Anal At Spectrom 11, 899–904. https://doi.org/10.1039/JA9961100899

Lord, R.A., Prichard, H.M., Sá, J.H.S., Neary, C.R., 2004. Chromite Geochemistry and PGE Fractionation in the Campo Formoso Complex and Ipueira-Medrado Sill, Bahia State, Brazil. Economic Geology 99, 339–363. https://doi.org/10.2113/GSECONGEO.99.2.339

Mallmann, G., O'Neill, H.S.C., 2009. The Crystal/Melt Partitioning of V during Mantle Melting as a Function of Oxygen Fugacity Compared with some other Elements (Al, P, Ca, Sc, Ti, Cr, Fe, Ga, Y, Zr and Nb). Journal of Petrology 50, 1765–1794. https://doi.org/10.1093/PETROLOGY/EGP053

Marchesi, C., Garrido, C.J., Godard, M., Belley, F., Ferré, E., 2009. Migration and accumulation of ultra-depleted subduction-related melts in the Massif du Sud ophiolite (New Caledonia). Chem Geol 266, 171–186. https://doi.org/10.1016/J.CHEMGEO.2009.06.004

Marocchi, M., Hermann, J., Tropper, P., Bargossi, G.M., Mair, V., 2010. Amphibole and phlogopite in "hybrid" metasomatic bands monitor trace element transfer at the interface between felsic and ultramafic rocks (Eastern Alps, Italy). Lithos 117, 135–148. https://doi.org/10.1016/J.LITHOS.2010.02.011

Marocchi, M., Mair, V., Tropper, P., Bargossi, G.M., 2009. Metasomatic reaction bands at the Mt. Hochwart gneiss-peridotite contact (Ulten Zone, Italy): Insights into fluid-rock interaction in subduction zones. Mineral Petrol 95, 251–272. https://doi.org/10.1007/s00710-009-0043-8

Marques, J.C., Dias, J.R.V.P., Friedrich, B.M., Frantz, J.C., Queiroz, W.J.A., Botelho, N.F., 2017. Thick chromitite of the Jacurici Complex (NE Craton São Francisco, Brazil): Cumulate chromite slurry in a conduit. Ore Geol Rev 90, 131–147. https://doi.org/10.1016/J.OREGEOREV.2017.04.033

Marques, J.C., Ferreira Filho, C.F., Carlson, R.W., Pimentel, M.M., 2003. Re–Os and Sm–Nd Isotope and Trace Element Constraints on the Origin of the Chromite Deposit of the Ipueira–Medrado Sill, Bahia, Brazil. Journal of Petrology 44, 659–678. https://doi.org/10.1093/PETROLOGY/44.4.659

Marques, J.C., Filho, C.F.F., 2003. The Chromite Deposit of the Ipueira-Medrado Sill, São Francisco Craton, Bahia State, Brazil. Economic Geology 98, 87–108. https://doi.org/10.2113/GSECONGEO.98.1.87

Matsufuji, Y., Arai, S., Morishita, T., Ishida, Y., 2006. Petrology of exotic high-Mg, Cr peridotite bodies in the Horoman Peridotite Complex, Japan. Japanese Magazine of Mineralogical and Petrological Sciences 35, 231–243. https://doi.org/10.2465/gkk.35.231

Matzen, A.K., Baker, M.B., Beckett, J.R., Stolper, E.M., 2013. The temperature and pressure dependence of nickel partitioning between olivine and silicate melt. Journal of Petrology 54, 2521–2545. https://doi.org/10.1093/petrology/egt055

Maunder, B., Prytulak, J., Goes, S., Reagan, M., 2020. Rapid subduction initiation and magmatism in the Western Pacific driven by internal vertical forces. Nature Communications 2020 11:1 11, 1–8. https://doi.org/10.1038/s41467-020-15737-4

Maya, J.M., Bhutani, R., Balakrishnan, S., Rajee Sandhya, S., 2017. Petrogenesis of 3.15 Ga old Banasandra komatiites from the Dharwar craton, India: Implications for early mantle heterogeneity. Geoscience Frontiers 8, 467–481. https://doi.org/10.1016/J.GSF.2016.03.007

McDade, P., Blundy, J.D., Wood, B.J., 2003. Trace element partitioning on the Tinaquillo Lherzolite solidus at 1.5 GPa. Physics of the Earth and Planetary Interiors 139, 129–147. https://doi.org/10.1016/S0031-9201(03)00149-3

McIntyre, T., Pearson, D.G., Szilas, K., Morishita, T., 2019. Implications for the origins of Eoarchean ultramafic rocks of the North Atlantic Craton: a study of the Tussaap Ultramafic complex, Itsaq Gneiss complex, southern West Greenland. Contributions to Mineralogy and Petrology 174. https://doi.org/10.1007/s00410-019-1628-9

McIntyre, T., Waterton, P., Vezinet, A., Szilas, K., Pearson, D.G., 2021. Extent and age of Mesoarchean components in the Nagssugtoqidian orogen, West Greenland: Implications for tectonic environments and crust building in cratonic orogenic belts. Lithos 106182. https://doi.org/10.1016/j.lithos.2021.106182

Mckenzie, D., Bickle, M.J., 1988. The Volume and Composition of Melt Generated by Extension of the Lithosphere. Journal of Petrology 29, 625–679. https://doi.org/10.1093/PETROLOGY/29.3.625

Mikuni, K., Hirano, N., Akizawa, N., Yamamoto, J., Machida, S., Tamura, A., Hagiwara, Y., Morishita, T., 2022. Lithological structure of western Pacific lithosphere reconstructed from mantle xenoliths in a petit-spot volcano. Progress in Earth and Planetary Science 2022 9:1 9, 1–22. https://doi.org/10.1186/S40645-022-00518-Y

Miura, M., Arai, S., 2014. PLATINUM-GROUP ELEMENT AND MINERAL CHARACTERISTICS OF SUB-ARC CHROMITITE XENOLITHS FROM THE TAKASHIMA ALKALI BASALT, SOUTHWEST JAPAN ARC. The Canadian Mineralogist 52, 899–916. https://doi.org/10.3749/CANMIN.1300049

Miyazaki, Y., Korenaga, J., 2022. A wet heterogeneous mantle creates a habitable world in the Hadean. Nature 603, 86–90. https://doi.org/10.1038/s41586-021-04371-9

Mondal, S.K., Khatun, S., Prichard, H.M., Satyanarayanan, M., Kumar, G.R.R., 2019. Platinum-group element geochemistry of boninite-derived Mesoarchean chromitites and ultramafic-mafic cumulate rocks from the Sukinda Massif (Orissa, India). Ore Geol Rev 104, 722–744. https://doi.org/10.1016/J.OREGEOREV.2018.11.027

Mondal, S.K., Ripley, E.M., Li, C., Frei, R., 2006. The genesis of Archaean chromitites from the Nuasahi and Sukinda massifs in the Singhbhum Craton, India. Precambrian Res 148, 45–66. https://doi.org/10.1016/J.PRECAMRES.2006.04.001

Mondal, S.K., Zhou, M.F., 2010. Enrichment of PGE through interaction of evolved boninitic magmas with early formed cumulates in a gabbro-breccia zone of the Mesoarchean Nuasahi massif (eastern India). Miner Depos 45, 69–91. https://doi.org/10.1007/S00126-009-0264-0/FIGURES/11

Morishita, T., 2015. Ancient Melting Residual Peridotites Producing Variable Source Mantle beneath Mid-ocean Ridges: Detection and Geodynamic Implications. Journal of Geography (Chigaku Zasshi) 124, 333–354. https://doi.org/10.5026/jgeography.124.333

Morishita, T., Hara, K., Nakamura, K., Sawaguchi, T., Tamura, A., Arai, S., Okino, K., Takai, K., Kumagai, H., 2009. Igneous, Alteration and Exhumation Processes Recorded in Abyssal Peridotites and Related Fault Rocks from an Oceanic Core Complex along the Central Indian Ridge. Journal of Petrology 50, 1299–1325. https://doi.org/10.1093/petrology/egp025

Morishita, T., Ishida, Y., Arai, S., 2005a. Simultaneous determination of multiple trace element compositions in thin (<30.MU.m) layers of BCR-2G by 193 nm ArF excimer laser ablation-ICP-MS: implications for matrix effect and elemental fractionation on quantitative analysis. Geochem J 39, 327–340. https://doi.org/10.2343/geochemj.39.327

Morishita, T., Ishida, Y., Arai, S., Shirasaka, M., 2005b. Determination of Multiple Trace Element Compositions in Thin (> 30 μm) Layers of NIST SRM 614 and 616 Using Laser Ablation-Inductively Coupled Plasma-Mass Spectrometry (LA-ICP-MS). Geostand Geoanal Res 29, 107–122. https://doi.org/10.1111/j.1751-908x.2005.tb00659.x

Morishita, T., Maeda, J., Miyashita, S., Kumagai, H., Matsumoto, T., Dick, H.J.B., 2007. Petrology of local concentration of chromian spinel in dunite from the slow-spreading Southwest Indian Ridge. European Journal of Mineralogy 19, 871–882. https://doi.org/10.1127/0935-1221/2007/0019-1773

Morishita, T., Tani, K., Shukuno, H., Harigane, Y., Tamura, A., Kumagai, H., Hellebrand, E., 2011. Diversity of melt conduits in the Izu-Bonin-Mariana forearc mantle: Implications for the earliest stage of arc magmatism. Geology 39, 411–414. https://doi.org/10.1130/G31706.1

Morishita, T., Tani, K.I., Soda, Y., Tamura, A., Mizukami, T., Ghosh, B., 2018. The uppermost mantle section below a remnant proto-Philippine Sea island arc: Insights from the peridotite fragments from the Daito Ridge. American Mineralogist 103, 1151–1160. https://doi.org/10.2138/AM-2018-6030

Mukherjee, R., Mondal, S.K., González-Jiménez, J.M., Griffin, W.L., Pearson, N.J., O'Reilly, S.Y., 2015. Trace-element fingerprints of chromite, magnetite and sulfides from the 3.1 Ga ultramafic–mafic rocks of the Nuggihalli greenstone belt, Western Dharwar craton (India). Contributions to Mineralogy and Petrology 169, 1–23. https://doi.org/10.1007/S00410-015-1148-1/FIGURES/13

Mukherjee, R., Mondal, S.K., Rosing, M.T., Frei, R., 2010. Compositional variations in the Mesoarchean chromites of the Nuggihalli schist belt, Western Dharwar Craton (India): Potential parental melts and implications for tectonic setting. Contributions to Mineralogy and Petrology 160, 865–885. https://doi.org/10.1007/S00410-010-0511-5/FIGURES/8

Mukherjee, R., Mondal, S.K., Zhong, H., Bai, Z.J., Balaram, V., Ravindra Kumar, G.R., 2014. Platinum-group element geochemistry of komatiite-derived 3.1 Ga ultramafic–mafic rocks and chromitites from the Nuggihalli greenstone belt, Western Dharwar craton (India). Chem Geol 386, 190–208. https://doi.org/10.1016/J.CHEMGEO.2014.08.007

Nagahashi, T., Miyashita, S., 2002. Petrology of the greenstones of the Lower Sorachi Group in the Sorachi-Yezo Belt, central Hokkaido, Japan, with special reference to discrimination between oceanic plateau basalts and mid-oceanic ridge basalts. Island Arc 11, 122–141. https://doi.org/10.1046/j.1440-1738.2002.00361.x

Nägler, T.F., Kramers, J.D., Kamber, B.S., Frei, R., Prendergast, M.D.A., 1997. Growth of subcontinental lithospheric mantle beneath Zimbabwe started at or before 3.8 Ga: Re-Os study on chromites. Geology 983–986.

Naldrett, A.J., Kinnaird, J., Wilson, A., Yudovskaya, M., McQuade, S., Chunnett, G., Stanley, C., 2009. Chromite composition and PGE content of Bushveld chromitites: Part 1 – the Lower and Middle Groups. Applied Earth Science 118, 131–161. https://doi.org/10.1179/174327509X12550990458004

Nguyen, D., Morishita, T., Soda, Y., Tamura, A., Ghosh, B., Harigane, Y., France, L., Liu, C., Natland, J., Sanfilippo, A., MacLeod, C., Blum, P., Dick, H., 2018. Occurrence of Felsic Rocks in Oceanic Gabbros from IODP Hole U1473A: Implications for Evolved Melt Migration in the Lower Oceanic Crust. Minerals 8, 583. https://doi.org/10.3390/min8120583

Nicklas, R.W., Puchtel, I.S., Ash, R.D., Piccoli, P.M., Hanski, E., Nisbet, E.G., Waterton, P., Pearson, D.G., Anbar, A.D., 2019. Secular mantle oxidation across the Archean-Proterozoic boundary: Evidence from V partitioning in komatiites and picrites. Geochim Cosmochim Acta 250, 49–75. https://doi.org/10.1016/J.GCA.2019.01.037

Nishio, I., Itano, K., Waterton, P., Tamura, A., Szilas, K., Morishita, T., 2022a. Compositional Data Analysis (CoDA) of Clinopyroxene From Abyssal Peridotites. Geochemistry, Geophysics, Geosystems 23, e2022GC010472. https://doi.org/10.1029/2022GC010472

Nishio, I., Morishita, T., Itano, K., Guotana, J.M., Tamura, A., Szilas, K., Harigane, Y., Tani, K., Pearson, D.G., 2022b. Metasomatic Modification of the Mesoarchaean Ulamertoq Ultramafic Body, Southern West Greenland. Journal of Petrology 63. https://doi.org/10.1093/PETROLOGY/EGAC004

Nishio, I., Morishita, T., Szilas, K., Pearson, G., Tani, K.-I., Tamura, A., Harigane, Y., Guotana, J.M., Nishio, I., Morishita, T., Szilas, K., Pearson, G., Tani, K.-I., Tamura, A., Harigane, Y., Guotana, J.M., 2019. Titanian Clinohumite-Bearing Peridotite from the Ulamertoq Ultramafic Body in the 3.0 Ga Akia Terrane of Southern West Greenland. Geosciences (Basel) 9(4), 153. https://doi.org/10.3390/GEOSCIENCES9040153

Nishio, I., Morishita, T., Tamura, A., Itano, K., Takamizawa, S., Ichiyama, Y., Arai, S., Barrett, N., Szilas, K., 2023. Formation of Ultra-Depleted Mantle Peridotites and Their Relationship With Boninitic Melts: An Example From the Kamuikotan Unit, Hokkaido, Japan. J Geophys Res Solid Earth 128, e2022JB025066. https://doi.org/10.1029/2022JB025066

Niu, Y., 2004. Bulk-rock Major and Trace Element Compositions of Abyssal Peridotites: Implications for Mantle Melting, Melt Extraction and Post-melting Processes Beneath Mid-Ocean Ridges. Journal of Petrology 45, 2423–2458. https://doi.org/10.1093/petrology/egh068

Ozawa, K., 2001. Mass balance equations for open magmatic systems: Trace element behavior and its application to open system melting in the upper mantle. J Geophys Res Solid Earth 106, 13407–13434. https://doi.org/10.1029/2001JB900001

Ozawa, K., Nagahara, H., 2013. Elucidating thermal history of the earth based on information of earth materials: retrospect and prospect. Japanese Magazine of Mineralogical and Petrological Sciences 42, 136–155. https://doi.org/10.2465/gkk.121105

Ozawa, K., Shimizu, N., 1995. Open-system melting in the upper mantle: Constraints from the Hayachine-Miyamori ophiolite, northeastern Japan. J Geophys Res Solid Earth 100, 22315–22335. https://doi.org/10.1029/95JB01967

Padrón-Navarta, J.A., Sánchez-Vizcaíno, V.L., Hermann, J., Connolly, J.A.D., Garrido, C.J., Gómez-Pugnaire, M.T., Marchesi, C., 2013. Tschermak's substitution in antigorite and consequences for phase relations and water liberation in high-grade serpentinites. Lithos 178, 186–196. https://doi.org/10.1016/J.LITHOS.2013.02.001

Pagé, P., Barnes, S.J., 2016. The influence of chromite on osmium, iridium, ruthenium and rhodium distribution during early magmatic processes. Chem Geol 420, 51–68. https://doi.org/10.1016/J.CHEMGEO.2015.11.002

Pagé, P., Barnes, S.-J., 2009. Using Trace Elements in Chromites to Constrain the Origin of Podiform Chromitites in the Thetford Mines Ophiolite, Québec, Canada. Economic Geology 104, 997–1018. https://doi.org/10.2113/ECONGEO.104.7.997

Pagé, P., Barnes, S.J., Bédard, J.H., Zientek, M.L., 2012. In situ determination of Os, Ir, and Ru in chromites formed from komatiite, tholeiite and boninite magmas: Implications for chromite control of Os, Ir and Ru during partial melting and crystal fractionation. Chem Geol 302–303, 3–15. https://doi.org/10.1016/J.CHEMGEO.2011.06.006

Palin, R.M., Santosh, M., Cao, W., Li, S.S., Hernández-Uribe, D., Parsons, A., 2020. Secular change and the onset of plate tectonics on Earth. Earth Sci Rev. https://doi.org/10.1016/j.earscirev.2020.103172

Paquet, M., Day, J.M.D., Brown, D.B., Waters, C.L., 2022. Effective global mixing of the highly siderophile elements into Earth's mantle inferred from oceanic abyssal peridotites. Geochim Cosmochim Acta 316, 347–362. https://doi.org/10.1016/J.GCA.2021.09.033

Park, J.W., Kamenetsky, V., Campbell, I., Park, G., Hanski, E., Pushkarev, E., 2017. Empirical constraints on partitioning of platinum group elements between Cr-spinel and primitive terrestrial magmas. Geochim Cosmochim Acta 216, 393–416. https://doi.org/10.1016/J.GCA.2017.05.039

Parkinson, I.J., Pearce, J.A., 1998. Peridotites from the Izu–Bonin–Mariana Forearc (ODP Leg 125): Evidence for Mantle Melting and Melt–Mantle Interaction in a Supra-Subduction Zone Setting. Journal of Petrology 39, 1577–1618. https://doi.org/10.1093/PETROJ/39.9.1577

Parkinson, I.J., Pearce, J.A., Thirlwall, M.F., Johnson, K.T.M., Ingram, G., 1992. Trace element geochemistry of peridotites from the Izu-Bonin-Mariana Forearc, Leg 125. Proc., scientific results, ODP, Leg 125, Bonin/Mariana region 487–506. https://doi.org/10.2973/ODP.PROC.SR.125.183.1992

Parman, S.W., Grove, T.L., 2004. Harzburgite melting with and without H 2 O: Experimental data and predictive modeling . J Geophys Res Solid Earth 109. https://doi.org/10.1029/2003jb002566

Pearce, J.A., 2014. Immobile Element Fingerprinting of Ophiolites. Elements 10, 101–108. https://doi.org/10.2113/GSELEMENTS.10.2.101

Pearce, N.J.G., Perkins, W.T., Westgate, J.A., Gorton, M.P., Jackson, S.E., Neal, C.R., Chenery, S.P., 1997. A compilation of new and published major and trace element data for NIST SRM 610 and NIST SRM 612 glass reference materials. Geostandards Newsletter 21, 115–144. https://doi.org/10.1111/j.1751-908X.1997.tb00538.x

Pearson, D.G., Canil, D., Shirey, S.B., 2014. Mantle Samples Included in Volcanic Rocks: Xenoliths and Diamonds. Treatise on Geochemistry: Second Edition 3, 169–253. https://doi.org/10.1016/B978-0-08-095975-7.00216-3

Pearson, D.G., Nowell, G.M., 2002. The continental lithospheric mantle: characteristics and significance as a mantle reservoir. Philosophical Transactions of the Royal Society of London. Series A: Mathematical, Physical and Engineering Sciences 360, 2383–2410. https://doi.org/10.1098/rsta.2002.1074

Pearson, D.G., Scott, J.M., Liu, J., Schaeffer, A., Wang, L.H., van Hunen, J., Szilas, K., Chacko, T., Kelemen, P.B., 2021. Deep continental roots and cratons. Nature 596, 199–210. https://doi.org/10.1038/s41586-021-03600-5

Pirard, C., Hermann, J., O'neill, H.S.C., 2013. Petrology and Geochemistry of the Crust–Mantle Boundary in a Nascent Arc, Massif du Sud Ophiolite, New Caledonia, SW Pacific. Journal of Petrology 54, 1759–1792. https://doi.org/10.1093/PETROLOGY/EGT030

Prendergast, M.D., 2008. Archean Komatiitic Sill-hosted Chromite Deposits in the Zimbabwe Craton. Economic Geology 103, 981–1004. https://doi.org/10.2113/GSECONGEO.103.5.981

Prichard, H.M., Sà, J.H.S., Fisher, P.C., 2001. PLATINUM-GROUP MINERAL ASSEMBLAGES AND CHROMITE COMPOSITION IN THE ALTERED AND DEFORMED BACURI COMPLEX, AMAPA, NORTHEASTERN BRAZIL. The Canadian Mineralogist 39, 377–396. https://doi.org/10.2113/GSCANMIN.39.2.377

Puchtel, I.S., Humayun, M., Campbell, A.J., Sproule, R.A., Lesher, C.M., 2004. Platinum group element geochemistry of komatiites from the Alexo and Pyke Hill areas, Ontario, Canada. Geochim Cosmochim Acta 68, 1361–1383. https://doi.org/10.1016/J.GCA.2003.09.013

Puchtel, I.S., Touboul, M., Blichert-Toft, J., Walker, R.J., Brandon, A.D., Nicklas, R.W., Kulikov, V.S., Samsonov, A. V., 2016. Lithophile and siderophile element systematics of Earth's mantle at the Archean–

Proterozoic boundary: Evidence from 2.4 Ga komatiites. Geochim Cosmochim Acta 180, 227–255. https://doi.org/10.1016/J.GCA.2016.02.027

Qin, B., Huang, F., Huang, S., Python, A., Chen, Y., ZhangZhou, J., 2022. Machine Learning Investigation of Clinopyroxene Compositions to Evaluate and Predict Mantle Metasomatism Worldwide. J Geophys Res Solid Earth 127, e2021JB023614. https://doi.org/10.1029/2021JB023614

Ramírez-Cárdenas, C.A., Pujol-Solà, N., Proenza, J.A., Weber, M., Castillo-Oliver, M., Tobón, M., Garcia-Casco, A., 2023. Mantle-hosted ophiolitic chromitites from Colombia: implications for petrogenesis and geodynamic evolution. Int Geol Rev 1–28. https://doi.org/10.1080/00206814.2023.2228361

Rampone, E., Hofmann, A.W., 2012. A global overview of isotopic heterogeneities in the oceanic mantle. Lithos 148, 247–261. https://doi.org/10.1016/J.LITHOS.2012.06.018

Reagan, M.K., Ishizuka, O., Stern, R.J., Kelley, K.A., Ohara, Y., Blichert-Toft, J., Bloomer, S.H., Cash, J., Fryer, P., Hanan, B.B., Hickey-Vargas, R., Ishii, T., Kimura, J.I., Peate, D.W., Rowe, M.C., Woods, M., 2010. Fore-arc basalts and subduction initiation in the Izu-Bonin-Mariana system. Geochemistry, Geophysics, Geosystems 11, 3–12. https://doi.org/10.1029/2009GC002871

Rollinson, H., 2007. Recognising early Archaean mantle: A reappraisal. Contributions to Mineralogy and Petrology 154, 241–252. https://doi.org/10.1007/s00410-007-0191-y

Rollinson, H., 1997. The Archean komatiite-related Inyala Chromitite, southern Zimbabwe. Economic Geology 92, 98–107. https://doi.org/10.2113/GSECONGEO.92.1.98

Rollinson, H., Adetunji, J., Lenaz, D., Szilas, K., 2017. Archaean chromitites show constant Fe3 +/ΣFe in Earth's asthenospheric mantle since 3.8 Ga. Lithos 282–283, 316–325. https://doi.org/10.1016/J.LITHOS.2017.03.020

Rollinson, H., Appel, P.W.U., Frei, R., 2002. A Metamorphosed, Early Archaean Chromitite from West Greenland: Implications for the Genesis of Archaean Anorthositic Chromitites. Journal of Petrology 43, 2143–2170. https://doi.org/10.1093/PETROLOGY/43.11.2143

Rospabé, M., Ceuleneer, G., le Guluche, V., Benoit, M., Kaczmarek, M.A., 2021. The Chicken and Egg Dilemma Linking Dunites and Chromitites in the Mantle–Crust Transition Zone beneath Oceanic Spreading Centres: a Case Study of Chromite-hosted Silicate Inclusions in Dunites Formed at the Top of a Mantle Diapir (Oman Ophiolite). Journal of Petrology 62, 1–27. https://doi.org/10.1093/PETROLOGY/EGAB026

Sakakibara, M., Ota, T., 1994. Metamorphic evolution of the Kamuikotan high-pressure and low-temperature metamorphic rocks in central Hokkaido, Japan. J Geophys Res Solid Earth 99, 22221–22235. https://doi.org/10.1029/94JB00958

Sanfilippo, A., Tribuzio, R., Ottolini, L., Hamada, M., 2017. Water, lithium and trace element compositions of olivine from Lanzo South replacive mantle dunites (Western Alps): New constraints into melt migration processes at cold thermal regimes. Geochim Cosmochim Acta 214, 51–72. https://doi.org/10.1016/j.gca.2017.07.034

Sanfilippo, A., Tribuzio, R., Tiepolo, M., 2014. Mantle-crust interactions in the oceanic lithosphere: Constraints from minor and trace elements in olivine. Geochim Cosmochim Acta 141, 423–439. https://doi.org/10.1016/j.gca.2014.06.012

Santosh, M., He, X.F., Waterton, P., Szilas, K., Pearson, D.G., 2020. Chromitites from an Archean layered intrusion in the Western Dharwar Craton, southern India. Lithos 376–377, 105772. https://doi.org/10.1016/J.LITHOS.2020.105772

Savard, D., Barnes, S.J., Meisel, T., 2010. Comparison between Nickel-Sulfur Fire Assay Te Co-precipitation and Isotope Dilution with High-Pressure Asher Acid Digestion for the Determination of Platinum-Group Elements, Rhenium and Gold. Geostand Geoanal Res 34, 281–291. https://doi.org/10.1111/J.1751-908X.2010.00090.X

Sawada, H., Morishita, T., Vezinet, A., Stern, R., Tani, K., Nishio, I., Takahashi, K., Graham Pearson, D., Szilas, K., 2023. Zircon within chromitite requires revision of the tectonic history of the Eoarchean Itsaq Gneiss complex, Greenland. Geoscience Frontiers 14, 101648. https://doi.org/10.1016/J.GSF.2023.101648

Schneider, C.A., Rasband, W.S., Eliceiri, K.W., 2012. NIH Image to ImageJ: 25 years of image analysis. Nat Methods. https://doi.org/10.1038/nmeth.2089

Schoneveld, L., Barnes, S., Puchtel, I.S., Tessalina, S., Locmelis, M., 2022. Distributions of Platinum Group Elements and Re-Os Isotope Systematics in Chromite from the Coobina Chromitite Deposit in Western Australia: Implications for Chromite as a Sulfide Mineralization Indicator. The Canadian Mineralogist 60, 1045–1069. https://doi.org/10.3749/CANMIN.2200006

Scott, J.M., Liu, J., Pearson, D.G., Harris, G.A., Czertowicz, T.A., Woodland, S.J., Riches, A.J.V., Luth, R.W., 2019. Continent stabilisation by lateral accretion of subduction zone-processed depleted mantle residues; insights from Zealandia. Earth Planet Sci Lett 507, 175–186. https://doi.org/10.1016/j.epsl.2018.11.039

Scott, J.M., Liu, J., Pearson, D.G., Waight, T.E., 2016. Mantle depletion and metasomatism recorded in orthopyroxene in highly depleted peridotites. Chem Geol 441, 280–291. https://doi.org/10.1016/j.chemgeo.2016.08.024

Searle, R., 2013. Mid-Ocean Ridges, Mid-Ocean Ridges. Cambridge University Press. https://doi.org/10.1017/CBO9781139084260

Secchiari, A., Gleissner, P., Li, C., Goncharov, A., Milke, R., Becker, H., Bosch, D., Montanini, A., 2020a. Highly siderophile and chalcophile element behaviour in abyssal-type and supra-subduction zone mantle: New insights from the New Caledonia ophiolite. Lithos 354–355, 105338. https://doi.org/10.1016/J.LITHOS.2019.105338

Secchiari, A., Montanini, A., Bosch, D., Macera, P., Cluzel, D., 2020b. Sr, Nd, Pb and trace element systematics of the New Caledonia harzburgites: Tracking source depletion and contamination processes in a SSZ setting. Geoscience Frontiers 11, 37–55. https://doi.org/10.1016/J.GSF.2019.04.004

Seyler, M., Brunelli, D., 2018. Sodium-chromium covariation in residual clinopyroxenes from abyssal peridotites sampled in the 43°–46°E region of the Southwest Indian Ridge. Lithos 302–303, 142–157. https://doi.org/10.1016/J.LITHOS.2017.12.018

Seyler, M., Lorand, J.P., Dick, H.J.B., Drouin, M., 2007. Pervasive melt percolation reactions in ultra-depleted refractory harzburgites at the Mid-Atlantic Ridge, 15° 20′N: ODP Hole 1274A. Contributions to Mineralogy and Petrology 153, 303–319. https://doi.org/10.1007/S00410-006-0148-6/FIGURES/8

Sharpe, M.R., Hulbert, L.J., 1985. Ultramafic sills beneath the eastern Bushveld complex: mobilized suspensions of early lower zone cumulates in a parental magma with boninitic affinities. Economic Geology 80, 849–871. https://doi.org/10.2113/gsecongeo.80.4.849

Shaw, D.M., 1979. Trace element melting models. Physics and Chemistry of the Earth 11, 577–586. https://doi.org/10.1016/0079-1946(79)90055-7

Shervais, J.W., 2022. The petrogenesis of modern and ophiolitic lavas reconsidered: Ti-V and Nb-Th. Geoscience Frontiers 13, 101319. https://doi.org/10.1016/J.GSF.2021.101319

Shervais, J.W., 1982. Ti-V plots and the petrogenesis of modern and ophiolitic lavas. Earth Planet Sci Lett 59, 101–118. https://doi.org/10.1016/0012-821X(82)90120-0

Shimizu, K., Liang, Y., Sun, C., Jackson, C.R.M., Saal, A.E., 2017. Parameterized lattice strain models for REE partitioning between amphibole and silicate melt. American Mineralogist 102, 2254–2267. https://doi.org/10.2138/am-2017-6110

Shirey, S.B., Richardson, S.H., 2011. Start of the wilson cycle at 3 Ga shown by diamonds from subcontinental mantle. Science (1979) 333, 434–436. https://doi.org/10.1126/science.1206275

Siepierski, L., Ferreira Filho, C.F., 2016. Spinifex-textured komatiites in the south border of the Carajas ridge, Selva Greenstone belt, Carajás Province, Brazil. J South Am Earth Sci 66, 41–55. https://doi.org/10.1016/J.JSAMES.2015.12.011

Sievwright, R.H., O'Neill, H.S.C., Tolley, J., Wilkinson, J.J., Berry, A.J., 2020. Diffusion and partition coefficients of minor and trace elements in magnetite as a function of oxygen fugacity at 1150 ºC. Contributions to Mineralogy and Petrology 175, 1–21. https://doi.org/10.1007/S00410-020-01679-Z/FIGURES/13

Silantyev, S.A., Bortnikov, N.S., Shatagin, K.N., Bychkova, Y. v., Krasnova, E.A., Bel'tenev, V.E., 2015. Peridotite-basalt association at MAR between 19°42′ and 19°59′ N: Evaluation of petrogenetic conditions and material balance during hydrothermal transformation of the oceanic crust. Petrology 2015 23:1 23, 1–21. https://doi.org/10.1134/S0869591115010051

Silantyev, S.A., Novoselov, A.A., Mironenko, M. v., 2011. Hydrothermal systems in peridotites at slow-spreading ridges. Modeling phase transformations and material balance: Role of gabbroids. Petrology 2011 19:3 19, 217–236. https://doi.org/10.1134/S0869591111030027

Smith, W.D., Maier, W.D., 2021. The geotectonic setting, age and mineral deposit inventory of global layered intrusions. Earth Sci Rev 220, 103736. https://doi.org/10.1016/J.EARSCIREV.2021.103736

Søager, N., Portnyagin, M., Hoernle, K., Holm, P.M., Garbe-Schönberg, D., 2018. Constraints on lithosphere-asthenosphere melt mixing in basaltic intraplate volcanism from olivine melt inclusions from southern Payenia, Argentina. Lithos 310–311, 225–240. https://doi.org/10.1016/J.LITHOS.2018.04.011

Sossi, P.A., Eggins, S.M., Nesbitt, R.W., Nebel, O., Hergt, J.M., Campbell, I.H., O'Neill, H.S.C., Kranendonk, M. Van, Rhodri Davies, D., 2016. Petrogenesis and Geochemistry of Archean Komatiites. Journal of Petrology 57, 147–184. https://doi.org/10.1093/PETROLOGY/EGW004

Spier, C.A., Ferreira Filho, C.F., Daczko, N., 2022. Zircon U-Pb isotopic and geochemical study of metanorites from the chromite-mineralised Bacuri Mafic-Ultramafic Complex: Insights of a Paleoarchean crust in the Amapá Block, Guyana Shield, Brazil. Gondwana Research 105, 262–289. https://doi.org/10.1016/J.GR.2021.09.010

Spier, C.A., Filho, C.F.F., 2001. The Chromite Deposits of the Bacuri Mafic-Ultramafic Layered Complex, Guyana Shield, Amapá State, Brazil. Economic Geology 96, 817–835. https://doi.org/10.2113/GSECONGEO.96.4.817

Staddon, L.G., Parkinson, I.J., Cavosie, A.J., Elliott, T., Valley, J.W., Fournelle, J., Kemp, A.I.S., Shirey, S.B., 2021. Detrital Chromite from Jack Hills, Western Australia: Signatures of Metamorphism and Constraints on Provenance. Journal of Petrology 62. https://doi.org/10.1093/PETROLOGY/EGAB052

Stracke, A., Willig, M., Genske, F., Béguelin, P., Todd, E., 2022. Chemical Geodynamics Insights From a Machine Learning Approach. Geochemistry, Geophysics, Geosystems 23, e2022GC010606. https://doi.org/10.1029/2022GC010606

Streckeisen, A., 1976. To each plutonic rock its proper name. Earth Science Reviews 12, 1–33. https://doi.org/10.1016/0012-8252(76)90052-0

Su, B., Chen, Y., Guo, S., Chu, Z.Y., Liu, J.B., Gao, Y.J., 2016. Carbonatitic metasomatism in orogenic dunites from Lijiatun in the Sulu UHP terrane, eastern China. Lithos 262, 266–284. https://doi.org/10.1016/j.lithos.2016.07.007

Su, B.X., Bai, Y., Cui, M.M., Wang, J., Xiao, Y., Lenaz, D., Sakyi, P.A., Robinson, P.T., 2020. Petrogenesis of the Ultramafic Zone of the Stillwater Complex in North America: constraints from mineral chemistry and stable isotopes of Li and O. Contributions to Mineralogy and Petrology 175, 1–20. https://doi.org/10.1007/S00410-020-01707-Y/FIGURES/11

Sun, S.S., McDonough, W.F., 1989. Chemical and isotopic systematics of oceanic basalts: Implications for mantle composition and processes. Geol Soc Spec Publ 42, 313–345. https://doi.org/10.1144/GSL.SP.1989.042.01.19

Szilas, K., Kelemen, P.B., Bernstein, S., 2015. Peridotite enclaves hosted by Mesoarchaean TTG-suite orthogneisses in the Fiskefjord region of southern West Greenland. GeoResJ 7, 22–34. https://doi.org/10.1016/j.grj.2015.03.003

Szilas, K., Tusch, J., Hoffmann, J.E., Garde, A.A., Münker, C., 2017. Hafnium isotope constraints on the origin of Mesoarchaean andesites in southern West Greenland, North Atlantic Craton. Geol Soc Spec Publ 449, 19–38. https://doi.org/10.1144/SP449.2

Szilas, K., van Hinsberg, V., McDonald, I., Morishita, T., Pearson, D.G., 2016. Highly Depleted Peridotites within Mesoarchaean Orthogneiss at the Seqi Olivine Mine, SW Greenland – Potential Implications for the Formation of Cratonic Keels, in: Goldschmidt. Yokohama, p. 3009.

Szilas, K., van Hinsberg, V., McDonald, I., Næraa, T., Rollinson, H., Adetunji, J., Bird, D., 2018. Highly refractory Archaean peridotite cumulates: Petrology and geochemistry of the Seqi Ultramafic Complex, SW Greenland. Geoscience Frontiers. https://doi.org/10.1016/j.gsf.2017.05.003

Szilas, K., van Hinsberg, V.J., Creaser, R.A., Kisters, A.F.M., 2014. The geochemical composition of serpentinites in the Mesoarchaean Tartoq Group, SW Greenland: Harzburgitic cumulates or melt-modified mantle? Lithos 198–199, 103–116. https://doi.org/10.1016/j.lithos.2014.03.024

Takahashi, E., Uto, K., Schilling, J., 1987. Primary magma compositions and Mg/Fe ratios of their mantle residues along Mid Atlantic Ridge 29° to 73° N. Institute for Study of the Earth's Interior, Okayama University.

Takashima, R., Kawabe, F., Nishi, H., Moriya, K., Wani, R., Ando, H., 2004. Geology and stratigraphy of forearc basin sediments in Hokkaido, Japan: Cretaceous environmental events on the north-west Pacific margin. Cretac Res 25, 365–390. https://doi.org/10.1016/J.CRETRES.2004.02.004

Takashima, R., Nishi, H., Yoshida, T., 2002. Geology, petrology and tectonic setting of the Late Jurassic ophiolite in Hokkaido, Japan. J Asian Earth Sci 21, 197–215. https://doi.org/10.1016/S1367-9120(02)00028-7

Takazawa, E., Frey, F., Shimizu, N., Obata, M., 1996. Evolution of the Horoman Peridotite (Hokkaido, Japan): Implications from pyroxene compositions. Chem Geol 134, 3–26. https://doi.org/10.1016/S0009-2541(96)00083-6

Takazawa, E., Okayasu, T., Satoh, K., 2003. Geochemistry and origin of the basal lherzolites from the northern Oman ophiolite (northern Fizh block). Geochemistry, Geophysics, Geosystems 4, 1021. https://doi.org/10.1029/2001GC000232

Takeshita, T., Hirajima, T., Ueda, H., Okamoto, A.S., Kinoshita, S., Shin, W., Kota, R., Ando, M., Nakayama, T., 2018. Tectonics in the Kamuikotan belt: The Journal of the Geological Society of Japan 124, 491–515. https://doi.org/10.5575/geosoc.2018.0041

Tamblyn, R., Hermann, J., 2023. A rock record of H2 production in the ancient Earth. Nature Geoscience 2023 1–2. https://doi.org/10.1038/s41561-023-01321-0

Tamblyn, R., Hermann, J., Hasterok, D., Sossi, P., Pettke, T., Chatterjee, S., 2023. Hydrated komatiites as a source of water for TTG formation in the Archean. Earth Planet Sci Lett 603, 117982. https://doi.org/10.1016/J.EPSL.2022.117982

Tamura, A., Arai, S., 2006. Geochemistry of clinopyroxene in peridotites from the Nukabira complex, Kamuikotan zone, Hokkaido, Japan : a LA-ICP-MS study. The science reports of the Kanazawa University 1–27.

Tamura, A., Arai, S., 2005. Unmixed spinel in chromitite from the Iwanai-dake peridotite complex, Hokkaido, Japan: A reaction between peridotite and high oxidized magma in the mantle wedge. American Mineralogist 90, 473–480. https://doi.org/10.2138/am.2005.1570

Tamura, A., Arai, S., Ishimaru, S., Andal, E.S., 2008. Petrology and geochemistry of peridotites from IODP Site U1309 at Atlantis Massif, MAR 30°N: Micro- and macro-scale melt penetrations into peridotites. Contributions to Mineralogy and Petrology 155, 491–509. https://doi.org/10.1007/s00410-007-0254-0

Tamura, A., Makita, M., Arai, S., 1999. Petrogenesis of ultramafic rocks in the Kamuikotan belt, Hokkaido, northern Japan. The Memoirs of the Geological Society of Japan. 52, 53–68.

Tamura, A., Morishita, T., Ishimaru, S., Arai, S., 2014. Geochemistry of spinel-hosted amphibole inclusions in abyssal peridotite: Insight into secondary melt formation in melt-peridotite reaction. Contributions to Mineralogy and Petrology 167, 1–16. https://doi.org/10.1007/S00410-014-0974-X/FIGURES/10

Tamura, A., Nishio, I., Iwata, Y., Arai, S., Morishita, T., 2024. Amphibole in ultra-depleted peridotites from the Horokanai ophiolite, Hokkaido, Japan: Boninite melt trapped in the mantle wedge. Ofioliti Accepted.

Tilhac, R., Morishita, T., Hanaue, N., Tamura, A., Guotana, J.M., 2021. Systematic LREE enrichment of mantle harzburgites: The petrogenesis of San Carlos xenoliths revisited. Lithos 106195. https://doi.org/10.1016/j.lithos.2021.106195

Tomlinson, E.L., Kamber, B.S., 2021. Depth-dependent peridotite-melt interaction and the origin of variable silica in the cratonic mantle. Nature Communications 2021 12:1 12, 1–15. https://doi.org/10.1038/s41467-021-21343-9

Toramaru, A., Fujii, N., 1986. Connectivity of melt phase in a partially molten peridotite. J Geophys Res Solid Earth 91, 9239–9252. https://doi.org/10.1029/JB091IB09P09239

Ueda, H., 2010. Structural Evolution of Forearcs by Subduction Erosion of Accretionary Complex. Chigaku Zasshi (Jounal of Geography) 119, 362–377. https://doi.org/10.5026/jgeography.119.362

Ueki, K., Hino, H., Kuwatani, T., 2018. Geochemical Discrimination and Characteristics of Magmatic Tectonic Settings: A Machine-Learning-Based Approach. Geochemistry, Geophysics, Geosystems 19, 1327–1347. https://doi.org/10.1029/2017GC007401

Ulrich, M., Picard, C., Guillot, S., Chauvel, C., Cluzel, D., Meffre, S., 2010. Multiple melting stages and refertilization as indicators for ridge to subduction formation: The New Caledonia ophiolite. Lithos 115, 223–236. https://doi.org/10.1016/J.LITHOS.2009.12.011

Umino, S., Kanayama, K., Kitamura, K., Tamura, A., Ishizuka, O., Senda, R., Arai, S., 2018. Did boninite originate from the heterogeneous mantle with recycled ancient slab? Island Arc 27, e12221. https://doi.org/10.1111/iar.12221

Umino, S., Kitamura, K., Kanayama, K., Tamura, A., Sakamoto, N., Ishizuka, O., Arai, S., 2015. Thermal and chemical evolution of the subarc mantle revealed by spinel-hosted melt inclusions in boninite from the Ogasawara (bonin) Archipelago, Japan. Geology 43, 151–154. https://doi.org/10.1130/G36191.1

Uno, M., Okamoto, A., Tsuchiya, N., 2017. Excess water generation during reaction-inducing intrusion of granitic melts into ultramafic rocks at crustal P–T conditions in the Sør Rondane Mountains of East Antarctica. Lithos 284–285, 625–641. https://doi.org/10.1016/j.lithos.2017.04.016

Urann, B.M., Dick, H.J.B., Parnell-Turner, R., Casey, J.F., 2020. Recycled arc mantle recovered from the Mid-Atlantic Ridge. Nature Communications 2020 11:1 11, 1–9. https://doi.org/10.1038/s41467-020-17604-8

van de Löcht, J., Hoffmann, J.E., Li, C., Wang, Z., Becker, H., Rosing, M.T., Kleinschrodt, R., Münker, C., 2018. Earth's oldest mantle peridotites show entire record of late accretion. Geology 46, 199–202. https://doi.org/10.1130/G39709.1

van de Löcht, J., Hoffmann, J.E., Rosing, M.T., Sprung, P., Münker, C., 2020. Preservation of Eoarchean mantle processes in ~3.8 Ga peridotite enclaves in the Itsaq Gneiss Complex, southern West Greenland. Geochim Cosmochim Acta 280, 1–25. https://doi.org/10.1016/j.gca.2020.03.043

Vaughan, A.P.M., Scarrow, J.H., 2003. Ophiolite obduction pulses as a proxy indicator of superplume events? Earth Planet Sci Lett 213, 407–416. https://doi.org/10.1016/S0012-821X(03)00330-3

Walker, R.J., Prichard, H.M., Ishiwatari, A., Pimentel, M., 2002. The osmium isotopic composition of convecting upper mantle deduced from ophiolite chromites. Geochim Cosmochim Acta 66, 329–345. https://doi.org/10.1016/S0016-7037(01)00767-0

Wallis, S.R., Yamaoka, K., Mori, H., Ishiwatari, A., Miyazaki, K., Ueda, H., 2020. The basement geology of Japan from A to Z. Island Arc. https://doi.org/10.1111/iar.12339

Walsh, C., Kamber, B.S., Tomlinson, E.L., 2023. Deep, ultra-hot-melting residues as cradles of mantle diamond. Nature 2023 615:7952 615, 450–454. https://doi.org/10.1038/s41586-022-05665-2

Walter, M.J., 2014. Melt Extraction and Compositional Variability in Mantle Lithosphere. Treatise on Geochemistry: Second Edition 3, 393–419. https://doi.org/10.1016/B978-0-08-095975-7.00208-4

Wang, C., Liang, Y., Dygert, N., Xu, W., 2016. Formation of orthopyroxenite by reaction between peridotite and hydrous basaltic melt: an experimental study. Contributions to Mineralogy and Petrology 171, 1–18. https://doi.org/10.1007/s00410-016-1287-z

Wang, C., Liang, Y., Xu, W., 2021. Formation of Amphibole-Bearing Peridotite and Amphibole-Bearing Pyroxenite Through Hydrous Melt-Peridotite Reaction and In Situ Crystallization: An Experimental Study. J Geophys Res Solid Earth 126, e2020JB019382. https://doi.org/10.1029/2020JB019382

Wang, C., Liang, Y., Xu, W., Dygert, N., 2013. Effect of melt composition on basalt and peridotite interaction: Laboratory dissolution experiments with applications to mineral compositional variations in mantle xenoliths from the North China Craton. Contributions to Mineralogy and Petrology 166, 1469–1488. https://doi.org/10.1007/s00410-013-0938-6

Wang, J., Zhou, H., Salters, V., Liu, Y., Sachi-Kocher, A., Dick, H., 2019. Mantle melting variation and refertilization beneath the Dragon Bone amagmatic segment (53°E SWIR): Major and trace element compositions of peridotites at ridge flanks. Lithos 324–325, 325–339. https://doi.org/10.1016/J.LITHOS.2018.11.014

Warren, J.M., 2016. Global variations in abyssal peridotite compositions. Lithos 248–251, 193–219. https://doi.org/10.1016/j.lithos.2015.12.023

Warren, J.M., Shimizu, N., 2010. Cryptic Variations in Abyssal Peridotite Compositions: Evidence for Shallow-level Melt Infiltration in the Oceanic Lithosphere. Journal of Petrology 51, 395–423. https://doi.org/10.1093/PETROLOGY/EGP096

Waterton, P., Arndt, N., 2024. Komatiites: thier geochemistry and origins, in: The Archaean Earth: Tempos and Events (2nd Edition of The Precambrian 12Earth). Elsevier.

Waterton, P., Guotana, J.M., Nishio, I., Morishita, T., Tani, K., Woodland, S., Legros, H., Pearson, D.G., Szilas, K., 2022. No mantle residues in the Isua Supracrustal Belt. Earth Planet Sci Lett 579, 117348. https://doi.org/10.1016/J.EPSL.2021.117348

Waterton, P., Hyde, W.R., Tusch, J., Hollis, J.A., Kirkland, C.L., Kinney, C., Yakymchuk, C., Gardiner, N.J., Zakharov, D., Olierook, H.K.H., Lightfoot, P.C., Szilas, K., 2020a. Geodynamic Implications of Synchronous Norite and TTG Formation in the 3 Ga Maniitsoq Norite Belt, West Greenland. Front Earth Sci (Lausanne) 8, 1. https://doi.org/10.3389/feart.2020.562062

Waterton, P., Mungall, J., Pearson, D.G., 2021. The komatiite-mantle platinum-group element paradox. Geochim Cosmochim Acta 313, 214–242. https://doi.org/10.1016/J.GCA.2021.07.037

Waterton, P., Pearson, D.G., Mertzman, S.A., Mertzman, K.R., Kjarsgaard, B.A., 2020b. A Fractional Crystallization Link between Komatiites, Basalts, and Dunites of the Palaeoproterozoic Winnipegosis Komatiite Belt, Manitoba, Canada. Journal of Petrology 61, 52. https://doi.org/10.1093/petrology/egaa052

Webb, A.A.G., Müller, T., Zuo, J., Haproff, P.J., Ramírez-Salazar, A., 2020. A non–plate tectonic model for the Eoarchean Isua supracrustal belt. Lithosphere. https://doi.org/10.1130/l1130.1

Wei, C., Powell, R., 2004. Calculated Phase Relations in High-Pressure Metapelites in the System NKFMASH (Na2O–K2O–FeO–MgO–Al2O3–SiO2–H2O). Journal of Petrology 45, 183–202. https://doi.org/10.1093/PETROLOGY/EGG085

Whattam, S.A., 2023a. Subduction initiation ophiolites of the SW Pacific II: second-stage melts of boninites, high-Mg andesites, and related rocks. Int Geol Rev. https://doi.org/10.1080/00206814.2023.2273374

Whattam, S.A., 2023b. Subduction initiation ophiolites of the SW Pacific I: first-formed MORB-like lavas. Int Geol Rev. https://doi.org/10.1080/00206814.2023.2248489

White, R.W., Palin, R.M., Green, E.C.R., 2017. High-grade metamorphism and partial melting in Archean composite grey gneiss complexes. Journal of Metamorphic Geology 35, 181–195. https://doi.org/10.1111/jmg.12227

White, R.W., Powell, R., Phillips, G.N., 2003. A mineral equilibria study of the hydrothermal alteration in mafic greenschist facies rocks at Kalgoorlie, Western Australia. Journal of Metamorphic Geology 21, 455–468. https://doi.org/10.1046/J.1525-1314.2003.00454.X

Whitney, D.L., Evans, B.W., 2010. Abbreviations for names of rock-forming minerals. American Mineralogist 95, 185–187. https://doi.org/10.2138/am.2010.3371

Whyatt, L., Peters, S., Pack, A., Kirkland, C.L., Balic-Zunic, T., Szilas, K., 2020. Metasomatic Reactions between Archean Dunite and Trondhjemite at the Seqi Olivine Mine in Greenland. Minerals 10, 85. https://doi.org/10.3390/min10010085

Wilde, S.A., Valley, J.W., Peck, W.H., Graham, C.M., 2001. Evidence from detrital zircons for the existence of continental crust and oceans on the Earth 4.4 Gyr ago. Nature 409, 175–178. https://doi.org/10.1038/35051550

Wilson, A.H., 1982. The Geology of the Great 'Dyke', Zimbabwe: The Ultramafic Rocks. Journal of Petrology 23, 240–292. https://doi.org/10.1093/PETROLOGY/23.2.240

Wilson, A.H., Prendergast, M.D., 2001. Platinum-Group Element Mineralisation in the Great Dyke, Zimbabwe, and its Relationship to Magma Evolution and Magma Chamber Structure. South African Journal of Geology 104, 319–342. https://doi.org/10.2113/GSSAJG.104.4.319

Windley, B.F., Garde, A.A., 2009. Arc-generated blocks with crustal sections in the North Atlantic craton of West Greenland: Crustal growth in the Archean with modern analogues. Earth Sci Rev. https://doi.org/10.1016/j.earscirev.2008.12.001

Wittig, N., Pearson, D.G., Webb, M., Ottley, C.J., Irvine, G.J., Kopylova, M., Jensen, S.M., Nowell, G.M., 2008. Origin of cratonic lithospheric mantle roots: A geochemical study of peridotites from the North Atlantic Craton, West Greenland. Earth Planet Sci Lett 274, 24–33. https://doi.org/10.1016/j.epsl.2008.06.034

Woodland, S.J., Pearson, D.G., Thirlwall, M.F., 2002. A Platinum Group Element and Re–Os Isotope Investigation of Siderophile Element Recycling in Subduction Zones: Comparison of Grenada, Lesser Antilles Arc, and the Izu–Bonin Arc. Journal of Petrology 43, 171–198. https://doi.org/10.1093/PETROLOGY/43.1.171

Workman, R.K., Hart, S.R., 2005. Major and trace element composition of the depleted MORB mantle (DMM). Earth Planet Sci Lett 231, 53–72. https://doi.org/10.1016/j.epsl.2004.12.005

Wu, W., Yang, J., Zheng, J., Lian, D., Milushi, I., Yang, Y., Qiu, T., Rui, H., Guo, G., Dai, Z., Masoud, A.E.I., 2022. The earliest stage of mantle-melt evolution during subduction initiation: Evidence from the Neo-Tethyan Mirdita Ophiolite, Albania. Lithos 434–435, 106937. https://doi.org/10.1016/J.LITHOS.2022.106937

Xu, Y., Liu, C. zhou, Lin, W., 2021. Melt extraction and reaction in the forearc mantle: Constraints from trace elements and isotope geochemistry of ultra-refractory peridotites of the New Caledonia Peridotite Nappe. Lithos 380–381, 105882. https://doi.org/10.1016/j.lithos.2020.105882

Xu, Y., Liu, C.Z., Lin, W., Shi, X.F., 2022. Ancient depletion signals in lherzolites from forearc region: Constraints from Lu-Hf isotope compositions. Geoscience Frontiers 13, 101259. https://doi.org/10.1016/J.GSF.2021.101259

Yakymchuk, C., Kirkland, C.L., Cavosie, A.J., Szilas, K., Hollis, J., Gardiner, N.J., Waterton, P., Steenfelt, A., Martin, L., 2021. Stirred not shaken; critical evaluation of a proposed Archean meteorite impact in West Greenland. Earth Planet Sci Lett 557, 116730. https://doi.org/10.1016/j.epsl.2020.116730

Yakymchuk, C., Kirkland, C.L., Hollis, J.A., Kendrick, J., Gardiner, N.J., Szilas, K., 2020. Mesoarchean partial melting of mafic crust and tonalite production during high-T–low-P stagnant tectonism, Akia Terrane, West Greenland. Precambrian Res 339, 105615. https://doi.org/10.1016/j.precamres.2020.105615

Yao, Z., Mungall, J.E., Jenkins, M.C., 2021. The Rustenburg Layered Suite formed as a stack of mush with transient magma chambers. Nature Communications 2021 12:1 12, 1–13. https://doi.org/10.1038/s41467-020-20778-w

Yoshida, K., Kuwatani, T., Hirajima, T., Iwamori, H., Akaho, S., 2018. Progressive evolution of whole-rock composition during metamorphism revealed by multivariate statistical analyses. Journal of Metamorphic Geology 36, 41–54. https://doi.org/10.1111/JMG.12282

Yu, C., Zhong, R., Tomkins, A.G., Cui, H., Chen, Y., 2023. Expanding the metamorphic devolatilization model: Komatiites as a source for orogenic gold deposits in high-grade metamorphic rocks. Geology. https://doi.org/10.1130/G51446.1

Yudovskaya, M.A., Naldrett, A.J., Woolfe, J.A.S., Costin, G., Kinnaird, J.A., 2015. Reverse Compositional Zoning in the Uitkomst Chromitites as an Indication of Crystallization in a Magmatic Conduit. Journal of Petrology 56, 2373–2394. https://doi.org/10.1093/PETROLOGY/EGV062

Zemeny, A., Kinney, C., Yakymchuk, C., Olierook, H.K.H., Kirkland, C.L., Gardiner, N., Szilas, K., 2023. Mesoarchaean peridotite-norite cumulates of SW Greenland – The Miaggoq ultramafic complex. Lithos 458–459, 107352. https://doi.org/10.1016/J.LITHOS.2023.107352

Zhang, L., Hyde, W.R., Kirkland, C.L., Han, Y., Szilas, K., 2023. Geochemical and thermodynamic constraints on Archean comagmatic volcanic and cumulate rocks from southern West Greenland. Geochim Cosmochim Acta 348, 122–139. https://doi.org/10.1016/J.GCA.2023.03.005

Zhang, L., Szilas, K., 2024. Eoarchean ultramafic rocks represent crustal cumulates: A case study of the Narssaq ultramafic body, southern West Greenland. Earth Planet Sci Lett 625, 118508. https://doi.org/10.1016/J.EPSL.2023.118508

8 Appendix

8.1 Supplementary information for chapter 2

Figure A1 Global distribution of residual abyssal peridotites (n = 1162)

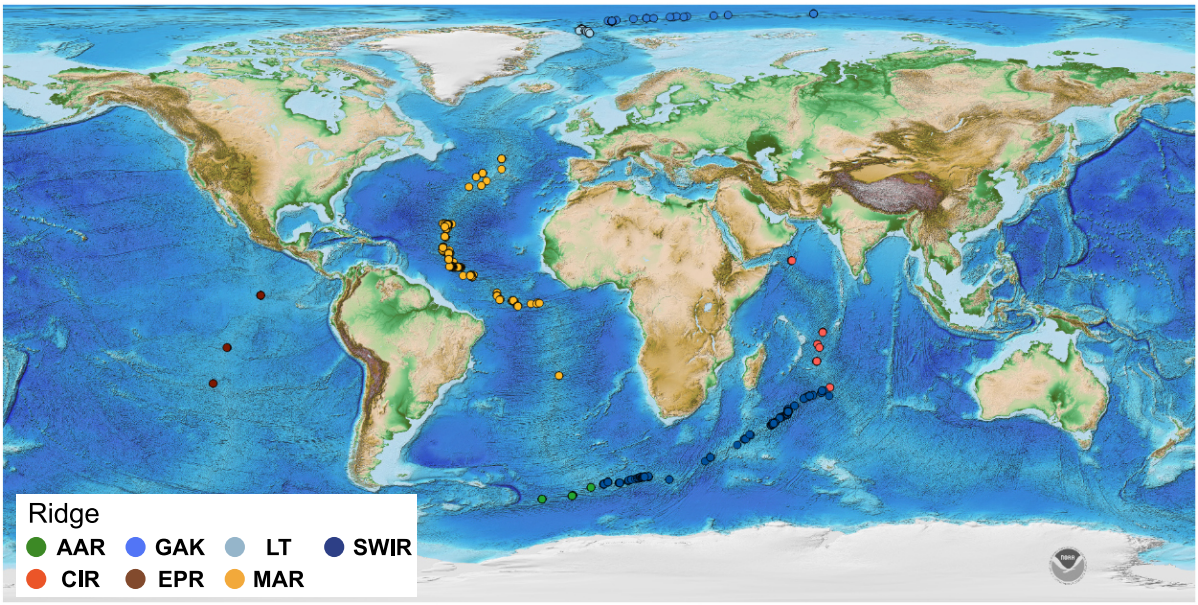

Figure A1: Global distribution of residual abyssal peridotite samples (n = 1162), are from the American-Antarctic Ridge (AAR; n = 43), Central Indian Ridge / Carlsberg Ridge (CIR; n = 35), East Pacific Rise (EPR; n = 49), Gakkel Ridge (GAK; n = 25), Lena Trough (LT; n = 25), Mid-Atlantic Ridge (MAR; n = 657), Southwest Indian Ridge (SWIR; n = 286).

Figure A2 Elbow method for identifying the optimal number of clusters

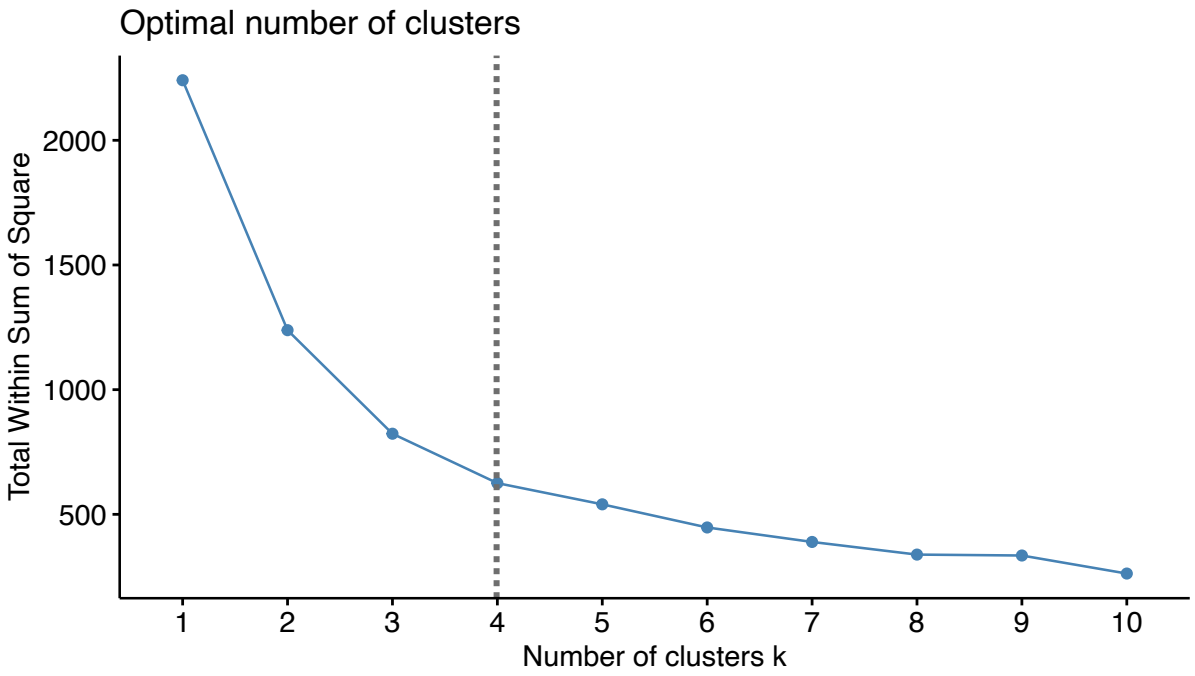

Figure A2: Elbow method for identifying the optimal number of clusters. The total within-cluster sum of the square is defined as follows. K is a cluster number and Ck is cluster k. x is a sample point belonging to cluster Ck. μk is the centroid of cluster k.

$$\text{Total within sum of square} = \sum_{k=1}^{k} \sum_{x \in C_k} (x_i - \mu_k)^2$$

Figure A3 Primitive mantle normalized trace elements patterns of modeled clinopyroxene

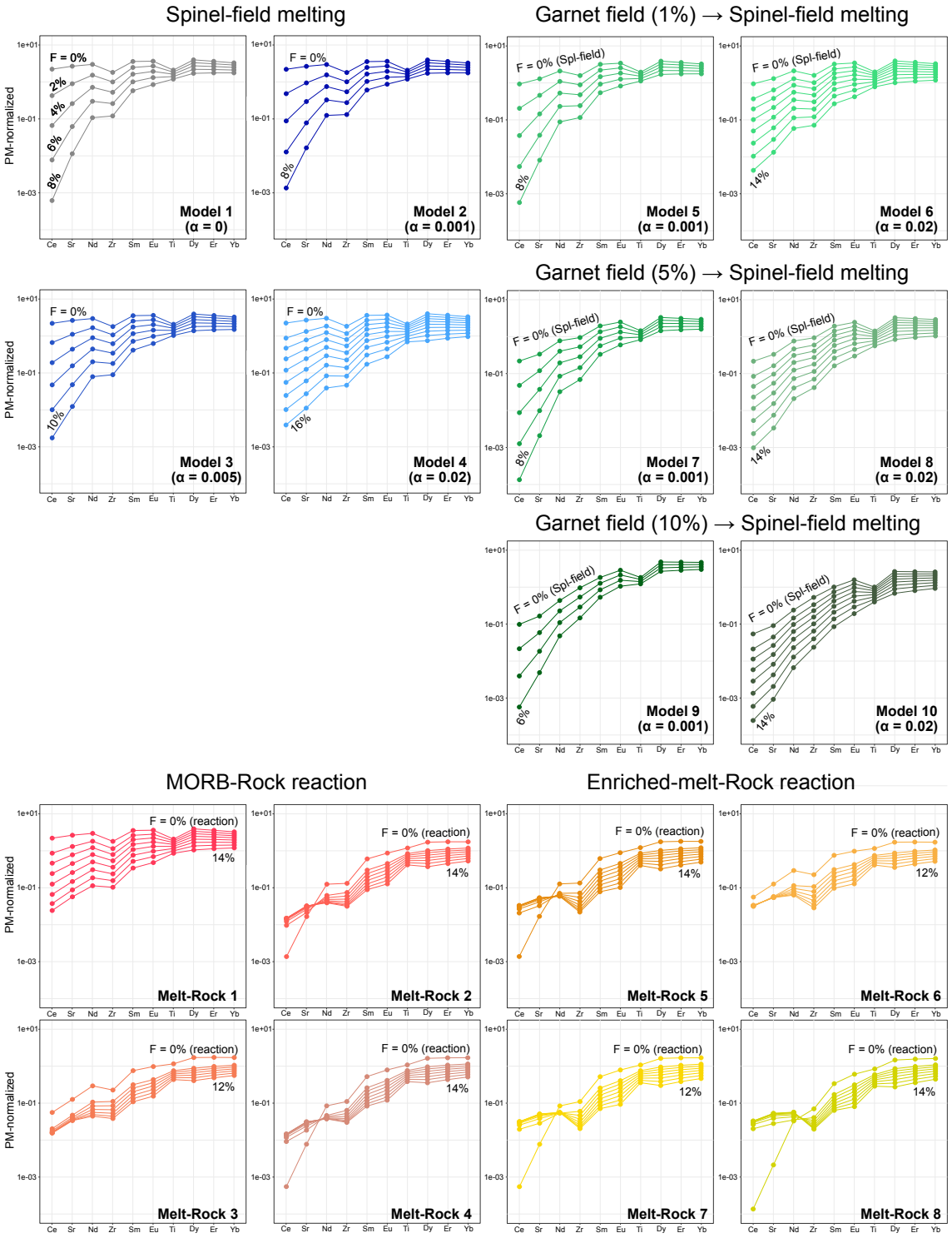

Figure A3: Primitive mantle normalized trace elements patterns of modeled clinopyroxene. See table 1/main text for description of melting parameters.

Figure A4 Olivine – spinel compositional relations in clusters 1–4

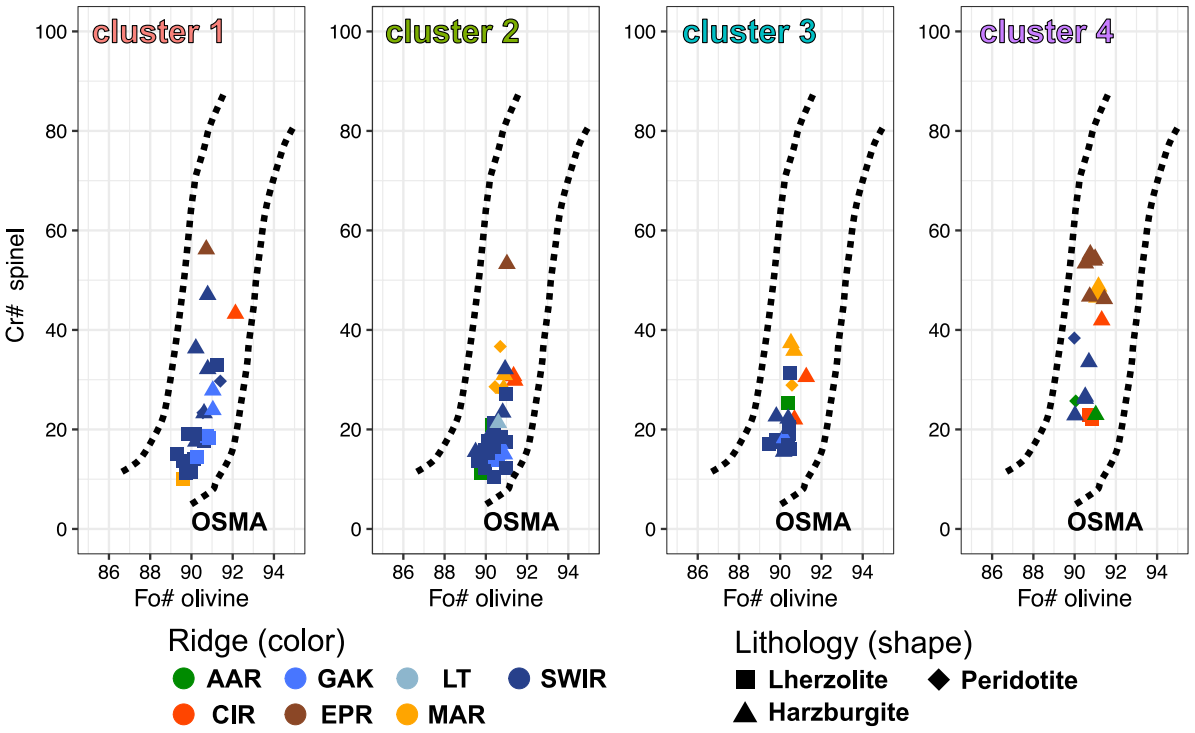

Figure A4: Olivine – spinel compositional relations in clusters 1–4. The field between the dashed lines is the olivine-spinel mantle array (OSMA) (Arai, 1994).

Figure A5 Correlations between principal components and mineral major elements compositions

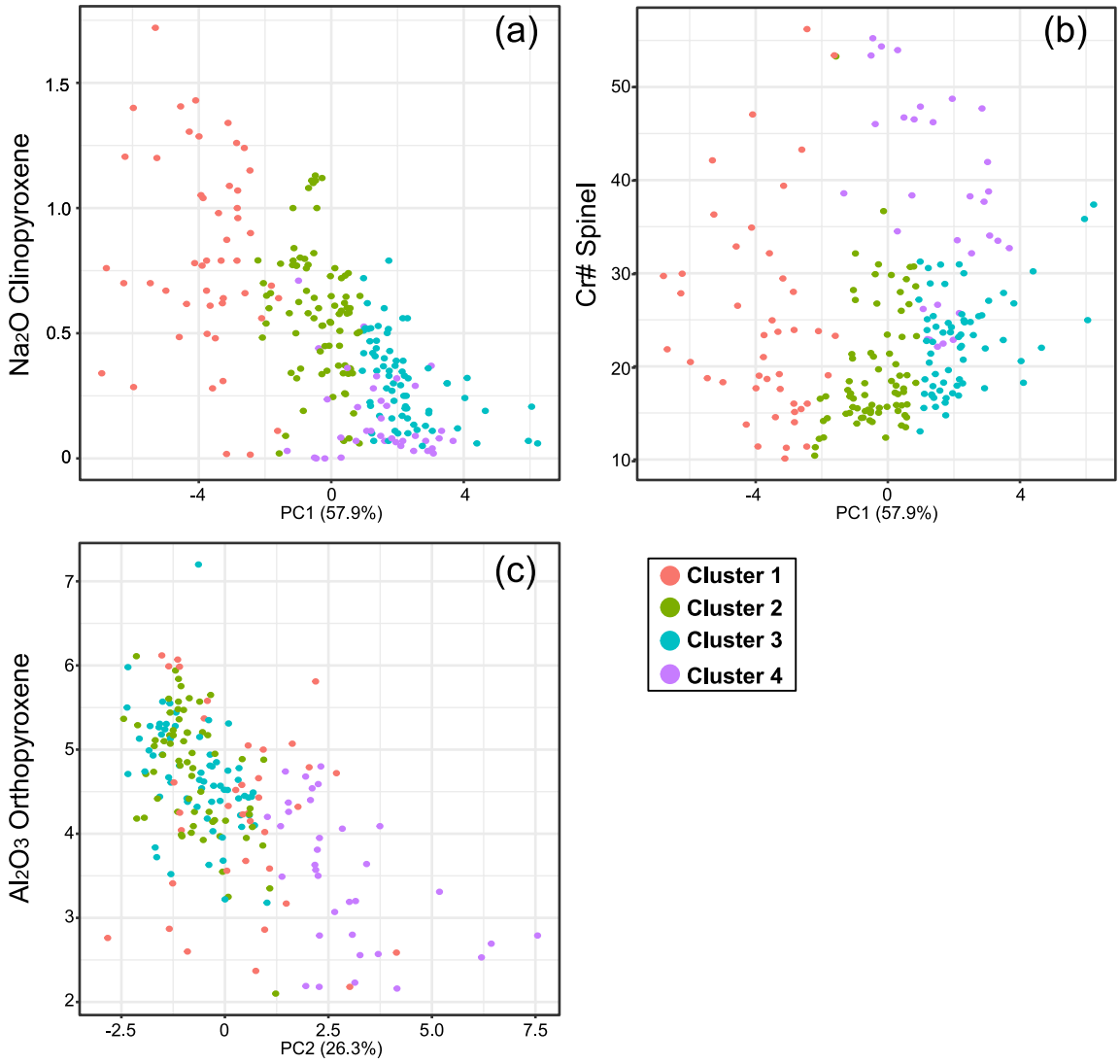

Figure A5: Correlations between principal components and mineral major elements compositions. (a) PC1 vs. Na_2O contents in clinopyroxene. (b) PC1 vs. Cr# of spinel. (c) PC2 vs. Al_2O_3 contents in orthopyroxene.

Figure A6 Global distribution of clusters 1–4 residual abyssal peridotites

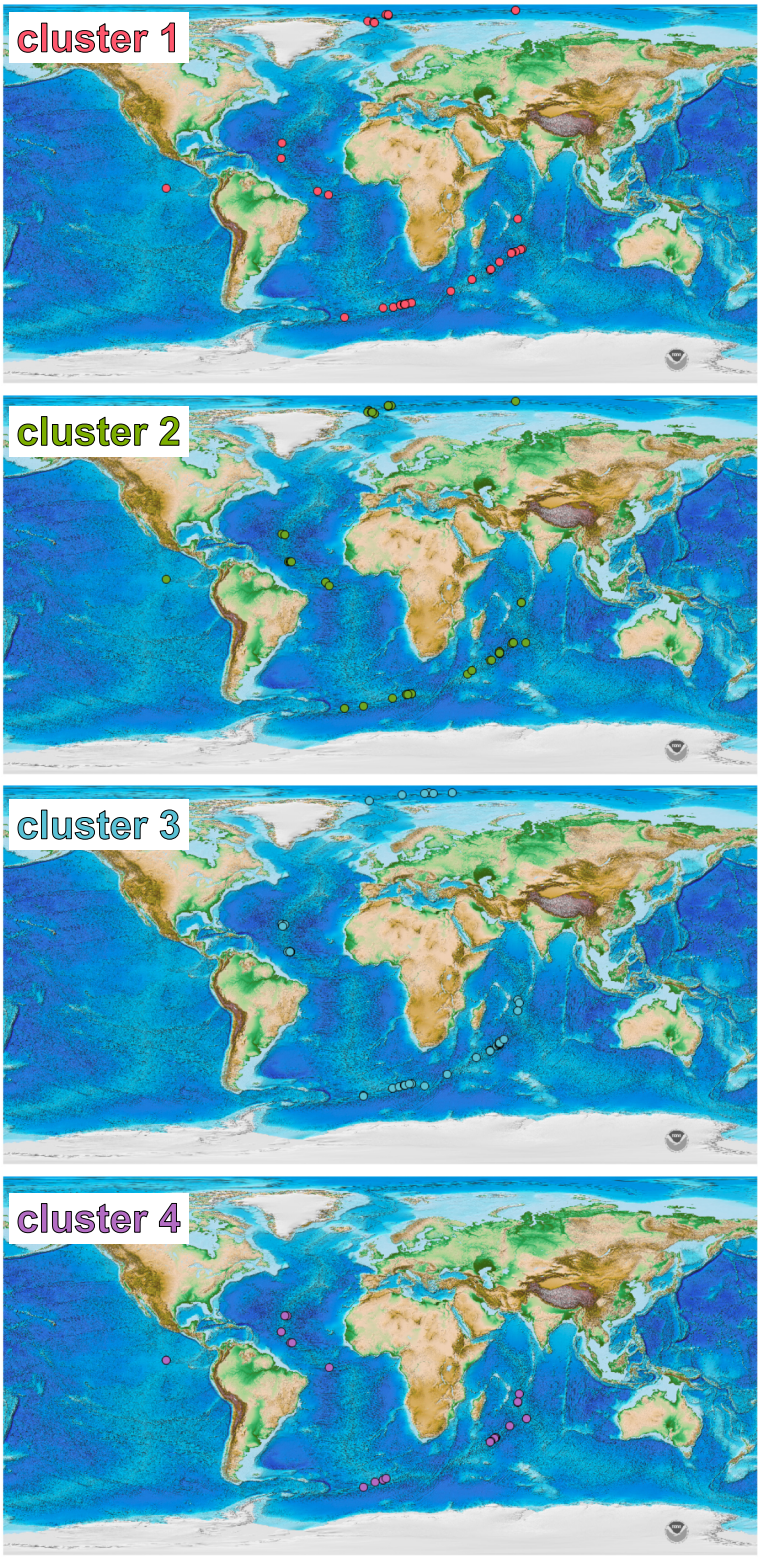

Figure A6: Global distribution of residual abyssal peridotite samples classified by cluster of clinopyroxene they contain.

8.2 Supplementary information for chapter 3

Figure A7 Mineral mode of the ultra-depleted peridotites

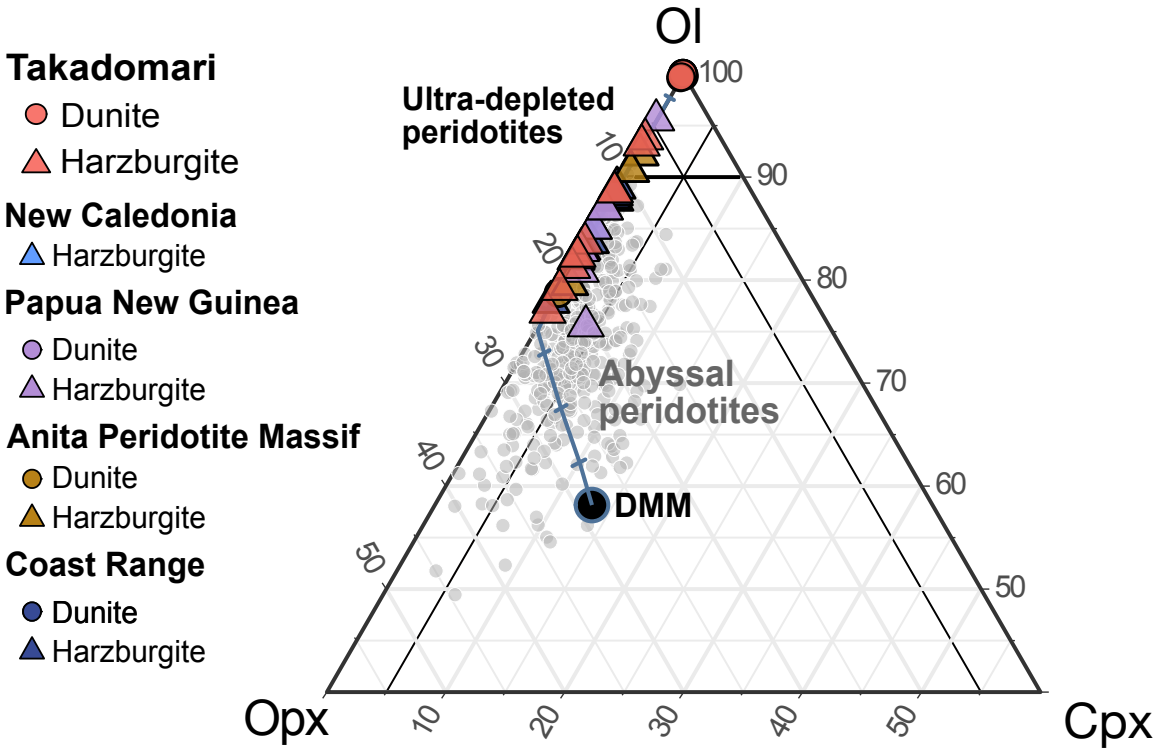

Figure A7: Clinopyroxene-free ultra-depleted peridotite modes. DMM indicates the depleted MORB mantle source composition from Workman and Hart (2005). The blue line shows the degree of melting for the melting reaction 0.05Spl + 0.45Opx + 0.75Cpx → 0.25Ol + 1Melt for clinopyroxene-bearing assemblage and 0.2Ol + 0.003Spl + 0.797Opx → 1Melt for clinopyroxene-free assemblage with tick marks indicating increments of 5% melting (simplified from Kinzler and Grove (1992) and Parman and Grove (2004)). Gray circles indicate residual abyssal peridotites mode (Nishio et al., 2022a; Warren, 2016).

Figure A8 Ti and Sr abundances in orthopyroxenes from the ultra-depleted peridotites

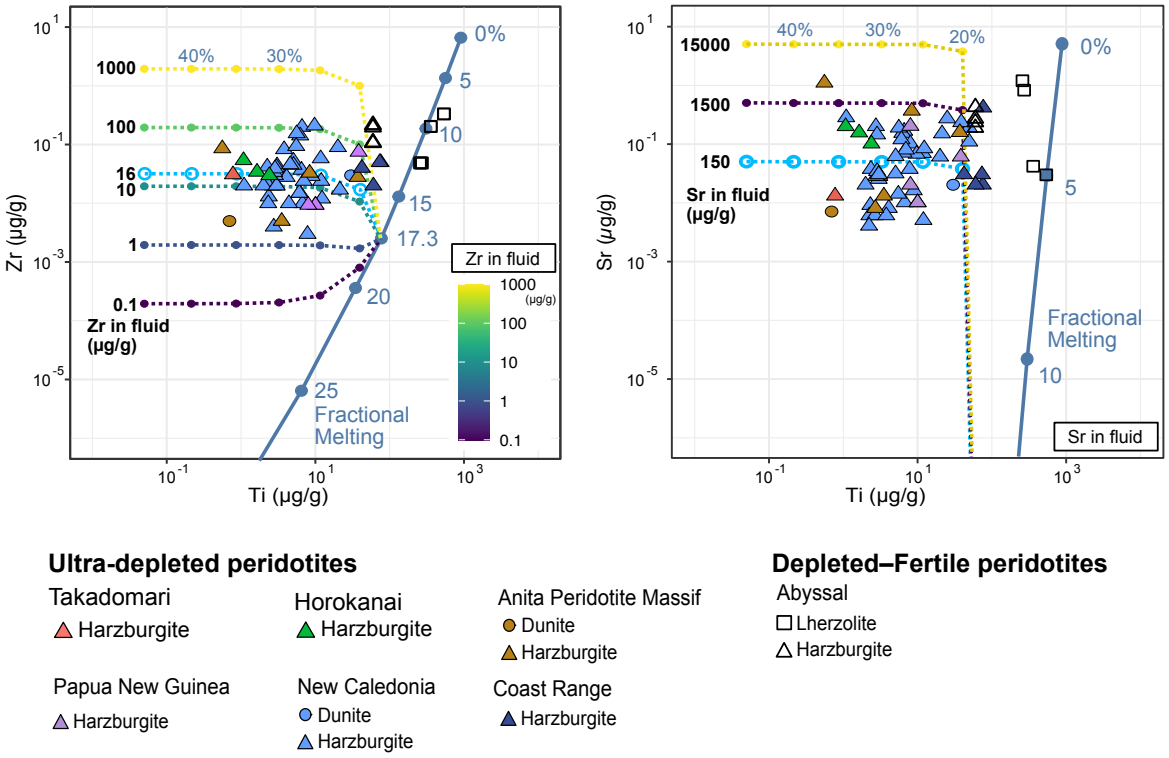

Figure A8: Zr and Ti (Fig. 7b) and Sr and Ti abundances in orthopyroxenes. Orthopyroxene compositions from abyssal peridotites are from D'Errico et al. (2016). The blue solid line is the compositional trend reproduced by the fractional melting model. The dotted lines are the compositional trend reproduced by the open-system melting model, i.e., influx melting with starting compositions formed after 17.3% of fractional melting from DMM. We varied Zr and Sr abundances in fluid ranging from 0.1–1000 µg/g and 150–15000 µg/g, respectively. References to the ultra-depleted peridotites data are listed in Figure 13.

8.3 Supplementary information for chapter 4

Figure A9 Microphotographs and BSE images of locality 1 Tr-Orthopyroxenite

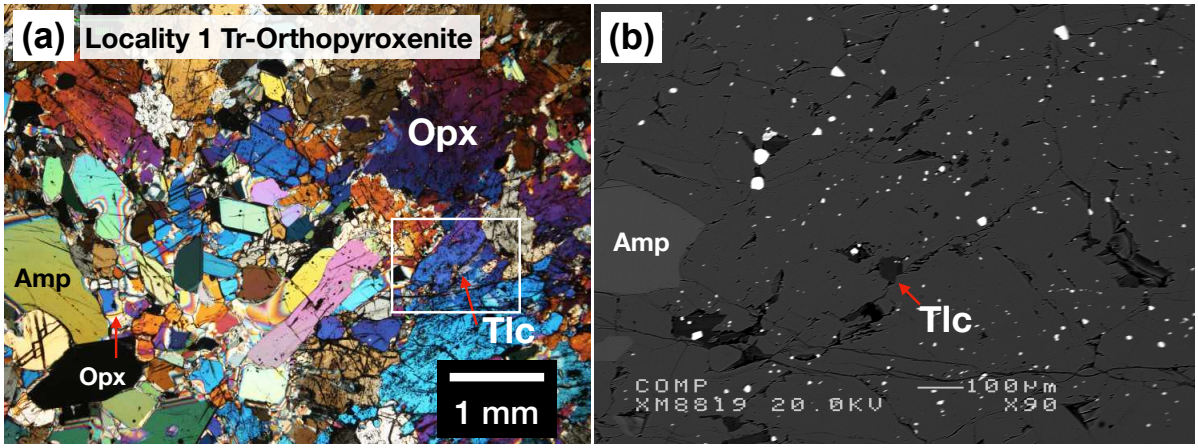

Figure A9: (a) Coarse-grained orthopyroxene (Opx) with spinel (Spl) grains in locality 1 Tr-Orthopyroxenite (Figure 25c). (b) Talc (Tlc) is observed at the grain boundary of orthopyroxene and along the cleavages.

Figure A10 Representative field photograph and interpretative sketches of the Locality 2 lithologies

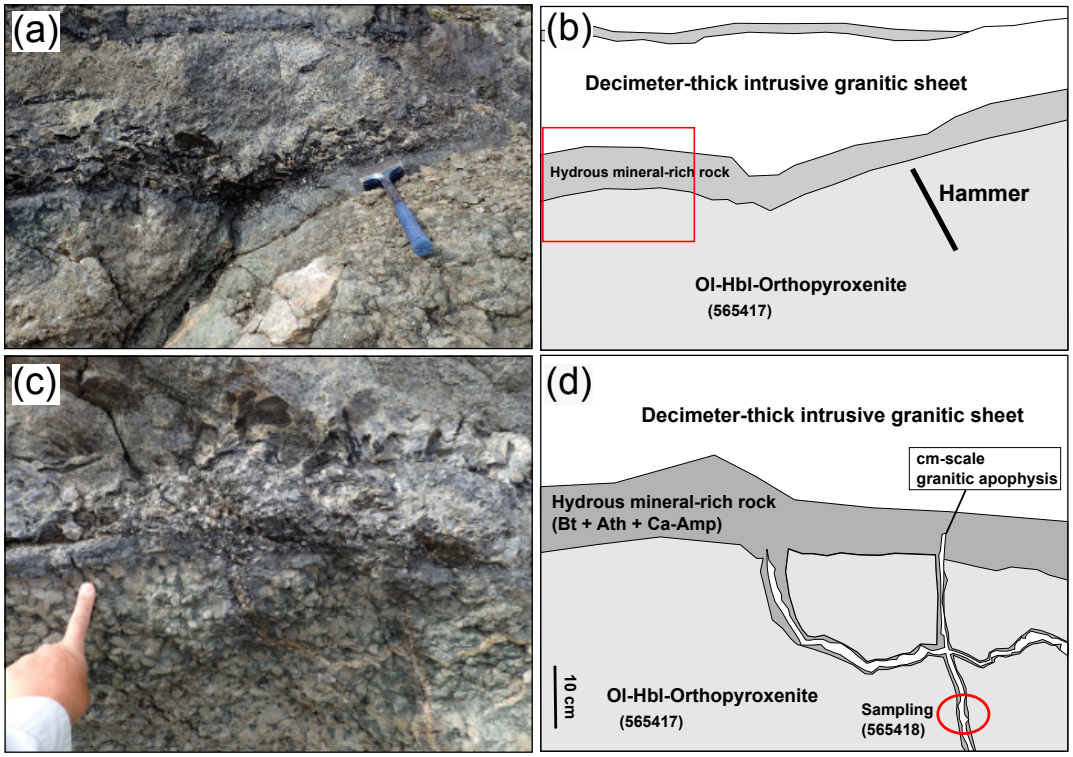

Figure A10: Field photos and simplified sketch of the Locality 2 lithologies. (a) the field photo and (b) the sketch of the decameter-thick granitic intrusion and related olivine-hornblende-orthopyroxenite (Ol-Hbl-Orthopyroxenite, Sample No. 565417). Red square is the area of (c) and (d). (c) the photo and (d) the sketch of the centimeter-scale granitic apophysis from decameter-scale granitic intrusion. The metasomatic rock (sample No. 565418) related to the cm-scale branch was collected in the red circle. Hydrous mineral-rich layer between decameter-scale granitic intrusion and Ol-Hbl-Orthopyroxenite consists of biotite (Bio), anthophyllite (Ath) and calcic amphibole (Ca-Amp).

Figure A11 Modal abundance of constituent minerals of the main body ultramafic rocks.

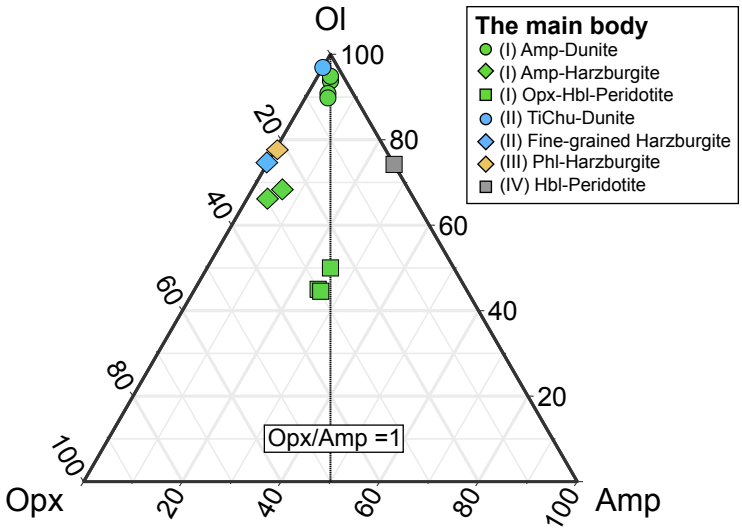

Figure A11: The ratio between orthopyroxene and amphibole are similar in type I Amp-Dunite and Opx-Hbl-Peridotite. The abundance of amphibole is less than that of orthopyroxene in type I Amp-Harzburgite.

Figure A12 Relationships between forsterite contents, Mg# of orthopyroxene, and modal abundance of orthopyroxene and/or amphibole

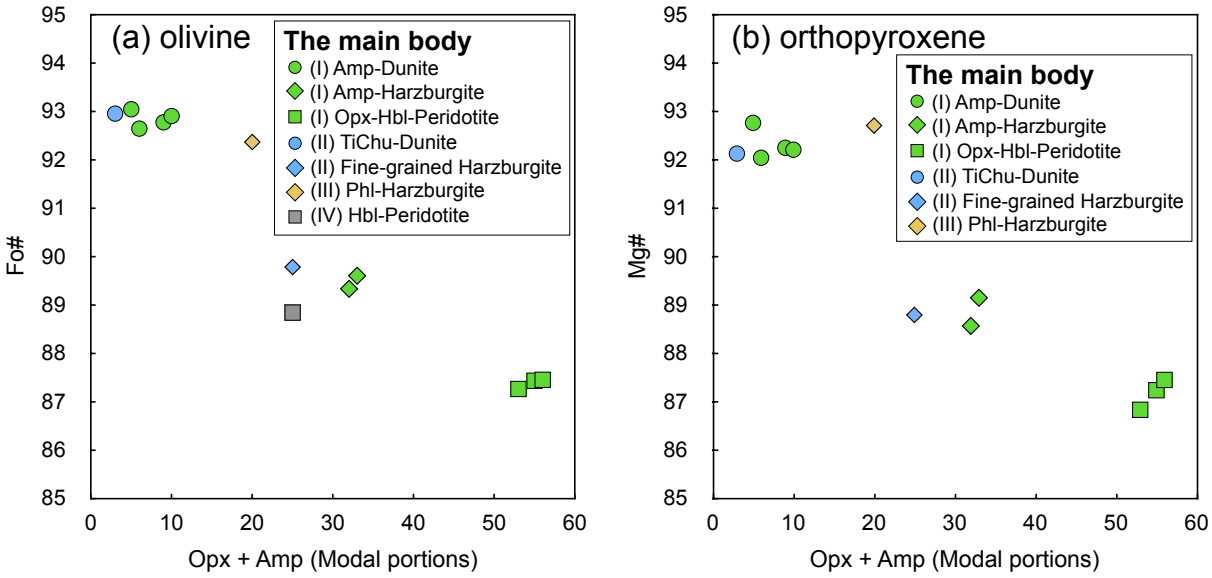

Figure A12: (a) Forsterite content (Fo#) and (b) Mg# of orthopyroxene vs. modal abundance of orthopyroxene and/or amphibole for the main body ultramafic rocks. Fo# and Mg# of orthopyroxene of type I ultramafic rocks negatively correlate with the modal abundance of orthopyroxene and/or amphibole.

Figure A13 Major elements compositions of orthopyroxene

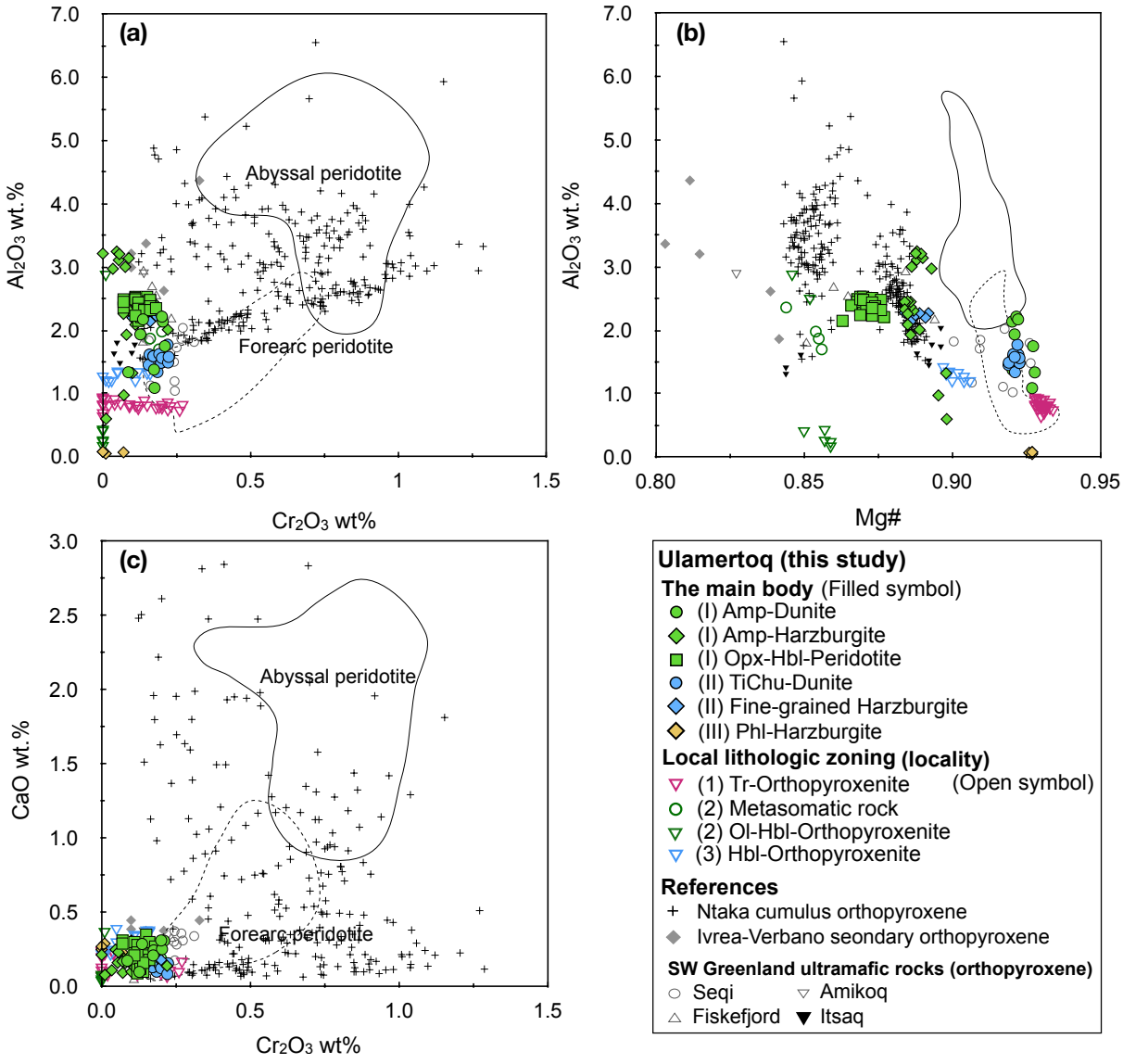

Figure A13: Major elements chemistry of orthopyroxene. (a) Al_2O_3 wt. % versus Cr_2O_3 wt. %; (b) Al_2O_3 wt. % versus Mg#; (c) CaO wt. % versus Cr_2O_3 wt. % plots of orthopyroxenes. Compositions of orthopyroxenes in peridotites from the Akia terrane (Aarestrup et al., 2020; Szilas et al., 2018, 2015), the Itsaq area of southern West Greenland (Friend et al., 2002), secondary orthopyroxenes which formed by cumulus-melt reaction (Berno et al., 2020), cumulus orthopyroxene from Ntaka ultramafic rock (Barnes et al., 2016). Compositional fields of primary orthopyroxene in abyssal peridotites and forearc peridotites are from Parkinson and Pearce (1998) and Warren (2016).

Figure A14 REE + Y compositions of crustal rocks from Akia terrane

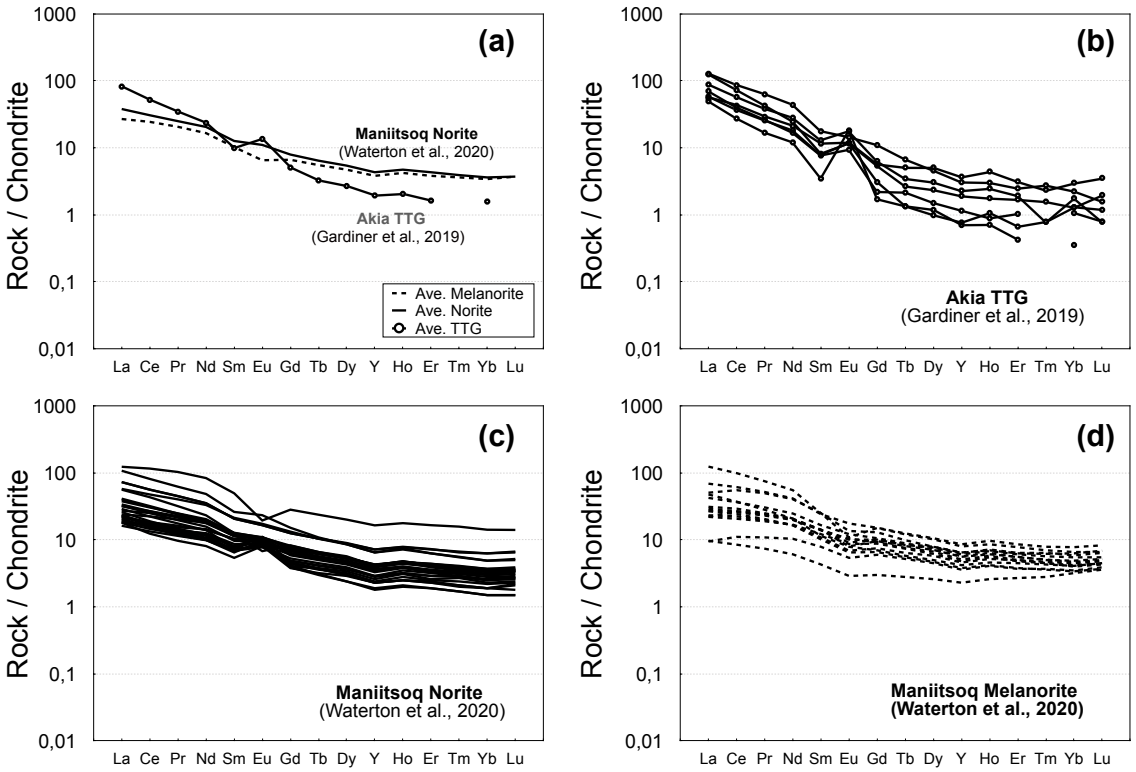

Figure A14: (a) Average REE + Y compositions of crustal rocks from Akia terrane, melanorite, orthopyroxene-rich norite, (Ave. Melanorite; n = 19) and norite (Ave. Norite; n = 27) from Maniitsoq region (Waterton et al., 2020a) and of TTG gneiss (Ave. TTG; n = 7) (Gardiner et al., 2019); (b) REE + Y compositions of TTG gneiss; (c) REE + Y compositions of norite; (d) REE + Y compositions of melanorite.

Figure A15 P-T pseudosections of the Ulamertoq ultramafic rocks

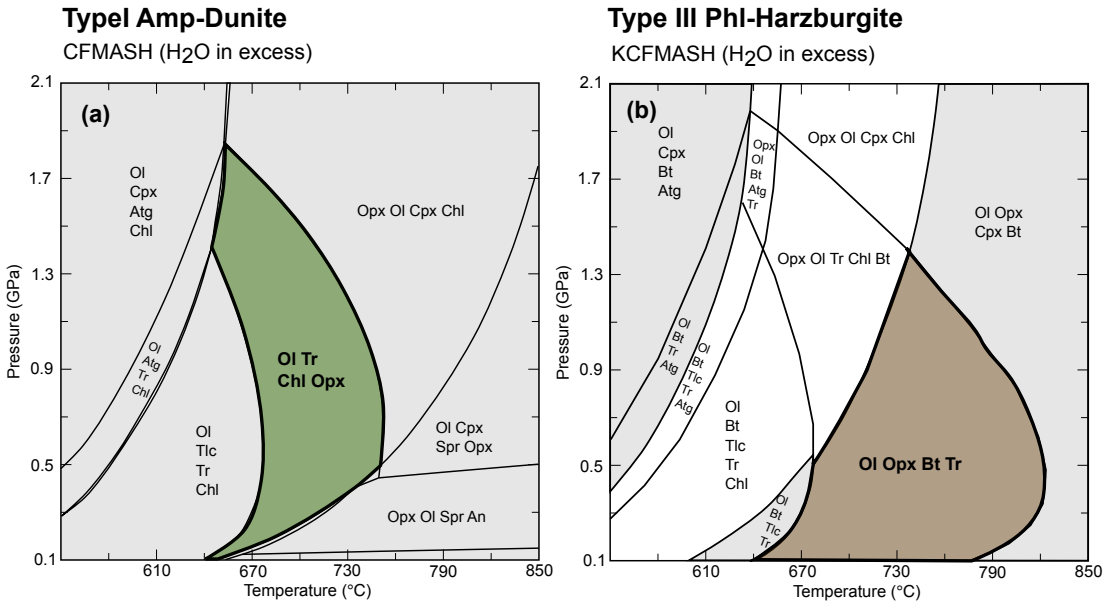

Figure A15: P-T pseudosections showing the stability fields of (a) type I Amp-Dunite, sample 565423 and (b) type III Phl-Harzburgite sample 565428. The abbreviations of the minerals are from Whitney and Evans (2010). Following solid-solution models of minerals were used for the pseudosection model: Orthopyroxene: Opx(HP), Olivine: Ol(HP), Clinopyroxene: Cpx(HP), Talc: T, Chlorite: Chl(HP), Biotite: Bio(HP), Amphibole:GlTrTsPg, Antigorite: Atg(PN), Anthophyllite: oAmph(DP). Solid-solutions of olivine, orthopyroxene, clinopyroxene, talc, chlorite and biotite are from Holland and Powell (1998). Amphibole is from White et al. (2003) and Wei and Powell (2004). Antigorite is from Padrón-Navarta et al. (2013). Anthophyllite is from Diener et al. (2007).

8.4 Supplementary information for chapter 5

8.4.1 Field observations

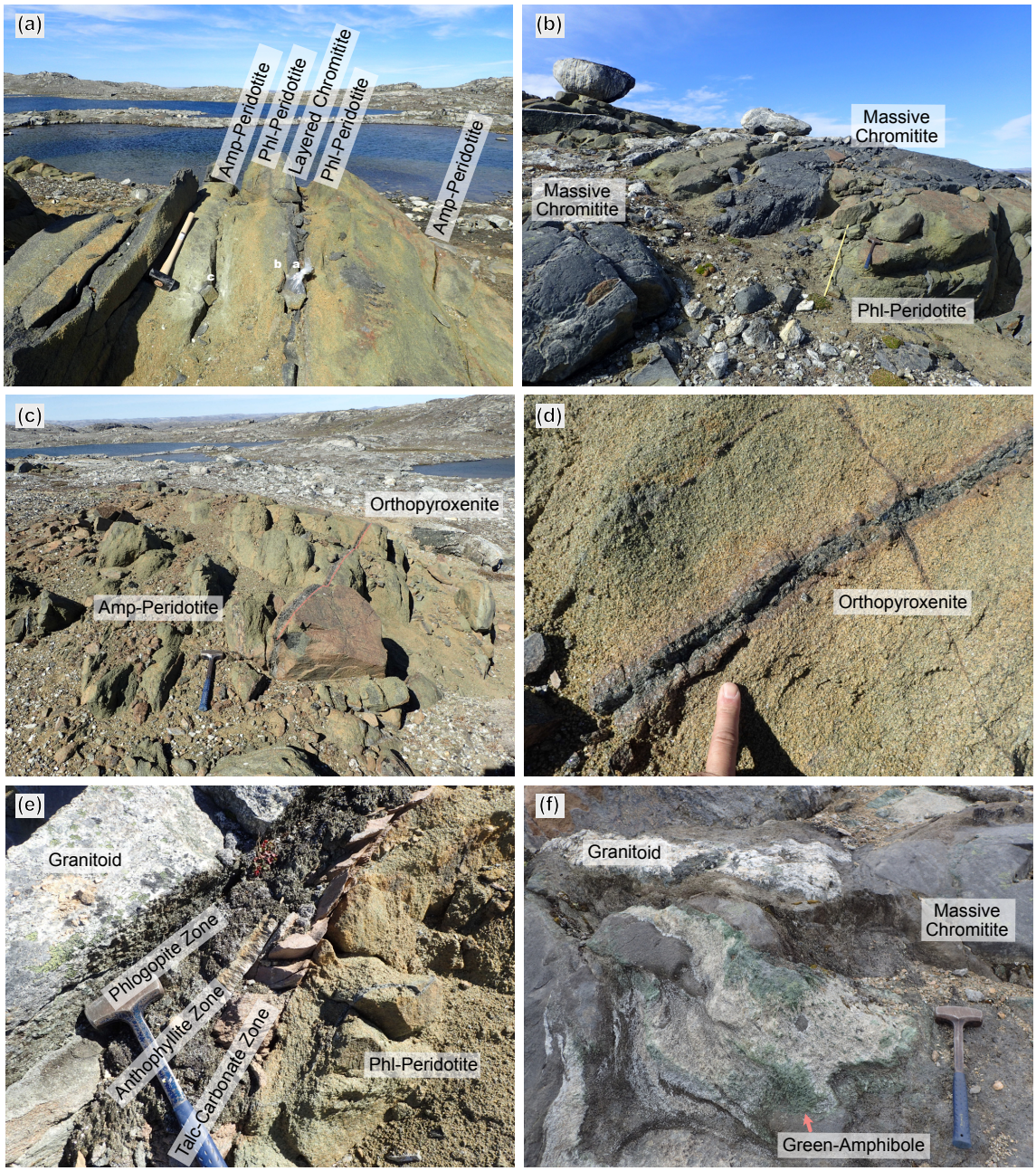

Figure A16: Representative field photographs of the Ujaragssuit ultramafic rocks. (a) Occurrence of layered chromitite and associated peridotite; (b) Occurrence of massive chromitite; (c) Amp-Peridotite which does not host chromitite; (d) Orthopyroxenite cutting peridotite; (e) Hydrous mineral-rich layers consisting of talc-carbonate zone, anthophyllite zone and phlogopite zone, between granitoid sheet and peridotite, (f) Green-amphibole rock between granitoid sheet and massive chromitite.

8.4.2 Methods

8.4.2.1 Micro-XRF analysis

Element-distribution images of entire thin sections and/or the rock chips were cut from for 19 samples were obtained by a micro x-ray fluorescence (XRF) using a Bruker M4-Tornado Plus at the University of Copenhagen and a Bruker M4-Tornado at the Geological Survey of Japan. The measurement was performed using 50 kV accelerating voltage and 600 μA probe current, with a 20–40 μm diameter beam spot and a measurement time was 1–1.5 msec/pixel. Modal abundances of minerals were determined based on the arbitrary element intensity and confirmed with the microphotograph observations and mineral composition.

8.4.2.2 Whole-rock major and trace element analysis

A total of 22 samples (7 chromitites, 12 peridotites, and 3 orthopyroxenites) were selected for whole-rock major and trace element analysis. They were cut using a diamond saw and then washed in an ultrasonic bath to avoid contamination. All sample powders were prepared by mild steel jaw crushing followed by agate milling. Ultramafic rocks require quartz dilution for XRF because the elevated Mg concentration can cause crystallization in the glass bead. Therefore, a separate aliquot was prepared for inductively coupled plasma mass spectrometry (ICP–MS) and was ground in a steel mill. Whole-rock major and trace element analyses were acquired from the geochemical laboratory at GeoAnalytical Lab, Washington State University, USA, using procedures involving flux-fusing of rock powders followed by applying standard XRF and ICP–MS methods. Potential contamination from the Li-tetraborate flux was corrected by a blank subtraction. Repetitive analyses (BCR-P and GSP-1) conducted for precision evaluation show relative a standard deviation of 0.5% for XRF major elements analysis, 5% for Rare Earth Elements (REEs), and 10% for the remaining trace elements analyzed using ICP–MS. The full analytical procedures are described by Johnson et al. (1999).

8.4.2.3 Platinum-group element (PGE) analysis

PGE data for 19 samples (6 chromitites, 10 peridotites, and 3 orthopyroxenites) were obtained at Université du Québec à Chicoutimi (UQAC) by NiS-FA pre-concentration and measurement by ICP-MS following the procedures of Savard et al. (2010), which are summarized below. 15 grams of sample powder is mixed in a ceramic crucible with analytical grade fluxes: sodium carbonate (10 g), sodium tetraborate (15 g), silica (5 g), nickel (5 g), and sulfur (3 g). A further 15 g of sodium tetraborate was added on top after mixing. After fusion in a muffle furnace (1050°C) for 90 min, the NiS bead was separated from the cooled slag and dissolved for 24 hr in 160 ml of 12 mol/l HCl (environmental grade) in a 180 ml closed PFA jar placed in a vented oven (110°C). After complete dissolution of the NiS bead,

stannous chloride dihydrate ($SnCl_2 \cdot 2H_2O$) (4 g) previously dissolved with 9 ml of 3.24 mol/l HCl and 3 ml of 2000 µg/g tellurium solution was added to the dissolved bead. The PFA jars were placed in the oven (at 110°C) for 24 hr. After cooling, the black precipitate was recuperated on a 0.45 lm cellulose membrane filter, thoroughly rinsed with ca. 50 ml of 1 mol/l HCl, and then dissolved in a mixture of 2 ml HCl and 2 ml HNO_3 (concentrated environmental grade) in the PFA jar with the lid sealed, on a hot plate (at 120°C) for 12 hr. After complete digestion, the acid solution was diluted with de-ionized water (18.2 MΩ cm) to a total volume of 25 ml, and the PGE and Au were determined by ICP-MS (Thermo Elemental X7 series; Thermo Fisher Scientific, Waltham, MA, USA) using thallium as a drift monitor. A multiple PGE-Au and Re stock solution (SCP Science, Baie D'Urfé, QC, Canada) was used for external calibration. OKUM, KPT, LK-NIP-1, and AMIS0005 were analyzed for the evaluation of the precision and the accuracy and detection limits are 0.025 ppb for Ir, 0.12 for Ru, 0.082 for Rh, 0.084 for Pt, and 0.471 for Pd (Savard et al., 2010) .

8.4.2.4 Mineral major element analysis

Major-element compositions of minerals were analyzed using an electron probe microanalyzer, a JEOL JXA-8800 at Kanazawa University, and a JEOL JXA-8200 at the University of Copenhagen. The analytical conditions at Kanazawa University were an accelerating voltage of 20 kV and a beam current of 20 nA, using a 3 µm beam diameter, and the conditions at the University of Copenhagen were an accelerating voltage of 15 kV and a beam current of 15 nA, using a 3 µm beam diameter. Natural and synthetic mineral standards were used for calibration, and JEOL software using ZAF corrections was used for data reduction. In-house mineral standards (wollastonite for Si and Ca, albite for Na, orthoclase for K, rutile for Ti, corundum for Al, hematite for Fe, Mn-Ti-oxide for Mn, Marjalathi olivine for Mg, chromite for Cr, Ni metal for Ni) were measured to monitor data quality. The measured concentrations of in-house mineral standards were consistent with the averaged values from long-term analyses, being within one standard deviation for major elements. Data precision was established through multiple analyses of one point in the house-prepared standard minerals and was better than 5% and 10 % relative standard deviation from the averaged values for elements with abundances of > 0.5 wt. % and < 0.5 wt. %, respectively.

8.4.2.5 Mineral trace element analysis

Rare earth element (REE) and trace element compositions of hydrous minerals and orthopyroxene were determined using 193 and 213 nm ArF excimer laser ablation-inductively coupled plasma-mass spectrometry (LA-ICP-MS) at Kanazawa University (Agilent 7500S equipped with MicroLas GeoLas Q-plus and New Wave Research UP-213). Hydrous minerals and orthopyroxene were analyzed by ablating 50-90 µm and > 90 µm spot diameters, respectively, at 6 Hz. The NIST SRM 612 standard was used as the primary calibration standard and was analyzed at the beginning of each batch ($n \leq 8$)

unknowns, with a linear drift correction applied within each analytical session. The NIST SRM 612 compositions were selected from the preferred values of Pearce et al. (1997). Data reduction was performed using ^{29}Si as an internal standard, based on SiO_2 contents obtained by EPMA following the protocol outlined by Longerich et al. (1996). NIST SRM 614 and BCR-2G were analyzed for quality control during measurement. The measured concentrations in NIST SRM 614 and BCR-2G were consistent with previously reported values (Morishita et al., 2005a, 2005b) to within 10 % relative standard deviation, and the data precision was better than 10 % relative standard deviation for all the analyzed elements. Details of the analytical method and data quality control are given by Morishita et al. (2005a, 2005b).

Trace element compositions (Sc, Ti, V, Mn, Co, Ni, Zn, Ga) of spinel from chromitite were determined using 193 nm ArF excimer laser ablation-inductively coupled plasma-mass spectrometry (LA-ICP-MS) at the University of Copenhagen (Agilent 7900 equipped with Teledyne Photon Machines Analyte Excite). Spinel was analyzed by ablating 50 μm spot diameters at 10 Hz. The NIST SRM 610 standard was used as the primary calibration standard and was analyzed at the beginning of each batch ($n \leq 8$) unknowns, with a linear drift correction applied within each analytical session. Data reduction was facilitated using ^{27}Al as an internal standard, based on Al_2O_3 contents obtained by EPMA. NIST SRM 612 (Pearce et al., 1997), KL2-G, ML3B-G, and StHs80/6-G (Jochum et al., 2006) were analyzed for quality control during measurement following the methodology from González-Jiménez et al. (2017) and Søager et al. (2018).

8.4.3 Archean to Proterozoic layered intrusion chromitites

8.4.3.1 Chromitite dataset

To understand the primary magma compositions of layered intrusions, we compiled spinel major and trace element compositions, and whole-rock PGE data of the Archean to Proterozoic layered intrusion chromitite hosted by ultramafic rock (Figure A17 and Table S1). The chromitite host ultramafic rocks are mostly peridotite (dunite), serpentinite, and orthopyroxenite. The location, age, and references for each intrusion are listed in Table S1. For comparison, we also collected spinel data from high-Cr chromitite in the mantle section of supra-subduction zone ophiolite and spinel data from volcanic rocks (komatiite, picrite and boninite), which are listed in Table S2.

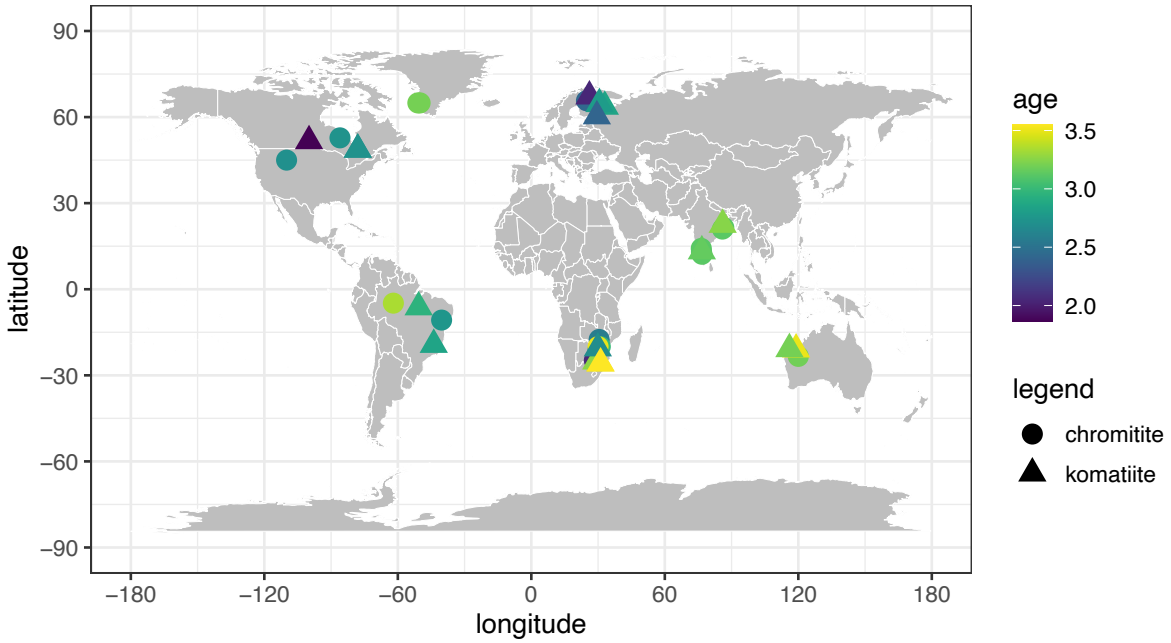

Figure A17: Location of the layered intrusion chromitite hosted by ultramafic rock. Location of komatiites were plotted for comparison (Chaudhuri et al., 2015; Maya et al., 2017; Siepierski and Ferreira Filho, 2016; Waterton et al., 2021). The ages of the layered intrusions are from Smith and Maier (2021).

Table S1: List of Archean to Proterozoic layered intrusion chromitite dataset

Location	Craton / Region	Age (Ga)	Spinel major	Spinel trace	Whole-rock PGE
Ujaragssuit	North Atlantic	3.2 (Sawada et al., 2023)	This study	This study	This study
Seqi, Ulamertoq	North Atlantic	3.2	(Guotana et al., 2018; Szilas et al., 2018)	(Szilas et al., 2018)	(Szilas et al., 2018)
Fiskenæsset	North Atlantic	2.973	(Rollinson et al., 2017)	-	-
Coobina	Pilbara	3.189	(Barnes and Jones, 2013)	(Schoneveld et al., 2022)	(Barnes and Jones, 2013)
Stillwater (G, B)	Wyoming	2.7	(Barnes et al., 2023; Su et al., 2020)	(Schoneveld et al., 2022)	Barnes et al. (2015)
Ring of Fire	Sperior	2.7341	(Laarman, 2014)	(Laarman, 2014)	Laarman (2014)
Sukinda, Nuasahi	Singhbhum	3.123	(Mondal et al., 2006)	-	(Khatun et al., 2014; Mondal et al., 2019; Mondal and Zhou, 2010)
Nuggihalli, Chithradurga etc.	Dharwar	3.12	(Datta et al., 2021; Mukherjee et al., 2015, 2010; Santosh et al., 2020)	(Mukherjee et al., 2015)	(Mukherjee et al., 2014; Santosh et al., 2020)
Inyala, Selukwe, Great dyke	Zimbabwe	Inyala 2.7, Selukwe 3.3 Great dyke 2.5 (Nägler et al., 1997)	(Barnes et al., 2023; Prendergast, 2008; Rollinson, 1997; Wilson, 1982)	(Barnes et al., 2023)	(Wilson and Prendergast, 2001)
Bacuri	Amazonian	3.34 (Spier et al., 2022)	(Prichard et al., 2001; Spier and Filho, 2001)	-	(Prichard et al., 2001)
Campo Formoso etc.	Sao Francisco	2.75 (Marques et al., 2003)	(Friedrich et al., 2020; Garuti et al., 2007; Lord et al., 2004; Marques et al., 2017; Marques and Filho, 2003)	-	(Garuti et al., 2007; Lord et al., 2004; Marques et al., 2003)
Kemi	Lapland	2.43	(Alapieti et al., 1989)	-	-
Bushveld, Uitkomst	Kaapvaal	2.056	(Barnes et al., 2023; Naldrett et al., 2009; Yudovskaya et al., 2015)	(Barnes et al., 2023)	(Naldrett et al., 2009)

Table S2: List of supra-subduction zone (+subarc xenolith) high-Cr chromitite and spinel from volcanic rocks dataset

Location	Type	Spinel major	Spinel trace	Whole-rock PGE
Tres Amigos	SSZ Ophiolite	(González-Jiménez et al., 2011)	(González-Jiménez et al., 2015)	(González-Jiménez et al., 2011)
Thetford	SSZ Ophiolite	(Pagé and Barnes, 2009)	(Pagé and Barnes, 2009)	(Pagé et al., 2012)
La Guajira	SSZ Ophiolite	(Ramírez-Cárdenas et al., 2023)	(Ramírez-Cárdenas et al., 2023)	(Ramírez-Cárdenas et al., 2023)
El Tigre, San Cristóbal, San Agustín	SSZ Ophiolite	(González-Jiménez et al., 2017)	(González-Jiménez et al., 2017)	(González-Jiménez et al., 2017)
Waji Rajimi	SSZ Ophiolite	(Miura and Arai, 2014)	-	(Miura and Arai, 2014)
Takashima	Subarc Xenolith	(Miura and Arai, 2014)	-	(Miura and Arai, 2014)
Location	Type	Spinel major	Spinel trace	Spinel PGE
	Komatiite/Picrite	(Barnes et al., 2023; Barnes and Roeder, 2001)	(Barnes et al., 2023; Park et al., 2017)	(Pagé et al., 2012; Pagé and Barnes, 2016; Park et al., 2017; Puchtel et al., 2016, 2004)
IBM, Thetford, Troodos etc.	Boninite	(Barnes and Roeder, 2001; Pagé and Barnes, 2009; Park et al., 2017)	(Hu et al., 2023; Pagé and Barnes, 2009; Park et al., 2017)	(Pagé and Barnes, 2016; Park et al., 2017)

8.4.3.2 Statistical analysis and machine learning methods

We conducted centered log-ratio transformation and independent component analysis following the method of Itano et al. (2023) and Nishio et al. (2022). Compositional data, including spinel major element compositions, consists of a matrix of nonnegative, relative values with a constant sum (Aitchison, 1982). Concentrations are dependent on the concentrations of other elements because the compositional data has a constant sum (i.e., values must sum to 100 wt.%). n-dimensional data (where n = number of elements) are plotted on an n−1 dimensional space. Therefore, there is potential for pseudo-correlations, for example, where increase in one major element causes the concentration of all others to decrease. Log-transformed ratios are key for the treatment of compositional data as they emphasize relative magnitudes and variations in components rather than absolute values.

We then conducted independent component analysis (ICA) on the log-transformed data. ICA reduces the dimensionality of a data set to find important factors or components from multivariate data (Hyvärinen and Oja, 2000), such as log-transformed compositional data. ICA is an extension of principal component analysis (PCA) where, in contrast to PCA, the various independent components derived are not required to be orthogonal. The various independent components (IC1, IC2, etc.) are chosen to describe the largest amount of variability in the data.

8.4.3.3 Results of statistical analysis and machine learning methods

The results of ICA highlight differences and similarities between spinel compositions from various tectonic settings and parental magma types. High IC1 values are generated primarily by low MgO/TiO_2 ratios, whereas high IC2 values correspond to high Fe_2O_3/Al_2O_3 ratios. Spinel from the Ujaragssuit body and other layered intrusion chromitites generally have higher IC1 (average -0.4 and 0.22, respectively) and IC2 (0.84 and 0.13) compared to spinel from other settings. SSZ ophiolite chromitite, on the other hand, shows lower IC1 (-1.5) and IC2 (-1.4) values. Therefore, differences in IC1 and IC2 values between SSZ ophiolite chromitite and layered intrusion chromitites largely reflect the lower MgO, and higher TiO_2 and Fe_2O_3 in layered intrusions than in SSZ ophiolites. Indeed, MgO is higher in spinel from SSZ ophiolite chromitite than spinel from layered intrusion chromitite (Barnes and Roeder, 2001). Komatiitic and boninitic spinels have wide ranges of IC1 and IC2 values, but generally, komatiitic spinel has higher IC1 than boninitic spinel.

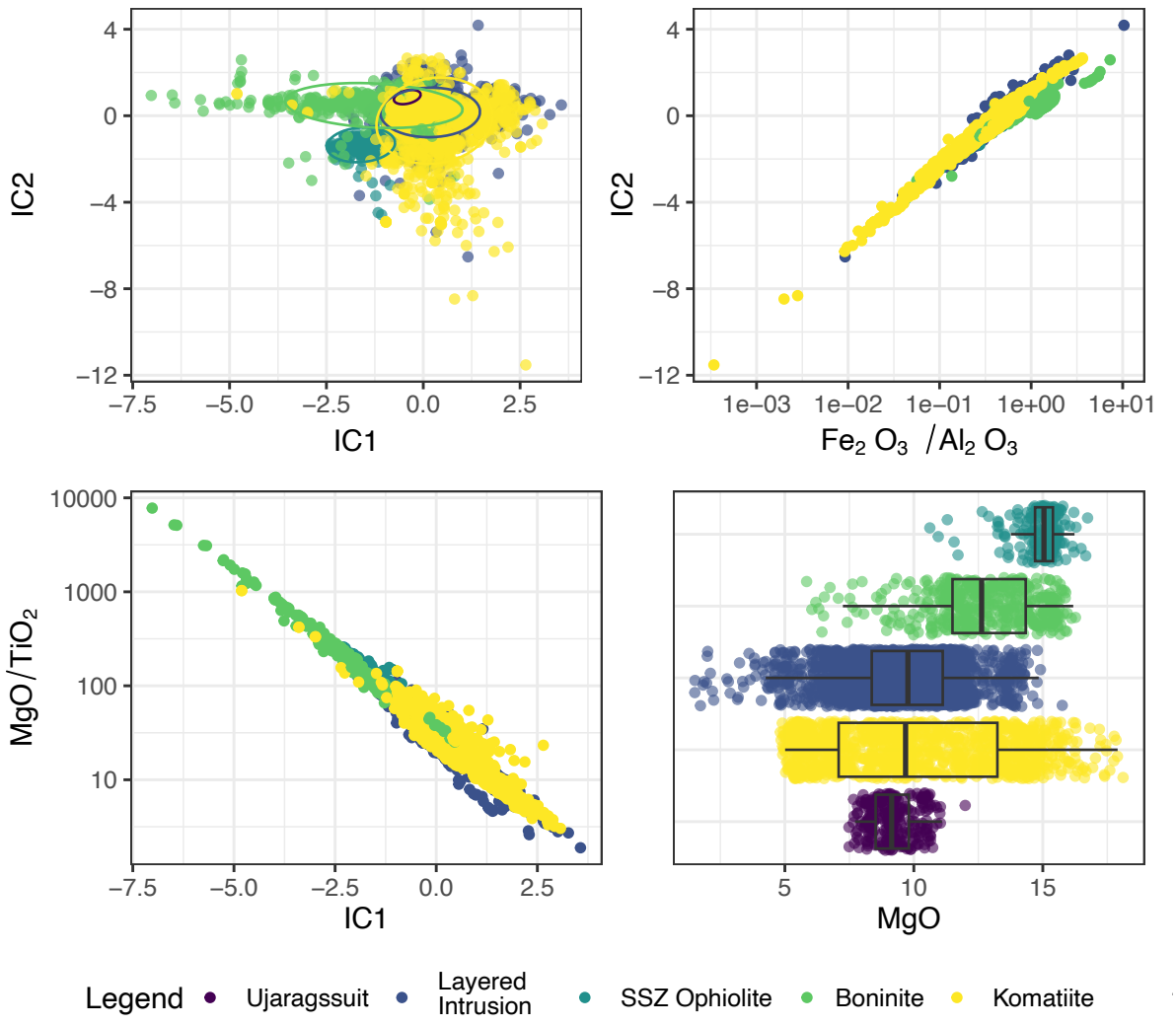

Figure A18: Result of independent component analysis.

8.4.1 Representative spinel major elements composition of the Ujaragssuit ultramafic rocks

Sample	Massive chromitite		Layered Chromitite	Heterogneous layered chromitite
	low-Fe	high-Fe		
TiO_2	0.3	0.8	0.3	0.8
Al_2O_3	13.1	11.2	13.0	13.2
Cr_2O_3	49.7	42.8	40.7	32.7
Fe_2O_3	8.7	12.2	16.0	21.5
FeO	17.6	30.0	25.0	28.1
MnO	0.3	0.6	0.5	0.6
MgO	10.8	2.5	6.1	3.9
NiO	0.1	0.1	0.1	0.1
Total	100.8	100.2	101.7	101.0
Mg#	0.52	0.13	0.30	0.20
Cr#	0.72	0.72	0.68	0.62
$Cr/(Fe^{3+}+Cr+Al)$	0.64	0.60	0.54	0.45
$Al/(Fe^{3+}+Cr+Al)$	0.25	0.23	0.26	0.27
$Fe^{3+}/(Fe^{3+}+Cr+Al)$	0.11	0.16	0.20	0.28

	Phl-Peridotite		Amp-Peridotite	
Massive Chromitite-hosting	Layered Chromitite-hosting	Chromitite-free	Fe-rich phase	Al-rich phase
0.8	0.5	1.1	0.8	1.0
11.2	4.3	0.6	1.8	2.0
42.8	37.4	14.3	10.5	11.3
12.2	25.5	53.4	55.7	54.4
30.0	27.1	29.5	29.1	28.7
0.6	0.5	0.3	0.2	0.2
2.5	3.0	1.0	1.3	1.5
0.1	0.2	0.2	0.3	0.3
100.2	98.7	100.4	99.8	99.6
0.13	0.16	0.06	0.07	0.08
0.72	0.85	0.94	0.80	0.79
0.60	0.55	0.22	0.16	0.17
0.23	0.09	0.01	0.04	0.05
0.16	0.36	0.77	0.80	0.78

Orthopyroxenite			
Phl-Peridotite (Massive Chr)	Phl-Peridotite (Chr-free)	Amp-Peridotite (Chr-free) Al-phase	Amp-Peridotite (Chr-free) Fe-phase
0.9	0.9	0.1	1.1
1.7	6.1	36.1	3.2
30.1	23.0	21.9	18.7
36.6	39.6	8.4	44.6
28.4	28.6	22.9	29.9
0.7	0.4	0.2	0.2
2.1	2.6	9.5	0.9
0.2	0.2	0.2	0.3
101.3	101.3	99.3	99.0
0.12	0.14	0.42	0.05
0.92	0.72	0.29	0.80
0.45	0.33	0.26	0.28
0.04	0.13	0.64	0.07
0.52	0.54	0.10	0.64

Talc-carbonate rock	Green-Amp rock
Phl-Peridotite (Massive)	
0.7	0.1
1.6	8.5
33.8	51.5
31.3	7.5
29.6	29.8
0.5	0.6
1.1	2.3
0.2	0.0
98.7	100.5
0.06	0.12
0.93	0.80
0.51	0.72
0.04	0.18
0.45	0.10

8.4.2 Spinel trace elements composition of the Ujaragssuit chromitites

Rock	massive chromitite	sd (n=70)	layered chromitite	sd (n=71)
Sc	4.9	0.3	4.9	0.2
Ti	1392.8	50.0	1797.4	82.3
V	596.8	19.6	623.2	19.2
Mn	2372.9	68.8	2994.9	97.8
Co	285.8	7.5	290.8	8.0
Ni	796.7	31.6	817.8	50.6
Zn	1281.3	56.3	2721.5	135.3
Ga	31.8	1.0	32.6	1.3

Ref	NIST612 (GeoRem preffered values)	Average	RSD %	KL2-G (GeoRem preffered values)	Average	RSD %
Sc	39.9 ± 2.5	38.8	0.8	31.8 ± 0.9	29.8	0.9
Ti	44 ± 2.3	39.6	1.5	15343 ± 539	14221.2	1.0
V	38.8 ± 1.2	38.6	0.8	309 ± 38	307.4	0.8
Mn	38.7 ± 0.9	38.5	0.8	1277 ±70	1219.8	1.0
Co	35.5 ± 1	35.0	0.7	41.2 ± 2.3	43.7	0.7
Ni	38.8 ± 0.2	38.8	1.3	112 ± 5	114.9	0.9
Zn	39.1 ± 1.7	38.2	1.7	110 ± 10	108.6	1.8
Ga	36.9 ± 1.5	36.5	1.0	20 ± 1.2	20.7	1.3

Ref	ML3B-G (GeoRem preffered values)	Average	RSD %	StHs680-G (GeoRem preffered values)	Average	RSD %
Sc	31.6 ± 1.6	28.2	1.0	11.5 ± 0.8	9.6	1.1
Ti	12766 ± 539	11538.5	0.7	4213 ± 125	3922.8	0.9
V	268 ± 23	278.2	0.8	90.3 ± 6.7	87.3	1.9
Mn	1316 ± 70	1238.6	0.9	589 ± 31	555.7	0.8
Co	41.2 ± 3.5	43.5	1.1	13.2 ±1.1	13.0	1.3
Ni	107 ± 9	109.3	1.1	23.7 ±3.8	20.0	1.9
Zn	108 ± 14	108.8	2.0	67 ± 8	42.5	4.8
Ga	19.6 ± 2.1	19.5	1.2	20.9 ± 2.7	20.5	1.4

8.4.3 Platinum-group element composition of the Ujaragssuit ultramafic rocks

Rock	Ir (ppb)	Ru	Rh	Pt	Pd
Massive Chromitite	82.3	176.2	10.9	9.9	4.1
Orthopyroxenite	3.2	12.8	1.5	0.9	1.1
Phl-Peridotite	2.6	7.0	1.3	1.4	1.7
Amp-Peridotite	1.6	7.9	1.1	1.6	0.6
Detection Limit	0.03	0.12	0.08	0.08	0.47
Reference *OKUM*					
MS35OK-1.D	0.88	4.14	1.29	11.11	11.23
MS36OK-1.D	0.93	4.02	1.32	11.14	11.36
Reference OKUM (OGS)	*0.99 ± 0.07*	*4.25 ± 0.30*	*1.40 ± 0.13*	*11.0 ± 0.6*	*11.7 ± 0.5*